Applications of Multiple Quantum Well Saturable Absorbers in Long Distance Ultrafast Optical Fibre Transmission Systems

Edman P. Burr

A thesis submitted to the University of London for the Degree of Doctor of Philosophy
in Electronic Engineering

Department of Electronic and Electrical Engineering
University College London
June 2003

ProQuest LLC
789 East Eisenhower Parkway
P.O. Box 1346
Ann Arbor, MI 48106-1346

Applications of Multiple Quantum Well Saturable Absorbers in Long Distance Ultrafast Optical Fibre Transmission Systems

Abstract

Optically non-linear multiple quantum wells (MQWs) can be used for regeneration in periodically amplified optical fibre transmission systems, or as the basis of all-optical switches with applications including wavelength conversion.

This thesis investigates the use of InGaAsP/InGaAsP MQW devices for regeneration and wavelength conversion in 10Gb/s to 40Gb/s fibre transmission systems. Computer modelling is used to investigate signal propagation in systems employing soliton signal pulses, and to show that regeneration with suitable MQW devices can result in significant performance improvements. MQW-based wavelength conversion is also modelled.

Three non-linear mechanisms are considered: excitonic absorption bleaching (EAB), absorption changes due to the transient electric field changes which occur in devices incorporating MQWs in reverse biased p-i-n junctions, and non-linear polarisation rotation (NPR). EAB-based devices are ion-implanted to increase the speed of the non-linearity, such that they are suitable for ultra-fast operation. High contrast devices are realised through incorporation of non-linear MQWs in asymmetric Fabry-Perot (AFP) cavities.

Characterisation experiments are developed to measure the magnitudes and temporal dynamics of optical non-linearities, and experimental results presented for devices based on each mechanism. EAB recovery faster than 6ps and 9dB non-linear reflectivity change are achieved in devices using an ion-implanted MQW in an AFP cavity.

Wavelength conversion of a low repetition rate pulse stream is demonstrated in p-i-n and ion-implanted EAB devices. Ion-implanted EAB devices are also used to demonstrate conversion of high repetition rate signals representative of those used in systems applications.

Together with the systems modelling, the experimental results form the basis of a final evaluation of the suitability of each of the three mechanisms for use at 10Gb/s to 40Gb/s. The analysis considers fundamental limitations of the mechanisms, and the effort required for further development. Ion-implanted EAB-based devices are concluded to be most promising.

Acknowledgements

Firstly, I must thank my supervisor, Professor Alwyn J. Seeds. Without his support and encouragement the work described in the thesis would not have been possible. Steve Bennett also provided invaluable help during the initial stages of my research.

I would like to acknowledge the help and friendship of past and present colleagues at University College London, particularly those in the Ultrafast Photonics and Optical Networks groups. Working with them has been both interesting and enjoyable.

My involvement with the ATLAS project during the course of this research has enabled me to meet and work with many interesting people, including Alex Schiffini and Arianna Paoletti of Pirelli Labs, Milan, whom I must thank for their help in making 40 Gb/s measurements.

Device development would not have been possible without the expertise of our collaborators from the EPSRC National Centre for III-V Technologies at the University of Sheffield, and the Surrey Centre for Research in Ion Beam Applications at the University of Surrey.

This work was supported by the EPSRC, by Racal Research Limited (now a part of the Thales Group) and by the ATLAS project, a part of the EU IST programme.

Table of contents

List of figures

List of tables

Chapter 1

Introduction

This chapter is an introduction to the work described in this thesis. It contains concise explanations of the devices investigated, and of their systems applications.

Section 1.1 reviews the basic concepts of long distance fibre optic communications using periodic amplification to overcome fibre loss, the factors limiting the performance of such systems, and the use of soliton signal pulses for better performance.

The performance of soliton systems can be further improved by implementing some form of soliton control. Various soliton control systems are described in Section 1.2, including soliton control using multiple quantum well (MQW) saturable absorbers (SAs), one of the two main subjects of this thesis. Published research in the area of SA soliton control is surveyed.

Section 1.3 explains the need for all-optical wavelength converters (AOWCs) in future wavelength division multiplexed (WDM) networks. Recent investigations of AOWC technologies which are described in the literature are surveyed, and the use of MQW SAs as AOWCs, the second of the two main subjects of this thesis, is explained.

The non-linear optical mechanisms which allow MQWs to be used as SAs and AOWCs, and which are investigated in this thesis, are introduced in Section 1.4. Published descriptions of switching based on these mechanism are surveyed.

Finally, Section 1.5 is an overview of the content of the remainder of this thesis.

1.1 Optical fibre transmission systems

This thesis investigates optical fibre data transmission systems operating in the low loss window around 1.55 μm at data rates of 10 Gb/s and above, and over distances of at least several hundred kilometres, such that optical amplification is required to overcome fibre loss. At these data rates the optical pulses representing bits of data are short enough to be subject to distortion as they propagate, primarily due to the effects of group velocity dispersion (GVD) and self phase modulation (SPM). These phenomena are respectively frequency and intensity dependent phase shifts.

1.1.1 Soliton transmission

A soliton is a pulse which has a sech^2 shape and satisfies the soliton condition (described in Section 2.1.7), such that the effects of GVD and SPM cancel as it propagates [1]. Optical fibre solitons can only exist in the so called anomalous dispersion regime, where pulse group velocity (v_g) decreases with wavelength. Since dispersion is anomalous in standard telecommunications fibre (STF) at 1.55 μm soliton propagation is a practical possibility.

Launching sech^2 pulses which exactly satisfy the soliton condition is not a practical possibility. However, a pulse which, when launched, approximates a soliton, will evolve to become a soliton, shedding excess energy as dispersive radiation. Interactions between this dispersive radiation and the signal pulses can degrade system performance.

A system which does not use soliton propagation can still use non-linear supported (NLS) propagation. Whilst the signal pulses in an NLS system do not satisfy the soliton condition, they still exploit GVD and SPM for improved propagation. The techniques for improving the performance of soliton systems which are discussed in this thesis are also applicable to the more general case of NLS systems.

1.1.2 Periodic amplification and average soliton transmission

Optical fibre is not lossless, losses of 0.25 dB/km are typical at wavelengths around 1.55 μm. In transmission systems longer than about 100 km amplification is required to overcome this loss. This is commonly provided by placing erbium doped fibre amplifiers (EDFAs) at regular intervals to implement periodic amplification. Distributed amplification, which can be achieved by exploiting the Raman effect, is less widely used, and is not considered in this thesis.

Strictly speaking, solitons cannot be supported in lossy fibre. A pulse launched as a soliton will be attenuated as it propagates, such that the strict relationship between its width and peak power which is the soliton condition is no longer satisfied. It has, however, been shown that a periodically amplified system with sufficiently short amplifier spacing can support 'average' solitons which periodically recover their initial shape [2]. The conditions required for average soliton propagation are discussed in Section 2.3.1.

Average soliton propagation is limited by the soliton-soliton interaction (SSI), and by Gordon-Haus jitter (GHJ) which is a consequence of interactions between the propagating pulses and noise resulting from amplification [3]. These effects are described in Sections 2.3.2 and 2.3.3 respectively. Many means of reducing propagation impairments due to GHJ and SSI in soliton systems have been investigated. These soliton control techniques are discussed in the following section.

1.1.3 Dispersion management

The maximum amplifier spacing in an average soliton system is inversely proportional to the GVD of the fibre used. Dispersion shifted fibre, in which GVD approaches zero around 1.55 μm, is manufactured to overcome this problem.

A transmission system using dispersion-shifted fibre (DSF) can be operated such that GVD is negligible at the signal wavelength. In practice, this is not desirable, since higher-order dispersive effects will become dominant and limit pulse propagation. This problem is avoided in a dispersion managed (DM) system. A common DM configuration uses short lengths of dispersion compensating fibre (DCF) with large normal dispersion to compensate the anomalous dispersion of the STF or DSF which comprises the majority of each span of the link. If the total per-span dispersion is slightly anomalous the link can still support average soliton propagation. Since the GVD at a given point in the DM span is non-negligible higher-order dispersion does not significantly affect pulse propagation.

Dispersion compensation can be used to upgrade installed STF systems in which GVD limits long-distance ultra-fast data transmission.

A reduction of total per-span dispersion through the use of DSF or DM also reduces the GHJ.

1.2 Soliton control

1.2.1 Soliton control using guiding filters

The simplest, and most frequently used, soliton control technique is guiding filtering [4]. A narrowband filter added after each EDFA, as shown in Figure 1.1, forces the signal pulses to uniform centre wavelength, hence avoiding the GHJ. In a system with many periodically amplified spans noise which builds up at the centre wavelength of the filters eventually limits soliton propagation.

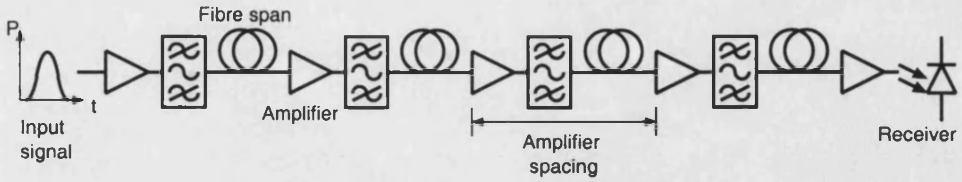

Figure 1.1: Soliton control using guiding filters in a system with four periodically amplified spans.

This accumulation of noise can be avoided if the centre wavelength of each successive filter is offset to implement sliding guiding filtering [5]. Whilst the chain of sliding filters is opaque to dispersive radiation, solitons are able to adjust their centre wavelength such that they can propagate through it. Since, in a practical transmission system, soliton control components following each amplifier should be identical, sliding guiding filters with their differing centre wavelengths are undesirable.

1.2.2 Soliton control using synchronous modulation

Effective soliton control can be achieved if the signal is remodulated at the data rate after each amplifier [6]. Such synchronous modulation is commonly used in conjunction with guiding filters, as shown in Figure 1.2. The modulation prevents the accumulation of dispersive radiation at the centre wavelength of the filters. The necessity of implementing clock recovery adds a level of complexity, such that synchronous modulation is unattractive as an option for soliton control in practical systems.

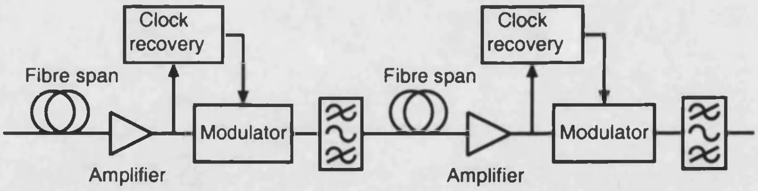

Figure 1.2: Two spans of a transmission system using a combination of guiding filters and synchronous modulation for soliton control.

The use of synchronous modulation and EDFAs in the system of Figure 1.2 is an example of a 3-R regeneration scheme, the signal is *re-amplified* by the EDFAs, and *re-shaped* and *re-synchronised* by the modulators.

1.2.3 Soliton control using saturable absorbers

Much of the benefit of synchronous modulation can be achieved if saturable absorbers (SAs) are used for soliton control, as shown in Figure 1.3. An SA is a device with a non-linear transmission characteristic, such that its transmission increases at high optical powers. The SAs in Figure 1.3 will thus attenuate dispersive radiation and noise relative to the high intensity, information bearing, solitons. This is a 2-R regeneration scheme; signal pulses are *re-amplified* by the EDFAs and *re-shaped* by the SAs.

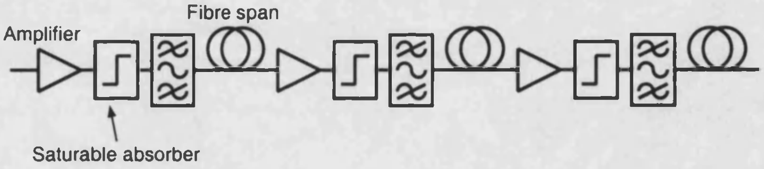

Figure 1.3: Two spans of a transmission system using a combination of guiding filters and saturable absorbers for soliton control.

If an SA is to be useful in soliton control applications the optical non-linearity which it employs must respond to changes of optical input power on a picosecond timescale. Speed and magnitude requirements for the optical non-linearity are studied in the systems modelling of Section 2.6. The optical non-linearity should be polarisation independent since, in a long transmission system, the state of polarisation of the propagating signal is essentially unknown.

1.2.4 Publications regarding soliton control using saturable absorbers

Soliton control using multiple quantum well (MQW) SAs was first proposed by Atkinson and Seeds. They showed through numerical modelling that the incorporation of MQW SAs could allow the amplifier spacing in a 9,000 km, 10 Gb/s soliton system with guiding filters to be increased from 50 km to 100 km [7]. In an extension of this work Bennett and Seeds showed that in a system with 50 km dispersion-decreasing amplifier spans and guiding filters and SAs for soliton control, soliton propagation at 80 Gb/s could be supported over a distance of 8,350 km [8]. An idealised, instantaneous, SA model was used in this work.

Audouin et. al. showed, also through numerical modelling, that SAs could improve the performance of a wavelength division multiplexed (WDM) system with four 10 Gb/s channels [9]. In one modelled configuration the channels were demultiplexed, passed through separate SAs, and then re-multiplexed, at the start of every other 50 km amplifier span. An alternate configuration which relied on the data on each channel becoming synchronised at regular intervals, such that a single SA could be inserted at each synchronisation point, was also modelled but gave reduced performance.

The saturable absorption of a non-linear amplifying loop mirror (NALM) was used by Rottwitt et. al. [10] to regenerate a single 1.5 μm soliton pulse propagating in periodically amplified system with 50 m spans. The span length was greater that the 45m period of the solitons used. The use of NALMs, and of fibre interferometers in general, is not desirable in a practical system due to their environmental instability.

Harper et. al. used saturable absorption based on a combination of fibre non-linear polarisation rotation (NPR) and polarisation dependent loss (PDL) in a narrowband filter to demonstrate error-free transmission of a 10 Gb/s soliton pseudo-random bit stream (PRBS) over 200 Mm [11] in a recirculating loop. Adjustment of the polarisation controllers in the loop such that saturable absorption due to the NPR and PDL was minimised resulted in a reduction of the error free distance to 2 Mm. Whilst this SA mechanism was shown to be effective, it could not be deployed in a real system where the state of polarisation of the propagating signal is not well defined.

A semiconductor optical amplifier (SOA) incorporating a saturable absorber region has been used by Bakonyi et. al. [12] to improve the performance of a 5 Gb/s 1.3 μm transmission system. The gain of the SOA was such that it compensated the excess loss of the SA. An additional SOA and an optical filter were used to compensate for the per-span fibre loss and to stabilise the wavelength of the signal pulses. In a further experiment which utilised a gain-clamped SOA to reduce patterning effects error free 10 Gb/s transmission over 5000 km was achieved [13].

The use of MQW SAs in a system using EDFAs for periodic amplification was first demonstrated by Mangeney et. al. in a 10 Gb/s recirculating loop experiment [14]. Incorporation of the SAs increased the error-free transmission distance from 10,000 km to 12,000 km. After increasing the noise figures of the EDFAs used from 5 dB to 8 dB error free distances with and without the SAs were 10,000 km and 4,000 km. The MQW SA used consisted of four groups of seven InGaAs/InAlAs quantum wells, positioned at the standing wave nodes of an asymmetric Fabry-Perot (AFP) cavity. Implantation with 11 MeV N^+ ions at a density of $10^{11}\,\mathrm{cm}^{-2}$ was used to reduce the SA recovery time to 10 ps. The same group used a similar device in a 20 Gb/s loop experiment. In this case the error free transmission distance was increased from 6,200 km to 7,800 km [15].

40 Gb/s regeneration using an MQW SA has been demonstrated by Rouvillain et. al. [16]. A Q-factor of 13 was measured after transmission over 7,600 km; without the SA the Q-factor fell below 6 after less the 4,000 km. The SA was also found to be beneficial when used to regenerate one 40 Gb/s channel of a five channel WDM multiplex.

1.3 All-optical wavelength conversion

1.3.1 Wavelength division multiplexing and wavelength routed optical networks

Exploiting the two terahertz of bandwidth available within the EDFA gain region is a problem in transmission system design since, even using state-of-the-art modulators, photodetectors and electronic processing components, data rates are restricted to tens of gigabits per second. This obstacle, sometimes referred to as the 'electronic bottleneck' can be surmounted by using optical processing. Optical data streams at rates compatible with available opto-electronic and electronic components can be interleaved through optical time division multiplexing (OTDM) or allowed to propagate through separate wavelength channels in a WDM system.

The ability to use optical components to switch and route the channels comprising optical multiplexes is highly desirable. All-optical routeing avoids the cost of performing optical to electrical and electrical to optical conversions at the network nodes, and the limitations imposed by electronic component speeds.

Coarse optical routeing can be achieved by manipulating the channels comprising OTDM or WDM multiplexes. Such manipulation for OTDM signals would require some form of buffering to synchronise low data rate tributaries prior to adding them to the multiplex. Since optical buffering is not yet a practical reality, wavelength routeing, in which signals propagate across a WDM network through 'virtual wavelength channels' is a subject of current interest. Whilst multiplexing and demultiplexing of WDM signals can be readily achieved, a fully flexible wavelength routed optical network (WRON) requires all-optical wavelength conversion [17].

Ideally, it should be possible to insert all-optical wavelength converters (AOWCs) transparently at any point in a transmission system or network. The wavelength converted output of the AOWC should thus propagate similarly to a non-wavelength converted signal.

AOWCs based on parametric processes described in Sections 1.3.2 and 1.3.3 are said to be strictly transparent; the shape of the output signal pulses is identical to that of the input pulses. Some parametric AOWCs deviate from the ideal in that the wavelength converted signal is spectrally inverted. This spectral inversion can be used to achieve dispersion compensation.

Similarly to soliton control devices, polarisation independence is desirable for AOWCs.

1.3.2 Cascaded difference frequency generation in periodically poled lithium niobate devices

In the cascaded difference frequency generation (CDFG) process a pump wave is frequency doubled from its initial frequency, ω_p, by second harmonic generation (SHG). Difference frequency generation (DFG) between the frequency doubled pump and an input signal at ω_s produces a wavelength converted signal at $\omega_c = 2\omega_p - \omega_s$.

CDFG wavelength conversion has been demonstrated in periodically poled lithium niobate (PPLN) waveguides by a number of researchers [18, 19, 20]. Whilst the operating wavelength range of such AOWCs is limited by the need to achieve phase matching for the SHG and DFG processes conversion bandwidths of greater than 70 nm [18], sufficient to cover the EDFA gain region, are possible.

PPLN waveguides are a passive devices, with only negligible noise being produced by spontaneous fluorescence. Wavelength conversion is these devices is thus an essentially noise-free process. The CDFG process is polarisation sensitive. Polarisation independence can be achieved if orthogonally polarised components of the signal are separated and wavelength converted in separate waveguides [20] or, in a more practical configuration, converted as they counter-propagate in the same waveguide [21].

Conversion gains, defined as the ratio of the average power of the signal at the output wavelength to that of the signal at the input wavelength, as high as 3 dB have been reported [22], albeit with the disadvantages that high optical powers ($\approx$ 20 dBm and greater) are required, and that the waveguide must be held at high temperature (100 °C, or greater) to avoid photorefractive effects. Successful transmission of a 40 Gb/s wavelength converted signal over five 100 km amplified spans has been reported [23].

1.3.3 Four wave mixing in semiconductor optical amplifiers

If input and pump signals, with frequencies ω_i and ω_p respectively, beat in a SOA the carrier density within the SOA is modulated, creating index and gain gratings [24]. Interactions of the signals with these gratings results in a wavelength converted signal at $\omega_c = 2\omega_p - \omega_i$. A signal at $2\omega_i - \omega_p$ is also generated but is small, provided that the power of the pump is large compared to that of the signal. This process, four wave mixing (FWM), is polarisation dependent.

The conversion gain of devices using this mechanism is strongly dependent on the frequency offset between the pump and signal inputs. Gains as high as 20 dB have been reported for up-conversion by 20 GHz [25]. However, the gains fell away rapidly as the offset increased, and were systematically smaller for down-conversion. Conversion gain can be flattened by launching two, orthogonally polarised, pump signals into the SOA. Reported results using such a scheme show conversion gain dependent on the SOA gain spectrum. [26]. This scheme also results in conversion which is independent of the input signal polarisation.

Whilst the active nature of AOWCs using FWM in SOAs means that, unlike those using CDFG in PPLN waveguides, they are a noise source, it gives them the advantage that the parametric processes are more efficient. The phase matching constraint is eased since wavelength conversion can be achieved in shorter devices.

Experiment investigation of wavelength conversion of a 10 Gb/s signal has shown the bit error rate (BER) penalty of a FWM SOA AOWC to be 1.2 dB [27].

1.3.4 Cross-gain modulation in semiconductor optical amplifiers

Gain saturation in a SOA can be used as a switching mechanism. In AOWC applications a pulse at the input wavelength causes a transient change of gain which modulates a continuous wave (CW) signal at the output wavelength. The SOA is operated with a small injection current such that, in the absence of the input pulses, the CW signal experiences a net loss. Absorption of an input pulse results in the creation of free carriers and population inversion, such that the CW signal experiences a net gain [28]. This mechanism is called cross-gain modulation (XGM).

Many investigations of AOWCs based on this mechanism have been published. Main points of concern have been the use of narrow-band filtering based on fibre Bragg gratings (FBGs) [29] or Fabry-Perot (FP) etalon filters [30] following the SOA. These schemes can reduce both the duration and the spectral width of the chirped output pulses. Wavelength conversion at speeds as high as 100 Gb/s has been demonstrated [31].

This type of wavelength converter is principally limited by leakage of the CW signal in the absence of any input pulses; this leakage determines the output signal contrast ratio. Also, the powers of the signal and CW inputs are critical. Increasing the powers reduces carrier lifetimes in the SOA, since carriers recombine through stimulated emission, but also reduces the signal to noise ratio at the output.

An AOWC based on cross-gain modulation in a SOA will be wavelength independent, provided that the SOA itself is wavelength independent.

1.3.5 Cross-phase modulation in semiconductor optical amplifiers

If a pulse and a CW signal propagate through a SOA the CW signal will experience a transient index change. This cross phase modulation (XPM) effect can be used to implement all-optical switching, and hence wavelength conversion, if the SOA is incorporated in some form of interferometer. A commonly used arrangement consists of a Mach-Zender interferometer (MZI) with a SOA incorporated in each arm. Injection of signal pulses into one of the SOAs unbalances the interferometer such that a CW signal passing through it will experience intensity modulation [32]. Production of such SOA MZI AOWCs is complicated by the need for monolithic integration if stable operation is to be achieved.

High contrast ratios can be achieved in these interferometers. Whilst this allows wavelength conversion to approach the ideal of optical transparency, the transfer function of the interferometers is still non-linear. Arrangements in which two or three SOA MZI interferometers are cascaded have been proposed to linearise the wavelength conversion process [33]. Alternatively, a suitable non-linear transfer characteristic could be exploited to implement 2R regeneration.

Leuthold et. al. have demonstrated 100 Gb/s wavelength conversion using a SOA MZI AOWC [34].

1.3.6 Saturable absorbers

As discussed in Section 1.2.3, an SA is a non-linear optical device, the transmission of which increases with incident optical power. SAs can be used for wavelength conversion if the transmission change due to absorption of signal pulses at the input wavelength is used to modulate a CW signal at the output wavelength.

This thesis investigates two saturable absorption mechanisms which are observed in MQW devices: field screening in reverse biased p-i-n diodes incorporating MQWs in the intrinsic region, and excitonic absorption bleaching in MQWs. These are described in Section 1.4.

If wavelength conversion is to be performed with optical transparency an SA with instantaneous switching, zero transmission under small signal conditions, and a linear saturation characteristic is required. These characteristics cannot be achieved in practical MQW SAs. Modelling in Section 2.7 investigates wavelength conversion in transmission systems, and determines the parameters required for devices to be used for wavelength conversion.

Wavelength conversion in an SA exploiting field screening in a waveguide electro-absorption modulator (EAM) has been demonstrated by Cho et. al. [35]. The SA recovery was 9.8 ps, resulting in a broadening of the 10 ps input pulses after wavelength conversion. Whilst the contrast ratio of the device is not stated, experimental results show eye opening following wavelength conversion of an input PRBS with significant CW background between the pulses, suggesting potential for 2R signal regeneration.

Wavelength conversion using the field screening and excitonic absorption bleaching non-linearities is investigated experimentally in Chapters 6 and 8 respectively.

1.3.7 Non-linear polarisation rotation in multiple quantum wells

The phenomenon of non-linear polarisation in multiple quantum wells, which is described in Section 1.4.3, can be used as the basis of an AOWC. A possible arrangement is shown in Figure 1.4

Under small signal conditions horizontally polarised CW light at the output wavelength is blocked by the vertically-aligned output analyser. Following absorption of a circularly polarised optical pulse at the input wavelength, the CW light experiences a transient change of state of polarisation in the MQW, and a short pulse of the CW light is thus transmitted by the analyser. This arrangement can be used to realise all-optical wavelength conversion if the wavelength of the switched CW light differs from that of the input pulses.

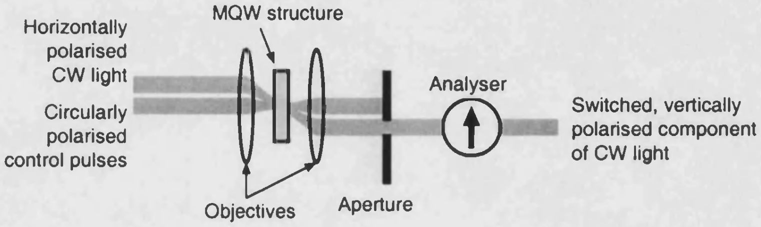

Figure 1.4: All-optical wavelength conversion using NPR in an MQW.

Optical switching using NPR has been demonstrated by Hyland et. al. [36] at 1.52 μm in an InGaAsP/InGaAsP MQW, and by Nishikawa et. al. [37] at 760 nm in a GaAs/AlGaAs MQW. Whilst, in both cases the switch recovery time was a few picoseconds, the switches were only shown to work at megahertz repetition rates. At high repetition rates a degradation of switching performance due to an accumulation of spin relaxed carriers is expected. This problem is discussed more fully in Section 3.5.

Whilst it is possible to switch short pulses, the interval between the pulses must be of the order of the free carrier lifetime, typically 5 ns, in order to allow the recovery of the overall free carrier population.

NPR switching also suffers from polarisation sensitivity. A circularly polarised control, or input signal is required. A complex polarisation diversity scheme, in which orthogonally polarised components were switched at different points on the same device, has been demonstrated by Takahashi et. al. [38].

1.4 Optically non-linear multiple quantum well devices

1.4.1 Excitonic absorption bleaching

Absorption of a photon in a direct bandgap semiconductor normally results in the creation of a free electron hole pair, provided that the photon energy is greater than the material bandgap energy. If the photon energy is coincident with the material exciton resonance, the free electron and hole are bound by the Coulomb attraction to form an exciton. In a bulk semiconductor at room temperature the exciton binding energy is small compared to the thermalisation energy, so excitonic effects are not observed. In an MQW the exciton binding energy is increased due to carrier confinement, with the consequence that excitonic effects can be observed and exploited at room temperature.

Excitonic absorption is of interest since it is non-linear; the probability of excitonic absorption of a photon decreases in the presence of a population of excitons or free carriers. This effect is referred to as excitonic absorption bleaching (EAB) [39]. An MQW exhibiting EAB is an example of a SA. Whilst excitons have a short lifetime, of the order of 300 fs in III-V MQWs, the free electrons and holes left following their decay still cause EAB. These free carriers have a long lifetime, typically 5 ns in good quality metal-organic vapour phase epitaxy (MOVPE) or molecular beam epitaxy (MBE) grown III-V structures.

1.4.2 Carrier lifetime reduction

If the EAB non-linearity is to be used as the basis for devices operating at 10 Gb/s and above the free carrier lifetime must be dramatically reduced. Carriers can be swept out of the wells by application of a perpendicular electric field but, as discussed in Section 1.4.4, this results in a device with non-linearity dominated by the transient electric field. An alternative approach is the introduction of lattice defects to create levels in the bandgap of the MQW and provide a path for rapid carrier recombination. Defects in MQWs grown by low temperature (LT) MBE result in suitably short carrier lifetimes [40, 41].

Since only MOVPE grown MQWs were available for the work described in this thesis an alternative technique was used. Wafers containing MQWs were implanted with high energy ions, such that the passage of high energy ions through the MQW regions created lattice defects [42]. Ion-implantation is discussed in Section 3.6.

1.4.3 Non-linear polarisation rotation

Depending on their spin state photons can be considered to have either left or right-handed circular polarisation. The spin of the photocarriers resulting from the absorption of a photon is dependent on the spin, and hence the handedness of the circular polarisation of that photon. It is thus possible to create a population of purely spin-up or spin-down photocarriers in an MQW by exciting it with a suitably circularly polarised optical pulse. The photocarrier population will quickly relax to an equilibrium state in which populations of spin-up and spin-down photocarriers are equal; spin-relaxation times of the order of 5 ps have been measured in III-V semiconductor MQWs. Following excitation by a pulse whose duration is short compared to the spin relaxation time, the MQW becomes optically anisotropic. This anisotropy can be used to change the state of polarisation of plane polarised light [43] and hence implement all-optical switching, as discussed in Section 1.3.7.

1.4.4 Field screening

If a perpendicular electric field is applied to an MQW device the band structure of the MQW will be tilted, as shown in Figure 1.5. The heights of the barriers seen by photogenerated carriers in the wells are reduced so that the carriers can escape by either quantum mechanical tunnelling or thermionic emission [44]. Once escaped the carriers are swept out of the intrinsic region at the saturated drift velocity. The dominant optical non-linear mechanism in such a device is not EAB. Application of the electric field modifies the wave functions of the electrons and holes confined in the wells, as also shown in Figure 1.5, and hence the absorption of the MQW. This is known as the quantum confined Stark effect (QCSE). As carriers travel out of the wells they screen the applied field, and hence reverse the QCSE absorption change.

A perpendicular electric field can be applied to an MQW which is incorporated in the intrinsic region of a reverse biased p-i-n diode. Such devices have potential for use as SAs for both soliton control and AOWC applications. Fast operation is dependent on both carrier transport across the intrinsic region, which is responsible for the rise of the field change, and diffusive conduction in the doped regions, which allows the field in the device to recover to its small signal state. The interactions between these mechanisms, and the limits which they place on the performance of SA devices, are discussed in Section 3.3.

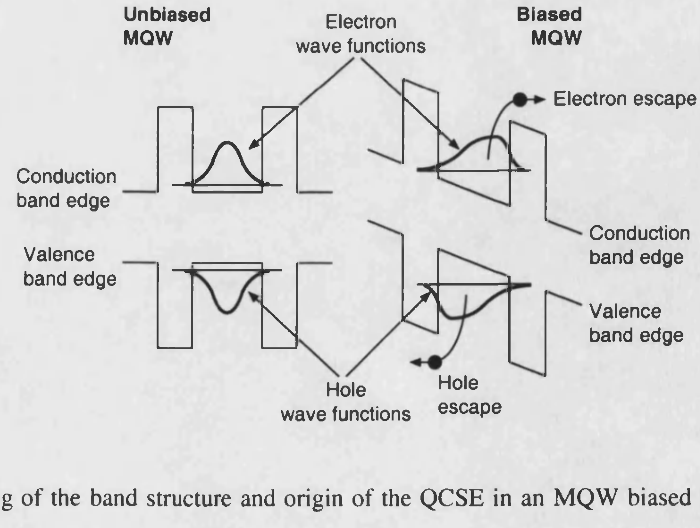

Figure 1.5: Tilting of the band structure and origin of the QCSE in an MQW biased by application of a perpendicular electric field.

Whilst the field screening mechanism was proposed as a basis for implementing optical SAs in 1990 [45], and optical switches and SAs based on field screening have been investigated [46, 47], most investigation of carrier transport in reverse-biased p-i-n MQW diodes has focused on sweeping photocarriers out of the MQW region to avoid field screening effects. This is important in the context of asymmetric Fabry-Perot modulators (AFPMs) which rely on reflectivity changes due to modulation of the bias voltage. Reflectivity changes due to field screening are undesirable in such devices.

1.4.5 Asymmetric Fabry-Perot cavities

For AOWC applications an SA must have a contrast ratio of at least 10dB, which is not a practical possibility using the EAB or field screening mechanisms. High contrast ratios can be realised if an MQW with a moderate non-linearity is incorporated in an AFP cavity, as shown in Figure 1.6 [48]. If the cavity round trip comprises an integer number of wavelengths then reflections from the rear mirror will be in phase with each other, but 180° out of phase with the reflection from the front mirror. If the mirror reflectivities and the small signal absorption of the MQW are chosen correctly there will be total destructive interference between reflections from the front and rear mirrors, and the aggregate reflectivity of the AFP will be zero. Following incidence of an optical pulse the absorption of the MQW will decrease, effectively increasing the rear reflection, so that there is no longer total destructive interference and the aggregate reflectivity of the AFP cavity is non-zero.

The use of an AFP cavity introduces two design problems: high contrast ratio is only observed across a small range of wavelengths, and the excess loss of the SA is increased.

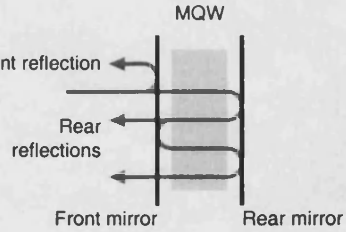

Figure 1.6: MQW in an AFP cavity to realise a high contrast ratio SA.

1.4.6 Publications regarding saturable absorbers based on field screening in p-i-n devices

Optical switching based on field screening in a p-i-n device has been reported by Yairi [46]. The device used consisted of a 94 period GaAs/AlGaAs MQW and a 20 period AlAs/AlGaAs distributed Bragg reflector (DBR). The top surface was not anti-reflection coated, such that a Fabry-

Perot cavity was formed. When excited with 2 ps pulses a reflectivity maximum was reached after approximately 20 ps; reflectivity recovered to the small signal value after another 30 ps. The measured contrast ratio was 2.6 dB. The rise and fall of the reflectivity change are attributed to vertical carrier transport and diffusive conduction respectively. The same authors reported faster behaviour (switch-on and switch-off within 20 ps) in a complex double diode structure [49]. The operating wavelengths made this device unattractive for telecommunication applications, light at 857 nm was switched using control pulses at 428 nm.

1.4.7 Publications regarding ultra-fast devices based on absorption bleaching

Hirano et. al. have published descriptions of a low temperature grown optical switch (LOTOS) [48]. Their device design consists of an InGaAs/InAlAs MQW within an AFP cavity. The cavity is formed between a DBR and a gold-coated surface of the wafer. Access to the cavity is through the opposite side of the wafer, which is anti-reflection coated, and the DBR. 10 dB contrast ratio measured with 2 pJ control pulses over a 10 nm wavelength range was reported in a LOTOS device [50]. The response time and insertion loss were 12 ps and 10 dB respectively. Use of the device as an optical gate operating at 10 Gb/s was also reported, with thermal effects due to heating of the device at high optical powers limiting switching performance [48].

Loka et. al. have developed a similar device based on absorption bleaching in bulk GaAs grown by LT MBE [51, 52]. Contrast ratios up to 15 dB and a 3 ps recovery time were measured. The operating wavelength of the device, at around 870 nm, made it unsuitable for telecommunications applications. Their discussion of AFP cavity design issues is, however, equally applicable to MQW based devices for 1550 nm.

Mangeney, Leclerc et. al. have developed devices incorporating ion-implanted InGaAs/InAlAs quantum wells (QWs) in an AFP cavity [53]. The excess loss of the SA was reduced by clustering the QWs at the nodes of the standing wave in the cavity. A contrast ratio of 5.4 dB, adequate for the intended application, 2R regeneration in optical transmission systems, a saturation energy of 12 pJ, and a relaxation time of 2.4 ps were reported.

The same authors have also compared implantation with different ion species [54]. They suggest that heavier ions create clustered defects which avoid the possibility of defect centre saturation by providing complete paths for carrier recombination.

1.5 Overview and objectives of this thesis

Sections 1.2 and 1.3 of this introductory chapter have discussed soliton control and all-optical wavelength conversion, techniques which can enhance the performance and flexibility of ultra-fast transmission systems.

This thesis investigates the possibility of using optically non-linear MQW devices, introduced in Section 1.4, to perform these functions. A number of objectives can be identified:

- Develop a theoretical understanding of fibre transmission systems, and techniques to determine the requirements which must be met by non-linear MQW devices for use in the systems applications of interest.
- Develop a theoretical understanding of optical non-linearities in MQWs, such that devices suitable for systems applications can be designed.
- Develop techniques by which devices can be characterised to determine whether they meet the systems requirements.
- Develop and characterise devices, evaluating their suitability for the applications of interest.

Work towards these objectives is presented in the remainder of this thesis, with the following arrangement:

Chapter 2 The propagation of pulses in optical fibre and numerical modelling of pulse propagation using the split-step Fourier method (SSFM) are described. Operation and modelling of the other principle system components is discussed.

A system model suitable for the investigation of soliton control and wavelength conversion using SAs is then developed, drawing from such theoretical concepts as average soliton propagation, the Gordon-Haus effect and dispersion management. The systems models are used to determine the SA parameters required for successful implementation of soliton control and wavelength conversion.

Chapter 3 The non-linear optical mechanisms in MQWs which are investigated experimentally later in the thesis are discussed. The theoretical discussion provides background for the descriptions of devices and experiments in Chapters 4 and 5, and later interpretation of experimental results.

The phenomena of field screening, EAB and NPR are explained. A two-dimensional model approximating the carrier dynamics which control field screening a p-i-n MQW devices is developed. AFP cavity optimisation and the conditions required if ion-implantation is to reduce significantly the photocarrier lifetime in an MQW, both critical to the investigations of Chapter 8, are also discussed.

The theoretical descriptions of SA operation in MQW devices also serve to validate the SA models used in the systems modelling of Chapter 2.

Chapter 4 The experiments used to characterise the various devices investigated, and to obtain the results presented in Chapters 6 to 8 are described. These include short pulse and CW saturation measurements, a pump-probe system for time resolved measurements, and wavelength conversion configurations.

A tunable figure-of-eight mode-locked fibre laser (F8L) which was built to provide a source of 2 ps pulses for the pulse saturation and pump-probe experiments is described in Appendix E.

Chapter 5 Some aspects of the design of the MQW structures and devices which are investigated in Chapters 6 to 8 are discussed.

Chapter 6 Field screening in p-i-n MQW devices is investigated. Experimental results are used to illustrate the transition between EAB and field screening regimes as the reverse bias applied to p-i-n device increases. Limitations to the speed of SAs and AOWCs based on this effect, which are primarily due to transit time effects in the p-i-n junction, are discussed.

Chapter 7 NPR is demonstrated in both transmission and reflection devices. The rotation angle observed, and hence also the NPR switching performance, is limited, Reasons for this are discussed.

Chapter 8 MQW devices implanted with different doses of nitrogen ions are investigated and the optimum conditions for reduction of the EAB recovery time are determined. Incorporation of the MQW region in a suitably designed AFP cavity is shown to significantly increase the measured optical non-linearity. Wavelength conversion of a low repetition rate pulse train from an F8L, a 10 GHz pulse train, and a 40 Gb/s PRBS is demonstrated. The results of high repetition rate experiments reveal thermal and patterning effects. The origin of these effects, and means of overcoming them, are discussed.

Final conclusions are drawn in Chapter 9. The possibilities of using the devices investigated as SAs or AOWCs in real transmission systems, based on the experimental data of Chapters 6 to 8 and the systems modelling of Chapter 2, is evaluated. Suggestions as to how the work could be usefully continued are made.

Chapter summary

This chapter has presented a basic description of ultra-fast long distance fibre communications and introduced the concepts of soliton control for wavelength conversion in future WDM networks.

Soliton control techniques, with a focus on soliton control using SAs have been surveyed, as have techniques for all-optical wavelength conversion.

The non-linear optical processes in MQW devices, which can allow them to be used as SAs for soliton control or AOWC applications, have been described. Ultra-fast optical switch and SA devices described in the literature have been surveyed.

The objectives of this thesis and the structure of the remaining chapters have been outlined.

References

[1] L. Mollenauer and R. Stolen, "Solitons in optical fibers," *Laser Focus*, vol. 18, pp. 193–8, April 1982.

[2] H. Kubota and M. Nakazawa, "Long-distance optical soliton transmission with lumped amplifiers," *IEEE Journal of Quantum Electronics*, vol. 26, pp. 692–700, April 1990.

[3] J. Gordon and A. Haus, "Random walk of coherently amplified solitons in optical fibre transmission," *Optics Letters*, vol. 11, pp. 665–667, October 1986.

[4] A. Mecozzi, J. Moors, H. Haus, and Y. Lai, "Soliton transmission control," *Optics Letters*, vol. 16, pp. 1841–1843, December 1991.

[5] L. Mollenauer, J. Gordon, and S. Evangelides, "The sliding-frequency guiding filter - an improved form of soliton control," *Optics Letters*, vol. 17, pp. 1575–1577, November 1991.

[6] H. Kubota and M. Nakazawa, "Soliton transmission control in time and frequency domains," *IEEE Journal of Quantum Electronics*, vol. 29, pp. 2189–2197, July 1993.

[7] D. Atkinson, W. Loh, V. Afanasjev, A. Grudinin, A. Seeds, and D. Payne, "Increased amplifier spacing in a soliton system with quantum-well saturable absorbers and spectral filtering," *Optics Letters*, vol. 19, pp. 1514–1516, October 1994.

[8] S. Bennett and A. Seeds, "80 Gb/s soliton transmission over trans-oceanic (>8,000 km) distances using fast saturable absorbers and dispersion decreasing fibre," in *OFC/IOOC '99. Technical Digest*, vol. 2, pp. 50–52, 1999.

[9] O. Audouin, E. Pallise, E. Desurvire, and E. Maunand, "Use of fast in-line saturable absorbers in wavelength-division-multiplexed soliton systems," *IEEE Photonics Technology Letters*, vol. 10, pp. 828–829, June 1998.

[10] K. Rottwitt, W. Margulis, and J. Taylor, "Spectral filtering of solitons by means of a nonlinear amplifying loop mirror," *Optics Letters*, vol. 20, pp. 1601–1603, Aug 1995.

[11] P. Harper, S. Penketh, I.S. Alleston, I. Bennion, and N. Doran, "10 Gbit/s dispersion managed soliton propagation over 200 Mm without active control," *Electronics Letters*, vol. 34, pp. 1997–1999, October 1998.

[12] Z. Bakonyi, G. Onishchukov, C. Knöll, M. Gölles, F. Lederer, and R. Ludwig, "In-line saturable absorber in transmission systems with cascaded semiconductor optical amplifiers," *IEEE Photonics Technology Letters*, vol. 12, pp. 570–572, May 2000.

[13] Z. Bakonyi, G. Onishchukov, C. Knoll, and F. Golles, M.and Lederer, "10 Gbit/s RZ transmission over 5000 km with gain-clamped semiconductor optical amplifiers and saturable absorbers," *Electronics Letters*, vol. 36, pp. 1790–1791, October 2000.

[14] J. Mangeney, S. Barré, G. Aubin, J. Oudar, and O. Leclerc, "System application of 1.5 μm ultrafast saturable absorber in 10 Gb/s long-haul transmission," *Electronics Letters*, vol. 36, pp. 1725–1727, September 2000.

[15] O. Leclerc, G. Aubin, P. Brindel, J. Mangeney, H. Choumane, S. Barre, and J. Oudar, "Demonstration of high robustness to SNR impairment in 20 Gbit/s long-haul transmission using 1.5 μm saturable absorber.," *Electronics Letters*, vol. 16, pp. 1944–1946, November 2000.

[16] D. Rouvillain, F. Seguinneau, L. Pierre, P. Brindel, H. Choumane, G. Aubin, J. Oudar, and O. Leclerc, "40 Gbit/s optical 2R regenerator based on passive saturable absorber for WDM long-haul transmission," in *OFC 2002 Postdeadline Papers*, pp. FD11–1, 2002.

[17] C. Brackett, A. Acampora, J. Sweitzer, G. Tangonan, M. Smith, W. Lennon, K. Wang, and R. Hobbs, "A scalable multiwavelength multihop optical network: a proposal for research on all-optical networks," *Journal of Lightwave Technology*, vol. 11, pp. 736–753, May/June 1993.

[18] M. Chou, I. Brener, M. Fejer, E. Chaban, and S. Christman, "1.5 μm wavelength conversion based on cascaded second-order nonlinearity in $LiNbO_3$ waveguides," *IEEE Photonics Technology Letters*, vol. 11, pp. 653–655, June 1999.

[19] K. Parameswaran, M. Chou, M. Fejer, I. Brener, and S. Kawanishi, "Waveguide frequency mixers for all-optical signal processing," in *Nonlinear Optics: Materials, Fundamentals, and Applications, 2000. Technical Digest*, pp. 156–158, 2000.

[20] I. Brener, M. Chou, E. Chaban, K. Parameswaran, M. Fejer, and D. Kosinski, S.and Pruitt, "Polarisation-insensitive wavelength converter based on cascaded nonlinearities in $LiNbO_3$ waveguides," *Electronics Letters*, vol. 36, pp. 66–67, January 2000.

[21] I. Cristiani, V. Degiorgio, L. Socci, F. Carbone, and M. Romagnoli, "Polarization-insensitive wavelength conversion in a lithium niobate waveguide by the cascading technique," *IEEE Photonics Technology Letters*, vol. 14, pp. 669–671, May 2002.

[22] G. Schreiber, W. Sohler, H. Suche, L. Socci, and M. Romagnoli, "Conversion efficiency exceeding 0dB in a Ti:PPLN waveguide converter," Tech. Rep. D411, ATLAS project, December 2000.

[23] H. Suche, G. Schreiber, Y. Lee, V. Quiring, R. Ricken, W. Sohler, A. Paoletti, F. Carbone, D. Caccioli, and A. Schiffini, "Efficient Ti:PPLN multi-wavelength converter for high bitrate WDM-transmission system," in *ECOC '01*, vol. 6, pp. 42–43, 2001.

[24] S. Diez, C. Schmidt, R. Ludwig, H. Weber, K. Obermann, S. Kindt, I. Koltchanov, and K. Petermann, "Four-wave mixing in semiconductor optical amplifiers for frequency conversion and fast optical switching," *IEEE Journal on Selected Topics in Quantum Electronics*, vol. 3, pp. 1131–1145, October 1997.

[25] A. D'Ottavi, F. Girardin, L. Graziani, F. Martelli, P. Spano, A. Mecozzi, S. Scotti, R. Dall'Ara, J. Eckner, and G. Guekos, "Four-wave mixing in semiconductor optical amplifiers: a practical tool for wavelength conversion," *IEEE Journal on Selected Topics in Quantum Electronics*, vol. 3, pp. 522–528, April 1997.

[26] G. Contestabile, F. Martelli, A. Mecozzi, L. Graziani, A. D'Ottavi, P. Spano, G. Guekos, R. Dall'Ara, and J. Eckner, "Efficiency flattening and equalization of frequency up- and down-conversion using four-wave mixing in semiconductor optical amplifiers," *IEEE Photonics Technology Letters*, vol. 10, pp. 1398–1400, October 1998.

[27] G. Contestabile, A. D'Ottavi, F. Martelli, R. Spano, and J. Eckner, "Broad-band polarization-insensitive wavelength conversion at 10Gb/s," *IEEE Photonics Technology Letters*, vol. 14, pp. 666–668, May 2002.

[28] A. Reale, A. Di Carlo, D. Campi, C. Cacciatore, A. Stano, and G. Fornuto, "Study of gain compression mechanisms in multiple-quantum-well $In_{1-x}Ga_xAs$ semiconductor optical amplifiers," *IEEE Journal of Quantum Electronics*, vol. 35, pp. 1697–1703, November 1999.

[29] P. Cho, G. Carter, and D. Mahgerefteh, "Transmission of 10 Gbit/s wavelength converted RZ data over 20000 km in a dispersion-managed system," *Electronics Letters*, vol. 34, pp. 2265–2267, November 1998.

[30] D. Mahgerefteh, P. Cho, and P. Tayebati, "Increased speed of semiconductor optical amplifier wavelength converter at multiple channels using Fabry-Perot and micro-electro-mechanical filters," *Electronics Letters*, vol. 35, pp. 482–484, March 1999.

[31] A. Ellis, A. Kelly, D. Nesset, D. Pitcher, D. Moodie, and R. Kashyap, "Error free 100 Gb/s wavelength conversion using grating assisted cross-gain modulation in 2 mm long semiconductor amplifier," *Electronics Letters*, vol. 34, pp. 1958–1959, October 1998.

[32] K. Stubkjaer, "Semiconductor optical amplifier-based all-optical gates for high-speed optical processing," *IEEE Journal on Selected Topics in Quantum Electronics*, vol. 6, pp. 1428–1435, November/December 2000.

[33] W. Burns, "Linearized optical modulator with fifth order correction," *Journal of Lightwave Technology*, vol. 18, pp. 1724–1727, August 1995.

[34] J. Leuthold, C. Joyner, B. Mikkelsen, G. Raybon, J. Pleumeekers, B. Miller, K. Dreyer, and C. Burrus, "100 Gbit/s all-optical wavelength conversion with integrated SOA delayed-interference configuration," *Electronics Letters*, vol. 36, pp. 1129–1130, June 2000.

[35] P. Cho, D. Mahgerefteh, and J. Coldhar, "All-optical 2R regeneration and wavelength conversion at 20 Gb/s using an electroabsorption modulator," *IEEE Photonics Technology Letters*, vol. 11, pp. 1662–1664, December 1999.

[36] J. Hyland, G. Kennedy, A. Miller, and C. Button, "Spin relaxation and all optical polarisation switching at 1.52 micrometres in InGaAs(P)/InGaAsP multiple quantum wells," *Semiconductor Science and Technology*, vol. 14, pp. 215–221, March 1999.

[37] Y. Nishikawa, A. Tackeuchi, M. Yamaguchi, S. Muto, and O. Wada, "Ultrafast all-optical spin polarization switch using quantum well etalon," *IEEE Journal of Selected Topics in Quantum Electronics*, vol. 2, pp. 661–667, September 1996.

[38] H. Takahashi, R.; Itoh and H. Iwamura, "Ultrafast high-contrast all-optical switching using spin polarization in low-temperature-grown multiple quantum wells," *Applied Physics Letters*, vol. 77, pp. 2958–2960, November 2000.

[39] D. Chemla and D. Miller, "Room-temperature excitonic nonlinear-optical effects in semiconductor quantum-well structures," *Journal of the Optical Society of America B*, vol. 2, pp. 1155–1173, July 1985.

[40] S. Gupta, J. Whitaker, and G. Mourou, "Ultrafast carrier dynamics in III-V semiconductors grown by molecular-beam epitaxy at very low substrate temperatures," *IEEE Journal of Quantum Electronics*, vol. 28, pp. 2464–2472, October 1992.

[41] R. Takahashi, Y. Kawamura, T. Kagawa, and H. Iwamura, "Ultrafast 1.55 μm photoresponses in low-temperature-grown InGaAs/InAlAs quantum wells," *Applied Physics Letters*, vol. 65, pp. 1790–1792, October 1994.

[42] E. Delpon, J. Oudar, N. Bouche, R. Raj, A. Shen, N. Stelmakh, and J. Lourtioz, "Ultrafast excitonic saturable absorption in ion-implanted InGaAs/InAlAs multiple quantum wells," *Applied Physics Letters*, vol. 72, pp. 759–761, February 1998.

[43] A. Tackeuchi, Y. Nishikawa, and O. Wada, "Room temperature electron spin dynamics in GaAs/AlGaAs multiple quantum wells," *Applied Physics Letters*, vol. 68, pp. 797–799, February 1996.

[44] A. Fox, D. Miller, G. Livescu, J. Cunningham, and W. Jan, "Quantum well carrier sweep out: relation to electroabsorption and exciton saturation," *IEEE Journal of Quantum Electronics*, vol. 27, pp. 2281–2295, October 1991.

[45] T. Wood, J. Pastalan, C. Burrus, B. Johnson, B. Miller, J. deMigual, U. Koren, and M. Young, "Electric field screening by photogenerated holes in multiple quantum well saturable absorbers: A new mechanism for absorption saturation," *Applied Physics Letters*, vol. 57, pp. 1081–1083, September 1990.

[46] M. Yairi, C. Coldren, D. Miller, and J. Harris, "High-speed, optically controlled surface-normal optical switch based on diffusive conduction," *Applied Physics Letters*, vol. 75, pp. 597–9, August 1999.

[47] E. Burr, J. Song, A. Seeds, and C. Button, "28 ps recovery time in an InGaAsP/InGaAsP multiple-quantum-well saturable absorber employing carrier sweepout," *Journal of Applied Physics*, vol. 90, pp. 3566–3569, October 2001.

[48] A. Hirano, H. Kobayashi, H. Tsuda, R. Takahashi, M. Asobe, K. Sato, and K. Hagimoto, "10 Gbit/s RZ all-optical discrimination using refined saturable absorber optical gate," *Electronics Letters*, vol. 34, pp. 198–199, January 1998.

[49] M. Yairi, H. Demir, and D. Miller, "Optically controlled optical gate with an optoelectronic dual diode structure-theory and experiment," *Optical and Quantum Electronics*, vol. 33, pp. 1035–54, July-October 2001.

[50] A. Hirano, H. Tsuda, H. Kobayashi, R. Takahashi, M. Asobe, K. Sato, and K. Hagimoto, "All-optical discrimination based on nonlinear transmittance of MQW semiconductor optical gates," *Journal of Lightwave Technology*, vol. 17, pp. 873–874, May 1999.

[51] H. Loka and P. Smith, "Ultrafast all-optical switching in an asymmetric Fabry-Perot device using low-temperature-grown GaAs," *IEEE Photonics Technology Letters*, vol. 10, pp. 1733–1735, December 1998.

[52] H. Loka, S. Benjamin, and P. Smith, "Optical characterization of low-temperature-grown GaAs for ultrafast all-optical switching devices," *IEEE Journal of Quantum Electronics*, vol. 34, pp. 1426–1437, August 1998.

[53] J. Mangeney, J. Oudar, J. Harmand, C. Mériadoc, G. Patriarche, and G. Aubin, "Ultrafast saturable absorption at 1.55 µm in heavy-ion-irradiated quantum-well vertical cavity," *Applied Physics Letters*, vol. 76, pp. 1371–1373, March 2000.

[54] J. Mangeney, H. Choumane, G. Patriarche, G. Leroux, G. Aubin, J. Harmand, J. Oudar, and H. Bernas, "Comparison of light- and heavy-ion-irradiated quantum-wells for use as ultrafast saturable absorbers," *Applied Physics Letters*, vol. 79, pp. 2722–2724, October 2001.

Chapter 2

Optical fibre transmission systems: theory and modelling

This chapter uses computer modelling to investigate transmission systems using saturable absorbers (SAs) for soliton control and all-optical wavelength conversion. The essential components comprising such a system, and numerical modelling of their behaviour, are described.

The non-linear Schrödinger equation (NLSE) and pulse propagation, including soliton propagation, in optical fibre are discussed in Section 2.1. Solution of the NLSE using the split-step Fourier method (SSFM) and symmetrised SSFM using a computer program is described.

Erbium doped fibre amplifiers (EDFAs), which are used to overcome fibre loss are described in Section 2.2. Modelling of saturated amplification and amplified spontaneous emission (ASE) noise are considered. The propagation of signals in a system using periodic lumped amplification, such as that provided by EDFAs, is discussed in Section 2.3.

A realistic optical receiver model, which considers photodetector noise and optical filtering, is described in Section 2.4. The model allows the Q-factor and bit error rate of the propagating signal to be determined.

Section 2.5 presents a simple SA model, applicable to devices based on excitonic absorption bleaching (EAB) in multiple quantum wells (MQWs).

Sections 2.6 and 2.7 describe modelling of systems using SAs for soliton control and wavelength conversion respectively.

2.1 Pulse propagation in optical fibre

The signal pulses in an optical fibre transmission system are subject to loss, group velocity dispersion (GVD) and self phase modulation (SPM). Since higher order dispersion, and higher order and time-delayed non-linearities can be safely ignored for pulses longer than 1 ps [1] they are not considered in this work.

2.1.1 Representation of the signal pulses

Ignoring its polarisation, the field of an optical pulse propagating in single mode fibre can be represented as a complex scalar quantity,

$$E(z,t) = A(z,t)\exp((i\beta z - \omega t)) \tag{2.1}$$

where z = displacement along the fibre, t = time, β = mode propagation constant, ω = angular frequency and $A(z,t)$ = normalised complex pulse envelope. The normalisation of $A(z,t)$ is such that its amplitude is the square root of the power,

$$P(z,t) = \mid A(z,t) \mid^2 . \tag{2.2}$$

In studying pulse propagation, the term in Equation 2.1 varying at the optical frequency can be ignored. The remaining pulse envelope, $A(z,t)$ travels at the group velocity, v_g. The transformation

$$T = t - z/v_g \tag{2.3}$$

can be used to obtain $A(T)$, a representation of the pulse envelope in a frame of reference travelling at v_g.

2.1.2 Loss

Fibre loss is principally due to material absorption at long wavelengths, and to Rayleigh scattering at short wavelengths. Impurities introduced during manufacturing cause further peaks in the absorption spectra, the most significant of these being due to OH ions. The aggregate absorption spectrum has low loss windows at wavelengths around 1.3 µm and 1.55 µm which are employed in communications systems. The 1.55 µm window is preferred due to its lower loss, and its coincidence with the operating wavelength of erbium doped fibre amplifiers (EDFAs).

A signal propagating for distance d in fibre with loss α will be attenuated by a factor $\exp(\alpha d)$. Fibre loss is commonly stated in dB/km,

$$\alpha_{dB} = 0.4343\alpha. \tag{2.4}$$

Commercially available fibres typically have losses of $\alpha_{dB} = 0.25\,\mathrm{dB/km}$ at 1.55 µm.

2.1.3 Group velocity dispersion

To account for fibre dispersion, β, the mode propagation constant in Equation 2.1, is expanded using a Taylor series,

$$\beta(\omega) = \beta_0 + \beta_1(\omega - \omega_0) + \frac{1}{2}\beta_2(\omega - \omega_0)^2 + \ldots \tag{2.5}$$

β_1 is the reciprocal of the group velocity,

$$\beta_1 = \frac{1}{v_g}, \tag{2.6}$$

and β_2 is the GVD,

$$\beta_2 = \frac{d\beta_1}{d\omega}. \tag{2.7}$$

The majority of deployed systems use standard telecommunications fibre (STF), in which the group velocity has a maximum at about 1.3 μm. The GVD is thus zero at this, the zero dispersion wavelength (λ_D), positive for $\lambda < \lambda_D$ (normal dispersion) and negative for $\lambda > \lambda_D$ (anomalous dispersion). The GVD in STF is typically $\beta_2 = -25\,\mathrm{ps}^2/\mathrm{km}$ in the 1.55 μm window. Since low absolute values of GVD are desirable for high performance systems dispersion shifted fibre (DSF) is manufactured with a complex index profile which shifts the λ_D to $\approx 1.55\,\mu$m. Dispersion compensating fibre (DCF) with a high positive β_2 designed to compensate the negative β_2 of STF is also available.

2.1.4 Self phase modulation

The field due to an optical pulse propagating in a fibre medium causes a non-linear polarisation response such that light with optical power P at the optical frequency ω experiences the non-linear refractive index,

$$\tilde{n}(\omega, P) = n(\omega) + n_2 P, \tag{2.8}$$

where n_2 is the non-linear index coefficient. This ignores higher order and time delayed non-linearities. The signal will experience a phase shift, dependent on its optical frequency and optical power density, due to this non-linearity. This phase shift, the SPM, can be described in terms of the non-linearity coefficient,

$$\gamma = \frac{n_2 \omega_0}{c A_{eff}}, \tag{2.9}$$

where A_{eff} is the effective core area of the fibre. A signal with optical power P propagating for distance L in fibre with the non-linearity coefficient γ will experience a non-linear phase shift

$$\Delta\phi = \gamma L P. \tag{2.10}$$

Typical fibres have a non-linearity coefficient of $\gamma = 10^{-3}$ /W/m.

2.1.5 The non-linear Schrödinger equation

Pulse propagation in optical fibre, considering GVD, SPM and loss, is described by the non-linear Schrödinger equation (NLSE),

$$i\frac{\partial A}{\partial z} + \frac{i}{2}\alpha A - \frac{i}{2}\beta_2\frac{\partial_2 A}{\partial T^2} + \gamma|A|^2 A = 0. \tag{2.11}$$

Numerical solution of the NLSE is discussed in Section 2.1.8.

2.1.6 The consequences of group velocity dispersion and self phase modulation

High data rate systems must employ short signal pulses to avoid inter-symbol interference (ISI). As the signal pulse width decreases in the time domain the spectral width will increase. An ideal Gaussian pulse, which has the envelope

$$A(T) = \left(P_0 exp\left(-\frac{T^2}{2T_0^2}\right)\right)^{1/2}, \tag{2.12}$$

is said to be transform limited. It has spectral width

$$\Delta\omega = 1/T_0. \tag{2.13}$$

The envelope of Equation 2.12 can be made more realistic by considering chirp. In the case of linear chirp

$$A(T) = \left(P_0 exp\left(-\frac{(1+iC)T^2}{2T_0^2}\right)\right)^{1/2}, \tag{2.14}$$

where C is the chirp parameter, and

$$\Delta\omega = (1+C^2)^{1/2}/T_0, \tag{2.15}$$

In a fibre with non-zero GVD the group velocity will vary across the spectrum of the signal pulse. As the signal pulse propagates it will therefore become broader in the time domain. This broadening is exacerbated in the case of negative chirp in the anomalous dispersion regime, and of positive chirp in the normal dispersion regime. The opposite cases, positive chirp in the anomalous dispersion regime and negative chirp in the normal dispersion regime lead to pulse narrowing.

As a signal pulse propagates $A(T)$ will acquire a time dependent phase shift, as a consequence of its time dependent amplitude and SPM. SPM thus results in chirping and spectral broadening of pulses. In the absence of GVD the temporal width of the pulse will be unaffected by SPM. However, chirping due to SPM makes the signal pulses susceptible to GVD induced temporal broadening.

2.1.7 Soliton pulse propagation

It has been shown that a pulse with a sech^2 envelope,

$$P(t) = P_0 \text{sech}^2\left(\frac{T}{T_0}\right), \tag{2.16}$$

can propagate undisturbed for an infinite distance in the anomalous dispersion regime in a lossless fibre, provided that its amplitude and length, P_0 and T_0, satisfy the condition

$$P_0 = \frac{|\beta_2|}{\gamma T_0^2}. \tag{2.17}$$

Such pulses are known as solitons, and Equation 2.17 is referred to as the soliton condition. Solitons are commonly characterised by their full width half maximum (FWHM) pulse length,

$$T_{FWHM} = 1.76 T_0. \tag{2.18}$$

The energy of a soliton, or of any sech^2 pulse is,

$$E = 2T_0 P_0. \tag{2.19}$$

The use of solitons in long distance fibre systems was proposed by Mollenauer [2].

The phase of a propagating soliton is subject to a periodic variation. The period of this is referred to as the soliton period. Another characteristic of solitons, which makes their use in real systems feasible, is that a pulse which is, when launched, similar to a soliton, will tend to evolve to become a soliton. This increases the robustness of soliton systems, and relaxes the requirement to launch pulses whose envelopes exactly satisfy Equations 2.16 and 2.17

2.1.8 Modelling pulse propagation using the split-step Fourier method

The split-step Fourier method (SSFM) is a numerical method used to solve the non-linear NLSE, and hence model pulse propagation in optical fibre. The SSFM represents the normalised pulse envelope, $A(T)$ (Section 2.1.1), as a series of discrete values, A_n. These are separated by a constant time step, ΔT, such that

$$A_n(z) = A(z, n\Delta T). \tag{2.20}$$

A_n is propagated over a short distance, dz, by applying a non-linearity operator in the time domain and a dispersion operator in the frequency domain. F_n, the frequency domain representation of A_n, is obtained using a fast Fourier transform (FFT),

$$F_n = \text{FFT}(A_n). \tag{2.21}$$

The inverse operation is

$$A_n = \mathrm{IFFT}(F_n). \tag{2.22}$$

A single SSFM step for A_n with N points can be written in pseudocode

```
for $i = 1$ to $N$ do
    $A_i \Leftarrow A_i \exp(i\gamma \mid A_i \mid^2 dz)$
end for
$F_n \Leftarrow FFT(A_n)$
for $i = 1$ to $N$ do
    $F_i \Leftarrow F_i \exp(dz(i\omega_i^2 \beta_2/2 + \alpha))$
end for
$A_n \Leftarrow IFFT(F_n)$
```

where α, γ and β_2 are defined in Section 2.1 and ω_i is the optical frequency corresponding to F_i.

2.1.9 The symmetrised split-step Fourier method

The error in the SSFM is reduced if the non-linearity operator is applied in the middle of each step. The algorithm is then known as the symmetrised SSFM. Propagation of A_n over M steps of length dz using the symmetrised SSFM can be written in pseudocode

```
$F_n \Leftarrow FFT(A_n)$
for $i = 1$ to $N$ do
    $F_i \Leftarrow F_i \exp(dz(i\omega_i^2 \beta_2/2 + \alpha)/2)$
end for
$A_n \Leftarrow IFFT(F_n)$
for $j = 1$ to $M - 1$ do
    for $i = 1$ to $N$ do
        $A_i \Leftarrow A_i \exp(i\gamma \mid A_i \mid^2 dz)$
    end for
    $F_n \Leftarrow FFT(A_n)$
    for $i = 1$ to $N$ do
        $F_i \Leftarrow F_i \exp(dz(i\omega_i^2 \beta_2/2 + \alpha))$
    end for
    $A_n \Leftarrow IFFT(F_n)$
end for
for $i = 1$ to $N$ do
    $A_i \Leftarrow A_i \exp(i\gamma \mid A_i \mid^2 dz)$
```

```
end for
$F_n \Leftarrow FFT(A_n)$
for $i = 1$ to $N$ do
    $F_i \Leftarrow F_i \exp(dz(i\omega_i^2\beta_2/2 + \alpha)/2)$
end for
```

The computer program which was used to produce the systems modelling results presented later in this chapter utilised the above symmetrised SSFM algorithm.

2.2 Erbium doped fibre amplifiers

2.2.1 Optical amplification in erbium fibre

Fibre loss can be compensated for by incorporating amplifiers in the transmission system. Distributed amplification using the Raman effect and point amplification using EDFAs or semiconductor optical amplifiers (SOAs) have been considered for this application. This thesis considers the use of EDFAs, since they are most common in practical systems.

An EDFA consists of a length of optical fibre which has been doped with Er^{3+} ions. If it is optically pumped at a suitable wavelength population inversion of the Er^{3+} ions occurs, enabling it to support stimulated emission. Practical EDFAs incorporate an optical isolator to inhibit lasing.

2.2.2 Amplified spontaneous emission noise

An EDFA will produce amplified spontaneous emission (ASE) noise around the signal wavelength, as a consequence of spontaneous decay of excited Er^{3+} ions. EDFAs are characterised by their noise figure, F_n. The lowest values of F_n are obtained when an EDFA is operated in saturation, that is with a large enough input that the output is limited by the pump power. The noise figure of an ideal saturated EDFA is 3 dB. Practical devices have noise figures of 5 dB to 6 dB.

F_n is related to the spectral density of the spontaneous emission noise from the EDFA, S_{sp}, through the expression

$$S_{sp}(\nu) = (G-1)n_{sp}h\nu \tag{2.23}$$

where ν = optical frequency, G = gain, n_{sp} = spontaneous emission factor, and h = Planck's constant. The spontaneous emission factor can be written in terms of the gain and the noise figure,

$$n_{sp} = \frac{GF_n}{2(G-1)}. \tag{2.24}$$

2.2.3 Modelling saturated amplification in erbium doped fibre amplifiers

In a saturated EDFA model the output power, P_{out}, is assumed to be fixed, such that the gain is dependent on the average input power, P_{in}.

A computer model can measure the average input power when it is executed,

$$P_{in} = \Delta T \sum_{i=1}^{N} |A_i|^2, \tag{2.25}$$

and hence calculate the gain,

$$G = \frac{P_{out}}{P_{in}}. \tag{2.26}$$

The slow relaxation time ($\approx 20\,\text{ms}$) of the EDFA makes the gain insensitive to variations of P_{in} on anything faster than a millisecond timescale.

2.3 Pulse propagation in periodically amplified systems

2.3.1 Average soliton systems

Soliton-like pulse propagation is possible in systems with periodic amplification, provided that the amplifier spacing is small compared to the soliton period. The pulses are referred to as guiding centre [3] or average [4] solitons since, whilst they do not satisfy the soliton condition at any point, their propagation over many amplifier spans resembles that of true solitons in lossless fibre.

An average soliton must be launched into the initial fibre span with the pulse envelope

$$A(T) = E\sqrt{(}P_0)\,\text{sech}\left(\frac{t}{\tau}\right), \tag{2.27}$$

where E is a pre-emphasis factor to compensate for the fibre loss. Blow and Doran [4] showed that

$$E = \frac{1}{2}\left(1 + \exp\left(-\frac{2\alpha L}{Z_0}\right)\right) \tag{2.28}$$

where L is the amplifier spacing. The requirement that the amplifier spacing should be small in relation to the soliton period,

$$Z_0 = \frac{\pi}{2}\frac{T_0^2}{|\beta_2|}, \tag{2.29}$$

is a significant limitation for average soliton systems. Long amplifier spacings are desirable for economic reasons.

Average solitons can apparently propagate for an unlimited distance in a periodically amplified system, provided that the amplifier spacing is sufficiently small. In reality this is not the case. The main factors limiting system length, interactions between adjacent signal pulses and ASE noise, are described in Sections 2.3.2 and 2.3.3.

2.3.2 The soliton-soliton interaction

Adjacent solitons have low intensity wings which can extend into adjacent bit slots. These low intensity wings allow the pulses to interact through the fibre non-linearities. This interaction is referred to as soliton-soliton interaction (SSI) or, in the case of systems employing non-linear supported (NLS) transmission, intra-channel cross phase modulation (XPM) by analogy with XPM in wavelength division multiplexed (WDM) systems. The interaction can take the form of an attractive or repulsive force between the adjacent pulses, depending on their relative polarisations, amplitudes and phases. Pulses in a data stream can be either advanced or retarded relative to their bit slots. The net result is a jittering of the pulses comprising the data stream.

2.3.3 Gordon-Haus jitter

As discussed in Section 2.2.2 EDFAs produce ASE noise. This mixes with the amplified pulses causing small random shifts to their centre wavelengths. As the pulses propagate these wavelength shifts translate to timing jitter due to GVD. In the case of soliton systems this is known as the Gordon-Haus jitter (GHJ) [5].

Analytic methods by which the magnitude of the GHJ can be calculated at the end of a long, periodically amplified, transmission system have been described by Gordon and Haus [5], and by Marcuse [6]. Since the computer modelling described in this thesis uses the SSFM to solve the NLSE numerically noise is added to the output of each EDFA as described in Section 2.2.2.

2.4 Optical receivers and received signal quality

2.4.1 Eye diagrams and eye closure

Figure 2.1 shows optical eye diagram representations of a 10Gb/s, pseudo-random bit stream (PRBS) of 64 10ps FWHM sech^2 pulses before and after propagation through a periodically amplified transmission system with many amplifier spans. The eye diagrams are created by overlaying the signals in each bit slot.

An optical receiver makes a decision as to the state of each received bit. A clock recovery strategy is used so that the decision is made at the centre of each bit slot. The instantaneous power at the centre of each bit slot is compared with the average for all bit slots (the decision level).

In the case of the launched pulse (Figure 2.1a) the signal powers for the '0' and '1' bits are well separated from the decision level at the centre of the bit slot. This is not true for the output pulse (Figure 2.1b), increasing the probability of the receiver making a wrong decision. Such an output pulse is said to have experienced eye closure.

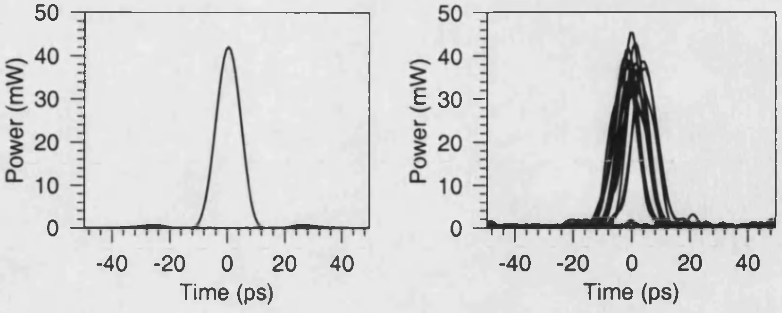

(a) (b)

Figure 2.1: Optical eye diagram representations of a group of 64 pseudo-random pulses (a) before and (b) after propagation through a periodically amplified system with many spans.

2.4.2 Realistic optical receiver

A real receiver converts the optical signal to an electrical one, before making a comparison based on the electrical signal level. A simple receiver model consists of a photodiode and an electrical filter.

The instantaneous current in a noise free photodiode is

$$i = P\mathscr{R} + I_{dark} \tag{2.30}$$

where P = instantaneous optical power, $\mathscr{R}$ = responsivity, and I_{dark} = dark current. i will be degraded by both shot and Johnson (or thermal) noise. Shot noise creates a noise current,

$$\overline{i_S^2} = 2e\bar{i}B \tag{2.31}$$

where $\bar{i}$ = average current, e = the electronic charge, and B = device bandwidth. The Johnson noise current is

$$\overline{i_J^2} = \frac{4k_BTB}{R_{eq}} \tag{2.32}$$

where k_B = Boltzmann's constant, T = absolute temperature, B = device bandwidth, and R = load resistance. The instantaneous voltage across the load resistance, on which the decision as to the state of each pulse is based, will be

$$v = (i + i_S + i_J)R \tag{2.33}$$

Figures 2.2a and 2.2b show the difference in the eye diagram due to using a simple receiver model based on Equations 2.30 to 2.33. The impact of the noise is small since, in the modelled system, the photodetector is preceded by an optical amplifier.

The quality of the receiver output signal can be improved by adding an electrical bandpass filter with a centre frequency equal to half of the repetition rate of the signal pulses. The effect of filtering with a 5 GHz bandwidth, second order, Butterworth filter with the transfer function

$$T(f) + \frac{1}{1+((f-f_0)/B)^2}, \tag{2.34}$$

where f_0 = centre frequency, and B = bandwidth, is shown in Figure 2.2c.

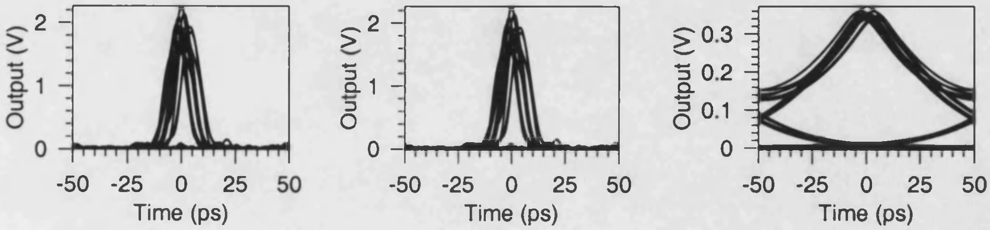

(a) (b) (c)

Figure 2.2: Modelled output voltage of an opto-electronic receiver for the optical input of Figure 2.1(b). (a) is the output voltage of a noise free photodetector with $\mathscr{R} = 1$, $I_{dark} = 1\,\mu$A and $R_L = 50\,\Omega$, calculated using Equations 2.30 and 2.33. (b) includes the shot and Johnson noise, using Equations 2.31 and 2.32. (c) shows the effect of adding a first order, 5 GHz bandwidth, Butterworth filter (Equation 2.34.)

2.4.3 Bit error rate and quality factor

The ultimate figure of merit for a transmission system is the received bit error rate (BER). A bit error rate less than 10^{-9} is required in deployed systems. BER can be measured experimentally using commercially available BER test-sets (BERTs).

Since computer models of transmission systems typically run many orders of magnitude more slowly than real time, BER calculations are not feasible and performance is evaluated using the quality (Q) factor. This is a measure of the likelihood of the receiver making the wrong decision as to the state of a received pulse. It is calculated from the distribution of signal levels at the bit slot centres,

$$Q = \frac{\sigma_1 + \sigma_0}{\mu_1 - \mu_1} \tag{2.35}$$

where σ_0 = standard deviation of levels of '0' pulses, σ_1 = standard deviation of levels of '1' pulses, μ_0 = mean of levels of '0' pulses, and μ_1 = mean of levels of '1' pulses. The BER can be calculated directly from the Q-factor using the expression

$$BER = \frac{1/2}{\text{erfc}} \left(\frac{Q}{\sqrt{2}} \right), \tag{2.36}$$

according to which a BER of 10^{-9} corresponds to a Q factor of 6.

This approach is limited in that it assumes the signal to be degraded only by Gaussian noise, which is not true in a system where the signal is affected by GHJ and the soliton-soliton interaction SSI.

2.5 Saturable absorber model

The saturable absorber (SA) model used was based on variable step size solution of Equations A.18 and A.19. The derivation of these equations is described in Appendix A.

The modelled SAs are described in terms of contrast ratio, R, and excess loss. The excess loss is the fully saturated transmission, T_s, expressed in decibels, that is $-10\log_{10}(T_s)$. The CW saturation characteristic of Figure 2.3 illustrates the physical significance of T_s and R.

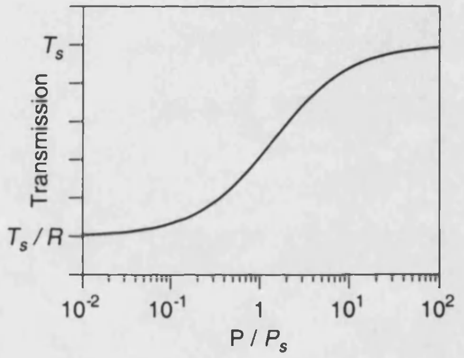

Figure 2.3: CW saturation characteristic of the modelled SAs. P and P_s are respectively the power incident on the SA and the SA saturation power.

2.6 Systems modelling: saturable absorbers for soliton control

2.6.1 Simple system

Propagation of 5 ps FWHM sech^2 pulses in a system consisting of 40 km spans of DSF is investigated. A single figure-of-merit, the maximum error free (Q-factor ≥ 6) transmission distance, is used to compare each variation of the modelled system. The soliton period in this system, calculated using Equation 2.29, is 31.5 km. Since the span length is not short compared to the soliton period this system will not support average soliton propagation. Signal propagation is therefore expected to be limited by the soliton-soliton interaction rather than by the accumulation of ASE noise and Gordon-Haus jitter.

Initially pulse propagation was modelled in the system of Figure 2.4 which contains no soliton control components. Parameters of the modelled system are summarised in Table 2.1. The EDFA output power was determined using a simple optimisation procedure. Results are shown in Figure 2.5. Error-free transmission was maintained for 360 km. Propagation is limited by an accumulation of dispersive radiation, and by attractive forces between adjacent signal pulses. The reach of the system could be extended by adding dispersion compensation to reduce the total per-span dispersion, by reducing the span length such that average soliton propagation was supported, or by implementing some soliton control techniques. Soliton control is investigated in the following sections.

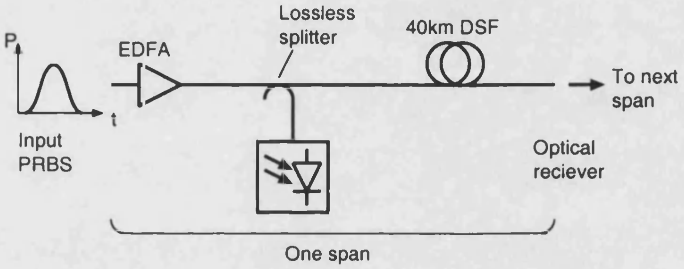

Figure 2.4: Configuration of modelled system with no soliton control.

Component	Parameter	Value
Fibre	GVD	$-0.58 \times 10^{-27}\,\mathrm{s/m^2}$
	SPM	0.0022 /W/m
	Loss	0.23 dB/km
	Span length	40 km
	SSFM step length	0.4 km
EDFA	Noise figure	6 dB
	Output power	15 mW
Signal	Pulse shape	sech^2
	Pulse width	5 ps FWHM
	Repetition rate	40 Gb/s
	PRBS length	256 bits
	SSFM time step	195 fs

Table 2.1: Parameters of modelled system with no soliton control.

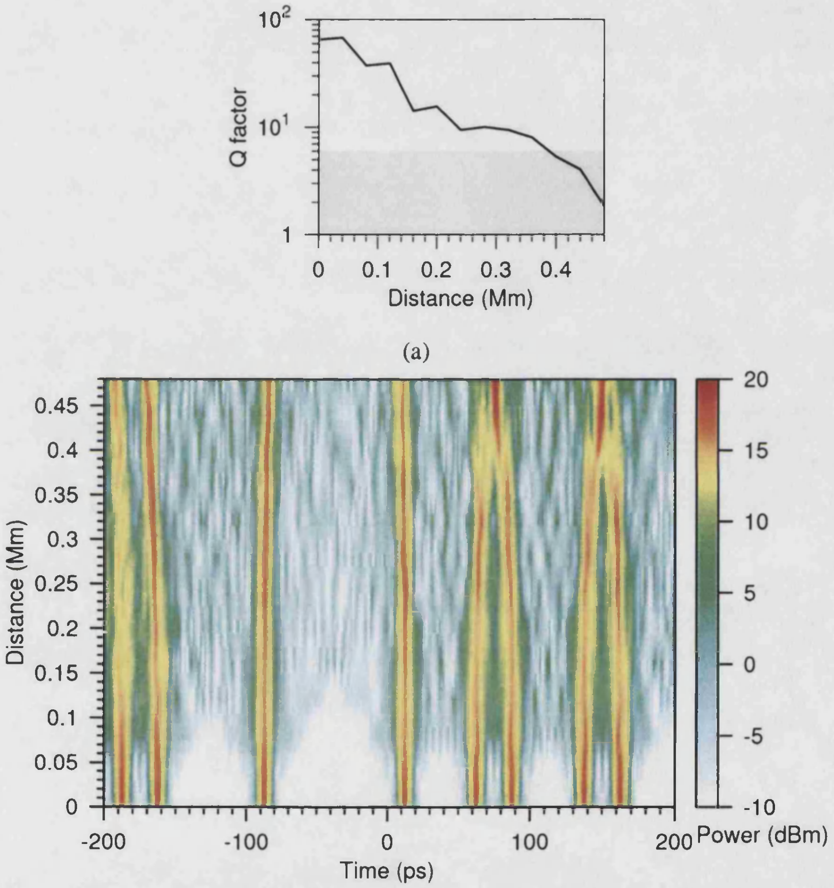

(a)

(b)

Figure 2.5: Modelled pulse propagation in a system with no soliton control. Q-factor is plotted as a function of distance in (a). The evolution of a part of the PRBS is shown in (b).

2.6.2 Systems with guiding filters

The effect of adding guiding filters to the system, as shown in Figure 2.6 was then investigated. The filters used had the complex transfer function

$$T(f) = \frac{1}{2i(f - f_0)/B} \tag{2.37}$$

where f_0 = filter centre frequency and B = filter bandwidth. Results for filters with bandwidths of 0.6 nm and 1.0 nm are shown in Figures 2.7 and 2.8 and summarised in Table 2.2. Whilst performance is improved with filters of either bandwidth 1.0 nm bandwidth filters are most effective, increasing the error-free distance to 1,200 km.

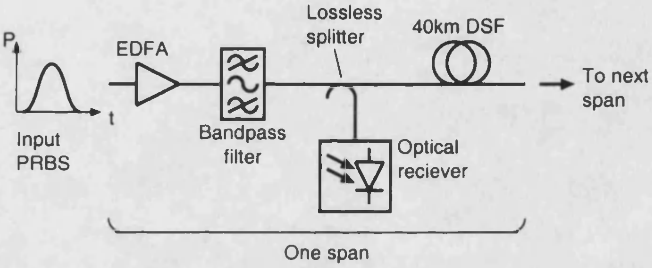

Figure 2.6: Configuration of modelled system using guiding filters for soliton control.

Filter bandwidth (nm)	EDFA output power (mW)	Error-free distance (km)
0.6	21.0	760
1.0	20.5	1200

Table 2.2: Summary of results of propagation modelling in system using guiding filters for soliton control.

2.6.3 Systems with saturable absorbers and guiding filters

The configuration of Figure 2.9 was used to investigate pulse propagation in systems using guiding filters and SAs for soliton control. The inclusion of a second EDFA allows the powers at the inputs to the SA and the DSF span to be independently optimised. The average power incident on the SA was kept constant; instead different values of SA saturation energy, and hence saturation power, were used. Pulse propagation in the system was modelled with the parameters shown in Table 2.3. Q-factor versus distance plots are shown in Figures B.1 to B.6 in Appendix B.

The results are summarised in Figures 2.10 to 2.12 in which error-free distance is plotted as a function of the maximum transmission change in the first SA in the system.

The significant scatter of the data points which is evident in these plots is attributable to the dependence of propagation on pattern of the propagating pulses. The scatter could have been

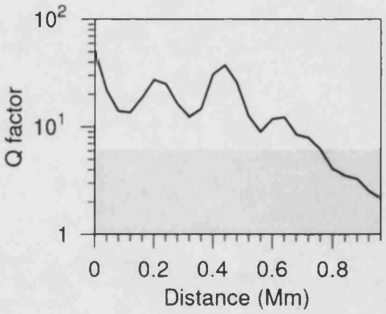

(a)

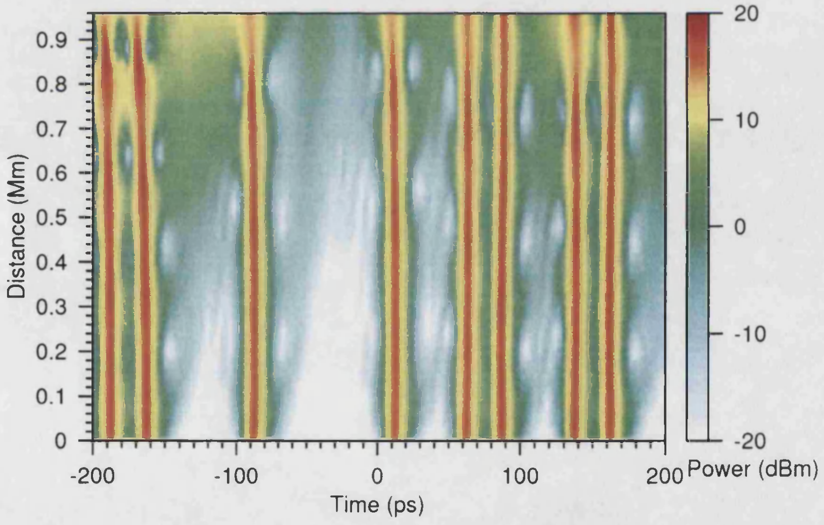

(b)

Figure 2.7: Modelled pulse propagation in a system using 0.6nm guiding filters. Q-factor is plotted as a function of distance in (a). The evolution of a part of the PRBS is shown in (b).

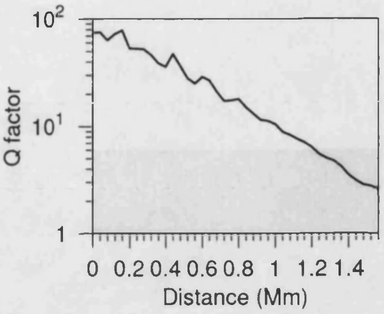

(a)

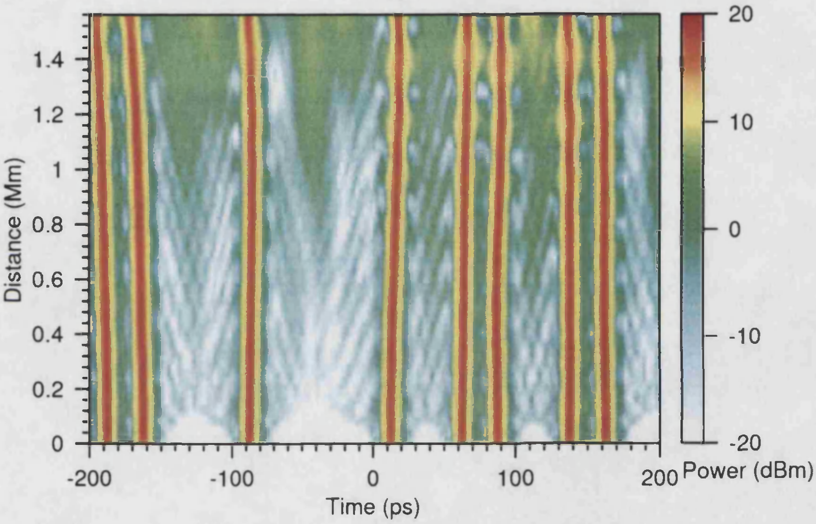

(b)

Figure 2.8: Modelled pulse propagation in a system using 1.0nm guiding filters. Q-factor is plotted as a function of distance in (a). The evolution of a part of the PRBS is shown in (b).

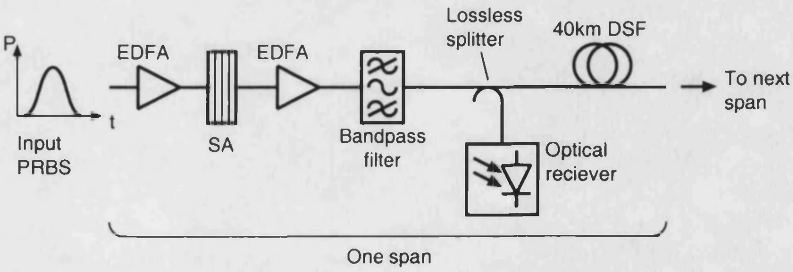

Figure 2.9: Configuration of modelled system using guiding filters and SAs for soliton control.

Component	Parameter	Value
Fibre	GVD	$-0.58 \times 10^{-27}\,\mathrm{s/m^2}$
	SPM	0.0022 /W/m
	Loss	0.23 dB/km
	Span length	40 km
	SSFM step length	0.4 km
EDFA 1	Noise figure	6 dB
	Output power	100 mW
EDFA 2	Noise figure	6 dB
	Output power	Optimised to compensate for SA loss
Signal	Pulse shape	sech^2
	Pulse width	5 ps FWHM
	Repetition rate	40 Gb/s
	PRBS length	256 bits
	SSFM time step	195 fs
Optical filter	Bandwidth	0.6 nm, 1.0 nm
SA	Recovery time	1 ps, 2 ps, 5 ps, 10 ps,
	Contrast ratio	10, 5, 2
	Pulse saturation energy	1 pJ, 2 pJ, 5 pJ, 10 pJ
	Excess loss	10 dB, 16 dB (with 0.6 nm filters only)

Table 2.3: SA parameters used in systems modelling.

reduced by using a longer PRBS, or by averaging the results obtained using different patterns. Sufficiently fast computers were not, however, available for such modelling to be carried out within a reasonable time. Bezier fits were therefore added to the plots to facilitate comparison of the scattered data sets. Inspection of these suggests that the maximum transmission change, rather than the parameters P_s and R, is critical.

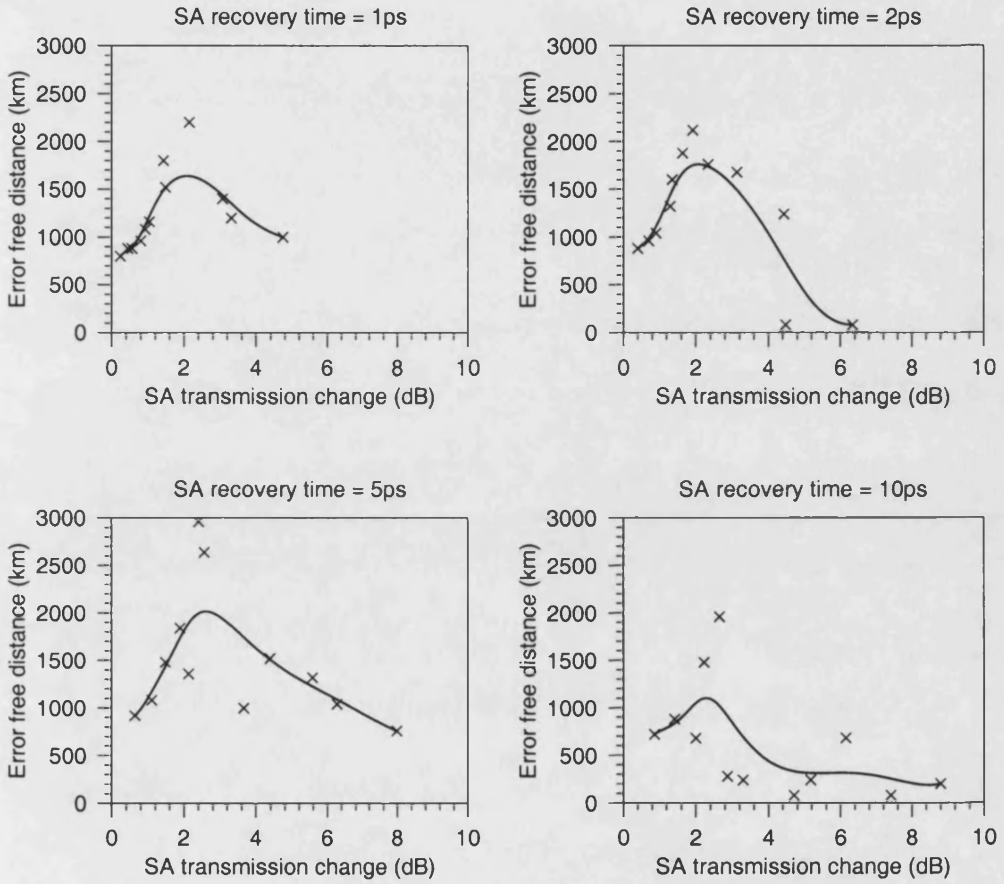

Figure 2.10: Error free transmission distance in systems with 0.6nm guiding filters and SAs with 10dB excess loss. Transmission distance is plotted as a function of measured transmission change in the SAs. The lines are Bezier curves fitted to the data points.

A comparison of Figures 2.10 and 2.11 shows that SA soliton control is more effective when 0.6nm, rather than 1.0nm guiding filters are used. It is possible that spectral broadening of the pulses in the narrower filters balances compression of the signal pulses in the non-linear SAs, resulting in a stabilisation of pulse width after propagation through many amplifier spans. Whilst this potential pulse stabilisation mechanism could be relevant to ultra-fast transmission system design, further investigation is beyond the scope of this thesis.

Referring to the results for systems with 0.6nm guiding filters (Figure 2.10), error free dis-

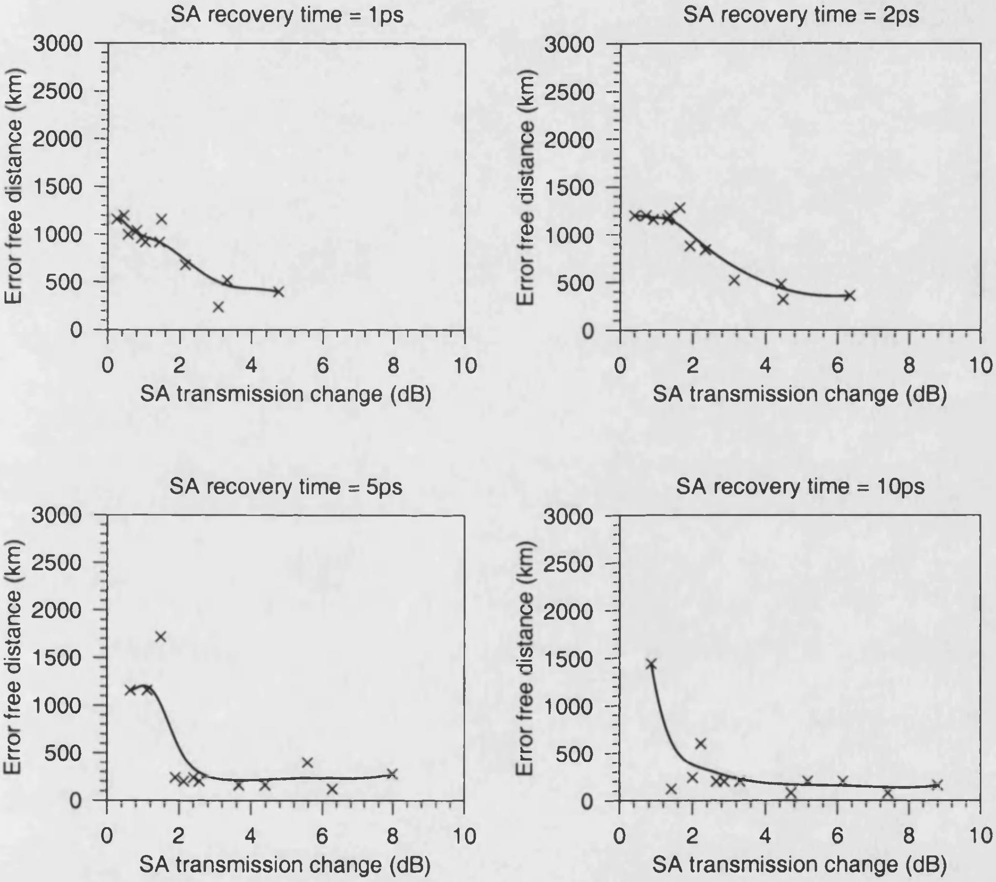

Figure 2.11: Error free transmission distance in systems with 1.0nm guiding filters and SAs with 10dB excess loss. Transmission distance is plotted as a function of measured transmission change in the SAs. The lines are Bezier curves fitted to the data points.

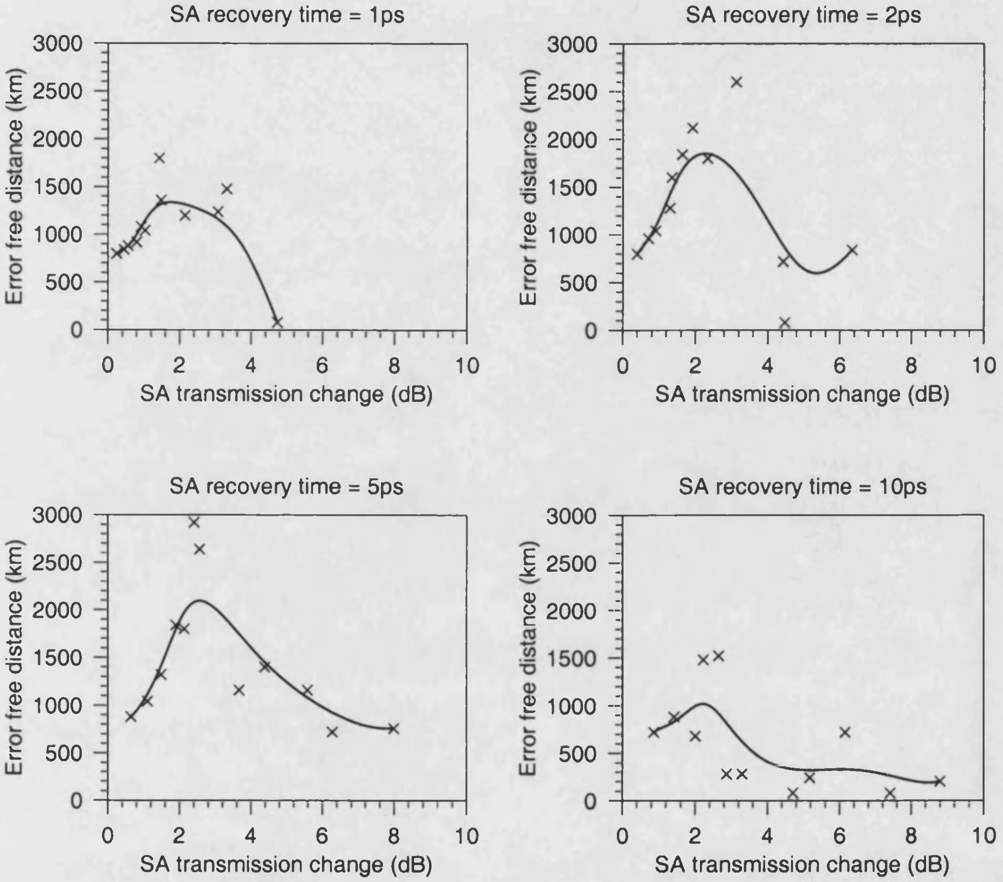

Figure 2.12: Error free transmission distance in systems with 0.6 nm guiding filters and SAs with 16 dB excess loss. Transmission distance is plotted as a function of measured transmission change in the SAs. The lines are Bezier curves fitted to the data points.

tances are greatest when the SA transmission change is approximately 2 dB, and the SA recovery time is 5 ps or less. For greater SA transmission changes there is a reduction in system performance. Whilst high SA contrast will increase the relative loss experienced by the inter-pulse noise and dispersive radiation, it will also result in strong reshaping of the signal pulses. The decreasing performance when the SA transmission change is higher is attributable to destabilisation of the signal pulses due to this reshaping.

For SA transmission changes of 2 dB and greater performance is best when the SA recovery time is 5 ps. This is consistent with the above suggestion that strong pulse reshaping will reduce the system performance; longer SA recovery times will reduce reshaping of the pulse tail. Poor performance with 10 ps SA recovery is attributable to incomplete SA recovery in the interval between adjacent signal pulses which will lead to patterning effects.

Comparison of the results of Figures 2.10 and 2.12 shows a negligible performance degradation due to a 6 dB increase in the excess loss of the SA. This is consistent with signal propagation being limited by the SSI. In a noise limited system the higher ASE levels resulting from the increased amplifier gains required to compensate for the large SA insertion loss would degrade the system performance.

2.6.4 Comparison of the modelled systems

Contour plots illustrating signal propagation in the systems with no soliton control, with 1.0 nm filters, and with 0.6 nm filters and SAs for soliton control are presented for comparison in Figure 2.13. The SA parameters used are those which were, according to the modelling of Section 2.6.3, optimal (contrast ratio = 2, excess loss = 10 dB, recovery time = 2 ps, pulse saturation energy = 1 pJ.) In each example degradation of the propagating signal is due to attractive or repulsive forces between adjacent signal pulses, suggesting that the performance of the modelled systems is, as expected, limited by the SSI.

No soliton control

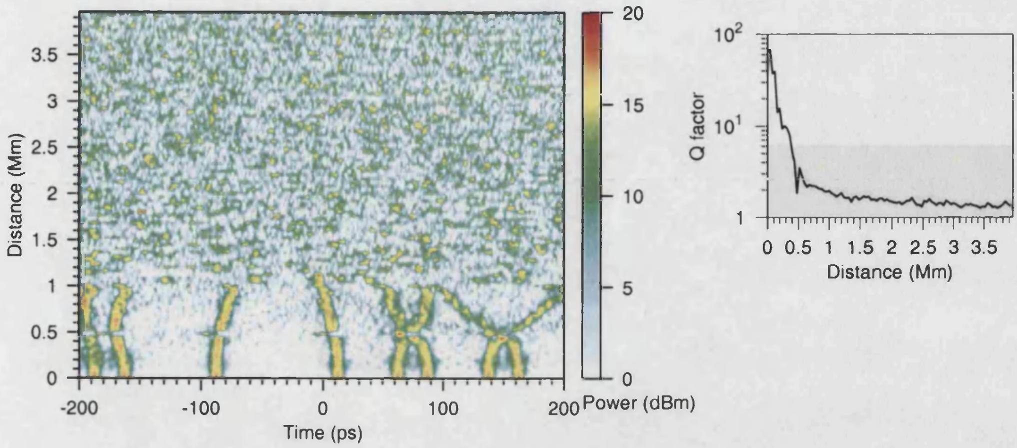

Soliton control using 1.0 nm filters

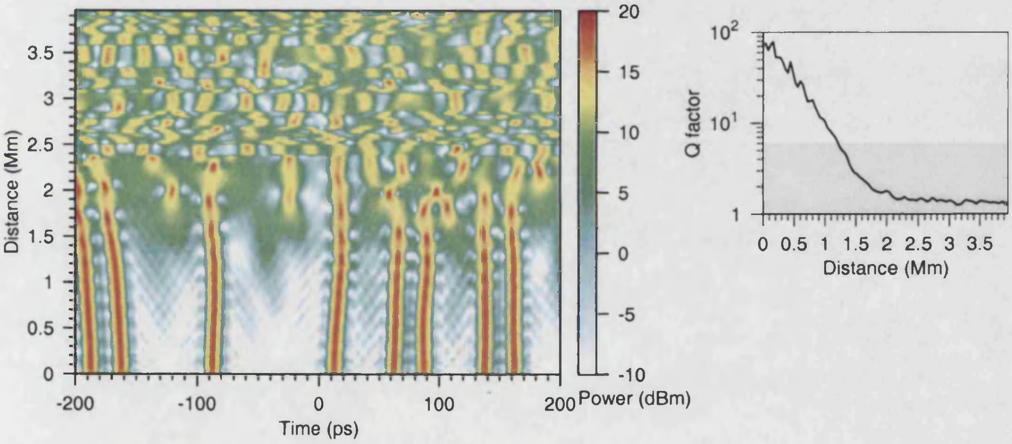

Soliton control using 0.6 nm filters and SAs

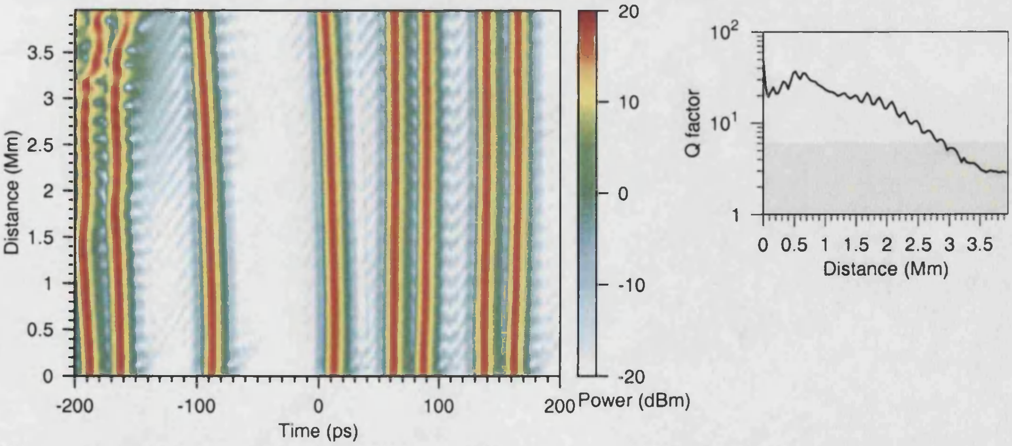

Figure 2.13: Comparison of pulse propagation in a systems, with no soliton control, with optical filters for soliton control, and with saturable absorbers and optical filters for soliton control.

2.7 Systems modelling: saturable absorbers for all-optical wavelength conversion

All-optical wavelength conversion was modelled in the system of Figure 2.14 using 1.0 nm guiding filters for soliton control. System parameters used are summarised in Table 2.4. 30 km fibre spans, comparable to the 31.5 km soliton period, were used. The control results of Figure 2.15 show stable pulse propagation with an error free transmission distance of 1,140 km in a system with no wavelength conversion. The continuous wave (CW) and PRBS powers incident on the device were maintained at 10 mW and 200 mW respectively whilst the saturation energy, and hence saturation power, of the SA was varied. Experimentation showed that this 20:1 power ratio resulted in optimal transmission of the wavelength converted signals. An ideal filter, with the square transfer function shown in Figure 2.16 followed the SA to prevent leakage of the signal at the initial wavelength.

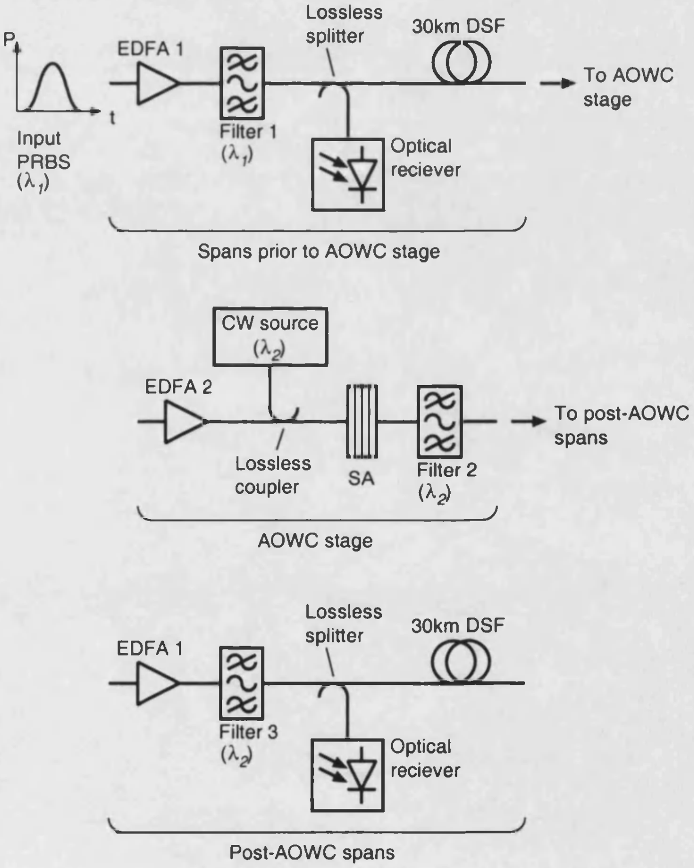

Figure 2.14: Configuration of modelled system used to investigate wavelength conversion using SAs.

A system in which SA wavelength conversion was implemented at the end of the fourth fibre

Component	Parameter	Value
Fibre	GVD	$-0.58 \times 10^{-27}\,\mathrm{s/m^2}$
	SPM	0.0022
	Loss	0.23 dB/km
	Span length	30 km
	SSFM step length	0.3 km
EDFA 1	Noise figure	6 dB
	Output power	15 mW
EDFA 2	Noise figure	6 dB
	Output power	200 mW
Signal	Pulse shape	sech^2
	Pulse width	5 ps FWHM
	Repetition rate	40 Gb/s
	PRBS length	256 bits
	SSFM time step	195 fs
Filter 1	Transfer function	$T(f) = 1/(2i(f-f_0)/B)$
	Bandwidth	1.0 nm
	Wavelength offset	0 nm
Filter 2	Transfer function	square
	Bandwidth	1.0 nm
	Wavelength offset	2 nm
Filter 3	Transfer function	$T(f) = 1/(2i(f-f_0)/B)$
	Bandwidth	1.0 nm
	Wavelength offset	2 nm
CW Source	Wavelength offset	2 nm
	Power	10 mW

Table 2.4: Parameters of modelled system used to investigate SA-based wavelength conversion.

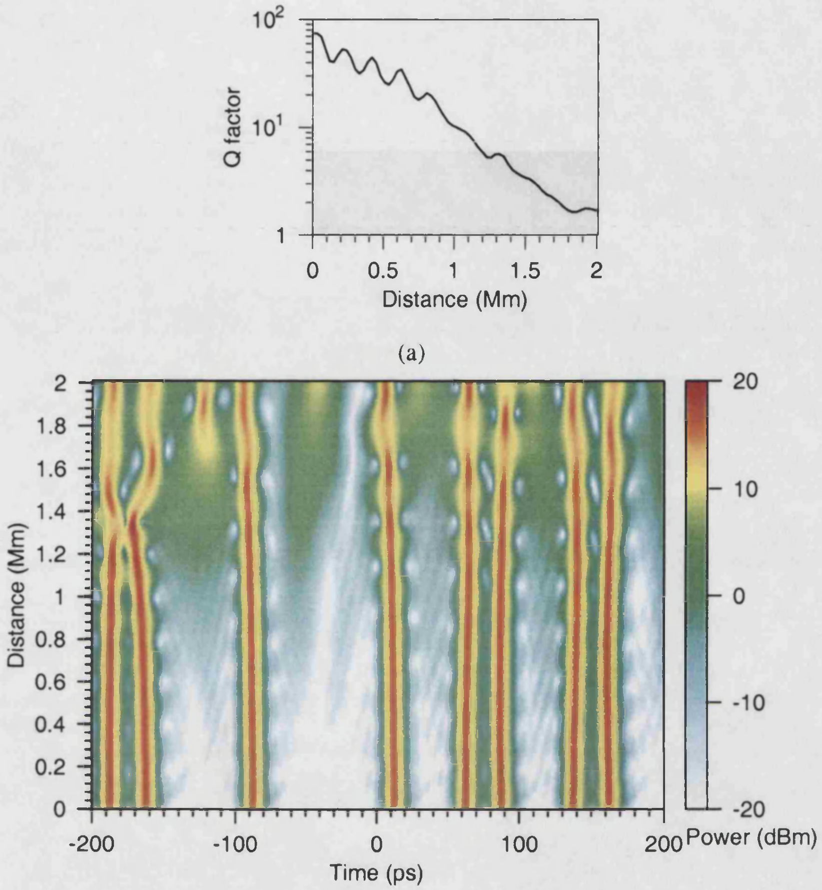

(a)

(b)

Figure 2.15: Control results for SA wavelength conversion modelling: pulse propagation in the absence of an SA wavelength converter. Q-factor is plotted as a function of distance in (a), (b) shows the evolution of a part of the PRBS

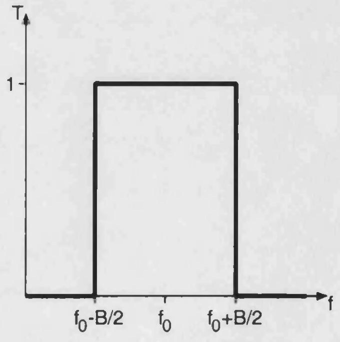

Figure 2.16: Transfer function of the ideal square filter using in modelling of SA-based wavelength conversion. f_0 and B are the filter centre frequency and bandwidth respectively.

span was modelled. Q factor versus distance plots are shown in Figures B.7 and B.8 in Appendix B. Error free distance is plotted as a function of peak transmission change in the SA in Figure 2.17. With the exception of a few data points, there is a systematic dependence of error-free distance on transmission change in the SA. The SA recovery time appears to have little influence on the performance, within the 1 ps to 10 ps range used.

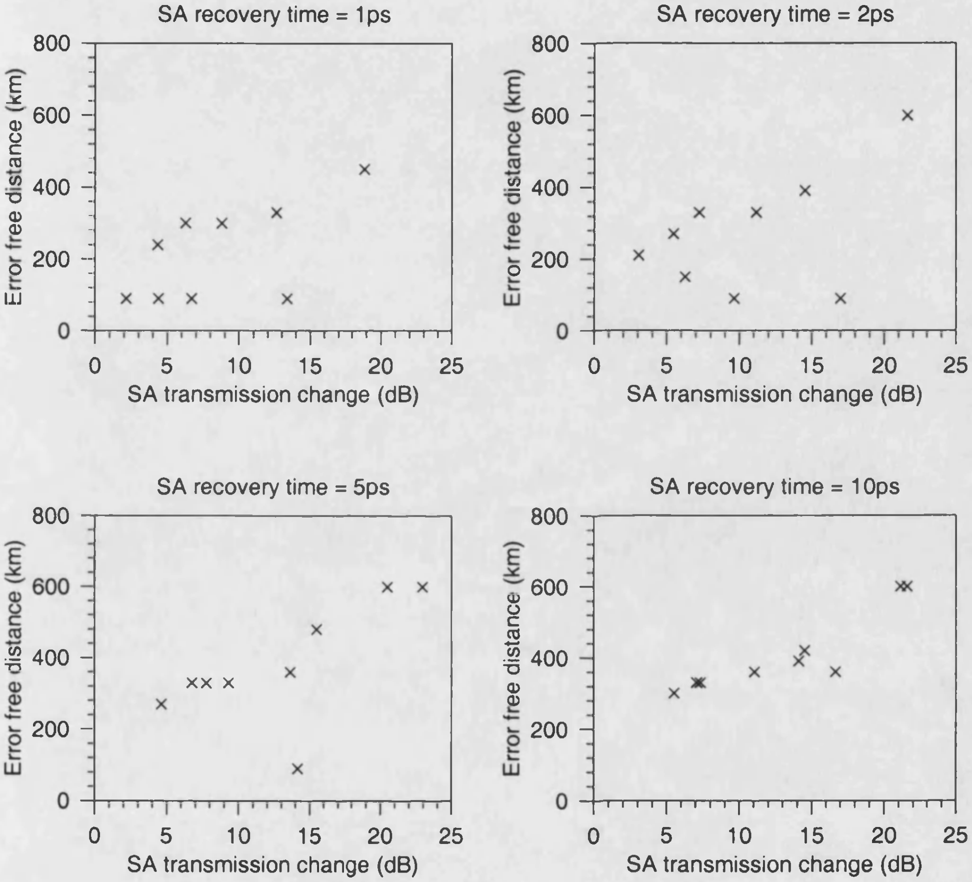

Figure 2.17: Error free transmission distance in systems using an SA as a wavelength converter. Transmission distance is plotted as a function of measured transmission change in the SAs.

Propagation of the signal in the system with SA recovery time of 5 ps, saturation energy of 1 pJ and contrast ratio of 1000 (one the combinations of SA parameters which maximised the transmission distance of the wavelength converted signal) is shown in Figure 2.18. The finite contrast ratio of the SA results in CW radiation in empty bit slots, and between adjacent signal pulses after 120 km where wavelength conversion is performed. Following wavelength conversion there is an exchange of energy between the signal pulses and the inter-pulse CW radiation, with a period of approximately 200 km. This interaction is a probable cause of the eventual collapse of the signal pulses.

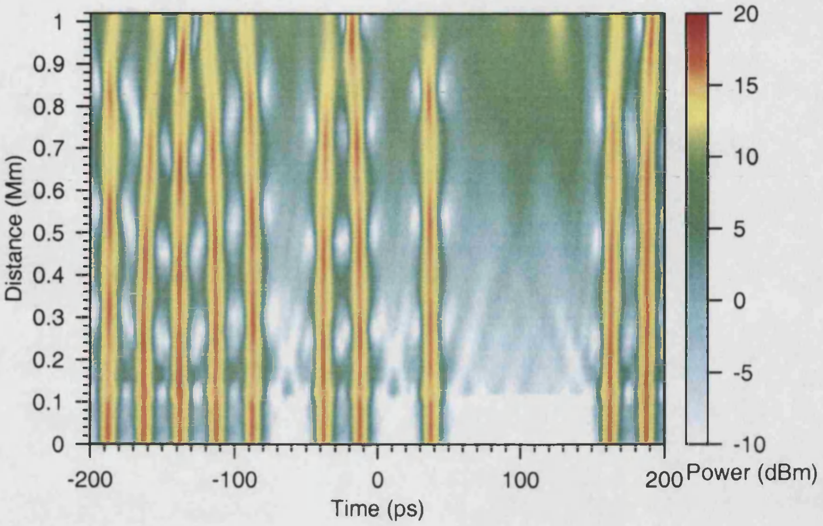

Figure 2.18: Signal propagation in a system with SA-based wavelength conversion after 90 km and optimum SA parameters.

Chapter summary

This chapter has described the operation of the principal components of an optical fibre transmission system, and computer modelling based on these components. The computer modelling focused on systems with a single 40 Gb/s channel and 5 ps FWHM sech^2 signal pulses.

The primary figure-of-merit used in the modelling was the maximum error-free transmission distance, defined to be the distance for which the signal propagated before the Q-factor fell below 6. An optical receiver model which could be used to determine the Q of the propagating signal, and the relationship between Q-factor and BER were discussed.

Factors limiting the performance of a long, periodically amplified system, interactions between adjacent signal pulses, and between signal pulses and EDFA noise have been discussed.

Modelling of transmission systems using guiding filters and SAs for soliton control showed system performance to be dependent on the actual transmission change in the SA, with best results when this transmission change was 2 dB. Reduced performance in modelled systems in which the change in SA transmission was larger was attributed to the consequent strong reshaping of the signal pulses. Systems using 0.6 nm guiding filters performed better than those using 1.0 nm guiding filters. This was attributed to pulses broadening in the narrower filters compensating for pulse narrowing in the SAs.

Computer modelling was also used to demonstrate transmission of 40Gb/s signal following wavelength conversion in SAs. The performance of such systems was again dependent on the actual transmission change in the SA. Performance improved systematically as the transmission change increased. The SA recovery time could be increased to be as long as 10ps without significantly impacting the further transmission of the wavelength converted signal.

References

[1] G. P. Agrawal, *Nonlinear fibre optics.* Academic Press, 1995.

[2] L. Mollenauer and R. Stolen, "Solitons in optical fibers," *Laser Focus*, vol. 18, pp. 193–8, April 1982.

[3] H. Kubota and M. Nakazawa, "Long-distance optical soliton transmission with lumped amplifiers," *IEEE Journal of Quantum Electronics*, vol. 26, pp. 692–700, April 1990.

[4] K. Blow and N. Doran, "Average soliton dynamics and the operation of soliton systems with lumped amplifiers," *IEEE Photonics Technology Letters*, vol. 3, pp. 369–371, April 1991.

[5] J. Gordon and A. Haus, "Random walk of coherently amplified solitons in optical fibre transmission," *Optics Letters*, vol. 11, pp. 665–667, October 1986.

[6] D. Marcuse, "An alternative derivation of the Gordon-Haus effect," *Journal of Lightwave Technology*, vol. 10, pp. 273–278, February 1992.

Chapter 3

Multiple quantum well saturable absorbers: theory and modelling

This chapter describes optically non-linear effects in multiple quantum wells (MQWs) which can be exploited for saturable absorber (SA) and all-optical wavelength converter (AOWC) applications, and which are the subject of experimental investigation in Chapters 6 to 8.

Section 3.1 discusses exciton absorption bleaching (EAB) which is fundamental to all the switching mechanisms studied. The dependence of MQW absorption on electric field resulting from the quantum confined Stark effect (QCSE) is discussed in Section 3.2.

If an MQW layer is incorporated in the intrinsic region of a p-i-n diode, an electric field can be applied to it by reverse biasing the diode. This can reduce the EAB recovery time by sweeping carriers out of the MQW layer, as well as resulting in absorption changes due to the QCSE. Such p-i-n MQW devices are described in Section 3.3. Computer modelling is used to illustrate the photocarrier and electric field dynamics in asymmetric Fabry-Perot (AFP) cavity p-i-n MQW devices following optical pulse absorption in Section 3.4.

Non-linear polarisation rotation (NPR) is described in Section 3.5. Simple techniques are used to model the transmission of an NPR-based switch suitable for use as an AOWC.

EAB itself can be used as a switching mechanism. The speed of EAB-based devices will be limited by the nanosecond lifetimes of free carriers in III-V MQWs. Dramatic reductions of this lifetime can be achieved in MQWs which are implanted with high energy ions in order to introduce defects which act as recombination centres. This technique is discussed in Section 3.6.

Section 3.7 describes the use of AFP cavities to enhance the contrast ratio of devices based on non-linear effects which result in only small absorption changes.

3.1 Excitonic absorption bleaching

The absorption of a photon in a semiconductor material can excite an electron into the conduction band (CB), leaving behind a hole in the valence band (VB). In the case of excitonic absorption, which occurs when the photon energy is equal to the difference between the bandgap energy and the exciton binding energy, the hole and electron are bound together by the Coulomb attraction. Excitonic absorption is not observed in bulk semiconductors at room temperature since the exciton binding energy is small compared to thermalisation energy. In a quantum well (QW) carrier confinement increases the exciton binding energy, such that excitonic behaviour is observed at room temperature.

The exciton lifetime in III-V QWs is typically 300 fs. When an exciton has decayed in a QW a free hole and electron will remain. The lifetimes of these free carriers are typically several nanoseconds [1].

The probability of excitonic absorption in a QW is reduced in the presence of excitons or free carriers. This effect is referred to as excitonic absorption bleaching (EAB). EAB is attributed to two mechanisms, Coulomb screening and phase space filling (PSF) [2].

Coulomb screening is a reduction of the electron-hole attraction in the presence of excitons or free carriers. It broadens, and reduces the magnitude, of the excitonic contribution to the absorption spectrum.

PSF is a manifestation of the Pauli exclusion principle (PEP). The existence of an exciton relies on the excitation of an electron into a state slightly below the bottom of the CB, the difference being due to the exciton binding energy. The probability of excitonic absorption decreases as these CB states become filled.

EAB can be described using a rate equation model which separately considers the population of photogenerated excitons, and that of free carriers into which they decay. Such a model is described in Appendix A.

Modelled absorption change in a multiple quantum well (MQW) with an exciton lifetime of 300 fs, a free carrier lifetime of 1 ns, and a saturation power of 10 mW following the absorption of a 10 pJ, 100 fs full width half maximum (FWHM), sech^2 pulse are shown in Figure 3.1a. The initial, fast, component is due to the quickly decaying exciton population. The following slow decay is due to the free carrier population. Figures 3.1b and 3.1c show similar modelling results for the cases of 1 and 10 ps FWHM pulses. It can be seen that, when the pulse duration is long compared to the exciton lifetime, no fast component to the absorption change is observed. This is discussed further in Appendix A.

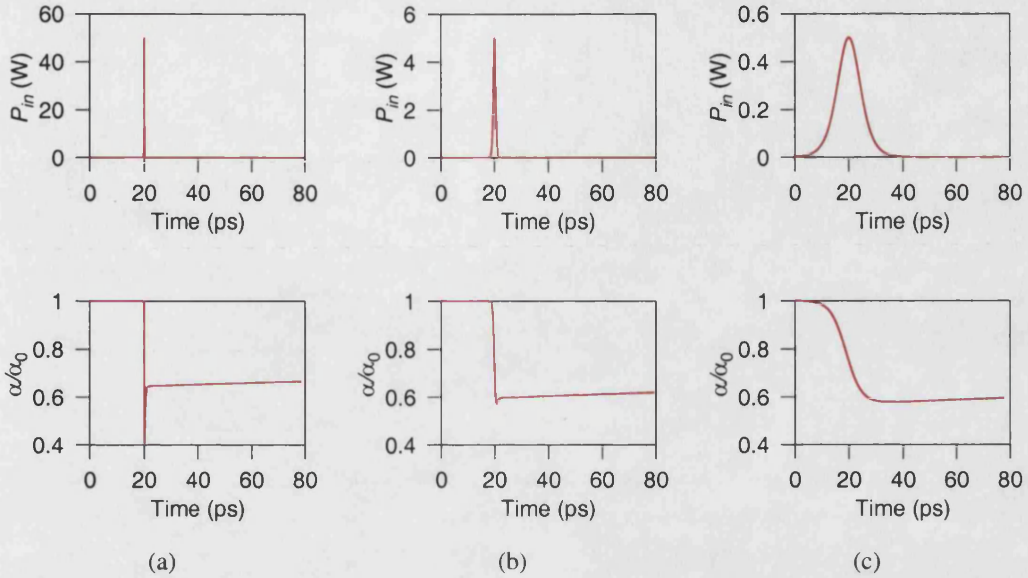

Figure 3.1: Absorption change due to EAB following the incidence of short optical pulses. The pulse width is 100 fs, 1 ps and 10 ps in (a), (b) and (c) respectively. The pulse energy is 10 pJ in each case.

3.1.1 Experimental investigation of excitonic absorption bleaching

Excitonic absorption bleaching can be investigated through measurements of absorption saturation in QW or MQW materials. Continuous wave (CW) saturation behaviour can be observed by measuring the material absorption as a function of intensity of optical excitation. The exciting signal can be modulated with a low duty cycle to reduce the average power incident on the device and avoid thermal effects [3].

More information about the bleaching process can be obtained from dynamic absorption measurements. Pump-probe spectroscopy can be used to make fast measurements [4]. The absorption of a sample is bleached following the incidence of a high energy 'pump' pulse and then, after some short delay, measured using a lower energy 'probe' pulse. By varying the delay between the pump and probe pulses the dynamics of the absorption bleaching process can be observed. The temporal resolution of the measurements is limited by the duration of the optical pulses employed.

Pulse lengths which are short compared to the exciton lifetime, that is of the order of 100 fs, are required to observe the component of the absorption bleaching due to the exciton population.

3.1.2 Polarisation and excitonic absorption bleaching

Purely circularly polarised light consists of photons of a single spin state. Right and left hand circular polarised (RCP and LCP) light can be associated with spin-up and spin-down photons

[5]. Plane polarised light can be considered to be a superposition of RCP and LCP components of equal intensity, and hence to consist of equal numbers of spin-up and spin-down photons. The angle of plane polarisation is dependent on the relative phases of the RCP and LCP components.

Spin-up and spin-down photons will excite spin-up and spin-down electrons respectively. This has some significance for EAB since the PEP, which is responsible for the PSF component of EAB, is spin selective.

Illumination of an MQW material by circularly polarised light will result in the excitation of electrons of a single spin state. PSF will result in light of the same circular polarisation experiencing a reduced absorption in the MQW material, relative to light of the opposite circular polarisation. Following such illumination spin-relaxation, such that the spin-up and spin-down populations are equalised, will occur on a picosecond timescale. Effects depending on spin-selective excitation can thus only be observed in experiments employing picosecond pulse optical sources.

Holden et. al. have used time resolved measurements of this circular dichroism to resolve the PSF and Coulomb screening contributions to EAB in a GaAs/AlGaAs MQW [2, 6].

3.2 The quantum confined Stark effect

The quantum confined Stark effect (QCSE) is a red-shifting of the excitonic component of the absorption spectrum which occurs when an MQW is placed in a perpendicular electric field. The field tilts the band structure in the MQW region, as shown in Figure 3.2, which is reproduced from Chapter 1. The wave functions of the electrons and holes in the conduction and valence band wells are distorted such that the electron and hole sub-band energies, and hence the photon energy required for excitonic absorption, are reduced. This is the origin of the red-shifting of the excitonic absorption. The reduction of the overlap between the electron and hole wave functions results in an overall decrease in absorption.

The QCSE can be observed in devices which incorporate an MQW layer in the intrinsic region of a p-i-n junction, as shown in Figure 3.3[3]. A perpendicular electric field can be applied to the MQW layer by reverse biasing the device. The device is designed to be used in a reflective configuration. Light enters through an optical window in the top metallic contact, passes through the MQW region, is reflected by a distributed Bragg reflector (DBR), passes back through the MQW region, and exits through the optical window. Alternative designs with no reflector, and with optical windows in both metallic contacts, can be used in transmission configurations.

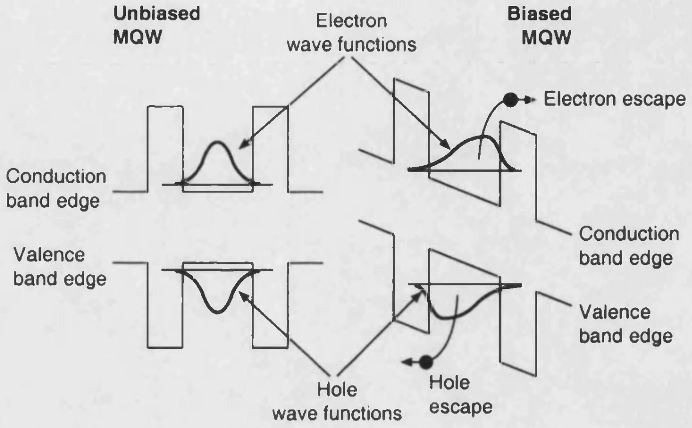

Figure 3.2: Tilting of the band structure and origin of the QCSE in an MQW biased by application of a perpendicular electric field.

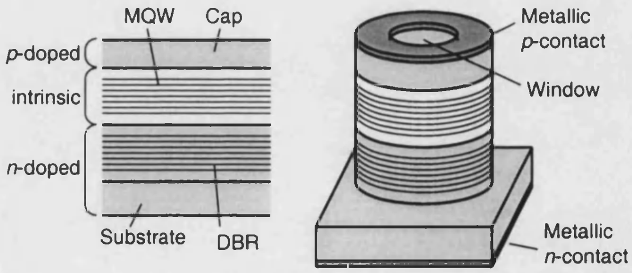

Figure 3.3: Schematic illustration of a p-i-n diode incorporating an MQW layer in the intrinsic region.

3.3 Behaviour of reverse biased p-i-n multiple quantum well devices

3.3.1 Electric field screening due to photogenerated space charge

When the p-i-n MQW device of Figure 3.3 is reverse biased the electric field in the intrinsic region, will be

$$\mathscr{E} = V_r / z_0 \tag{3.1}$$

where V_r = reverse bias voltage and z_0 = intrinsic region length, as shown in Figure 3.4(a). This assumes zero doping in the intrinsic region. The field will result in a change of the absorption spectrum due to the QCSE, and will sweep photocarriers out of the wells.

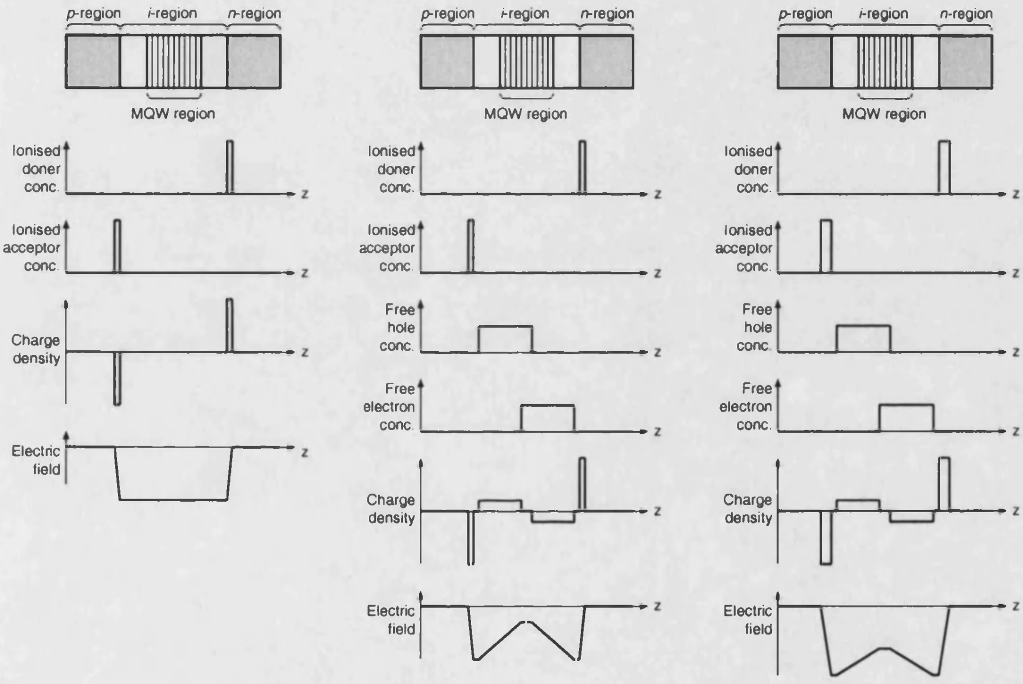

(a) (b) (c)

Figure 3.4: Schematic illustration of charge density and electric field in a p-i-n MQW diode. (a) is the small signal case, the doped regions are depleted such that the field due to ionisation of the donors and acceptors satisfies the boundary condition of Equation 3.3. (b) shows the situation following a short pulse optical excitation if no boundary condition is imposed. In (c) depletion has extended further into the doped region to satisfy the boundary condition.

The holes will be swept towards the p-region, and the electrons towards the n-region. This separation of space charge will result in a reduction of the field since

$$\mathscr{E}_z = \frac{1}{\varepsilon_0 \varepsilon_r} \int_0^z \rho dz \tag{3.2}$$

where ρ = space charge density, ε_0 = permittivity of free space and ε_r = relative permittivity of the intrinsic region, must be satisfied in the intrinsic region. The z-axis is that perpendicular to the plane of the MQW; $z = 0$ at the intrinsic region/p region interface. The reduced field is shown in Figure 3.4(b). The dynamics of this effect will be dependent on the carrier drift velocity, and the process by which the field, and the charge distribution, recover to their small signal states.

Simple analysis can be used to show that these electric field screening effects can be significant in a practical device. The intrinsic region lengths and maximum reverse bias voltages of the devices investigated in this thesis were typically 1 μm and 20 V respectively. A field of 200 kV/cm could thus be applied. If a 40 Gb/s pseudo-random bit stream (PRBS) with a moderate average power of 40 mW is incident on the device, the energy of the incident signal pulses will be 2 pJ. In the coupling system used experimentally (Chapter 4) the area of the optical spot on the device is 79 μm^2. The incident energy density due to one signal pulse is thus 25 fJ/μm^2. The solution of Equation 3.2 can be simplified by assuming a 'worst case' situation in which all the photocarriers generated by the pulse contribute to field screening in the intrinsic region. According to Equation 3.2 the holes and electrons will result in electric field step changes of 2350 kV/cm and −2350 kV/cm respectively, assuming $\varepsilon_r = 12$.

In reality, the sign of the field in the intrinsic region will not be thus reversed. As the field in the intrinsic region approaches zero the drift velocity of the carriers will fall, leading to slower carrier sweep-out.

The above discussion ignores the potential boundary condition due to the reverse bias voltage,

$$V = -\frac{1}{\varepsilon_0 \varepsilon_r} \int_0^{z_0} \rho dz = V_r. \tag{3.3}$$

This is satisfied by increases of the depletion region widths in the p and n-regions, as shown in Figure 3.4(c). The aggregate charge density, due to depletion and space charge, must be such that $\mathscr{E} = 0$ in the undepleted parts of the doped regions.

In a device with the structure of Figure 3.3 V_r will be maintained in the region of the top metallic contact. This will not, however, be the case in the area of the optical window, since the thin p-region has a significant resistance.

Livescu et. al. have described the recovery of such a device through movement of carriers in the n and p-doped regions [7]. A diffusion equation is used to model the potential in the region of the optical window,

$$\frac{d}{dt} V(x,y) = D \nabla_{2D} V(x,y) \tag{3.4}$$

The diffusion coefficient, D, is

$$D = \frac{1}{C_A R_{sq}} \tag{3.5}$$

where C_A = device capacitance per unit area and R_{sq} = the sum of the resistances per square of the n and p-regions. In calculating R_{sq} the metallic contacts are considered to constitute part of the doped regions. The n-region contribution is small, due to the high conductivity of the bottom metallic contact, and can hence be ignored.

3.3.2 Carrier sweep-out

Many investigations of carrier sweep-out in QCSE-based asymmetric Fabry-Perot modulators (AFPMs) have been described in the literature. The structure of such an AFPM, which incorporates an MQW layer in an asymmetric Fabry-Perot (AFP) cavity, is similar to that shown in Figure 3.3. Application of an electric signal and an appropriate direct current (DC) reverse bias to the AFPM results in the absorption of the MQW, and hence the reflectivity of the AFPM, varying in sympathy with that signal. The changing reflectivity is used to modulate a CW optical signal.

The reflectivity of the AFPM should ideally be a function only of the applied electric signal. EAB, an optical non-linearity, is thus undesirable. EAB can be avoided if the AFPM is operated with a reverse bias voltage such that the barriers seen by photocarriers in the QWs of the MQW are reduced, and the photocarriers quickly escape to be swept away in the reverse bias field.

Investigations of sweep-out have used pump-probe techniques to observe the reflectivity of the AFPM following the absorption of a high energy optical pulse [8].

Such investigations have shown that carrier sweep-out is not an appropriate mechanism for reduction of carrier lifetime in EAB based MQW saturable absorbers (SAs) since absorption changes due to EAB are dominated by those due to screening of the reverse bias field as carriers traverse the intrinsic region.

3.4 Field screening under picosecond pulse illumination

A computer model, which is described in Appendix C, was used to investigate the behaviour of field screening devices excited by short optical pulses. The model considers carrier drift, and the diffusive conduction process responsible for device recovery.

The basic set of parameters used for the modelling is listed in Table 3.1. The following subsections show the results of simulations exploring the consequences of varying different parameters. Results are presented in the form of plots of the potential across depletion region at the centre of the device as a function of time. This will determine the electric field and hence, through the QCSE, the absorption in the MQW region.

Plots showing the evolution of the electric field distribution in the intrinsic regime within the duration of the simulation are gathered in Appendix D.

Parameter	Value
Relative permittivity of cavity medium	12
Refractive index of cavity medium	3.17
MQW region absorption coefficient	6×10^5 /m
p-region resistivity	4×10^{-4} Ωm
Length of MQW region (L_{mqw})	1 µm
p-region length (L_p)	0.3 µm
Spacer length (L_s)	0.3 µm
Cavity length (L)	Set automatically, such that $L > L_p + 2L_s + L_{mqw} + 0.1$ µm and the cavity is resonant at 1.55 µm.
Optical spot radius	5 µm
Optical window radius	20 µm
Exciting pulse FWHM	2 ps
Exciting pulse energy	500 fJ
Optical wavelength	1.55 µm
Reverse bias voltage	−20 V

Table 3.1: Basic parameters used for modelling of field screening in p-i-n multiple quantum well devices

3.4.1 Exciting pulse energy

Figure 3.5 shows the results, in the form of plots of potential at centre of the device optical window as a function of time, of varying the exciting pulse energy in the simulation. Pulse energies between 250 fJ and 5 pJ were used, parameters were otherwise those of Table 3.1. It can be seen that, when the pulse energy is 250 fJ or less the potential change recovers quickly. The time taken for the potential to fall from its maximum to 50 % of its maximum is approximately 10 ps. When the pulse energy is 500 fJ or higher the recovery from the field screening condition becomes slower. Lengthening of the recovery time coincides with the onset of the regime in which the electric field in the MQW region of the device approaches zero, leading to a reduction of carrier drift velocity. This is clearly visibly in the plots of Appendix D. The model is not, as discussed in Appendix C, expected to be accurate in this regime, since a simplified drift velocity/electric field relation is used, and since the expected increase in the time take for carriers to escape from the quantum wells in which they are generated is not considered.

These modelling results are useful in that they suggest that, if the modelled device is to be used in ultra-fast applications, the energy of the exciting pulse used should be restricted to be less than

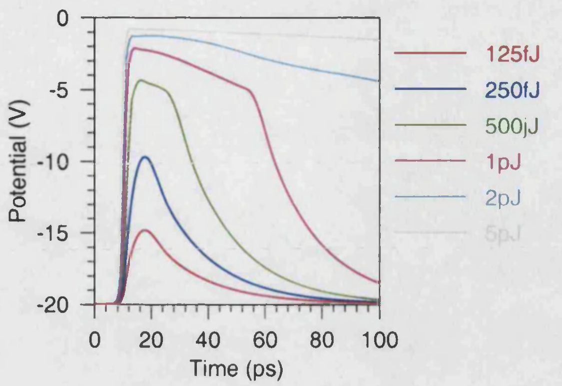

Figure 3.5: Modelled potential difference across the depletion region of a device illuminated by optical pulses of different energies.

about 500 fJ; operation in the low electric field regime being clearly undesirable. A pulse energy of 500 fJ was therefore used in the exercises described in the following subsections.

An additional point of interest is the delay between the time of incidence of the pulse and the time at which the potential change due to field screening is greatest. In the case of the low energy results this rise time is approximately 8 ps. It can be attributed to the finite time take for positive and negative photocarriers to drift apart in, and hence screen, the electric field in the intrinsic region of the device. Such a delay is undesirable in devices which are to be used in soliton control applications, where the maximum potential change (and hence the maximum absorption change due to the QCSE) should be coincident with the centre of the exciting pulse.

Whilst a reduction of rise time is observed when in the case of higher energy exciting pulses, this is at the expense of increased recovery times.

3.4.2 Exciting pulse width

The results of simulations in which the width of the exciting pulse was increased from 2 ps to 10 ps are shown in Figure 3.6. The change of pulse length does not result in any significant changes in the behaviour of the device. This suggests that device characterisations carried out using 2 ps pulses, such as those described later in this thesis, can reasonably be used as the basis of an analysis of the suitability of field screening devices for 10 Gb/s and 40 Gb/s systems applications.

3.4.3 Length of the multiple quantum well region

The results of simulations in which the length of the MQW region was varied between 0.5 μm and 2 μm are shown in 3.7. The device in which the length of the MQW region is reduced to 0.5 μm

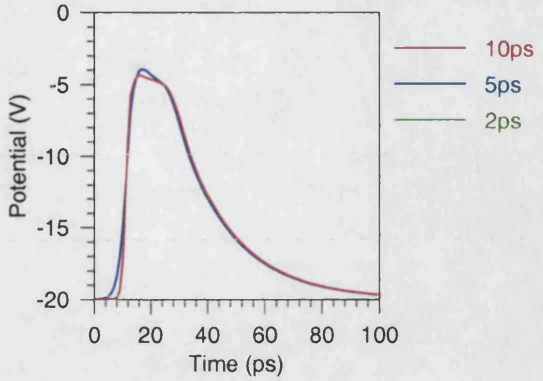

Figure 3.6: Modelled potential difference across the depletion region of a device illuminated by optical pulses of different lengths.

is significantly faster than the 1 μm device. The predicted magnitude of the potential change, and hence of the QCSE absorption change is similar in each device. The 2 μm device is relatively slow. This is, again, due to it entering the low electric field regime.

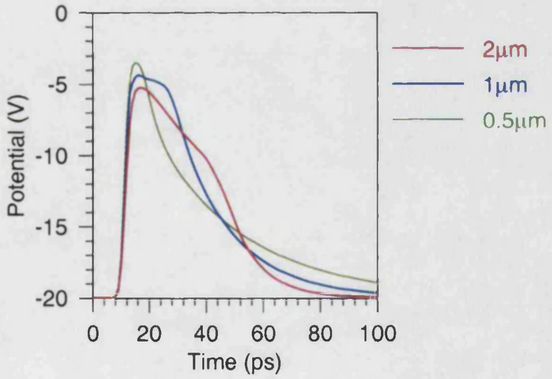

Figure 3.7: Modelled potential difference across the depletion region of devices with MQW regions of different lengths.

The faster behaviour of the shorter device can be attributed to the higher electric field within the intrinsic region; and the subsequently larger amounts of photogenerated charge required to screen the field such that it approaches zero. Practically, the higher fields in shorter devices could result in reduced breakdown voltages. Shorter devices have an additional disadvantage. Whilst, from the results of Figure 3.7 potential, and hence absorption, changes are similar in the 0.5 μm and 1 μm devices, overall reflectivity changes will be smaller in devices in which the MQW region is shorter.

3.4.4 Length of the top p-region

The thickness of the p-region of the p-i-n MQW device will determine the sheet resistivity of that region, and hence have an impact on the speed of device performance. Results of simulations in which the p-region length was set to 150 nm, 300 nm and 600 nm are shown in Figure 3.8. The expected results are observed; as the p-region thickness, and hence the potential diffusion coefficient, are increased, operation of the device becomes faster. It should be noted that whilst fast performance is observed in the device with the 600 nm p region, this is at the expense of a reduction of the magnitude of the potential change.

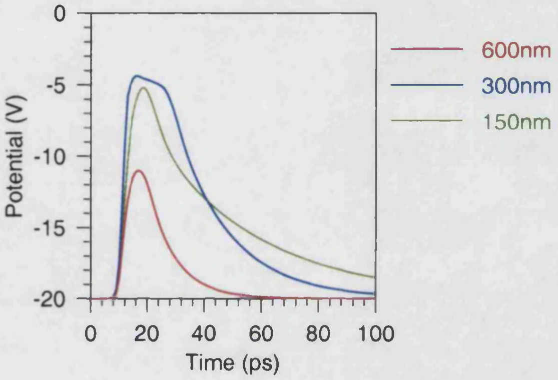

Figure 3.8: Modelled potential difference across the depletion region of devices with p regions of different lengths.

3.5 Non-linear polarisation rotation

3.5.1 Non-linear polarisation rotation switching

The creation of transient circular dichroism in MQW materials following excitation by a short pulse of circular polarised light has been discussed in Section 3.1.2. If plane polarised light propagates through the circularly dichroic material, the state of polarisation of the light will be modified such that it is elliptical.

This transient polarisation change can be used to realise all-optical switching, as discussed in Section 1.3.7. The switching arrangement is reproduced in Figure 3.9. Plane polarised CW light propagates through an MQW structure and is then, under small signal conditions, blocked by an analyser. Part of the CW light will pass through the analyser following excitation of the MQW structure by circularly polarised pulses.

Experimental investigations of all-optical switching using such arrangements have been re-

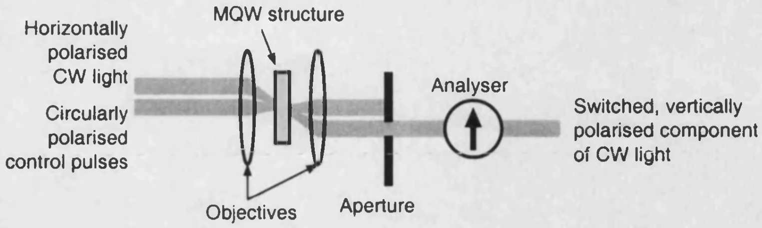

Figure 3.9: Optical switching based in optically excited transient circular anisotropy in an MQW.

ported. Results suggested that the transient optical anisotropy is dominated by circular birefringence, rather than circular dichroism, and that the polarisation change experienced by plane polarised light is thus dominated by rotation, rather than by a change of ellipticity [9]. The origin of the circular birefringence is not well-understood.

The reliance of this switching mechanism on rotation of plane polarised light has led to it being referred to as non-linear polarisation rotation (NPR).

Experimentally, the spin relaxation time can be determined with a switching experiment, or by comparing the dynamic transmission changes observed in pump-probe experiments in which the pump and the probe pulses have the same circular polarisation (SCP), or opposite circular polarisations (OCP) [10]. A trace representing the degree of spin selective excitation can be obtained by subtracting the OCP trace from the SCP trace. A majority of the investigations of spin relaxation in the literature have used such SCP/OCP experiments.

3.5.2 Spin-resolved rate equation model

In this simplified model, which is based on Equation A.19, separate normalised populations of spin-up and spin-down photocarriers, $n_\uparrow$ and $n_\downarrow$, are considered. The contributions to the total optical input power due to spin-up and spin-down photons, denoted $P_\uparrow$ and $P_\downarrow$, are also considered separately. The dynamics of the populations are governed by τ_s, the spin relaxation time, and τ_{fc}, the free carrier recovery time. The rate equations used are

$$\frac{dn_\uparrow}{dt} = \frac{P_\uparrow(1-n_\uparrow-n_\downarrow)}{E_s} - \frac{n_\uparrow - n_\downarrow}{\tau_s} - \frac{n_\uparrow}{\tau_{fc}} \tag{3.6}$$

and

$$\frac{dn_\downarrow}{dt} = \frac{P_\downarrow(1-n_\downarrow-n_\uparrow)}{E_s} - \frac{n_\downarrow - n_\uparrow}{\tau_s} - \frac{n_\downarrow}{\tau_{fc}} \tag{3.7}$$

where E_s is the MQW pulse saturation energy.

Absorption bleaching is considered to be spin independent; the probability of absorption of both spin-up and spin-down photons is reduced by a factor $(1-n_\uparrow-n_\downarrow)$. In reality the PSF contribution is spin-dependent.

This analysis only considers the dynamics of the spin-up and spin-down carrier populations. Whilst the absorption changes due to the spin-selective nature of PSF which cause circular dichroism could be modelled, circular birefringence, which has been stated to play a dominant role in switching, cannot be modelled based on information in the literature.

3.5.3 Dynamics of the spin-resolved photocarrier populations

Population dynamics with the device and pulse parameters of Table 3.2, modelled using Equations 3.6 and 3.7, are shown in Figure 3.10. The normalised spin-up and spin-down populations, $n_\uparrow$ and $n_\downarrow$, are plotted, together with the difference between them, $n_\uparrow - n_\downarrow$. There is a fast transient in the population difference showing that, even with a 5 ns free carrier relaxation time, spin-dependent mechanisms have the potential to switch picosecond pulses.

Parameter	Value
Pulse shape	sech^2
Pulse width	5 ps FWHM
Pulse energy	5 pJ
Pulse polarisation	circular, such that spin-up carriers are excited
MQW E_s	5 pJ
MQW τ_{fc}	5 ns
MQW τ_s	5 ps

Table 3.2: Parameters for rate equation modelling of NPR switching

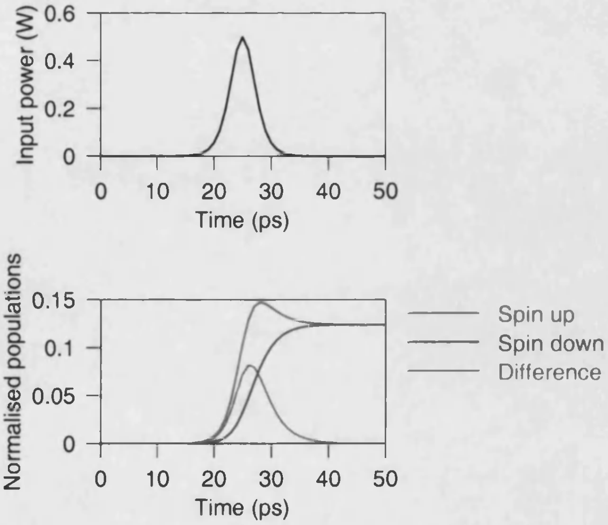

Figure 3.10: Spin-resolved population dynamics in an MQW following absorption of a single optical pulse.

Such a device will not be useful for switching a high repetition rate pulse stream, as illustrated by the results of Figure 3.11 which shows the response to a 40 GHz stream of pulses. The parameters used were those of Table 3.2. Since the pulse interval is short compared to the free carrier recovery time there are accumulations of both spin-up and spin-down photocarriers.

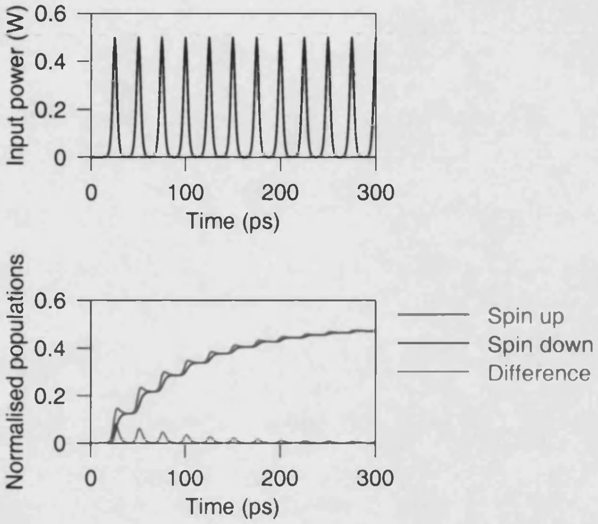

Figure 3.11: Spin-resolved population dynamics in an MQW following absorption of a stream of optical pulses.

This problem can be overcome if the free carrier lifetime is reduced such that the free carrier population will recover in the interval between successive pulses, as shown by the results of Figure 3.12 for which τ_{fc} was reduced to 5 ps.

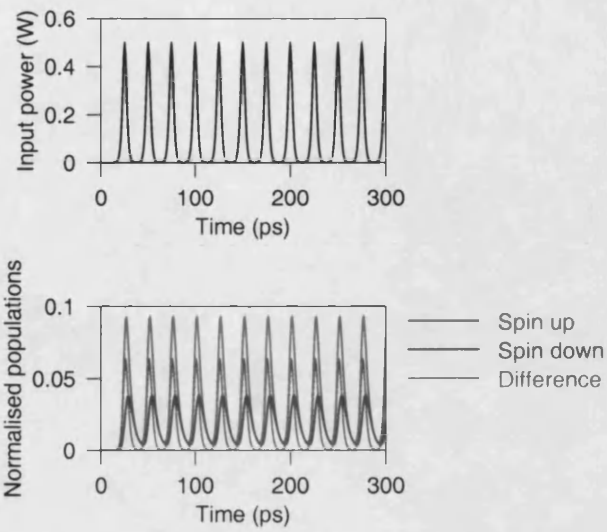

Figure 3.12: Spin-resolved population dynamics in an MQW with $\tau_{fc} = 5\,\text{ps}$ following absorption of a stream of optical pulses.

3.6 Fast excitonic absorption bleaching and ion implantation

Devices which rely on EAB to realise all-optical switching or saturable absorption are attractive. EAB does not suffer from the polarisation dependence of NPR, or the dependence of the dynamics of the optical non-linearity on the exciting pulse energy which characterises field screening.

Since the free carrier lifetime, τ_{fc}, is typically a few nanoseconds in III-V MQW, it must be reduced considerably if devices which are useful for ultra-fast communications applications are to be realised. For most applications the recovery time of the non-linearity must be comparable with, or smaller than, the length of the signal pulses (typically 10 ps in a 10 Gb/s soliton system).

τ_{fc} can be reduced in devices in which a perpendicular electric field is applied to an MQW layer to sweep out photocarriers. However, as discussed in Section 3.3.2, the behaviour of such devices will be characterised by field screening effects.

Alternative techniques for the reduction of τ_{fc} rely on the deliberate introduction of defects in the MQW layer (Section 3.6). Suitable defects can result in mid-gap levels which facilitate carrier recombination, and hence reduce the free carrier lifetime. Suitable defects are present in GaAs MQWs grown by low-temperature (LT) molecular beam epitaxy (MBE) and result in high resistivity [11], as well as ultra-fast optical properties [12]. Fast carrier recombination is due to the resulting As precipitates and empty Ga sites in the structure [13]. Further carrier lifetime reductions are achieved in LT MBE-grown which is doped with Be during growth [14].

Alternatively, defects can be introduced by implanting an epitaxially grown structure with high energy protons [15] or ions [16]. Defects are created along the damage tracks which are created as the particles propagate through the MQW layer.

The structures considered in this thesis consisted of MQW layers, approximately 1 μm thick, grown on InP substrates by metal organic vapour phase epitaxy (MOVPE). In some cases DBRs were grown on the substrates prior to the MQWs. In all cases the MQWs were close enough to the top of the structure that ions could be implanted with sufficient energy that they were deposited deep below them [17]. Fast SAs have also been produced by ion-implanting one facet of semiconductor laser diodes (LDs) to allow them to be passively mode-locked [16].

Comparisons of implantation with different ion species have shown heavier ions to be more effective in reducing the carrier lifetime [17], as well as avoiding defect centre saturation [18]. Defect centre saturation occurs when an ion-implanted MQW is excited by a high-repetition rate pulse train. High average optical powers can result in an accumulation of carriers in the defect states and hence patterning or tailing effects in soliton control and wavelength conversion applications. It has been suggested that heaver ions create clusters of point defects and hence clusters of mid-gap levels, which allow carriers to escape from the defect states [18]. Investigations have shown carrier lifetime to decrease systematically when increasing ion doses are used [17].

Experimental investigations of EAB non-linearities have, as discussed in Section 3.1.2, revealed polarisation dependencies arising from the spin selective nature of PSF. It is desirable that polarisation dependence should be avoided in devices intended for systems applications where the state of polarisation of the propagating signal is generally not well defined.

3.7 Asymmetric Fabry-Perot cavities

3.7.1 Contrast ratio enhancement

The contrast ratio, defined as the ratio of fully saturated transmission to small signal transmission, is a fundamental parameter of all-optical switches and SAs. If a device is to be useful a sufficiently high contrast ratio must be achieved with pulses of realistic energy. Contrast ratio requirements for SA soliton control and wavelength conversion are investigated in the systems simulations of Chapter 2.

The structure of Figure 3.13 allows significant contrast ratios to be achieved, even in the case of small absorption changes in the SA region. An AFP cavity is formed between the two mirrors. If the mirror reflectivities and the cavity length are chosen correctly there will be total destructive interference between the reflections from the front and back mirrors, such that the reflectivity of the AFP cavity approaches zero.

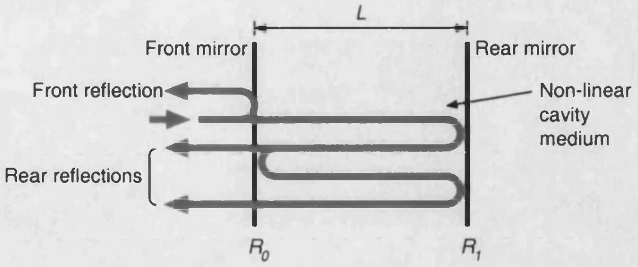

Figure 3.13: Schematic illustration of a resonant optical cavity device.

The behaviour of such a cavity is dependent on the reflectivities of the front and rear mirrors, R_0 and R_1, the length of the cavity, L, and the absorption and refractive index of the cavity medium, α and n. To combine the reflections in the cavity it is necessary to sum the reflected fields. It is therefore convenient to use the reflection and transmission coefficients of the mirrors,

$$r_0 = \sqrt{R_0}, \tag{3.8}$$

$$t_0 = \sqrt{1-T_0}, \tag{3.9}$$

$$r_1 = \sqrt{R_1}, \tag{3.10}$$

and

$$t_1 = \sqrt{1-T_1}. \tag{3.11}$$

It is also convenient to use $r_{1_{eff}}$, the effective reflection coefficient of the rear mirror taking into account the phase shift and absorption due to one cavity round trip,

$$r_{1_{eff}} = \exp\left((4\pi in/\lambda - \alpha)L\right) \tag{3.12}$$

where λ = optical wavelength and $i = \sqrt{-1}$.

The reflection coefficient of the cavity, r, is obtained summing the contributions from the front and rear mirrors,

$$r = r_0 - t_0^2 r_{1_{eff}} \sum_{n=0}^{\infty} \left(r_0 r_{1_{eff}}\right)^n. \tag{3.13}$$

Since the summation is a geometric progression,

$$r = r_0 - \frac{t_0^2 r_{1_{eff}}}{1 - r_0 r_{1_{eff}}}. \tag{3.14}$$

Destructive interference between the front and back reflections requires $r_{1_{eff}}$ to be real and positive. This is true when

$$2L = N\lambda, \tag{3.15}$$

where N is some positive integer. Total destructive interference occurs when $r_0 = r_{1_{eff}}$, that is when the reflection coefficient of the front mirror is equal to the effective reflection coefficient of the rear mirror. This condition is known as impedance matching.

A change in the absorption of the cavity medium, such as that which can occur due to EAB in an MQW, will result in a change in the total reflectivity of the cavity. To achieve high contrast ratios the cavity must be designed to be impedance matched under small signal conditions, requiring accurate control of the mirror reflectivities and the small signal absorption of the cavity medium.

The range of wavelengths over which an SA using an AFP offers enhanced contrast ratio is limited. As the operating wavelength moves away from the optimum, at which Equation 3.15 is satisfied, the contrast ratio will decrease.

3.7.2 Absorption profiles

The absorption profile of the MQW region in a device used in a transmission configuration will resemble that of Figure 3.14; there will be an exponential decrease of power across the MQW region. The width and absorption of the MQW region in the example, $L_{mqw} = 1\,\mu\text{m}$ and $\alpha = 6 \times 10^5\,\text{m}^{-1}$ respectively, were chosen to typify the devices investigated. The z-axis is that normal to the plane of the MQW.

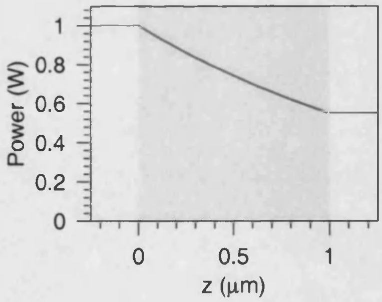

Figure 3.14: Absorption profile of the MQW region in a device used in a transmission configuration. The shaded region shows the extent of the MQW.

In a reflective device interference between forward and backward propagating light in the MQW region results in a standing wave, as shown in Figure 3.15. This example assumes that there is no reflection at the front of the device ($z = 0$), as will be the case if it is anti-reflection coated, and that the reflectivity of the mirror behind the MQW region is 100%. The optical wavelength is assumed to be $\lambda = 1.555\,\mu\text{m}$, and the refractive index of the MQW region $n = 3.17$.

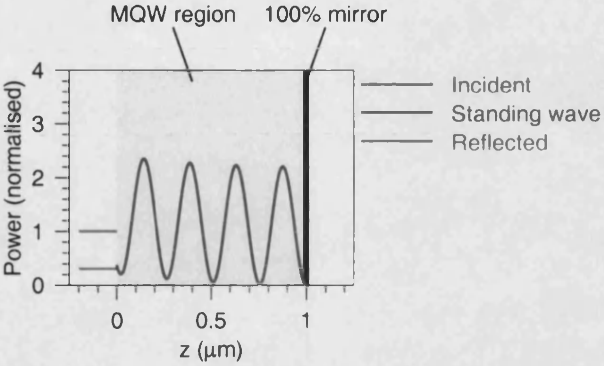

Figure 3.15: Absorption profile of the MQW region in a device used in a reflection configuration.

The situation in an AFP cavity device is illustrated in Figure 3.16. InP spacers, of total length 0.223 μm, are added in front of and behind the MQW region so that the cavity resonance is coincident with the 1.55 μm wavelength of illumination. The front reflection is assumed to be due to an air/InP interface without anti-reflection coating; the reflectivity of such an interface is such that the cavity is close to impedance matched and the power of the reflected wave is small. Interference between the multiple reflections in the cavity results in higher power at the nodes of the standing waves.

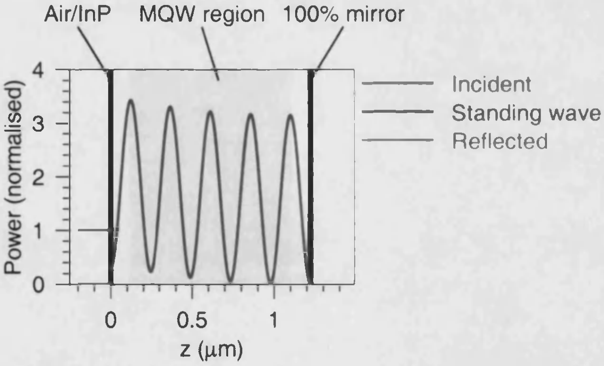

Figure 3.16: Absorption profile of the MQW region in an AFP cavity device.

Absorption of photons will result in periodic free carrier populations, with maxima at the nodes of the standing wave. Optical non-linearities will thus be localised around the standing wave nodes. The quantum well material at the antinodes of the wave is never saturated; it simply adds unsaturable loss to the cavity. Mangeney et. al. have used devices in which quantum wells are clustered at the nodes of the standing wave to overcome such losses [19].

3.7.3 Electric field profile in asymmetric Fabry-Perot cavity p-i-n devices

The p-i-n devices studied in this thesis used reflective designs, since the back-side processing fabrication steps which would have been required to create the rear optical windows which would be required for transmissive operation were not available. Optical excitation of such reflective and AFP cavity devices will, as discussed in Section 3.7, result in the creation of periodic populations of free carriers, and hence also periodic electric field profiles. This section considers the consequences of these periodicities in highly reverse biased AFP cavity devices under CW illumination.

In devices illuminated by CW light the depletion regions will extend to maintain the reverse bias potential across the area of the device; it is not necessary to consider diffusive conduction which is responsible for device recovery following short-pulse excitation.

The following discussion assumes that the free carriers generated in the wells compromising the MQW region immediately escape from those wells. This is reasonable when a large reverse bias voltage is applied to the device, such that the optical non-linearity is dominated by field screening. The geometry of Figure 3.17 is used. The p-region extends from $z = 0$ to $z = L_p$, the MQW region from $z = L_p$ to $z = L_p + L_{mqw}$, and the n-region from $z = L_p + L_{mqw}$ to $z = L$, where $L = L_p + L_{mqw} + L_n$, is used. This is a simplification of practical structures. That the DBR is represented by a 100% reflective mirror and there are no spacers between the MQW and doped regions.

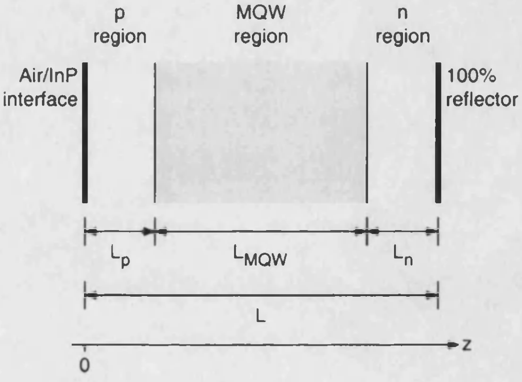

Figure 3.17: Geometry used in discussion of AFP cavity devices.

Assuming electron-hole pair generation to occur with unit quantum efficiency, the electron flux at position z within the intrinsic region must be

$$F_e(z) = \int_{L_p}^{z} \frac{\alpha(z')P(z')}{hf} dz', \text{ for } x > L_p \text{ and } x < L - L_n. \tag{3.16}$$

where $\alpha(z')$ = absorption coefficient at z' and $P(z')$ = optical power at z'. Since electrons can be expected to have drifted out of the intrinsic region before they recombine, the electron flux is independent of the time taken for carriers to escape from the wells. Assuming the CW illumination to be uniform, the three dimensional electron density at z will be

$$N_e = \int_{L_p}^{z} \frac{\alpha(z')I(z')}{hf}\frac{1}{v_e}dz', \text{ for } x > L_p \text{ and } x < L - L_n, \tag{3.17}$$

where v_e = electron drift velocity $I(z')$ = optical intensity at z'. Similarly, the three dimensional hole density will be

$$N_h = \int_{z}^{L-L_n} \frac{\alpha(z')I(z')}{hf}\frac{1}{v_h}dz', \text{ for } x > L_p \text{ and } x < L - L_n, \tag{3.18}$$

where v_h = hole drift velocity. From Equations 3.17 and 3.18, the total free carrier charge density in the intrinsic region is

$$\rho(z) = \int_{z}^{L-L_n} \frac{eI}{hfv_h}dz' - \int_{L_p}^{z} \frac{eI}{hfv_e}dz', \text{ for } x > L_p \text{ and } x < L - L_n, \tag{3.19}$$

where e = the electronic charge.

The example electric field distributions of Figure 3.18 were obtained by solving Equation 3.2 for the change density distribution of Equation 3.19 with the boundary condition

$$\int_{0}^{L} \mathscr{E} dz = V_R. \tag{3.20}$$

The parameters used are summarised in Table 3.3. v_e is assumed to be 10^7 cm/s, the standard value for electron saturated drift velocity in InP. v_h is assumed to be 8×10^6 cm/s; based on the ratio of v_e/v_h determined for a similar GaInAs device [20].

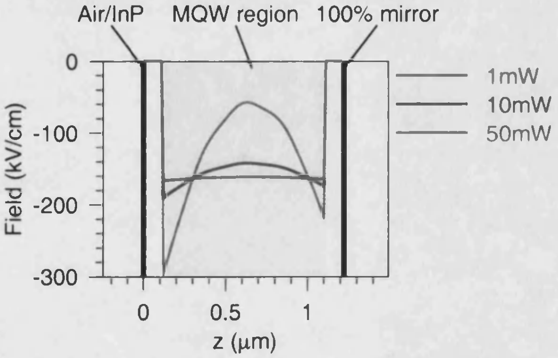

Figure 3.18: Calculated electric field profile in a CW illuminated AFP p-i-n MQW device.

Parameter	Symbol	Value
MQW region length	L_{mqw}	$1\,\mu m$
n-region length	L_n	$0.107\,\mu m$
p-region length	L_p	$0.107\,\mu m$
Relative permittivity	ε_r	12
Refractive index	n	3.17
Electron velocity	v_h	$10^7\,cm/s$
Hole velocity	v_e	$0.8 \times 10^7\,cm/s$
Incident optical power	P	$1, 10, 50\,mW$
Optical spot area	A	$79\,\mu m^2$
Reverse bias	V_R	20V

Table 3.3: Parameters used for calculation of electric field profile in a CW illuminated AFP p-i-n MQW device.

When the incident optical power is 10 mW it can be seen that there is negligible field screening, since the electric field distribution appears uniform across the intrinsic region. However, when the optical power is increased to 50 mW significant field screening is evident. Results for even high optical powers could not be obtained using this method, since it does not consider the reduction of carrier drift velocity which will occur as the screened field approaches zero. The periodic nature of the absorption profile does not visibly affect the electric field profile.

Chapter summary

This chapter has described three approaches which can potentially be used to produce fast SAs or all-optical wavelength converters (AOWCs): the use of electric field screening in p-i-n devices, NPR, and EAB in ion implanted devices.

The structure of a p-i-n MQW device in which field screening optical non-linearities can be observed has been described. The dynamics of the electric field and space charge distribution in such a device following the absorption of an optical pulse were discussed. Carrier drift in the intrinsic region and diffusive conduction in the doped regions were identified as controlling the rise and fall of the resulting absorption change. Computer modelling was used to investigate the influence of various parameters on the speed of field screening devices.

A simple rate equation model was used to demonstrate that NPR can be used to implement a switch capable of switching picosecond optical pulses, but that a reduction of MQW free carrier lifetime is required if high repetition rate pulses streams are to be switched.

Ion-implantation, which can reduce the free carrier lifetime in MQWs by creating recombination centres, and hence allow ultra-fast operation of EAB based devices has been discussed.

It was shown that incorporation of an optically non-linear MQW region in an AFP cavity can be used to create high-contrast devices.

References

[1] D. Chemla and D. Miller, "Room-temperature excitonic nonlinear-optical effects in semiconductor quantum-well structures," *Journal of the Optical Society of America B*, vol. 2, pp. 1155–1173, July 1985.

[2] T. Holden, G. Kennedy, A. Cameron, P. Riblet, and A. Miller, "Exciton saturation in room temperature GaAs/AlGaAs multiple quantum wells," *Applied Physics Letters*, vol. 71, pp. 936–938, August 1997.

[3] A. Fox, D. Miller, G. Livescu, J. Cunningham, J. Henry, and Y. Yan, "Exciton saturation in electrically biased quantum wells," *Applied Physics Letters*, vol. 57, pp. 2315–2317, April 1990.

[4] G. Livesu, A. Fox, D. Miller, T. Sizer, W. Know, J. Cunningham, A. Gossard, and A. English, "Optical detection of resonant tunnelling of electrons in quantum wells," *Semiconductor Science and Technology*, vol. 5, pp. 594–556, 1089.

[5] E. Hecht, *Optics*, ch. 8. Addison Wesley, 2nd ed., 1989.

[6] A. Miller, P. Riblet, M. Mazilu, S. White, T. Holden, A. Cameron, and P. Perezzo, "Excitonic saturation in GaAs multiple quantum wells at room temperature," *Journal of Applied Physics*, vol. 86, pp. 3734–3744, October 1999.

[7] G. Livescu, D. Miller, T. Sizer, D. Burrows, and J. Cunningham, "High-speed absorption recovery in quantum well diodes by diffusive conduction," *Applied Physics Letters*, vol. 54, pp. 748–750, February 1989.

[8] J. Cavaillés, D. Miller, J. Cunningham, P. Wa, and A. Miller, "Simultaneous measurements of electron and hole sweep-out from quantum wells and modelling of photoinduced field screening dynamics," *IEEE Journal of Quantum Electronics*, vol. 28, pp. 2486–2497, October 1992.

[9] Y. Nishikawa, A. Tackeuchi, M. Yamaguchi, S. Muto, and O. Wada, "Ultrafast all-optical spin polarization switch using quantum well etalon," *IEEE Journal of Selected Topics in Quantum Electronics*, vol. 2, pp. 661–667, September 1996.

[10] J. Hyland, G. Kennedy, A. Miller, and C. Button, "Picosecond all-optical polarization switching in InGaAsP MQWs at 1.52 μm," *IEEE Photonics Technology Letters*, vol. 10, pp. 1419–1421, October 1998.

[11] F. Smith, A. Calawa, C. Chen, M. Manfra, and L. Mahoney, "New MBE buffer used to eliminate backgating in GaAs MESFETs," *IEEE Electron Device Letters*, vol. 9, pp. 77–80, February 1988.

[12] S. Gupta, J. Whitaker, and G. Mourou, "Ultrafast carrier dynamics in III-V semiconductors grown by molecular-beam epitaxy at very low substrate temperatures," *IEEE Journal of Quantum Electronics*, vol. 28, pp. 2464–2472, October 1992.

[13] C. Carmody, H. Boudinov, H. Tan, C. Jagadish, M. Lederer, V. Kolev, B. Luther-Davies, L. Dao, , and M. Gal, "Ultrafast trapping times in ion implanted InP," *Journal of Applied Physics*, vol. 92, pp. 2420–2423, September 2002.

[14] R. Takahashi, Y. Kawamura, T. Kagawa, and H. Iwamura, "Ultrafast 1.55 μm photoresponses in low-temperature-grown InGaAs/InAlAs quantum wells," *Applied Physics Letters*, vol. 65, pp. 1790–1792, October 1994.

[15] Y. Silberberg, P. Smith, D. Miller, B. Tell, A. Gossard, and W. Wiegmann, "Fast nonlinear optical response from proton-bombarded multiple quantum well structures," *Applied Physics Letters*, vol. 46, pp. 701–703, April 1985.

[16] E. Zarrabi, J.H. Portnoi and A. Chelnokov, "Passive mode locking of a multistripe single quantum well GaAs laser diode with an intracavity saturable absorber," *Applied Physics Letters*, vol. 56, pp. 1526–1528, September 1991.

[17] E. Delpon, J. Oudar, N. Bouche, R. Raj, A. Shen, N. Stelmakh, and J. Lourtioz, "Ultrafast excitonic saturable absorption in ion-implanted InGaAs/InAlAs multiple quantum wells," *Applied Physics Letters*, vol. 72, pp. 759–761, February 1998.

[18] J. Mangeney, H. Choumane, G. Patriarche, G. Leroux, G. Aubin, J. Harmand, J. Oudar, and H. Bernas, "Comparison of light- and heavy-ion-irradiated quantum-wells for use as ultrafast saturable absorbers," *Applied Physics Letters*, vol. 79, pp. 2722–2724, October 2001.

[19] J. Mangeney, S. Barré, G. Aubin, J. Oudar, and O. Leclerc, "System application of 1.5 μm ultrafast saturable absorber in 10 Gb/s long-haul transmission," *Electronics Letters*, vol. 36, pp. 1725–1727, September 2000.

[20] K. Williams and R. Esman, "Design considerations for high-current photodetectors," *Journal of Lightwave Technology*, vol. 17, pp. 1443–1454, August 1999.

Chapter 4

Experimental systems

This chapter describes the experimental configurations which were used to perform the device characterisation experiments of Chapters 6 to 8. Section 4.1 provides an overview of the experiments performed, and the motivations for the different experiments. The free space optical components used to couple light into, and out of, reflection and transmission devices are described in Section 4.2. The remain sections describe the configurations used for different experiments:

Section 4.3: measurements of transmission, reflectivity, and photocurrent spectra.

Section 4.4: measurements of saturation, made using both continuous wave (CW) and picosecond pulse sources.

Section 4.5: time resolved measurements of transmission, reflectivity and polarisation rotation.

Section 4.6: demonstrations of wavelength conversion.

The procedures used to align the experimental configurations are described in Appendix F.

4.1 Objectives of the experimental work

The initial aim of the experimental work described in this thesis was to characterise devices using exciton absorption bleaching (EAB), non-linear polarisation rotation (NPR) and electric field screening in multiple quantum well (MQW) structures, and hence assess their suitability for soliton control and all-optical wavelength conversion applications.

Measurements of the transmission or reflection, and in the case of biasable devices, photocurrent, spectra were made to locate band edges and exciton resonances. For biasable devices, changes to the spectra due to the quantum confined Stark effect (QCSE) could be observed as the applied reverse bias was varied.

Measurements of continuous wave (CW) saturation were used to observe optical non-linearity in as-grown MQW structures. This measurements could not, however, be performed for ion implanted structures in which significant carrier lifetime reductions had been achieved, as a consequence of the corresponding increase in saturation power (Section A.7.) Typically, pulse saturation energies greater than 20 pJ were observed in structures with recovery times as short as 5 ps. From the relation presented in Section A.7 the saturation power is such a structure is 4 W. Such high CW optical powers were not available. Saturation characteristics of the devices were instead measured using pulses which were short compared to the free carrier lifetime.

The modelling of Section 3.7.3 shows that incidence of a significant CW power (10 mW) on a p-i-n device, under conditions such that field screening is the dominant non-linear optical mechanism, should result in only small changes to the electric field distribution in the intrinsic region. Since the electric field changes are responsible, through the QCSE, for the non-linearity of field screening devices, CW saturation measurements of such devices cannot be expected to reveal significant non-linearities. They can, however, be used to demonstrate the transition from EAB to field screening as increasing reverse bias voltages are applied to p-i-n devices.

Short pulse saturation measurements were not appropriate for the investigation of the field screening non-linearity, since, as shown by the modelling of Section 3.4, screening of the electric field in the intrinsic region reaches a maximum some time after the incidence of a short optical pulse. In the devices investigated this time was long compared to the duration of the 2 ps pulses produced by the figure-of-eight mode-locked laser (MLL) described in Appendix E which were used for such measurements.

A proper understanding of the behaviour of the field screening devices, and observation of carrier lifetime reduction in ion-implanted MQWs, required time resolved measurements of device transmission or reflectivity. These were made using a pump-probe technique; photocarriers were excited in the MQW by a high energy optical pump pulse, and a relatively small optical probe pulse was used to measure the transmission or reflectivity after some time delay. Such measurements can be used to observe the dynamics of the transmission or reflectivity change by varying the relative arrival times of the pump and probe pulses at the device. These measurements were made using 2 ps pulses. This placed a lower limit on their temporal resolution.

A modification of this pump-probe technique, where the state of polarisation rather than the energy of the transmitted or reflected probe pulses was measured, was used to observe NPR in MQWs.

Wavelength conversion experiments were also performed. Pulses at the input wavelength were used to control the reflectivity of the devices being investigated. The changing reflectivity modulated CW light at the output wavelength. The modulation could be detected using a suitably fast photodetector and sampling oscilloscope. Initial wavelength conversion experiments, used the low repetition rate (4 MHz) pulse stream from the figure-of-eight MLL of Appendix E.

A majority of the experiments were automated using National Instruments LabView, allowing data to be collected quickly, and without the possibility of human error.

4.2 Optical coupling in free space

4.2.1 Requirements

When investigating non-linear devices some system is required to couple light into the devices used test, and collect the reflected or transmitted light for measurement. The requirements for such a system are:

Low loss coupling light into the device: In measurements which investigate non-linear effects a loss prior to the device results in a reduction of the magnitude of the observable reflectivity or transmission change. Such a loss will also result in a reduction of the signal-to-noise ratio (SNR) of measurements.

Low loss coupling light out of the device: Loss in this part of the system will result in a reduction of measurement SNR, as described above.

Polarisation independence: Some of the non-linear effects in MQWs described in Chapter 3 are polarisation dependent. Investigation of these effects, or demonstration of their absence, requires a polarisation independent coupling system.

Ease of alignment: A simple alignment process is desirable, since it will facilitate efficient and repeatable measurements.

4.2.2 Optical coupling for reflection devices

Two polarisation independent configurations were used to couple light onto reflection devices, whilst simultaneously collecting reflected light for measurement.

A configuration using an optical circulator, which was used for a majority of the experiments, is illustrated in Figure 4.1. Light exiting the port 2 pigtail of the circulator is collimated by objective 1, and allowed to propagate for some distance before being focused to a small spot on the device by objective 2. The reflected light is then collimated and focused back into the port 2 pigtail by the same two objectives. If objectives 1 and 2 are identical this system has the property that, when the alignment is such that light launched from port 2 of the optical circulator is well collimated and the efficiency of coupling of the reflected light back into the fibre is maximised, the spot size of the beam at the device is the same as that exiting the fibre. An optical chopper wheel is in included the free space path to allow synchronous detection of the signal reflected from the MQW using a lock-in amplifier. The alignment procedure for this configuration is described in Section F.2.

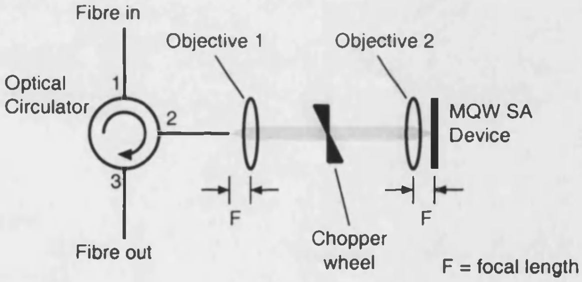

Figure 4.1: Reflective device coupling system using an optical circulator.

The alternative configuration, which employs a single mirror and a non-normally incident beam such that light reflected from the non-linear device is coupled into a separate output fibre, is shown in Figure 4.2. Since the system is aligned such that the collimated input light is not incident on the centre of objective 2 the reflected light follows a different path. When this light has been collimated by objective 2 it is diverted by a mirror and focused onto the output fibre by objective 3. A chopper wheel is again included in the free space optical path. The alignment procedure for this configuration is described in also Section F.2.

The loss of the system of Figure 4.1 in both the forward and reflection directions is greater than that of Figure 4.2 due to the port-to-port loss of the circulator. In the circulator used, this was 1.25 dB. However, experimental experience showed that alignment of the system employing the circulator considerably simpler. It was therefore preferred for experimental measurements.

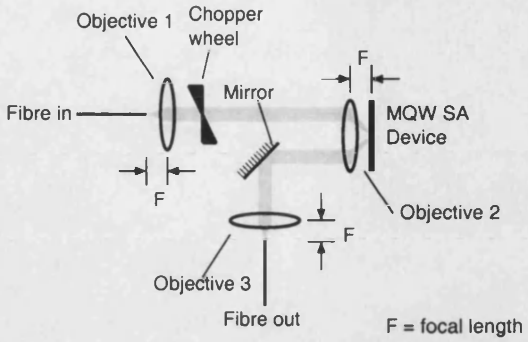

Figure 4.2: Device coupling system using non-normal incidence.

4.2.3 Optical coupling for transmission devices

The optical coupling arrangement of Figure 4.3 was used for transmission devices. When the free space beam between the first two objectives is well collimated the radius of the beam waist between the second and third objectives will be the same as that of the light launched from the input fibre. A chopper wheel is included in the free space optical path.

The alignment procedure for this configuration, including the method used to locate the beam waist, is described in Section F.3.

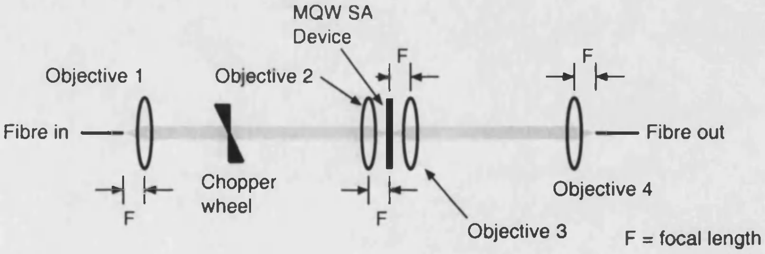

Figure 4.3: Coupling system for transmission MQW devices.

4.3 Spectrum measurements

The configuration used for spectrum measurements is illustrated in Figure 4.4. The device coupling systems of Figures 4.1 and 4.3 were used for reflection and transmission devices. The lock-in amplifier used to measure the photocurrent at the output photodetector is synchronised with the control signal for the chopper wheel adjacent to the device (Figures 4.1 and 4.3.) A second lock-in amplifier, synchronised with the same control signal, was used to measure the photocurrent from p-i-n MQW devices.

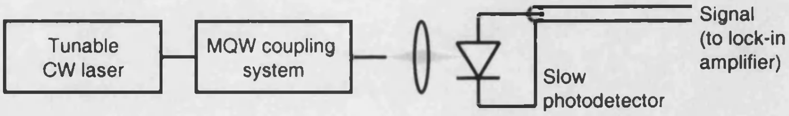

Figure 4.4: Configuration used for CW spectra measurements.

Measurements were calibrated by measuring the loss of the various components in the coupling system, the free space power incident on the device for a given nominal laser output power laser, and the responsivity of the output photodetector. The linearity and wavelength independence of the measurements in the absence of device non-linearity were verified experimentally. The LabView program used to control the system allowed the wavelength of the tunable laser to be swept across its full range, 1500 nm to 1580 nm, whilst measuring transmitted or reflected power and where applicable, the photocurrent.

4.4 Saturation measurements

4.4.1 CW saturation measurements

CW saturation measurements were made using the configuration of Figure 4.5. The device coupling arrangement used was that of Figure 4.1 or 4.3, with the optical chopper wheel omitted.

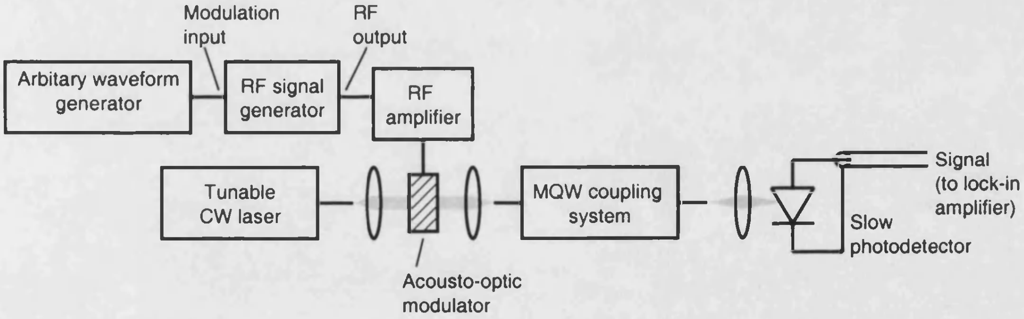

Figure 4.5: Configuration used for CW saturation measurements.

An acousto-optic modulator (AOM) is used to chop the light prior to the device under test, reducing the average power incident on it by a factor of 200 to avoid the possibility of transmission changes due to thermal effects. The AOM is driven at ≈ 27 MHz by a Marconi Instruments 2022C signal generator, the output of which is amplified by a MiniCircuits amplifier. The signal generator is modulated by an Agilent 33120A arbitrary waveform generator, such that the AOM passes 5 μs pulses at a repetition rate of 1 kHz.

The photocurrent in the final photodetector is measured by a lock-in amplifier synchronised to the 1 kHz signal modulating the signal generator. The linearity of this measurement in the absence of the non-linear device under test was verified experimentally. The power incident on the device was controlled by setting the output power of the tunable laser.

4.4.2 Short pulse saturation measurements

Measurements of device saturation with 2 ps full width half maximum (FWHM) pulses were made using the configurations of Figure 4.6. The pulse source is the figure-of-eight MLL described in Appendix E.

The coupling systems of Figures 4.1 and 4.3 are used for reflection and transmission devices. Modulation of the optical path by a chopper wheel allowed synchronous detection of photocurrent and output power using lock-in amplifiers, similarly to the system described in Section 4.3.

The LabView program used to control the experiment automatically adjusted the output gain of the lock-in amplifiers, effectively increasing the dynamic range of measurements.

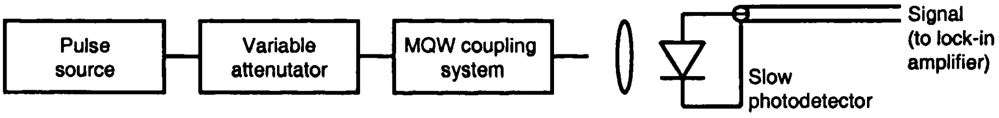

Figure 4.6: Configuration used for pulse saturation measurements.

4.5 Short pulse pump-probe measurements

4.5.1 Variable delay

Short pulse pump-probe measurements require a variable delay in either the pump or probe path. Figure 4.7 shows the variable delay used in these experiments. Light is launched from fibre, collimated, reflected from a gold mirror, and focused back into the same fibre. The gold mirror is mounted on a translation stage, allowing the optical path length to be varied. The stage used was 150 mm long, and could be adjusted with a resolution of 1 μm. In the reflecting configuration used, this resulted in a delay with a resolution of 6.7 fs and a range of 1 ns. The alignment of the variable delay is described in Section F.4.

4.5.2 Time resolved transmission and reflectivity

The systems used to make pump-probe measurements of reflection and transmission samples are shown in Figures 4.8 and 4.9 respectively. Pump and probe signals are produced by asymmetri-

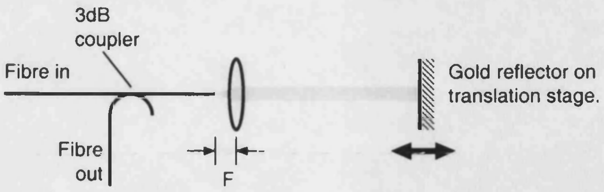

Figure 4.7: Variable delay used for short pulse pump-probe measurements.

cally splitting the output of the pulse source, which is the figure-of-eight MLL of Appendix E. The repetition rate of the MLL was ≈ 4 MHz, ensuring complete recovery of the MQW between successive pump pulses. The variable delay is described in Section 4.5.1. Polarisation controllers in the pump and probe paths allow control of the state of polarisation of the light incident on the device.

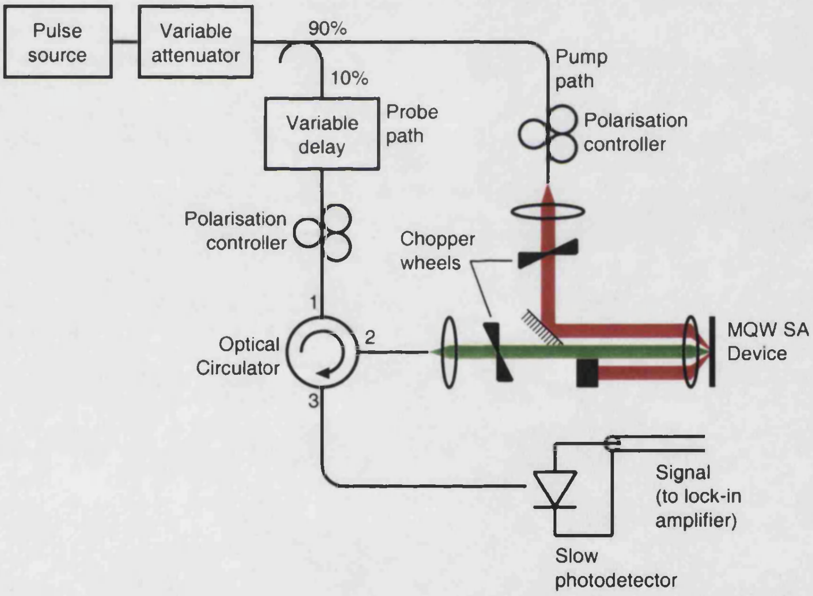

Figure 4.8: Configuration used for pump-probe measurements of reflection devices.

A combination of the arrangements of Figures 4.1 and 4.2 is used to couple the pump and probe light to the same point on the device. The use of separate pump and probe paths allows the probe light to be detected in the final photodetector independently. If the pump light also entered the final photodetector spurious responses would be observed when the variable delay was set such that the probe pulse arrived at the sample before the pump pulses. Changes in device transmission or reflectivity caused by the probe would modulate the pump. Whilst these changes would be small, the relatively large power of the pump would result in a significant detected signal.

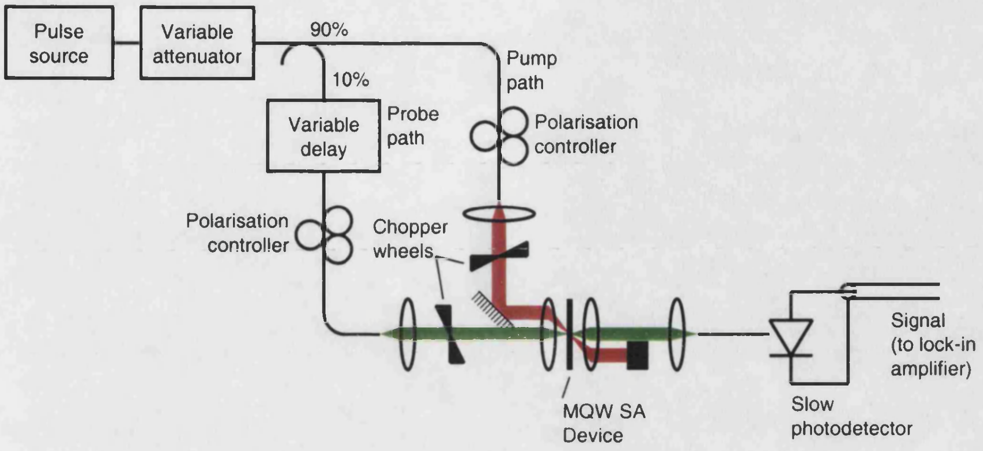

Figure 4.9: Configuration used for pump-probe measurements of transmission devices.

Independent detection of the probe light could also be achieved if it was polarised orthogonally to the pump. Such an arrangement was considered but rejected since it would preclude investigation of polarisation effects.

Mechanical chopper wheels modulate the pump and probe light at frequencies of 1.1 kHz and 1.0 kHz respectively. The lock-in amplifier which processes the output of the slow photodetector allows independent synchronous detection of signals at these two frequencies.

The combined sensitivity of the photodetector and the lock-in amplifier can be expressed by a single constant, C, such that the lock-in amplifier output voltage is CP when optical power P is incident on the photodetector. If P and P_0 are the probe powers at the photodetector in the presence and absence of pump light respectively then the lock-in outputs corresponding to the probe and pump chopping frequencies will be

$$V_1 = C\frac{P+P_0}{2} \tag{4.1}$$

and

$$V_2 = C\frac{P-P_0}{2}. \tag{4.2}$$

P and P_0 can be expressed in terms of V_1, V_2 and C,

$$P = \frac{V_1+V_2}{C} \tag{4.3}$$

and

$$P_0 = \frac{V_1-V_2}{C} \tag{4.4}$$

The pump-probe experiment must determine the fractional transmission or reflectivity change experienced by the probe due to the pump, $\Delta T/T$ or $\Delta R/R$. This is equal to $(P-P_0)/P_0$, the fractional change of the probe power at the photodetector. From Equations 4.3 and 4.4

$$\frac{P-P_0}{P_0}=\frac{2V_2}{V_1-V_2}. \tag{4.5}$$

The LabView program used to control this experiment sweeps the variable delay by stepping the translation stage whilst reading data from the lock-in amplifier to make time resolved transmission measurements. The program also performs the calculation of Equation 4.5.

Alignment of the systems for the measurements reflection and transmission devices is described in Section F.5.

4.5.3 Time resolved non-linear polarisation rotation

The configuration of Figure 4.10, based on that of Figure 4.8 was used to make time-resolved observations of NPR in reflection MQW devices.

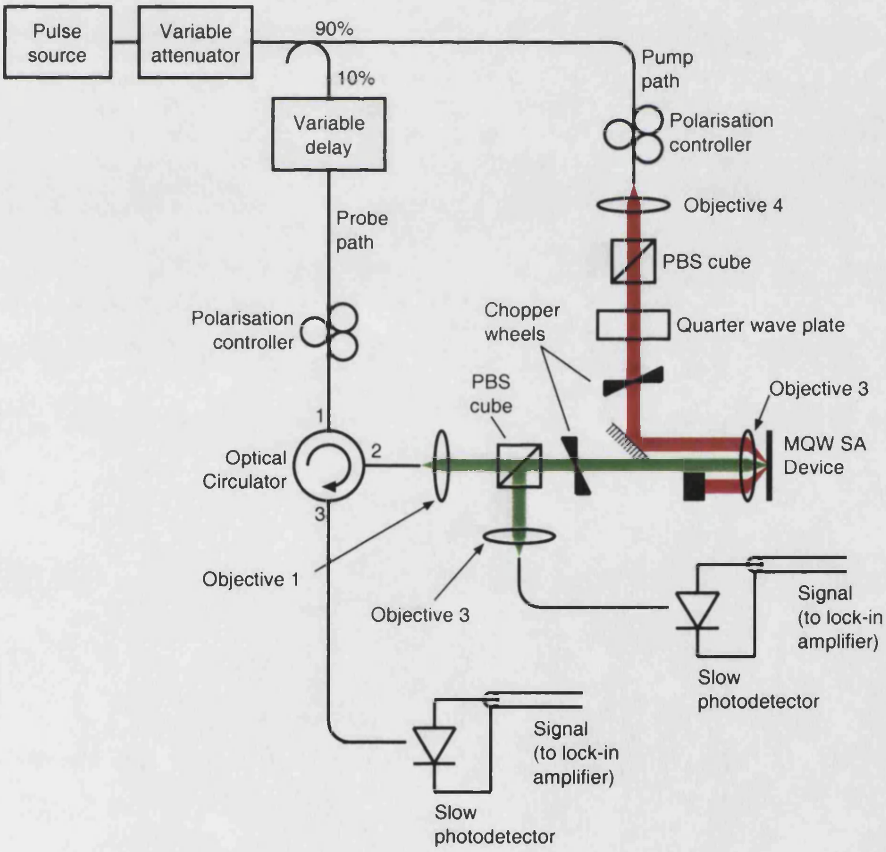

Figure 4.10: Configuration used for pump-probe measurements of non-linear polarisation rotation in reflection devices.

Light from the 2 ps pulses source is again split into separate pump and probe paths. The pump pulses are collimated in free space, pass through a polarising beam splitter (PBS) cube to ensure pure plane polarisation, and then through a quarter wave plate aligned such that they are circularly polarised when they are focused onto on the MQW device. These circularly polarised pulses should selectively excite either spin-up or spin-down photocarriers in the MQW, and hence enable NPR to be observed.

The probe pulses are collimated in free space and pass through a PBS cube, again to ensure plane polarisation, and are focused onto the device. They are reflected back to the PBS cube, at which point the polarisation-rotated component is deflected and focused into a fibre which is used to carry it to a slow photodetector. A circulator is used to allow separate monitoring of the non-polarisation rotated component of the pump signal. The ability to monitor this component of the signal is useful during alignment of the system.

The fibre polarisation controllers in the pump and probe paths are set to ensure maximum transmission of pump and probe pulses through the PBS cubes.

Chopper wheels in the pump and probe paths allow the fractional change of the polarisation rotated component of the reflected probe at the output due to the presence of the pump to be measured, similarly to the configurations of Section 4.5.2.

The alignment procedure for this configuration is described in Section F.7.

Figure 4.11 shows a similar configuration used to make time resolved measurements of NPR in transmission devices.

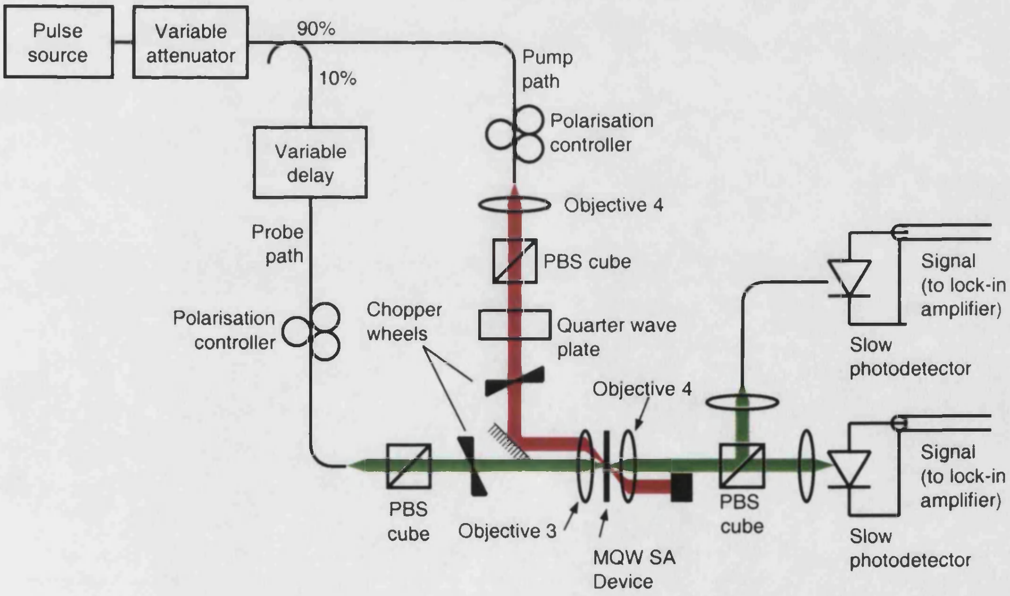

Figure 4.11: Configuration used for pump-probe measurements of non-linear polarisation rotation in transmission devices.

4.6 Wavelength conversion experiments

4.6.1 Wavelength conversion configurations with two free space paths

Initial demonstrations of wavelength conversion in reflection devices used the configuration of Figure 4.12. The pulse source used was the figure-of-eight MLL described in Appendix E; the pulse repetition rate was thus fixed at ≈ 4 MHz.

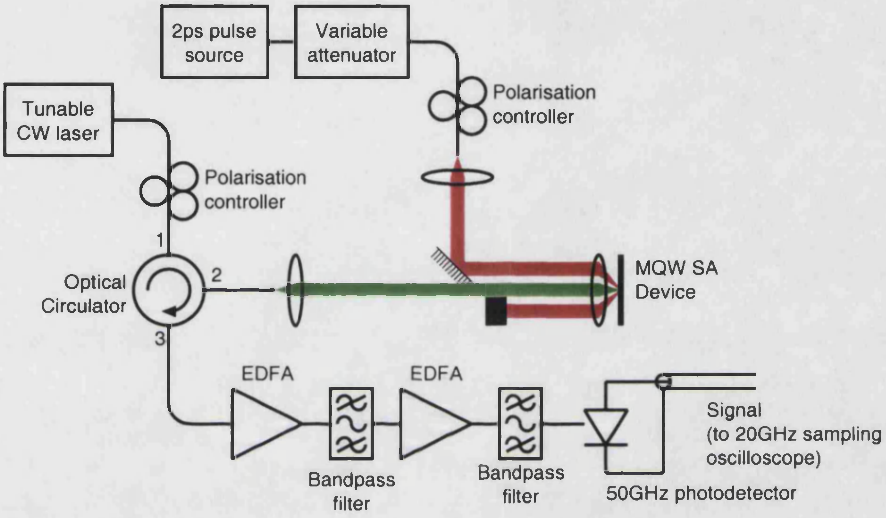

Figure 4.12: Wavelength conversion configuration for reflection devices.

The free space optical coupling arrangement focuses pulses at the input wavelength and CW light at the output wavelength onto the same point on the device. The high energy pulses cause transient reflectivity changes in the MQW device which modulate the reflected CW light. The reflected, modulated light is focused back into fibre and amplified by cascaded erbium doped fibre amplifiers (EDFAs). Optical filtering prevents leakage of light at the input wavelength to the fast photodetector, as well as reducing the level of amplified spontaneous emission (ASE) noise.

A similar arrangement, shown in Figure 4.13 was used to demonstrate wavelength conversion in transmission devices.

The alignment procedures for the reflection and transmission device configuration resembled those for pump-probe measurements described in Section F.6.

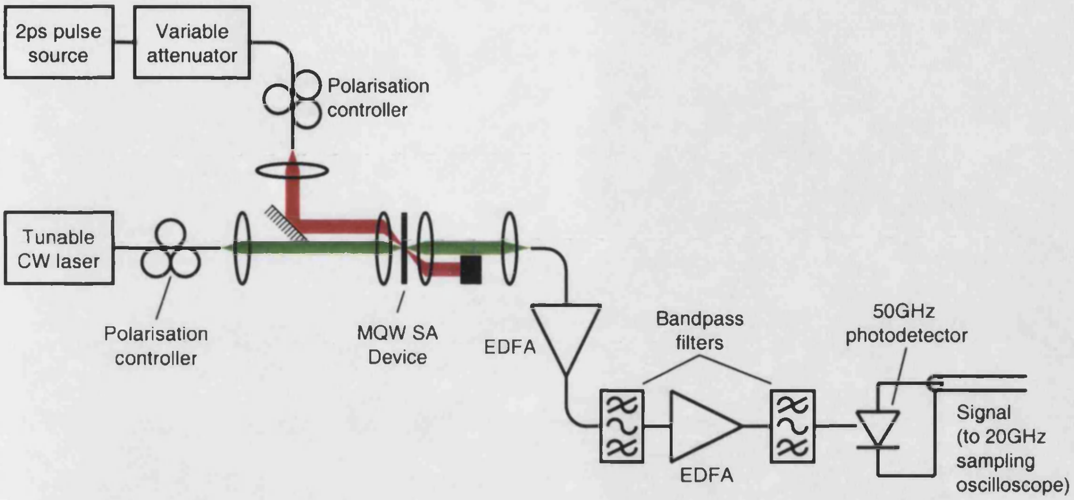

Figure 4.13: Wavelength conversion configuration for transmission devices.

Chapter summary

This chapter has described experimental systems designed and constructed to investigate optical non-linearities in MQW devices. The systems can be used to make measurements of transmission, reflection and photocurrent spectra, saturation characteristics using CW light or picosecond pulses, and the dynamics of transmission or reflectivity change following excitation by a picosecond pulse. Systems for the demonstration of wavelength conversion have also been described.

These systems were used in carrying out the experimental work which is described in Chapters 6 to 8.

Chapter 5

Wafer growth and ion implantation

This chapter describes issues relating to the design and growth of the structures which were the subject of the experimental work, as well as to post-growth ion implantation.

The InGaAsP quaternary material system in which the devices were grown, and the design of multiple quantum well (MQW) and distributed Bragg reflector (DBR) structures in this material system, are discussed in Section 5.1

The design which was used for optically resonant structures for asymmetric Fabry-Perot devices is described in Section 5.2.

The metal organic vapour phase epitaxy process by which the structures were grown imposed some practical limitations on device design which are discussed in Section 5.3.

Section 5.4 discusses ion implantation, the technique used to reduce carrier lifetime and hence produce fast excitonic absorption bleaching (EAB) based devices.

5.1 Wafer design

5.1.1 Lattice matching

The multiple quantum well (MQW) structures investigated consisted of InP and quaternary InGaAsP grown on InP substrates. To avoid anisotropy in the normal incidence configurations in which the MQWs were used it was necessary to avoid strain. This is achieved in structures which are lattice matched, such that the lattice constant of the barrier and well materials is equal to that of the substrate. From Katz [1] the condition for lattice matching in InGaAsP in which the relative concentrations of In and G are x and $1-x$ and those of As and P are y and $1-y$ is

$$1-x=\frac{0.1896y}{0.4175-0.012y}. \tag{5.1}$$

From the same source, the bandgap of lattice matched InGaAsP is

$$E_g(y)=1.35-0.7675y+0.149y^2 \tag{5.2}$$

This expression is used to plot bandgap energy, and hence wavelength, as a function of y in Figure 5.1. From these graphs it is apparent that lattice matched InGaAsP can be grown with bandgaps from about 0.9 μm to 1.7 μm.

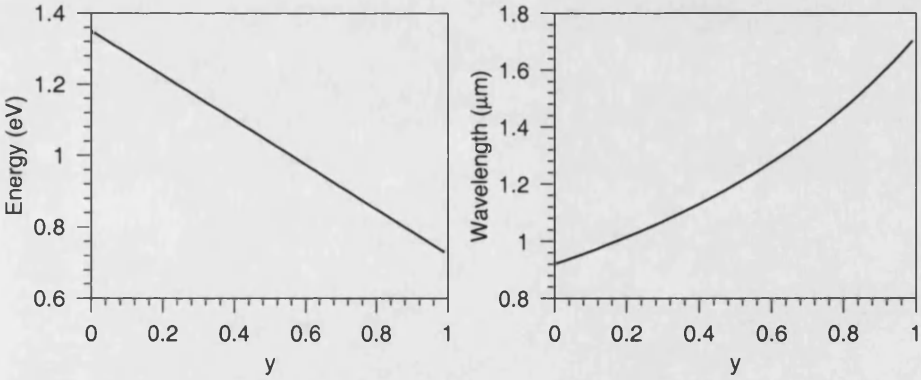

Figure 5.1: Dependence of bandgap energy and wavelength on the As concentration, in lattice matched InGaAsP.

A simple notation based on bandgap wavelength is commonly used to described lattice matched InGaAsP. Material with a 1.1 μm bandgap is referred to as Q1.1, material with a 1.2 μm bandgap is referred to as Q1.2, and so forth.

5.1.2 Multiple quantum wells

For the work described in this thesis an MQW exciton wavelengths within the erbium doped fibre amplifier (EDFA) gain region, typically 1.535 μm to 1.565 μm, were required. In the case of structures from which biasable devices were fabricated shorter exciton wavelengths, such that the exciton would be red-shifted to the desired wavelength by the quantum confined Stark effect (QCSE) when the device was reverse biased, were desirable.

The most significant factor determining the exciton wavelength is the bandgap of the wells in the MQW. There are additional contributions due to the quantisation of allowed energy levels in the wells, and the exciton binding energy.

In devices employing field screening low barriers, which increase the escape rate of carriers from the wells in the MQW are desirable. In devices employing excitonic absorption bleaching (EAB) high barriers which enhance carrier confinement, and hence increase the excitonic absorption, are desirable.

5.1.3 Distributed Bragg reflectors

The reflection devices described in this thesis employed distributed Bragg reflectors (DBRs). DBRs and MQWs were grown in integrated structures, such at that illustrated schematically in Figure 5.2.

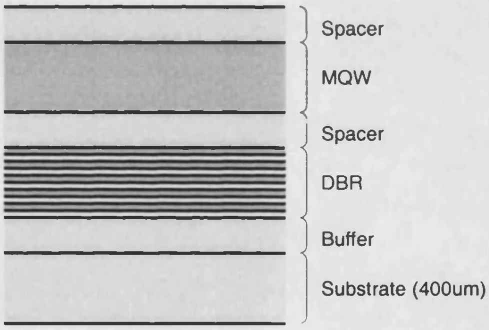

Figure 5.2: Schematic representation of wafer incorporating an MQW and a DBR.

The DBR is composed of a number of pairs of half-wave layers of materials with different refractive indices. Each such pair referred to as a period. Reflections from each interface within the DBR interfere constructively resulting in a high aggregate reflectivity. Ideally the refractive index difference between the two materials from which the DBR is made should be large to maximise the reflection at each interface. The range of usable refractive indices can be limited by the constraint that material bandgaps must be large enough that material absorption is low at the operating wavelength. This limits the range of refractive indices which can be used. In the case of a small refractive index difference the aggregate reflectivity of the DBR can be increased by using a greater number of periods.

The devices investigated in this thesis used half wave layers of InP and Q1.4 InGaAsP. The refractive indices of these materials at 1550 are 3.15 [1] and 3.46 [2] respectively. Figure 5.3 shows the reflectivity of such DBRs with different numbers of periods, obtained using scattering matrices [3].

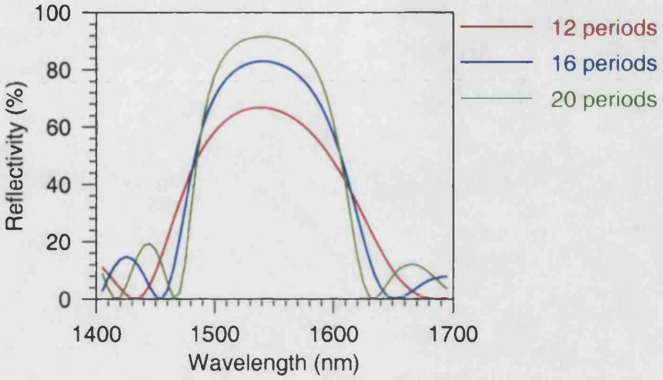

Figure 5.3: Reflectivity spectra of 1550 nm DBRs composed of different numbers of InP/Q1.4 InGaAsP periods.

5.2 Asymmetric Fabry-Perot cavities

Section 3.5 discusses devices in which an MQW is incorporated in an asymmetric Fabry-Perot (AFP) cavity for enhanced contrast ratio. If top surface of the structure of Figure 5.2 is not anti-reflection (AR) coated an AFP cavity is formed between it and the DBR. Whilst this approach limits flexibility in the design of the AFP, since the reflectivity of the air-semiconductor interface is fixed at approximately 30 %, it has the advantage that the top of the structure can be etched after growth to adjust the cavity wavelength. Alternative designs incorporate an additional DBR above the MQW.

5.3 Wafer growth

5.3.1 Metal organic vapour phase epitaxy growth

The InGaAsP MQW structures investigated were grown by the EPSRC III-V semiconductor central facility at the University of Sheffield. Growth was done in a metal organic vapour phase epitaxy (MOVPE) reactor. This had some implications for possible device designs. Large changes in material composition could not be reliably achieved in the MQW region, limiting barrier height and hence, as discussed in Section 5.1.2, the strength of excitonic absorption. Practically, wafers were grown with Q1.6 wells and Q1.1 barriers, using designs previously optimised at the University of Sheffield.

Reliability fell as the thickness of the structure grown increased. This limited the number of DBR periods which could practically be used. In earlier structures 16 period DBRs were used, as they were decided to make the best compromise between reflectivity and reliability. In later structures it was found that 20 period DBRs could reliably be grown. These were therefore used to take advantage of the increased reflectivity.

Wafers were not rotated during growth. This resulted in a lack of uniformity of deposition rate across each wafer.

5.3.2 Background doping

Doped wafers, incorporating MQWs and DBRs were grown to allow fabrication of p-i-n MQW devices, such as those shown in Figure 3.3. In reality, some background doping was present in the nominally intrinsic regions of these wafers, with typical dopant densities in the range $5 \times 10^{14}\,\mathrm{cm}^{-3}$ to $7 \times 10^{14}\,\mathrm{cm}^{-3}$.

Under reverse bias the nominally intrinsic region of a device fabricated from such a material will become depleted. The charge density due to depletion will affect the electric field distribution since

$$\frac{d\mathscr{E}}{dz} = \frac{\rho}{\varepsilon_0 \varepsilon_r} \tag{5.3}$$

where $\mathscr{E}$ = electric field, ε_0 = permittivity of free space, ε_r = relative permittivity, ρ = charge density, and the z axis is normal to the plane of the MQW.

In a device with $7 \times 10^{14}\,\mathrm{cm}^{-3}$ background doping the electric field gradient will be 10.5 kV/cm per micron using $\varepsilon_r = 12$, the standard value for InP. If the device has a 1 µm nominally intrinsic region, typical of those studied in this thesis, and 10 V reverse bias is applied, there will be a linear variation of $\mathscr{E}$ across the nominally intrinsic region, from 95 kV/cm to 105 kV/cm.

As a consequence of the QCSE, this variation will result in a broadening of excitonic feature in the MQW absorption spectrum, and hence a reduction of excitonic absorption at any given wavelength.

5.3.3 Dopant diffusion

Zinc was used as a p-type dopant in the doped wafer. The zinc dopant diffused into the intrinsic region during the growth process, with a typical diffusion length of 100 nm.

From the argument of Section 5.3.2, depletion of the diffused dopants will lead to a non-uniform electric field in the intrinsic region. Structures grown with p-i-n doping incorporated a spacer between the boundary of the intentionally p-doped region and the MQW to avoid dopant diffusion and its consequent problems.

5.4 Ion implantation

When ions are implanted into a semiconductor they propagate through it, colliding with the lattice atoms. These collisions can displace the lattice atoms, creating vacancy and interstitial defects. As the ions travel further into the semiconductor and lose energy to the lattice the probability that these collisions will lead to the ion stopping increases. A high concentration of defects is created in the region in which the atoms stop.

Carrier lifetime reduction can be achieved if the MQW is positioned such that the ions have propagated through it before they begin to stop. This results in a moderate population of defects which act as recombination centres for free carriers, and hence reduce the free carrier lifetime, in the MQW.

The structures used in this work were ion-implanted by the Surrey Centre for Research into Ion Beam Applications at the University of Surrey. The available implantation energy was limited to 4MeV. This precluded the use of heavy ions, such as Ni, which other researchers have suggested to be more effective for carrier lifetime reduction [4] since the depth of implantation would be limited. Implantation was instead done with N ions.

Figure 5.4 show the results of TRIM [5] simulations of the implantation of 4MeV ions into InP. There is a maximum in the distribution of deposited ions, and hence in the defect concentration, at a depth of approximately 3 μm. Since in the wafers studied the MQWs were close to the surface, and were typically 1 μm thick, implantation such as that of Figure 5.4 will result in the desired moderate defect populations in the MQW. The ions will be deposited deep below the MQW, within the DBR region in reflective structures.

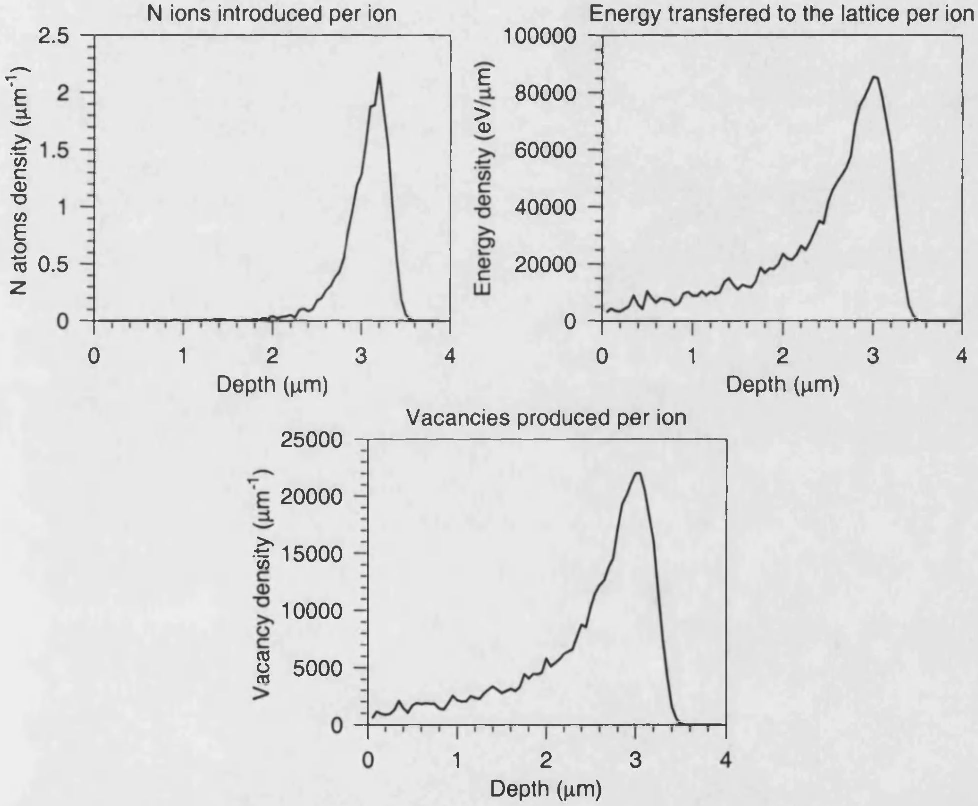

Figure 5.4: Results of TRIM simulations of the implantation of InP with 4 MeV N ions.

Chapter summary

The chapter has discussed the design of MQWs and DBRs, and their integration in epitaxially grown structures in the InGaAsP material system. The need to lattice match the InGaAsP places some constraints DBR and MQW design.

The MOVPE process used to growth the structures suffers from some limitations. Diffusion of the zinc dopant from p-doped regions and background doping modifies the electric field profile in p-i-n doped devices. Variation in the deposition rate results in non-uniform wafers with variations in the MQW and DBR characteristics. Regions in which these characteristics are suitable must thus be chosen. The transitions which could be made whilst maintaining reliable growth of MQWs were limited, limiting possible barrier heights.

The ion implantation process used to reduce the carrier lifetime in EAB-based devices has also been discussed. Due to limitations to the implantation energy at the ion implantation facility used, ions with relatively small mass were used. Simulations of the damage profiles produced due to implantation with these ions have been presented.

References

[1] A. Katz, ed., *Indium phosphide and related materials*, ch. 1. Artech House, 1992.

[2] S. Adachi, "Refractive indices of III-V compounds: Key properties of InGaAsP relevant to device design," *Journal of Applied Physics*, vol. 53, pp. 5863–5869, August 1982.

[3] A. Siegman, *Lasers*. University Science Books, 1986.

[4] J. Mangeney, H. Choumane, G. Patriarche, G. Leroux, G. Aubin, J. Harmand, J. Oudar, and H. Bernas, "Comparison of light- and heavy-ion-irradiated quantum-wells for use as ultrafast saturable absorbers," *Applied Physics Letters*, vol. 79, pp. 2722–2724, October 2001.

[5] J. Ziegler, J. Biersack, and U. Littmark, *The Stopping and Range of Ions in Solids*. Pergamon Press, 1985.

Chapter 6

Investigations of field screening in multiple quantum well p-i-n devices

This chapter presents the results of investigations of p-i-n multiple quantum well (MQW) devices. The experimental results illustrate the transition of the dominant optical non-linearity from excitonic absorption bleaching (EAB) to field screening. The experiments focus on the high reverse bias regime in which field screening optical non-linearities with speeds approaching those required for 10 Gb/s and 40 Gb/s systems applications are observed.

The behaviours expected from devices in which the EAB and field screening non-linearities are dominant are described in Section 6.1. Investigations of three different devices are presented in Sections 6.2 to 6.4:

Section 6.2 Low reverse bias measurements illustrate the transition between the EAB and field screening optical non-linearities. High reverse bias measurements show a fast reflectivity change due to the field screening non-linearity.

Section 6.3 Time-resolved measurements made under high reverse bias condition are used to study fast field screening behaviour. Dependencies of recovery time and reflectivity change magnitude on reverse bias voltage and exiting pulse energy are identified.

Section 6.4 Time resolved measurements under high and low reverse bias conditions are described and wavelength conversion is demonstrated. The high power continuous wave signal incident on the device in the wavelength conversion experiments results in qualitative changes in the observed field screening reflectivity changes.

The results of Sections 6.2 to 6.4 are brought together in the discussion of Section 6.5.

6.1 Expected behaviour of the devices

6.1.1 Small signal responsivity and reflectivity

In the case of devices in which the multiple quantum well (MQW) region is not incorporated in an asymmetric Fabry-Perot (AFP) cavity, the band edge should be clearly visible in both the responsivity and reflectivity spectra. Application of a reverse bias to the device will result in a reduction of electron and hole sub-band energies in the quantum wells (QWs), and hence a red-shifting of the band edge. Application of the field also increases the possibility of carriers tunnelling out of the wells which results in a broadening of the band edge. This effect, the quantum confined Stark effect (QCSE), is discussed in Section 3.2.

A feature due to excitonic absorption should also be visible in devices in which the spectra are not dominated by AFP cavity effects.

In the case of devices in which the MQW is incorporated in an AFP cavity, the spectra will be dominated by the effects due to the cavity. Whilst the AFP resonance should be clearly visible, it will not necessarily be possible to identify features due to excitonic absorption.

6.1.2 Sense of the reflectivity change in measurements of non-linearity

Excitonic absorption bleaching (EAB) will always result in a decrease of MQW absorption. This is not true of field screening. At wavelengths shorter than that of peak exciton absorption red-shifting and broadening of the absorption spectrum due to application of a reverse bias will result in reduction of absorption. Screening of the reverse bias field by photocarriers will result in increased absorption. At wavelengths longer than that of peak exciton absorption, the opposite will be true.

6.1.3 Continuous wave saturation measurements

Under low reverse bias conditions, when device non-linearity is dominated by EAB, it should be possible to fit Equation A.22 to measured continuous wave (CW) saturation data for non-AFP cavity devices, and hence determine values for the saturation power and contrast ratio.

Broadening and red-shifting of the excitonic component of the absorption spectrum due to application of reverse bias should be visible as a reduction and red-shifting of CW non-linearities.

Application of reverse bias will also reduce the photocarrier lifetime, due to sweep-out from the QWs. As discussed in Section A.7, this will result in a proportionate increase of saturation power, and therefore a decrease in the magnitude of the observed non-linear change.

As discussed in Section 4.1 it is expected that significant optical non-linearities will not be observed in CW saturation measurements made under conditions such that field screening is dominant.

6.1.4 Pulse saturation measurements

The field screening non-linearity results in an absorption change occurring some time after the incidence of a short exciting pulse, with the delay between the pulse and the absorption change being due to the time taken for positive and negative photocarriers to escape from the QWs in which they are generated and separate as they drift in opposite directions across the intrinsic region (see Section 3.4.1). If the rise time of the absorption change is long compared to the duration of the exciting pulses, negligible non-linearity will be observed in saturation measurements.

Since the absorption change due to EAB occurs immediately on the generation of photocarriers there is no lower limit to the length of pulses which can be used detect EAB in saturation measurements. If, for a given device, non-linearity is observed in time resolved measurements, but not in short pulse saturation measurements, field screening must be the dominant non-linear mechanism.

6.1.5 Time resolved reflectivity change measurements

As discussed above, the rise times of non-linearities due to field screening will be slow compared to those due to EAB. This difference can be directly observed in time resolved measurements, provided that a sufficiently short time step is used.

A further difference between the behaviours of the two mechanisms should be apparent in time resolved measurements. Recovery following EAB is due to the exponential decay of the photocarrier population; observed recovery times will hence be independent of the exciting pulse energy used in pump-probe measurements. In the case of field screening non-linearities recovery time is not expected to be independent of pulse energy, as demonstrated and discussed in Section 3.4.1.

6.2 MR1352 p-i-n multiple quantum well device

6.2.1 Device structure

This section presents measurements of a p-i-n diode with the structure of Figure 6.1. The optical window is anti-reflection coated, such that no AFP cavity is formed.

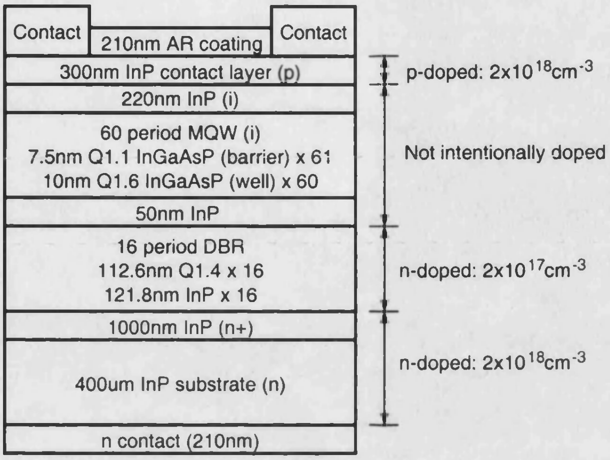

Figure 6.1: Cross section of MR1352 p-i-n MQW device.

6.2.2 Small signal responsivity and reflectivity

Figure 6.2 shows small signal reflectivity and responsivity spectra measured with a different reverse bias voltages and an incident CW power of 7 μW. An excitonic absorption peak at 1540 nm is clearly visible in the responsivity curve with $V_R = 0\,\text{V}$. The peak shifts to 1544 nm and broadens considerably when V_R is increased to 4 V. At higher values of V_R there is no clearly visible excitonic absorption feature.

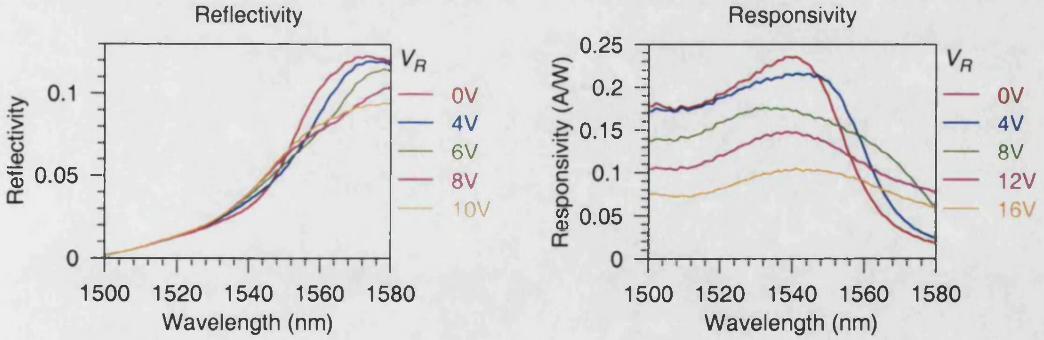

Figure 6.2: MR1352 device: small signal reflectivity and responsivity spectra.

6.2.3 Continuous wave saturation

Figure 6.3 shows the results of CW saturation measurements made at 1530 nm, 1540 nm and 1545 nm using the configuration of Section 4.4.1. These wavelengths were chosen to bracket the wavelength of peak excitonic absorption in the absence of reverse bias, 1540 nm. Table 6.1 shows the contrast ratio (R) and saturation power (P_S), as determined by fitting Equation A.22.

Curve fitting was not performed for the results with $V_R = 8\,\mathrm{V}$ since negligible reflectivity change was observed.

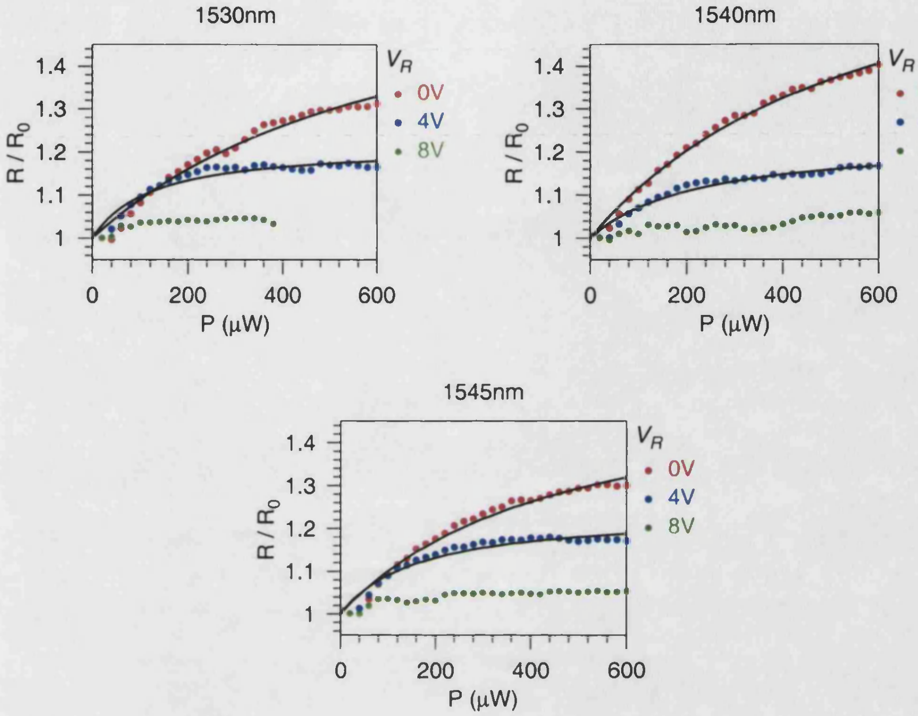

Figure 6.3: MR1352 device: CW saturation characteristics. The lines are fitted curves.

Wavelength (nm)	V_r (V)	R	P_s (μW)
1530	0	1.69	1010
1530	4	1.21	223
1540	0	1.80	878
1540	4	1.23	402
1545	0	1.56	738
1545	4	1.24	296

Table 6.1: MR1352 device: parameters for CW saturation obtained by curve fitting to measured results.

6.2.4 Time resolved reflectivity change

Figure 6.4 shows time resolved measurements of reflectivity change made at 1528.1 nm, 1539.6 nm and 1543.7 nm. As in the case of the CW saturation measurements, the wavelengths were chosen to bracket the $V_R = 0\,\mathrm{V}$ exciton wavelength. The measurements were made using the configuration of Section 4.5.2, with pump and probe pulse energies of 2.5 pJ and 50 fJ respectively.

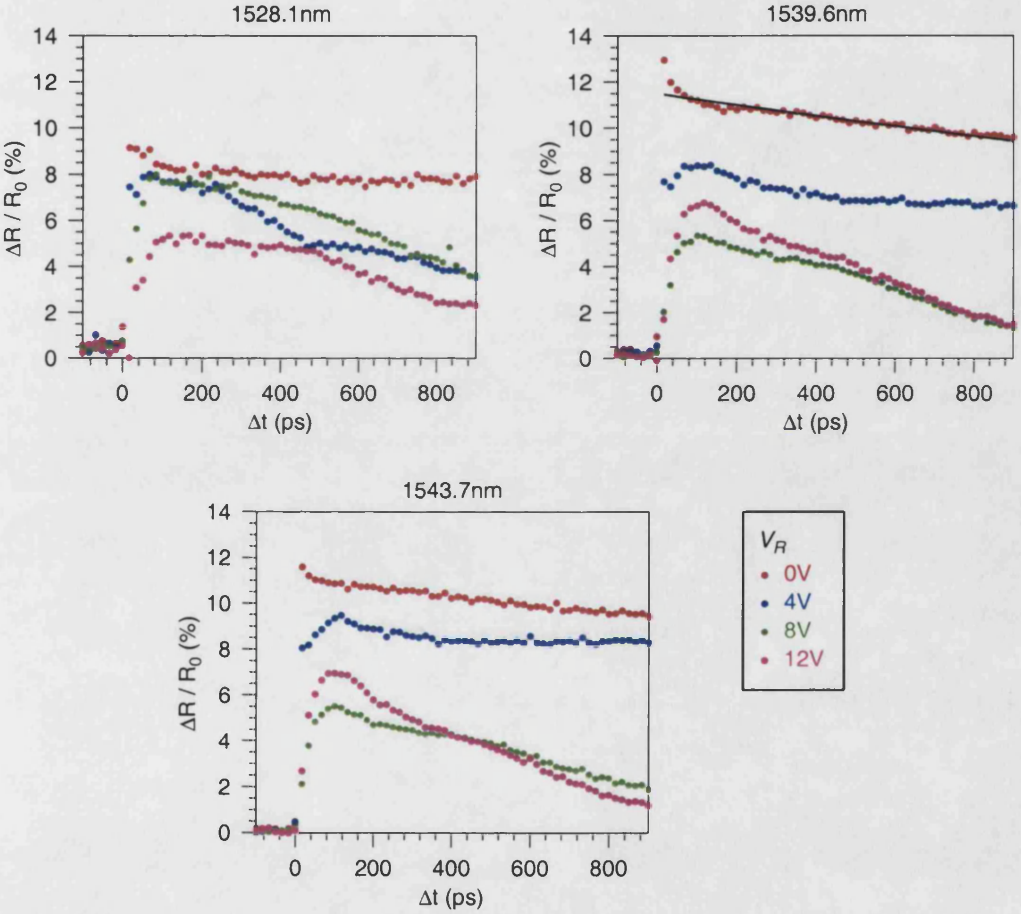

Figure 6.4: MR1352 device: time resolved saturation with low reverse bias voltages.

Fast recovery was observed when the device was reverse biased with $V_R = 20\,\text{V}$ (corresponding to a field of 156 kV/cm in the intrinsic region.) Measurements made at 1565 nm with $V_R = 20\,\text{V}$ are shown in Figure 6.5. Exponential decay curves of the form

$$\frac{\Delta R(\Delta t)}{R_0} = \frac{\Delta R(0)}{R_0}\exp(-\Delta t/\tau), \tag{6.1}$$

where $\Delta R(\Delta t)$ = the transmission change measured by the probe pulse when it is delayed by Δt relative to the pump pulse, R_0 = the small signal transmission and τ = the exponential decay time constant, were fitted to the measured data. The parameters obtained from the curve fitting are listed in Table 6.2.

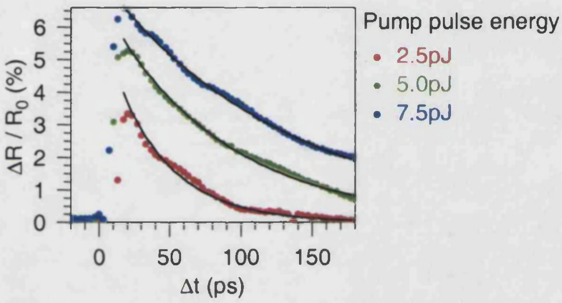

Figure 6.5: MR1352 device: time resolved saturation at 1565 nm with 20 V reverse bias and a range of pump pulse energies. The lines are exponential decay curves fitted to the measured characteristics.

Pump energy (pJ)	$\Delta R(0)/R_0$ (%)	τ (ps)
2.5	6.13	39.3
5.0	6.88	84.6
7.5	7.57	130.4

Table 6.2: MR1352 device: parameters for time resolved saturation measurements at 1565 nm with 20 V reverse bias, found by fitting exponential decay curves to measured data.

6.2.5 Interpretation of results

From the small signal spectra of Section 6.2.2, the unbiased device has an excitonic absorption peak at 1540 nm. This is broadened and red-shifted when the device is reverse biased. For reverse biases of 8 V and higher the broadening is such that no excitonic absorption peak is discernible.

CW saturation measurements (Section 6.2.3) are consistent with peak excitonic absorption occurring at 1540 nm in the absence of reverse bias. The largest reflectivity changes are observed at this wavelength. Application of 4 V reverse bias results in a reduction of the observed non-linear change. Little wavelength dependence is evident in the magnitude of the non-linear change, suggesting that behaviour is dominated by QCSE broadening rather than QCSE red-shifting. No linearity is observed when the reverse bias is increased to 8 V. This could be attributed to a reduction of the free carrier lifetime in the MQW due to carrier sweep-out, or to a reduction of the probability of excitonic absorption which occurs in wells when tilting of the band structure reduces carrier confinement.

Inspection of the $V_R = 4\,\text{V}$ characteristics reveals that they flatten off at lower powers than the corresponding $V_R = 0\,\text{V}$ characteristics, suggesting a reduction of P_s. This is confirmed by the P_s values of Table 6.1. If the dominant consequence of application of the reverse bias voltage was a reduction of the in-well carrier lifetime due to sweep-out an increase in P_s would be expected. The results are thus consistent with behaviour being dominated by QCSE absorption changes rather than carrier sweep-out.

The behaviour observed in the low reverse bias time resolved measurements of Section 6.2.4 is attributable to a combination of EAB and field screening. When no reverse bias is applied to the device, the observed reflectivity change must be a consequence of EAB. Whilst the reduction of recovery time observed as V_R increases is consistent with EAB the long rise times of the results with $V_R = 8\,\text{V}$ and $V_R = 12\,\text{V}$ are not. These rise times, which are as long as 50 ps, can be more clearly seen in the enlargement of Figure 6.6.

According to the argument of Section 6.1.2, field screening can be expected to result in a transient reduction of the MQW region absorption, and hence reflectivity, at the wavelengths at which these measurements were made. The small signal spectra measurements of Section 6.2.2 which show reflectivity to increase, and responsivity to decrease, as increasing reverse bias voltages are applied to the device are consistent with this argument. Field screening can be equated to a reduction of reverse bias.

However, no negative going components are evident in the pump-probe traces. This suggests that whilst, under these relatively low reverse bias conditions, field screening makes a significant contribution to the reflectivity change observed in the pump-probe measurements, it does not dominate the EAB.

The non-instantaneous nature of the transmission change rises, and the dependence of recovery time on exciting pulse energy apparent in the time resolved measurements with $V_R = 20\,\text{V}$, suggest that the device non-linearity is due to field screening. The positive sign of the observed reflectivity change is that expected for non-linearity due to field screening at wavelengths significantly longer than the $V_R = 0\,\text{V}$ exciton resonance.

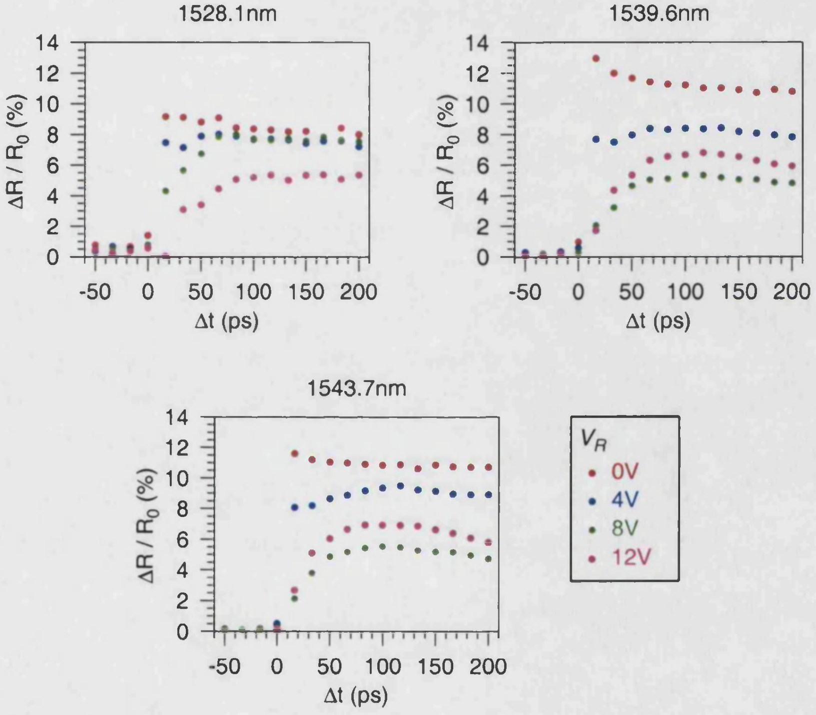

Figure 6.6: MR1352 device: time resolved saturation with low reverse bias voltages. The region where $\Delta t < 200\,\text{ps}$ is enlarged to allow inspection of the rise of the time resolved characteristics

6.3 MR1438 p-i-n multiple quantum well device

6.3.1 Device structure

This section presents measurements of a p-i-n diode with the structure of Figure 6.7. The optical window is not anti-reflection coated. An AFP cavity is therefore formed between the distributed Bragg reflector (DBR) and the front air-semiconductor interface. The MQW design is such that the exciton absorption peak in the unbiased device should be at a wavelength of 1540 nm.

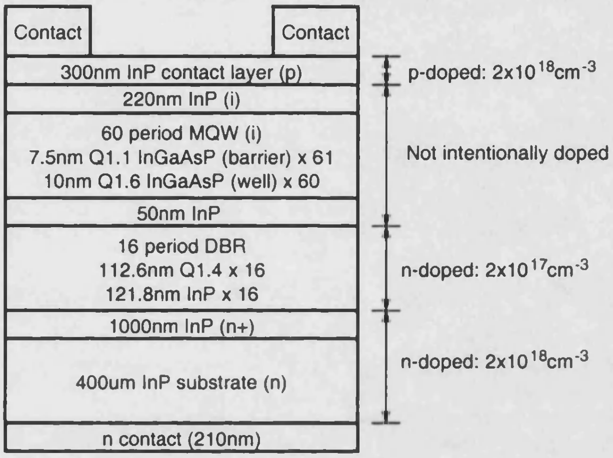

Figure 6.7: Cross section of MR1438 p-i-n MQW device.

6.3.2 Small signal reflectivity

Figure 6.8 shows small signal reflectivity spectra measured with reverse biases from 0 V to 20 V. AFP anti-resonances are evident at wavelengths of approximately 1510 nm and 1580 nm. Since the MQW is incorporated in an AFP cavity it is not possible determine the wavelength of the $V_R = 0\,\mathrm{V}$ exciton feature.

6.3.3 Time resolved reflectivity change

Time resolved measurements of reflectivity were made at wavelengths of 1561 nm and 1566 nm where, from inspection of the spectra of Figure 6.8, there is a strong dependence of reflectivity on reverse bias. Figure 6.9 illustrates these dependencies. Ideally measurements would have been made at longer wavelengths; 1566 nm was the longest to which the pulse source used could be tuned.

Measurements were made with V_R in the range 16 V to 20 V, where fast optical non-linearities could be observed. Results are shown in Figures 6.10 and 6.11. Exponential characteristics fitted

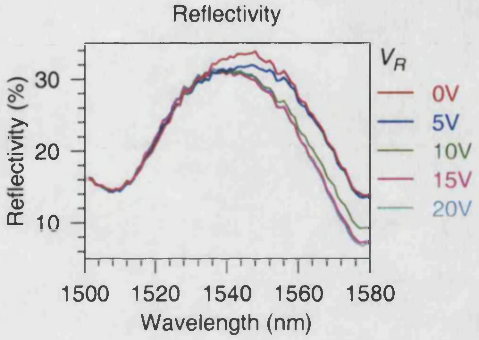

Figure 6.8: MR1438 device: small signal reflectivity spectra.

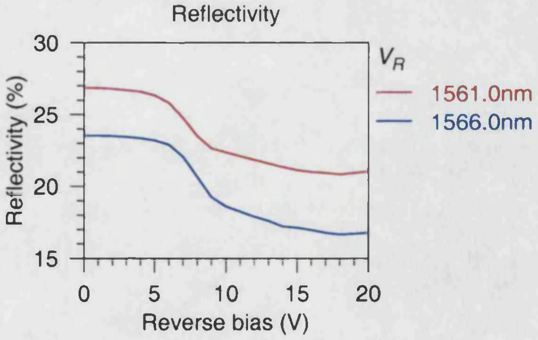

Figure 6.9: MR1438 device: small signal reflectivity as a function of reverse bias.

to the decay of the measured data are also plotted. The parameters of these characteristics are listed in Table 6.3, and summarised by the plots of Figures 6.12 and 6.13. The validity of the low recovery times obtained from curve fits for the 1566 nm results with 2.5 pJ pump pulse energies is questionable, given the high levels of noise on the measured data.

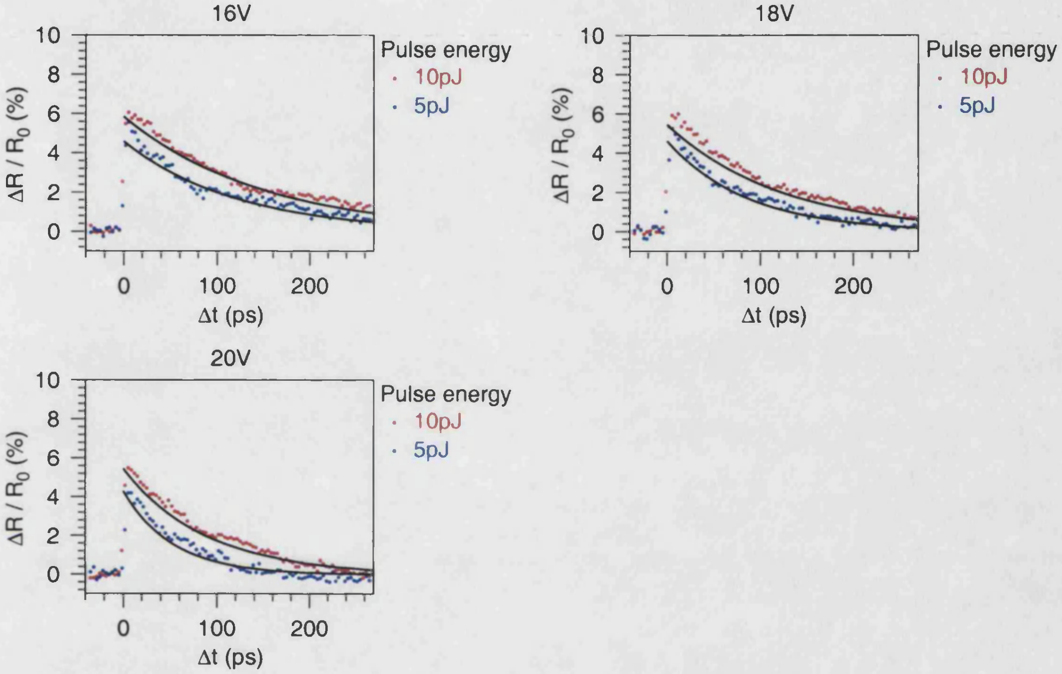

Figure 6.10: MR1438 device: time resolved reflectivity change at 1561 nm. The lines are exponential decay curves fitted to the measured data.

6.3.4 Interpretation of results

Assuming the exciton absorption peak of the MQW to be in the region of the design wavelength, 1540 nm, the time resolved measurements of Section 6.3.3 were made at significantly longer wavelengths. Figure 6.9, which shows reflectivity to decrease as higher reverse bias voltages are applied to the device, is consistent with this assumption.

The recovery time plots of Figure 6.12 show systematic reductions of recovery time as the pulse energy reduces, and as the reverse bias voltage increases. Whilst the reverse bias dependence is compatible with the non-linearity being due to EAB, the pump pulse energy dependence is not. The reflectivity change must therefore be attributed to field screening.

Similarly to the high reverse bias time resolved reflectivity measurements of the MR1352 device discussed in Section 6.2.5, the positive sign of the observed reflectivity change is consistent with field screening effects at the measurement wavelength, which was long compared to the zero

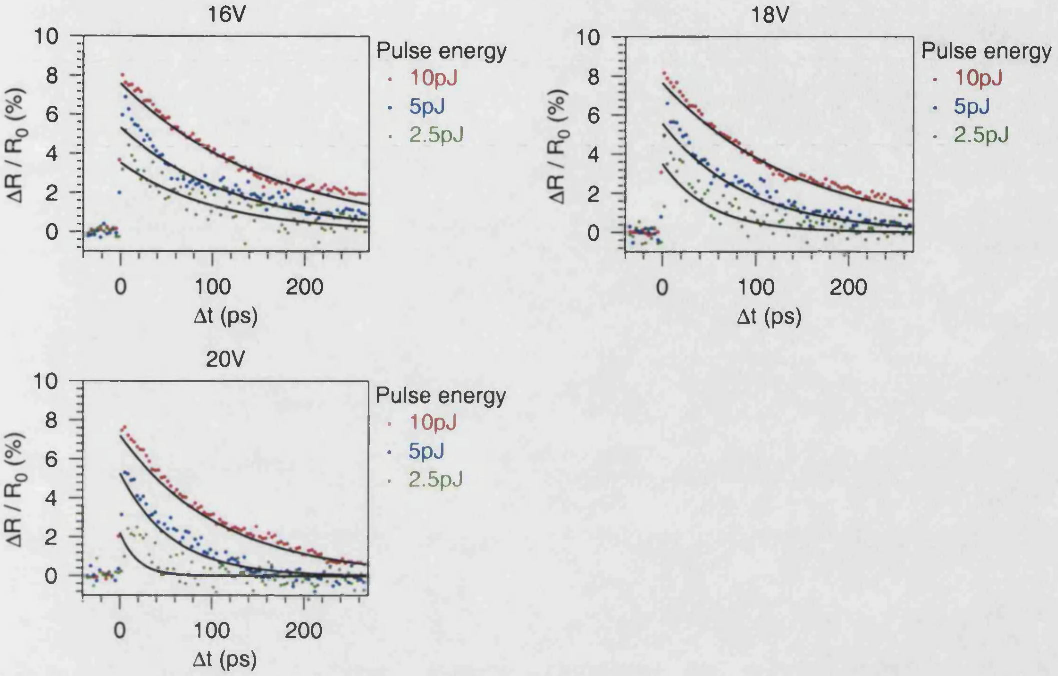

Figure 6.11: MR1438 device: time resolved reflectivity change at 1566 nm. The lines are exponential decay curves fitted to the measured data.

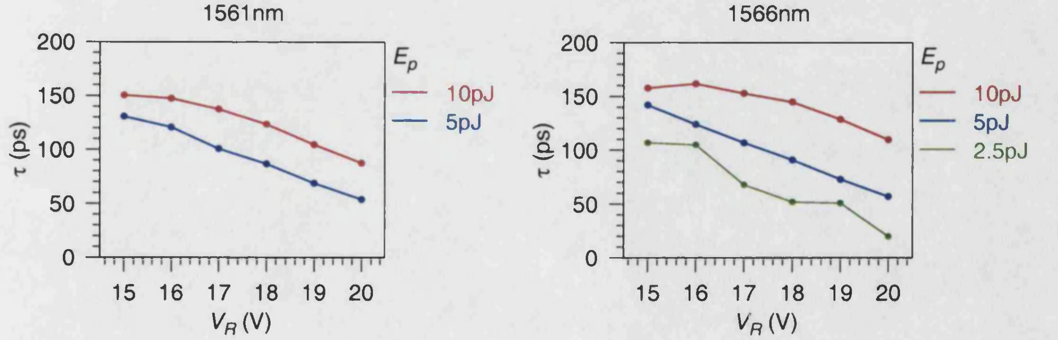

Figure 6.12: MR1438 device: recovery time obtained by fitting exponential decay curves to the results of time resolved reflectivity change measurements.

Wavelength (nm)	Pump pulse energy (pJ)	V_R (V)	$\Delta R(0)/R_0$ (%)	τ (ps)
1561	10	15	5.83	150
1561	10	16	5.86	147
1561	10	17	5.81	137
1561	10	18	5.45	123
1561	10	19	5.67	104
1561	10	20	5.45	87
1561	5	15	4.67	130
1561	5	16	4.60	120
1561	5	17	4.67	100
1561	5	18	4.61	86
1561	5	19	4.45	68
1561	5	20	4.30	53
1566	10	15	7.55	157
1566	10	16	7.60	161
1566	10	17	7.73	152
1566	10	18	7.65	144
1566	10	19	7.53	128
1566	10	20	7.21	109
1566	5	15	5.28	141
1566	5	16	5.32	123
1566	5	17	5.56	106
1566	5	18	5.55	90
1566	5	19	5.36	72
1566	5	20	5.27	56
1566	2.5	15	3.88	106
1566	2.5	16	3.53	104
1566	2.5	17	3.42	67
1566	2.5	18	3.50	51
1566	2.5	19	2.62	50
1566	2.5	20	2.22	19

Table 6.3: MR1438 device: parameters obtained by fitting exponential decay curves to the results of time resolved reflectivity change measurements.

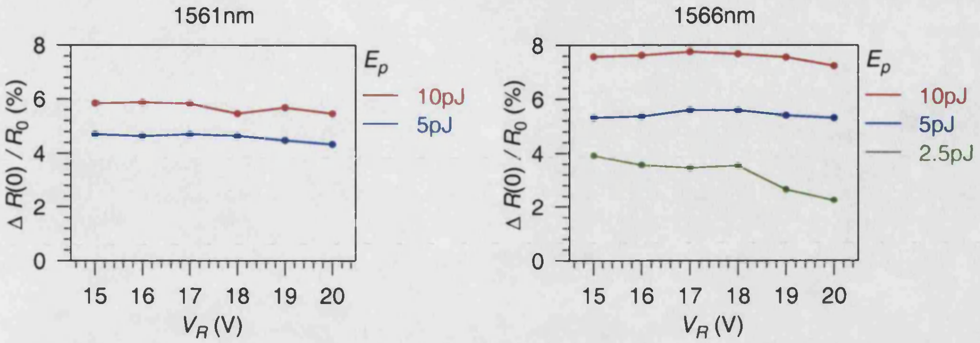

Figure 6.13: MR1438 device: maximum reflectivity change obtained by fitting exponential decay curves to the results of time resolved reflectivity change measurements.

bias excitonic absorption peak at 1540 nm.

Due to the comparatively large interval between the data points in these measurements (3.3 ps) it is not possible to comment on the rise times of the reflectivity changes.

6.4 MR1419 p-i-n multiple quantum well device

6.4.1 Device structure

This section presents measurements of a p-i-n diode with the structure of Figure 6.14. The optical window is not anti-reflection coated, such that an AFP cavity is formed between the DBR and the front air-semiconductor interface. The design wavelength for the excitonic absorption peak is again 1540 nm.

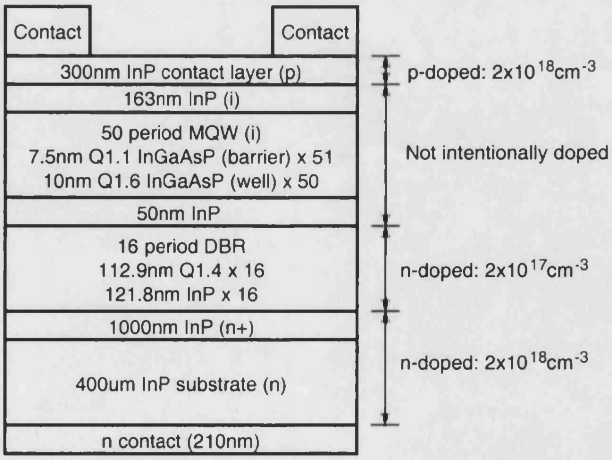

Figure 6.14: Cross section of MR1419 p-i-n MQW device.

6.4.2 Small signal responsivity and reflectivity

Photocurrent and responsivity spectra measured using the configuration of Section 4.3 with an incident CW power of 4 μW, are shown in Figure 6.15. A strong AFP resonance at ≈ 1518 nm precludes determination of the wavelength of peak excitonic absorption from the measured data.

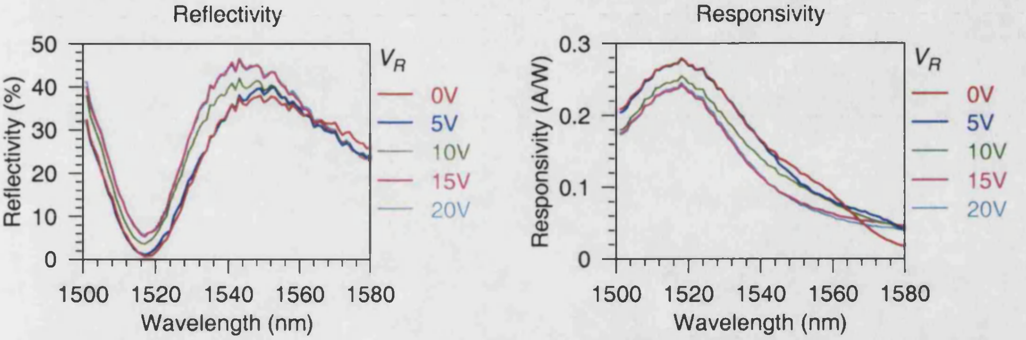

Figure 6.15: MR1419 device: small signal CW reflectivity and responsivity spectra.

6.4.3 Continuous wave saturation

Figure 6.16 shows CW saturation characteristics measured at four wavelengths close to the AFP resonance.

The non-linear change is largest when the measurement wavelength coincides with the reflectance minimum due to the AFP cavity (1518 nm from the spectra of Figure 6.15.) Similarly to the MR1352 device, the non-linearity reduces as the reverse bias applied to the device is increased.

6.4.4 Pulse saturation

Figure 6.17 shows the transmission of the device measured with 2 ps pulses using the configuration of Section 4.4.2. Measurements were made at 1528 nm, the shortest wavelength to which the pulse source used could be tuned. Ideally, measurements would have been made at the AFP resonance.

6.4.5 Time resolved reflectivity change

Time resolved measurements were made at a wavelength of 1528 nm. As with the pulse saturation measurements, the choice of wavelength was dictated by the tuning range of the pulse source. Figure 6.18 shows results with reverse biases from 0 V to 20 V. The lines on the plots show the results of fitting Equation 6.1 to the measured data. Parameters obtained from the curve fitting are summarised in Table 6.4. Measurements at high reverse biases, 15 V, 17.5 V and 20 V were

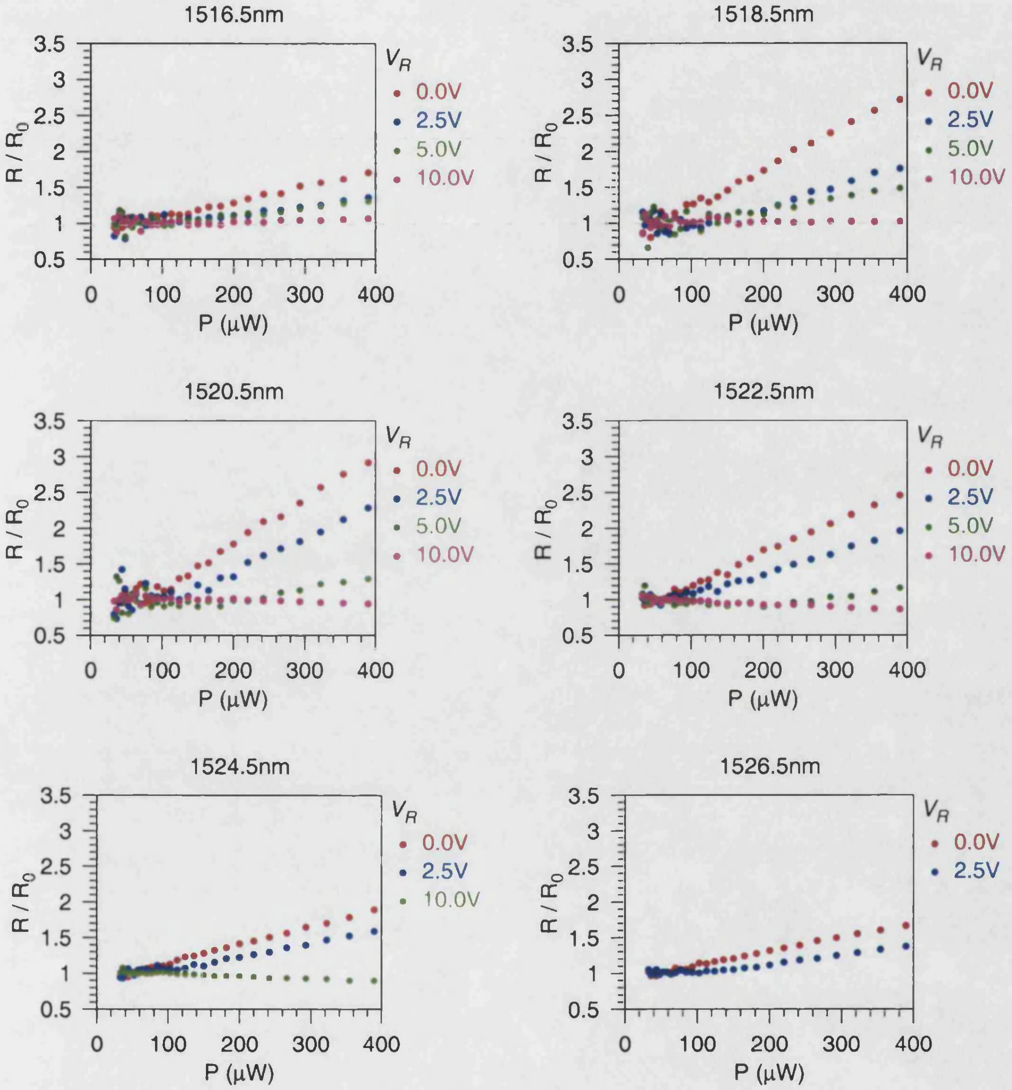

Figure 6.16: MR1419 device: CW saturation characteristics.

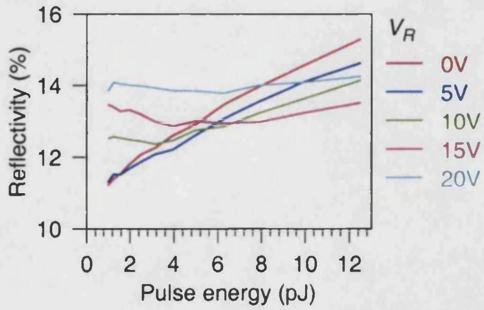

Figure 6.17: MR1419 device: saturation characteristic measured with 2 ps pulses.

made on a fast timescale to enable the rise of the transmission change to be observed. Results are presented in Figure 6.19.

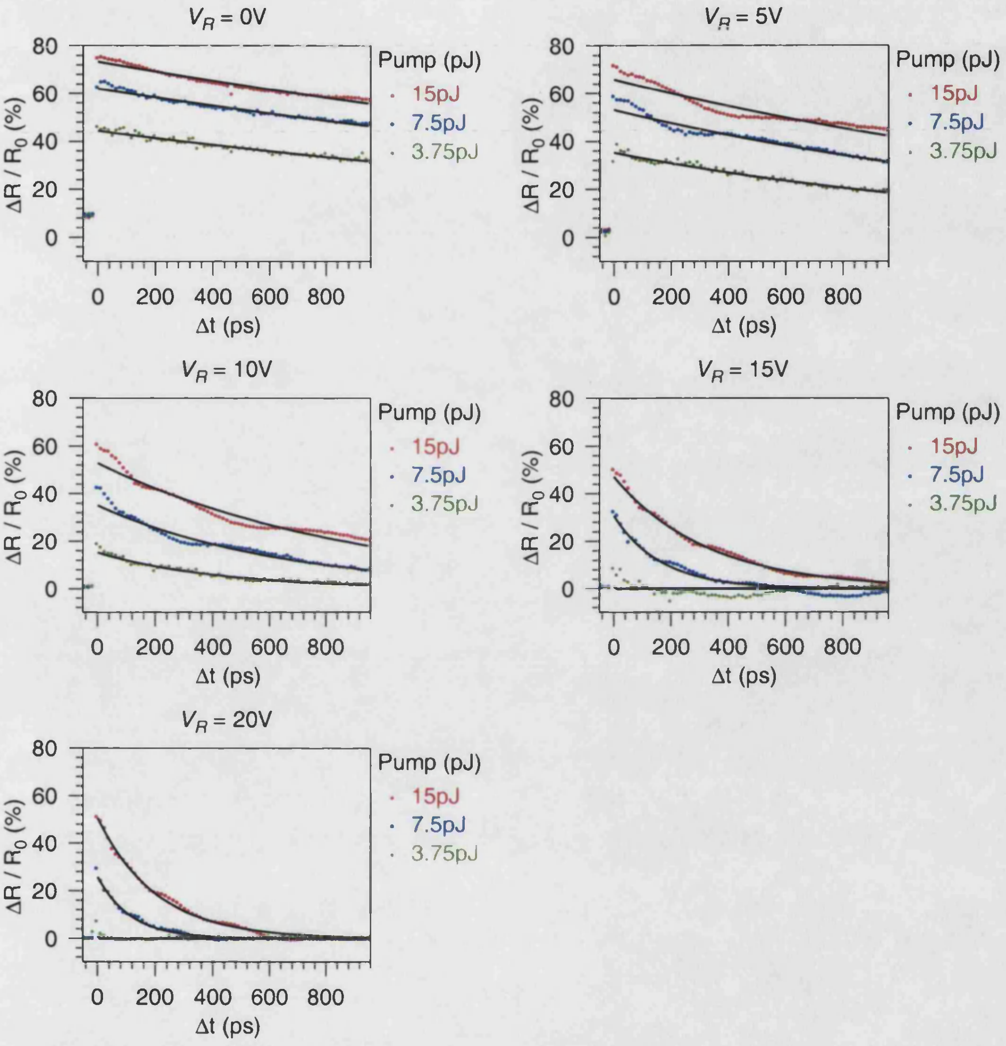

Figure 6.18: MR1419 device: time resolved saturation. This lines are exponential decay curves fitted to the measured data.

6.4.6 Wavelength conversion

Figure 6.20 shows the results of demonstrations of wavelength conversion in the MR1419 device carried out using the experimental system of Section 4.6.1. The measurements were made with 13 pJ pulses and a 2.5 mW CW signal incident on the device. A reverse bias voltage of 20 V was used.

V_r (V)	Pump energy (pJ)	a (%)	τ (ps)
0.0	3.75	44	2751
0.0	7.5	62	3129
0.0	15.0	73	3360
5.0	3.75	35	1465
5.0	7.5	54	1690
5.0	15.0	67	2016
10.0	3.75	16	393
10.0	7.5	37	585
10.0	15.0	55	827
15.0	7.5	32	163
15.0	15.0	49	316
20.0	7.5	27	111
20.0	15.0	51	203

Table 6.4: MR1419 device: parameters obtained by fitting exponential decay curves fitted to the measured time resolved saturation data.

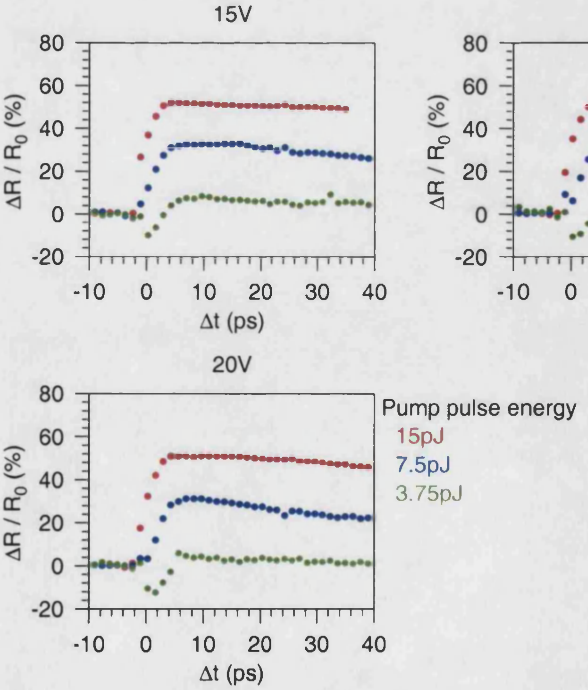

Figure 6.19: MR1419 device: time resolved measurements on a fast timescale.

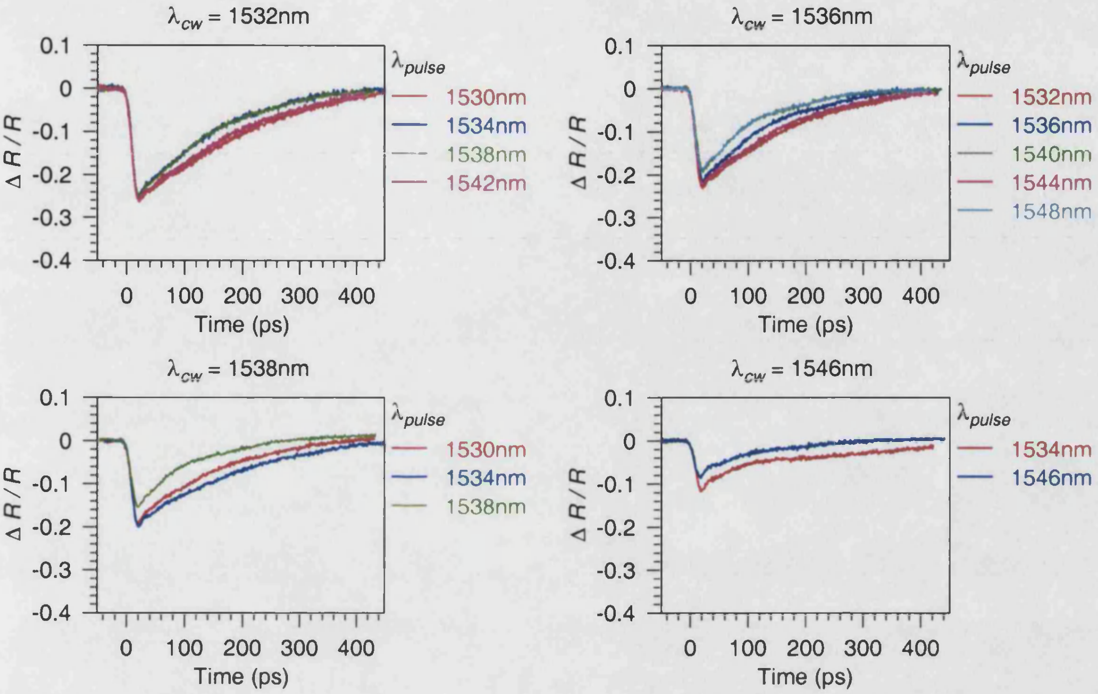

Figure 6.20: MR1419: Results of wavelength conversion experiments

6.4.7 Interpretation of results

Whilst the incorporation of the MQW in an AFP cavity prevented determination of the wavelength of peak excitonic absorption it can be seen from the $V_R = 0\,\mathrm{V}$ results of Sections 6.4.3 to 6.4.5 that EAB occurs in the wavelength range of the measurements (1516.5 nm to 1526.5 nm).

Maximum non-linearity is observed in CW saturation measurements at 1518 nm which, from the spectra of Section 6.15 is the AFP resonance. The systematic reduction of the magnitude of the observed non-linear change is, as in the case of the device investigated in Section 6.2.5, attributable to QCSE broadening and red-shifting of the excitonic component of the absorption spectrum.

The pulse saturation measurements of Figure 6.4.4 also show a decrease in non-linearity (indicated by a decrease in the gradient of the plotted characteristic) as the applied reverse bias increases. The reduction in non-linearity is attributable to QCSE broadening and red-shifting of the excitonic component of the absorption spectrum.

Whilst significant non-linearities were observed in the pump-probe and pulse saturation measurements with $V_R = 20\,\mathrm{V}$, the non-linearity in pulse saturation measurements under similar conditions was small. This is, as discussed in Section 6.1.4, indicative of optical non-linearity which is dominated by field screening. The strong dependence of recovery time on exciting pulse energy in the $V_R = 15\,\text{V}$ and $V_R = 20\,\text{V}$ pump-probe results (Table 6.4) is again consistent with optical non-linearity dominated by field screening.

The pump-probe measurements of Figures 6.18 and 6.19 present an apparent anomaly. At the measurement wavelength, 1528 nm, which is shorter than the design band-edge wavelength for the structure, under high reverse conditions where field screening is dominant, a negative going response should be observed in pump-probe measurements. This expectation is explained in Section 6.1.2 and supported by the measured small signal reflectivity spectra of Figure 6.15. These show the device reflectivity at 1528 nm to decrease as the reverse bias voltage decreases, a relationship which is more clearly visible in Figure 6.21.

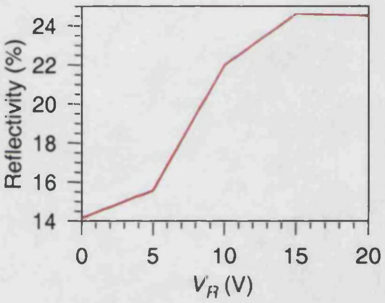

Figure 6.21: MR1419 device: reflectivity at 1528 nm.

A possible explanation for this anomaly is that when the electric field in the intrinsic region is screened, carriers are swept out of the QWs less rapidly. As the carriers spend more time in the QWs increased EAB occurs. If this argument is to explain the above results, transiently enabled EAB, rather than QCSE absorption changes, must dominate the observed optical non-linearity.

Small initial negative going components visible in the 3.75 pJ pump-probe results of Figure 6.19, are consistent with the above description of device operation. As positive and negative photocarriers start to drift apart following incidence of the exciting pulse there is initially a small reduction of the electric field in the intrinsic region which results in a QCSE absorption change but is not sufficient to restore excitonic absorption at the measurement wavelength. Negative going features also appear in the tails of the $V_R = 15\,\text{V}$ measurements of Figure 6.18. These tails again correspond to a regime in which there will be only a small reduction of the intrinsic region electric field due to field screening.

This effect, restoration of EAB at the measurement wavelength, cannot be expected in the high reverse bias time resolved measurements of Sections 6.2.4 and 6.3.3, which were performed at wavelengths around 1560 nm, which were longer than the device bandgap wavelengths.

The reflectivity changes observed in the wavelength conversion results of Section 6.4.6 were, unlike those in the $V_R = 20\,\text{V}$ pump-probe measurements, negative. This is despite similar measurement wavelengths, exciting pulse energies, and reverse bias voltage being used the two experiments. The results show that the input pulse wavelength, an additional variable in the wavelength conversion experiments, to have little impact on the measured responses.

The only significant difference between the two experiments is the presence of the 2.5 mW CW input used for wavelength conversion. This will result in changes to the quiescent electric field distribution (that is, the distribution in the absence of high energy pump pulses) in the intrinsic region. However, from the calculations of Section 3.7.3, the changes expected are not substantial. There is no reason to expect that they would lead to the observed qualitative changes of the device behaviour. A more reasonable explanation for the different behaviours is that the constant photocarrier population excited by the CW input in the wavelength conversion experiment is sufficiently large to bleach excitonic absorption in the MQW, even when the electric field is screened such that excitonic absorption would otherwise occur.

6.5 Conclusions

The experimental results described in the preceding three sections are consistent with the theoretical descriptions of the field screening and EAB mechanisms developed in Chapter 3. When the devices were unbiased, or only low reverse bias voltages were applied, behaviour was dominated by EAB. Application of higher reverse bias voltages resulted in behaviour which was dominated by field screening. This is in accordance with the assertion of Section 3.3.2, that application of a large reverse bias voltage to enable fast sweep-out of carriers from the QWs, and hence fast recovery from EAB, is not an appropriate method to achieve fast non-linearities in these devices. The EAB contribution to the non-linearity is reduced when high fields are applied, since carrier confinement in the QWs is weakened. When the reverse bias is increased so that carriers can escape rapidly from the QWs field screening becomes dominant. A transition between EAB and field screening behaviour is evident for each of the devices investigated.

The transition is most clearly demonstrated by referring to the pulse saturation and time resolved measurements of Section 6.4. Whilst the reflectivity change observed in the pulse saturation measurements becomes negligible at high reverse biases, substantial responses are still observed in the pump-probe measurements. This can be readily explained since, in the case of field screening, the reflectivity change is delayed relative to the exciting pulse. The delay, which is due to the time taken for carriers to drift across the intrinsic region of the device, is long compared to the short 2 ps pulses used in these experiments. The reflectivity change can however be observed using pump-probe measurements.

Behaviour is complicated by the effect observed in the pump-probe and wavelength conversion measurements of Section 6.4, whereby the sign of the transmission change in the pump-probe measurements is the opposite of that expected. An explanation for this, based on the fact that, under strong field screening conditions, EAB can occur in a heavily reverse biased device, is given in Section 6.4.7.

The recovery times observed in pump-probe measurements, which were as short as 39 ps (Table 6.2) suggest that field screening devices are potentially fast enough for gigabit per second applications. However, these results also confirm the problem revealed by the modelling of Section 3.4.1, that as the pulse energy incident on the device is increased, such that the reflectivity change is maximised, the recovery time is also increased. The finite rise times of the observed reflectivity changes ($\approx$ 6 ps from Figure 6.19) suggest that field screening devices would be more suitable for wavelength conversion, or other switching, applications, rather than for soliton control.

Whilst further exploration of aspects of the field screening device behaviour, avoiding the focus on achieving fast and high contrast optical non-linearities which was essential for the purposes of this thesis, would be of interest, it was not pursued. Ion-implanted devices, investigations of which are discussed in Chapter 8, were determined to be most suitable for the systems applications under consideration.

Such further investigation would, ideally, employ anti-reflection coated devices to avoid the complexity added by the AFP cavity resonance, although the smaller observed reflectivity changes mean that investigation of such non-resonant devices is generally more difficult, and that they are not well suited for system applications. Further investigations would be most effective if supported by an improved computer model of field screening behaviour, based on that of Appendix C, but considering accurately the velocity of photocarriers, and their QW escape times, under strong field screening conditions.

Chapter summary

Experimental investigations of p-i-n MQW devices, in which fast non-linear operation can be achieved through exploitation of field screening effects have been described. These experiments used experimental techniques described in Chapter 4. After an initial analysis of the expected device behaviours, characterisation results for three devices were presented and discussed.

These experimental results have demonstrated the potential of the field screening mechanism as a basis for ultra-fast devices, with recovery times as fast as 39 ps being observed. They confirmed the slow rise times for field screening devices predicted in Section 3.4.1, rise times $\approx$ 6 ps were observed. Wavelength conversion has been demonstrated, with a recovery time of 75 ps

Two distinct regimes in which fast field screening operation can occur have been identified. At wavelengths longer than the band edge, field screening simply results in a change of device reflectivity due to the QCSE absorption change. Results observed at shorter wavelengths were not consistent with such device operation. They could be explained by considering the transient enabling of excitonic absorption which occurs when the electric field in the MQW region is screened.

The experimental work forms the basis of a discussion of the practicality of developing device exploiting field screening for 10 Gb/s and 40 Gb/s systems applications in Chapter 9.

Chapter 7

Investigations of non-linear polarisation rotation

This chapter describes investigations of all-optical switching using non-linear polarisation rotation (NPR) in a transmissive and reflective multiple quantum well (MQW) structures. NPR switching is observed in one of the four structures studied. The NPR rotation angle is small compared to those observed in similar experiments by other investigators.

This apparent anomaly is discussed, and attributed to the use of picosecond signal pulses in the switching experiment. The practicality of developing NPR switching based devices for systems application in the face of this and other limitations is evaluated.

7.1 Experiments

The experimental configurations of Section 4.5.3 were to used to investigate non-linear polarisation (NPR) effects in four wafers containing multiple quantum well (MQW) layers. The structures of the wafers are shown in Figures 7.1 to 7.4.

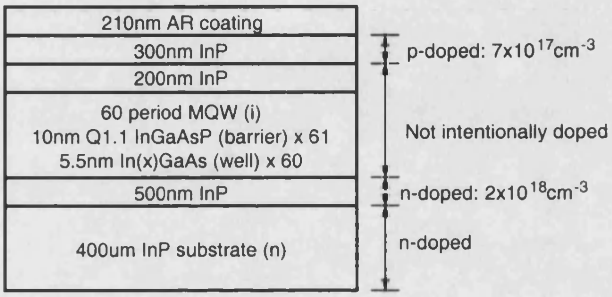

Figure 7.1: Structure of MR611 transmission wafer. One side of the wafer is anti-reflection coated to prevent cavity effects.

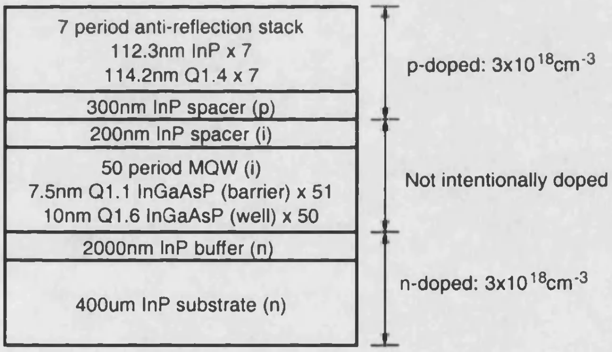

Figure 7.2: Structure of MR850 transmission wafer. The wafer incorporates a top anti-reflection stack.

Whilst excitonic absorption bleaching (EAB) could be observed in all the structures, NPR was only observed in the MR850 transmission structure of Figure 7.2. Results of these successful measurements are described in Section 7.2 below.

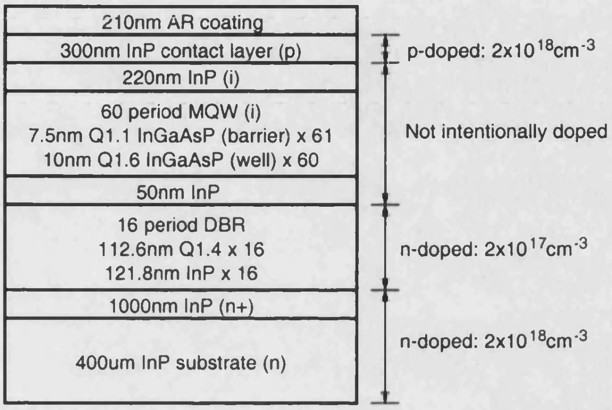

Figure 7.3: Structure of MR1352 reflective wafer. The top of the structure is anti-reflection coated to prevent cavity effects.

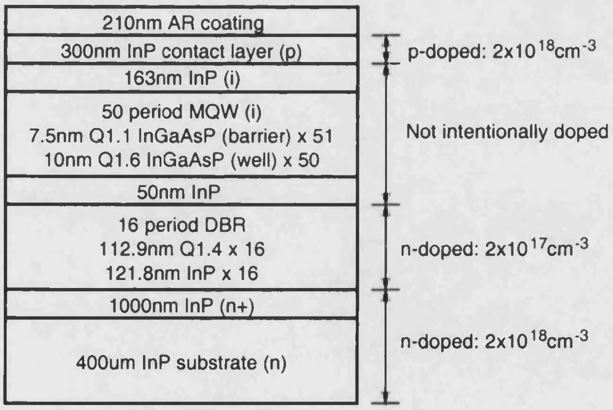

Figure 7.4: Structure of MR1419 reflective wafer. The top of the structure is anti-reflection coated to prevent cavity effects.

7.2 MR850 wafer

7.2.1 Experimental results

The parameters used in the measurements of NPR in the MR850 wafer are summarised in Table 7.1. The measurement wavelength, 1525 nm, was close to the 1528 nm exciton resonance of the MQW region. Results are shown in Figure 7.5. The fast component in the response has a recovery time of 8.6 ps. The non-polarisation rotated component of the probe pulses transmitted by the MQW structure, that is the component passing directly through the output polarising beam splitter (PBS) cube (Figure 4.11), is plotted in Figure 7.6. From exponential curve fitting to this data the free carrier lifetime in the MQW was 2.1 ns.

Parameter	Value
Wavelength	1528 nm
Pump pulse energy	15 pJ
Probe pulse energy	0.75 pJ
Pulse duration	2 ps

Table 7.1: Summary of parameters for NPR switching experiment

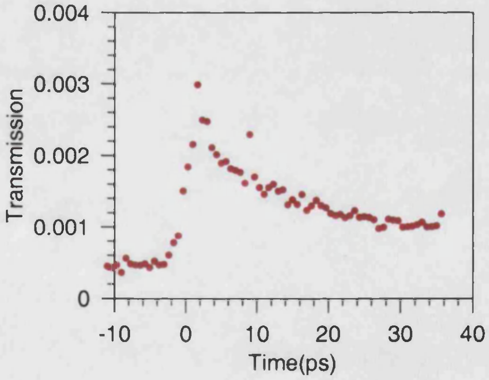

Figure 7.5: MR850 wafer: NPR switching result.

7.2.2 Discussion

Referring to Figure 7.5, the transmission of the combination of MQW and PBS cube in the region where the probe pulse is incident prior to the pump pulse is 4.5×10^{-4}. From Figure 7.6, the transmission in the same region is 0.21. The extinction ratio of the PBS cube can thus be calculated to be 26.7 dB.

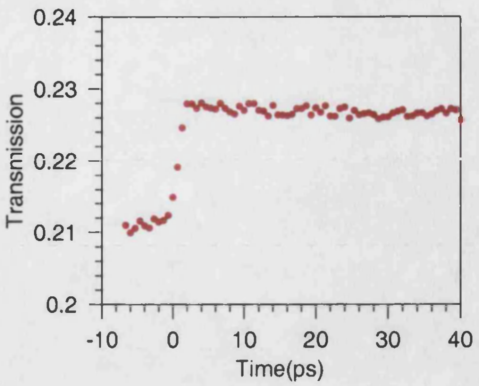

Figure 7.6: MR850 wafer: non-rotated component in pump-probe experiment.

In the following discussion the transmission of the analyser for plane-polarised light is assumed to be

$$T = T_0 + (1 - T_0)sin(\theta), \tag{7.1}$$

where $\theta =$ the of angle plane polarisation relative to the axis of maximum extinction and T_0 is the reciprocal of the extinction ratio (2.1×10^{-3} in the case of 26.7 dB extinction).

From the results of Figure 7.5, the switching contrast ratio is 5.6. If the transient change in the transmission of the combination of MQW and PBS cube is assumed to be due purely to optical anisotropy in the MQW layer, and that anisotropy dominated by circular birefringence, as suggested by previous investigators [1] then according to Equation 7.1 a contrast ratio of 5.6 corresponds to a maximum probe pulse rotation of 0.26°. The above calculation is an over-estimation of the rotation angle, since a small contribution to the transmission change evident in Figure 7.5 in due to the overall increase in MQW transmission.

Hyland et. al. at the University of St. Andrews have reported substantial rotation angles in measurements of similar transmissive InGaAsP/InGaAsP and InGaAs/InGaAsP MQW structures, which were also grown at the University of Sheffield. Their experimental configuration differed from that used for the work described in this thesis in that it was implemented using free space optical components and a mode-locked Nd:YAG laser. Results published by the St. Andrews group are compared with those of Section 7.2.1 in Table Figure 7.2.

Considerably larger polarisation rotation angles were observed in the St. Andrews experiments. The principle difference between the St. Andrews and UCL experiments was in the energy density and duration of the pump pulses. The considerably greater pump pulse energy density used in the UCL measurements was found to be a requirement for the observation of NPR.

The fibre mode-locked laser (MLL) used in the UCL experiments, which is described in Appendix E, produced 2 ps pulses whilst the Nd:YAG laser used at St. Andrew produced 150 ps

Institution	Citation	Structure	Pump energy density	Pulse length	Rotation angle	Contrast ratio
UCL	This thesis	60 period Q1.1/Q1.6 InGaAsP MQW	150fJ/μm^2	2ps	< 0.26°	5.6
St. Andrews	[2]	60 period Q1.1/Q1.6 InGaAsP MQW	21.6fJ/μm^2	150fs	45°	1.09
St. Andrews	[1]	60 period InGaAs/Q1.6 InGaAsP MQW	9.0fJ/μm^2	150fs	45°	1.15

Table 7.2: Comparison of NPR switching results obtained at UCL and St. Andrews.

pulses. This is the only significant difference between the two experiments which can be identified. It is therefore reasonable to attribute the small rotation angles in the UCL experiments to the use of long exciting pulses.

It should be noted that the low contrast ratio observed in the St. Andrews switching experiments are attributed to poor extinction in the PBS cube used as the output analyser. The extinction ratio of this component is stated to be 'a few percent.' [1]

7.3 Conclusions

NPR was detectable in only one of the four wafers investigated. The rotation angle in this wafer was calculated to be 0.26°, which was significantly smaller than vales determined in similar experiments at St. Andrews. The small rotation angle was attributed to the use of 2ps pulses in the NPR switching experiments, compared to the sub-picosecond pulses used by other researchers.

This requirement for extremely short exciting pulses means than NPR is not a suitable mechanism for all-optical switching applications, such as wavelength conversion, in 10Gb/s and 40Gb/s communications systems. The signal pulse length in such systems is typically 5ps or greater.

Polarisation independence is desirable in systems applications since the state of polarisation of the signal after it has propagated through many kilometres of optical fibre is neither well known or constant. The dependence of NPR switching on the state of polarisation of the input light is undesirable for systems applications.

The small NPR rotation angle observed in the MR850 wafer, and the absence of observable NPR in the other three wafer surveyed, suggests that spin-selective effects, and hence polarisation dependent effects will not play a significant role in the operation of devices relying on excitonic absorption bleaching, such as those which are investigated in Chapter 8.

Chapter summary

NPR switching was demonstrated in a transmissive InGaAsP MQW structure. However, rotation of the probe pulse due to NPR was limited to 0.26°. Investigations of other three others structures did not reveal NPR. These results were attributed to the use of 2 ps exciting pulses; other investigations of NPR in the literature have used femtosecond pulses.

Apart from this requirements for sub-picosecond input pulses, NPR based switching is dependent on the input pulse polarisation. Practical deployment in systems applications would require some polarisation diversity scheme to overcome this dependence. Additionally some strategy, such as ion implantation, would be needed to reduce the free carrier lifetime to enable high repetition operation, as discussed in Section 3.5.3.

Investigations of NPR switching were not followed further; later work focused on devices which exploited EAB in ion-implanted MQW structures.

References

[1] J. Hyland, G. Kennedy, A. Miller, and C. Button, "Spin relaxation and all optical polarisation switching at 1.52 micrometres in InGaAs(P)/InGaAsP multiple quantum wells," *Semiconductor Science and Technology*, vol. 14, pp. 215–221, March 1999.

[2] J. Hyland, G. Kennedy, A. Miller, and C. Button, "Picosecond all-optical polarization switching in InGaAsP MQWs at 1.52 μm," *IEEE Photonics Technology Letters*, vol. 10, pp. 1419–1421, October 1998.

Chapter 8

Investigations of excitonic absorption bleaching in ion-implanted devices

This chapter presents the results of a study of devices in which multiple quantum well (MQW) structures are incorporated in resonant asymmetric Fabry-Perot (AFP) cavities to realise high-contrast optical switching based on excitonic absorption bleaching (EAB). Ion implantation is used to accelerate EAB recovery, such that devices can be made sufficiently fast for 10 Gb/s and 40 Gb/s applications.

An initial implantation study, in which samples of a transmission structure incorporating an InGaAsP MQW are implanted with nitrogen ions is described in Section 8.2. The resulting devices are characterised to determine the influence of the ion dose on the recovery time.

Section 8.3 describes a similar study of AFP cavity devices. In Sections 8.4 and 8.5 a high speed reflective device is used to demonstrate wavelength conversion of a 10 GHz pulse stream, and of a 40 Gb/s pseudo-random bit stream.

8.1 Introduction

The InGaAsP devices described in this chapter were implanted at the University of Surrey Ion Beam Centre. As discussed in Section 5.4, constraints imposed by this facility led to the choice of implantation with relatively light 4 MeV nitrogen ions. This implantation energy is such that, in the structures investigated, the nitrogen ions propagate through the MQW layer, creating defect levels which result in fast recovery from excitonic absorption bleaching (EAB). The ions are deposited below the multiple quantum well (MQW) layer. There is a possibility that this will result in damage to the distributed Bragg reflector (DBR) which is positioned below the MQW layer in asymmetric Fabry-Perot (AFP) cavity devices.

The characterisation experiments aim to determine the ion doses required to achieve picosecond EAB recovery times. Pump-probe measurements are used to determine the recovery times of the implanted devices. As stated above, the possibility that ion implantation might damage the DBR in AFP cavity structures, and hence reduce device contrast ratios, is a point of concern. Pulse saturation measurements are used to ensure that AFP cavity devices retain high contrast ratios following implantation.

The possibility of polarisation dependence in EAB-based devices has been discussed in Section 3.6. Such dependencies can result from selective excitation of either spin-up or spin-down carriers by circularly polarised signal pulses. The investigations of Chapter 7 have, however, suggested that such effects are unlikely to play a significant role in the operation of devices which are excited by picosecond pulses.

Whilst making the pump-probe measurements described in this chapter the states of polarisation of the pump and probe pulses incident on the devices in the pump-probe measurements were set to the same, and to the opposite, circular polarisations (SCP and OCP), as in the experiments of Hyland et. al. which are summarised in Section 3.5.1. Comparison of the SCP and OCP results provided additional reassurance that no polarisation dependent behaviour was occurring.

Additional experiments are carried out to investigate the possibility of using the devices in high-repetition rate, systems, applications.

8.2 Ion implantation of MR846 transmission structure

8.2.1 Wafer structure

The structure of the MR846 wafer is shown in Figure 8.1. The free carrier lifetime and exciton resonance wavelength of the unimplanted wafer were measured to be 5 ns and 1525 nm respectively. The use of a transmission wafer in this initial implantation study allowed a simple investigation of the MQW non-linearity which did not need to consider AFP cavity effects, or the possibility of DBR degradation.

It was planned that samples of the wafer should be implanted with doses between 10^9 ions/cm^2 and 10^{13} ions/cm^2 to create five devices. However, the ion source used failed during the implantation of the 10^{13} ions/cm^2 device. It was calculated that a dose of 9.8×10^{12} ions/cm^2 had been delivered at the time of the source failure.

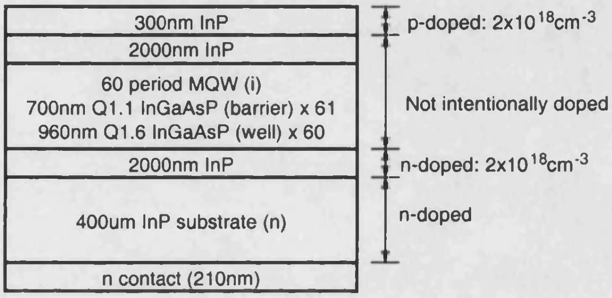

Figure 8.1: MR846 wafer structure.

8.2.2 Pump-probe measurements

Initial pump-probe measurements of the implanted devices made using the configuration of Section 4.5 showed substantial reductions of recovery time. Results of measurements made at 1528 nm using 14 pJ energy pump pulses are shown in Figure 8.2 for devices implanted with doses up to 10^{12} ions/cm^2. No non-linearity could be observed with the 9.8×10^{12} ions/cm^2 device. Each data set plotted is normalised against the maximum transmission change. Exponential curves are fitted to the measured data. Recovery times obtained from this curve fitting are summarised in Table 8.1.

Device	Dose (ions/cm^2)	Recovery time (ps)
C	1×10^9	65
A	1×10^{10}	69
B	1×10^{11}	2.6
D	1×10^{12}	518
E	9.8×10^{12}	

Table 8.1: MR846 ion-implantation study: device recovery times.

The 2.6 ps recovery time obtained for device B is not accurate, due to the comparatively long duration of the 2 ps pulses used in the pump-probe experiment. This device is, however, clearly sufficiently fast for both 10 and 40 Gb/s systems applications.

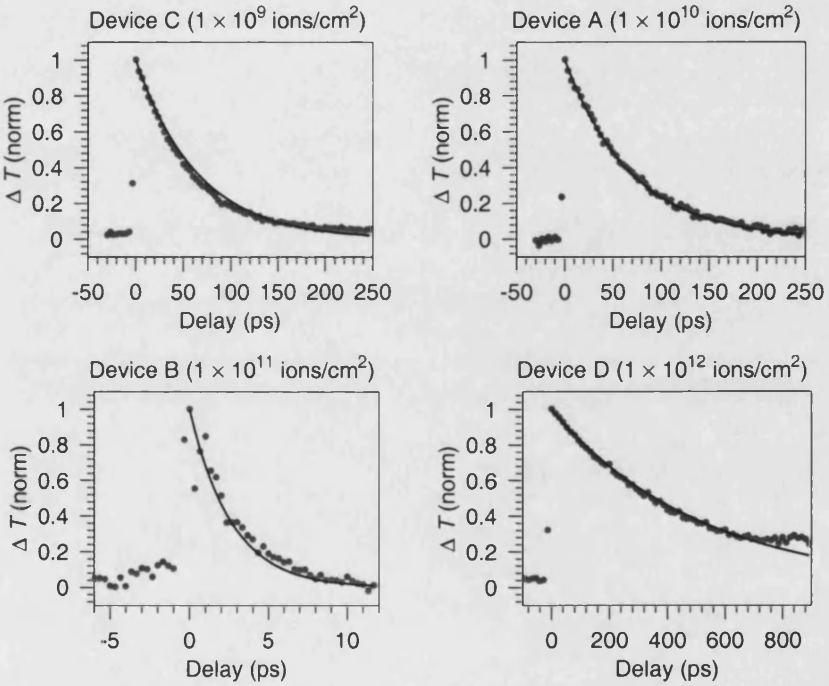

Figure 8.2: MR846: pump-probe measurements of ion-implanted devices. The time scales of the plots are varied according to the device recovery times. The lines are exponential curves fitted to the recovery of the measured data.

Pump-probe measurements were repeated with a range of pump pulse energies ranging from 14 pJ, the maximum available, to 3.75 pJ, the minimum resulting in a readily detectable transmission change. No dependence of the dynamics of the recovery change on the pump pulse energy was observed.

The results were independent of the state of polarisation of the pump and probe signals at the device. It was not possible to replicate the SCP and OCP experiments discussed in Section 3.5.1 and hence observe spin relaxation in these devices.

8.2.3 Low repetition rate wavelength conversion

The configuration of Section 4.6 was used to perform a demonstration of wavelength conversion using device B. The input signal used was a 4 MHz stream of 2 ps, 16 pJ pulses at a wavelength of 1528 nm. The power of the continuous wave (CW) signal incident on the device was 3 mW. Figure 8.3 shows the wavelength converted signal plotted from data acquired using a 50 GHz photodetector and a 20 GHz bandwidth sampling oscilloscope. The width of the output pulses in these results is determined by the bandwidth of oscilloscope.

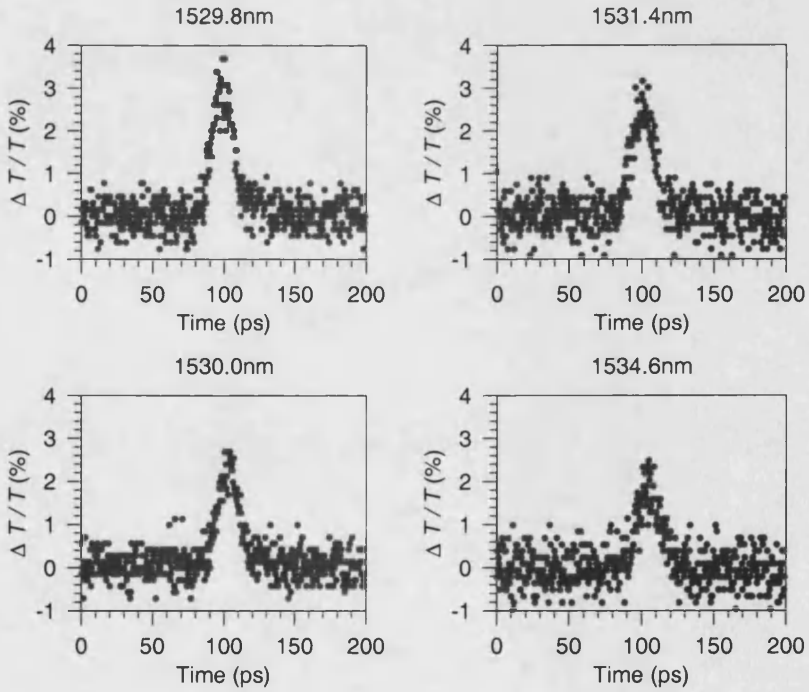

Figure 8.3: MR846 device B: output signals from low repetition rate wavelength conversion experiment. Results are shown for several different output wavelengths.

A reduction of the magnitude of the pulses visible in the oscilloscope traces is observed as the output wavelength is increased from 1529.8 nm to 1534.6 nm. This is the expected behaviour. As the output wavelength moves away from the exciton resonance at 1525 nm the EAB non-linearity becomes weaker.

8.2.4 Summary

A transmissive device with a recovery time faster than 2.6 ps has been created by ion-implanting a structure containing a Q1.1/Q1.6 MQW structure with 4 MeV nitrogen ions. The dose used was 10^{12} ions/cm^2. The device has been used to demonstrate low contrast wavelength conversion of a 4 MHz stream of 2 ps pulses.

The expected systematic dependence of recovery time on ion dose was not observed. There is little difference between the devices implanted with 10^9 ions/cm^2 and 10^{10} ions/cm^2 (devices C and A). Since implantation of these low dose devices was manually controlled it is possible that the intended ion doses were not delivered.

This source of experimental error cannot explain the long recovery time measured for device D.

However, as discussed earlier, the ion source used failed during the implantation of device E. This implantation was performed immediately after that of device D. It is possible that the anomalous behaviour of device D is associated with the failing source.

8.3 Ion implantation of MR1419 reflection structure

8.3.1 Wafer structure

The structure of the wafer from which the devices investigated in this section were made is shown in Figure 8.4. Samples of the wafer were implanted with 4 MeV nitrogen ions at doses between 5×10^{10} ions/cm^2 and 10^{12} ions/cm^2. The top surfaces of the devices were not anti-reflection coated, such that AFP cavities were formed. The exciton resonance in the MQW structure was at 1534 nm. Free carrier lifetimes $\approx$ 3 ns were measured prior to implantation.

8.3.2 Time resolved measurements

The results of pump-probe measurements of the implanted devices are shown in Figure 8.5. Recovery times, as determined by fitting exponential curves to the measured data, are summarised in Table 8.2. A systematic dependence of recovery time on ion dose is observed. As with the MR846 transmission devices there was no variation of the recovery time when the pump pulse energy was varied between 3.75 pJ and 14 pJ.

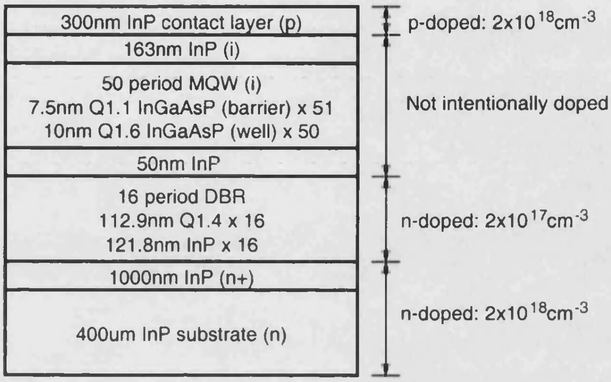

Figure 8.4: MR1419 wafer structure.

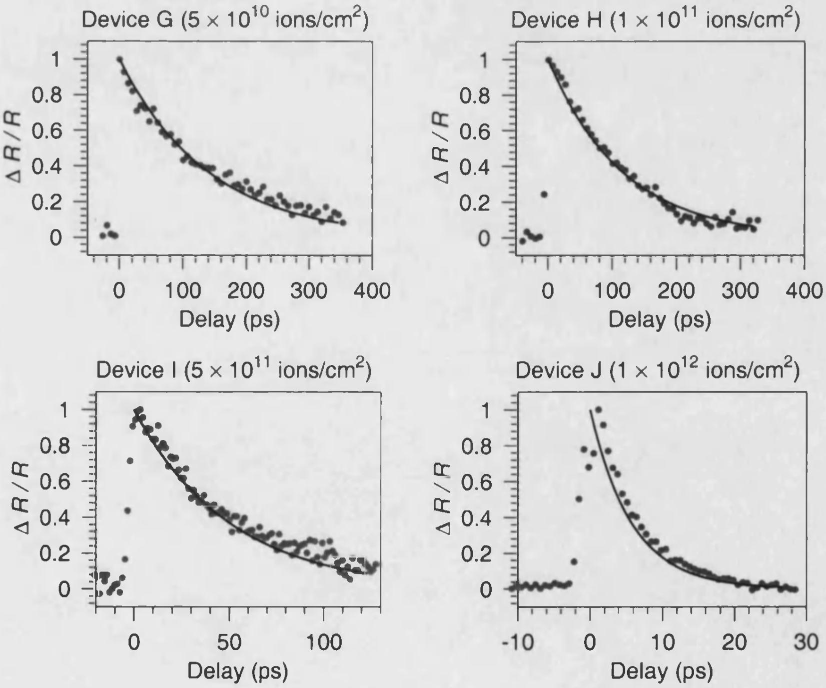

Figure 8.5: MR1419: pump-probe measurements of ion-implanted devices. The time scales of the plots are varied according to the device recovery times. The lines are exponential curves fitted to the recovery of the measured data.

Device	Dose (ions/cm^2)	Recovery time (ps)
G	5×10^{10}	139
H	1×10^{11}	116
I	5×10^{11}	50
J	1×10^{12}	5.8

Table 8.2: MR1419 ion-implantation study: device recovery times determined by fitting exponential curves to the measured data.

As with the similar measurements of a transmission device (Section 8.2.2), results were independent of the state of polarisation of the pump and probe pulses incident on the device.

8.3.3 Low repetition rate wavelength conversion

Device J was used to perform a demonstration of low repetition rate wavelength conversion. As in the similar experiment described in Section 8.2.3, the input signal used was a 4 MHz stream of 2 ps pulses. The pulse wavelength was 1530.8 nm. Results for a number of output wavelengths are shown in Figure 8.6. The observed pulse shape and contrast ratio of the output pulses is again determined by the 20 GHz bandwidth of the sampling oscilloscope used to acquire the data.

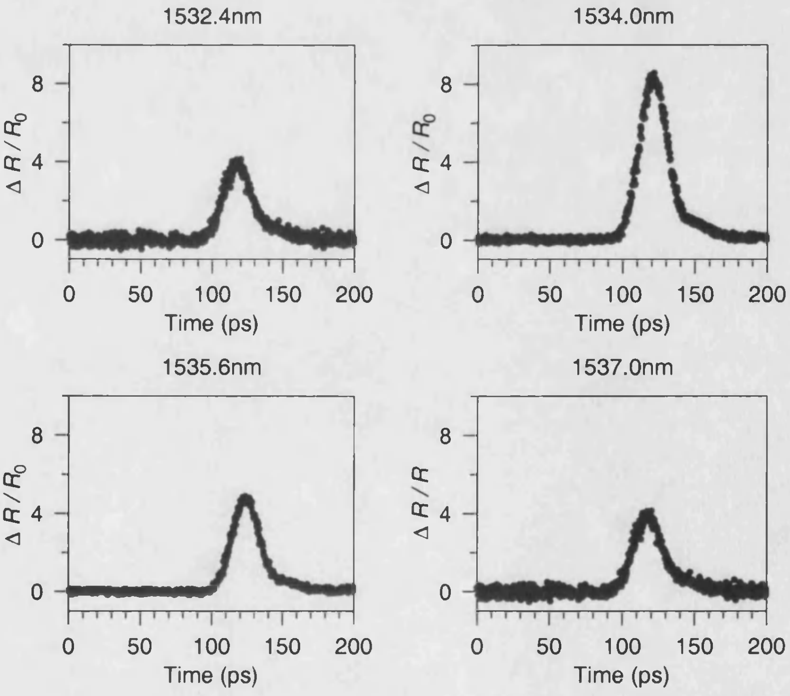

Figure 8.6: MR1419 device J: output signals from low repetition rate wavelength conversion experiment. Results are shown for several different output wavelengths.

Optimal contrast was observed when the output wavelength was 1534 nm. The results of Figure 8.7, in which small signal reflectivity measured with a low power CW source is plotted as a function of wavelength, confirm this to be the wavelength at which the AFP cavity is resonant. A rapid reduction of the contrast ratio is observed as the output wavelength deviates from the resonance wavelength. This behaviour was predicted in the theoretical discussion of Section 3.7.

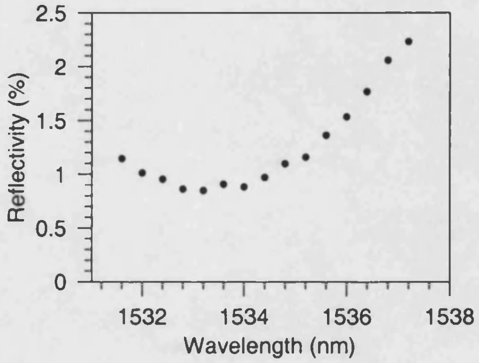

Figure 8.7: MR1419 device J: small signal reflectivity spectrum.

8.3.4 Pulse saturation measurements

Pulse saturation measurements, made with the experimental configuration of Section 4.4.2 were used to determine the contrast ratio of the device. The characteristic measured at 1534 nm is shown in Figure 8.8. A contrast ratio, defined as the ratio between the minimum and maximum measured reflectivities, of 9 dB is observed.

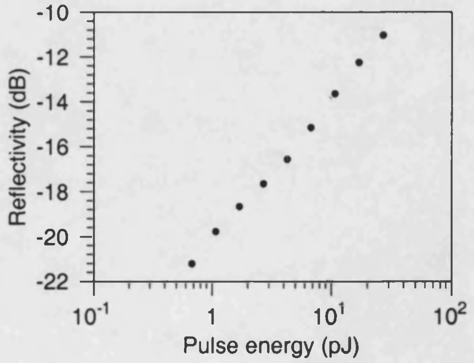

Figure 8.8: MR1419 device J: results of pulse saturation measurement at 1534 nm.

8.3.5 Summary

A number of fast high-contrast devices have been made by implanting a structure incorporating an InGaAsP MQW and an InGaAsP/InP DBR with different doses of 4 MeV ions. The switching recovery time of the device implanted with 10^{12} ions/cm^2 was measured to be 5.8 ps.

A contrast ratio of 9 dB, as determined through pulse saturation measurements using a 2 ps pulse source, was obtained for this device. This high contrast implies that the ion implantation did not affect the impedance matching condition for which the cavity was designed. The implantation process could not therefore have significantly degraded the DBR reflectivity.

8.4 MR1419 device: wavelength conversion of 10GHz pulse stream

8.4.1 Experiment

This section describes an experiment designed to demonstrate the suitability of the fast recovery device made from the MR1419 wafer (device J) for high repetition rate wavelength conversion. Characterisation of this device has been described in Section 8.3.

The experimental configuration used is shown in Figure 8.9. It is based on that described in Section 4.6 which was used for low repetition rate wavelength conversion, but with the significant difference that the input and CW signals incident on the device are combined in a single fibre. Whilst this approach requires the use of multiple optical filters following the device to block light at the input wavelength it has the advantage of considerably simplifying the free space optical arrangement since there is no requirements to align separate beams to be incident at the same point on the device.

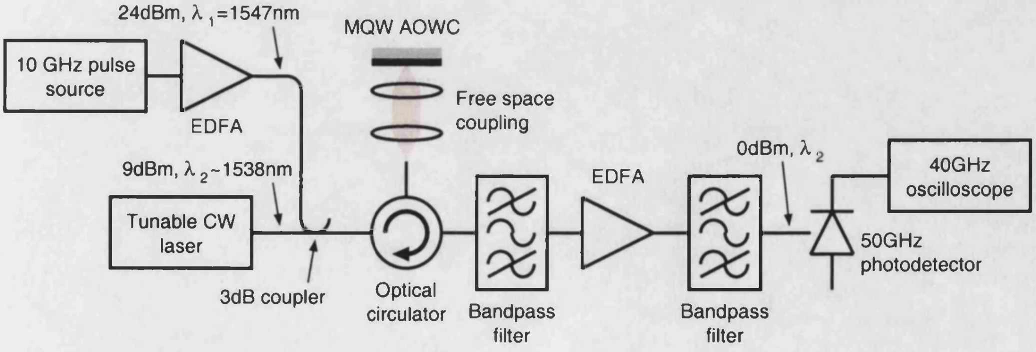

Figure 8.9: Wavelength conversion of 10 GHz pulse stream: experimental configuration.

The 10 GHz source used produced an unmodulated stream of 11 ps full-width half maximum (FWHM) sech^2 pulses at a fixed wavelength of 1547 nm. These were amplified to an average power of 24 dBm using an erbium-doped fibre amplifier (EDFA) before being combined with the 9 dBm output of a tunable CW laser in a 3dB coupler. The combined signals were coupled to the device using a fibre-pigtailed optical circulator and the free space arrangement described in Section 4.2.2. Allowing for the circulator and coupler, the total average power incident on the device was 20 dBm. The reflected signal from the device was coupled back though the circulator. Narrow-band optical filters and an EDFA were used to block the 1547 nm input and amplify the wavelength converted output signal. The output was observed using a 50 GHz bandwidth photodetector and a 40 GHz bandwidth sampling oscilloscope.

8.4.2 Results

Optimal wavelength conversion was observed when the output wavelength was 1538.2 nm. The oscilloscope trace observed at this wavelength is shown in Figure 8.10. The input signal is shown for comparison.

The contrast ratio of the wavelength converted signal is significantly degraded. The 10 GHz pulses have also acquired visible tails following wavelength conversion. These tails extend for some 50 ps after the pulses.

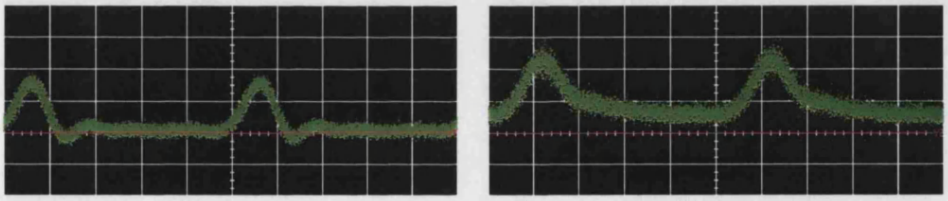

Input (1547 nm) Output (1538.2 nm)

Figure 8.10: Wavelength conversion of 10 GHz pulse stream: input and output signals. The oscilloscope timebase was set to 20 ps per division. The red cursor indicates the zero level.

These degradations can be seen more clearly in the plots of time-averaged oscilloscope data shown in Figure 8.11. Results are shown for output wavelengths between 1536.7 nm and 1597.7 nm. As in the low repetition rate measurements of Section 8.3, the use of an AFP cavity results in a strong dependence of contrast ratio on the output wavelength.

The output contrast ratio, obtained from the time averaged data of Figure 8.11, is plotted as a function of output wavelength in Figure 8.12.

8.4.3 Discussion

The experiment described in this section has demonstrated the potential of an ion-implanted device incorporating an MQW structure in an AFP cavity for 10 Gb/s systems applications.

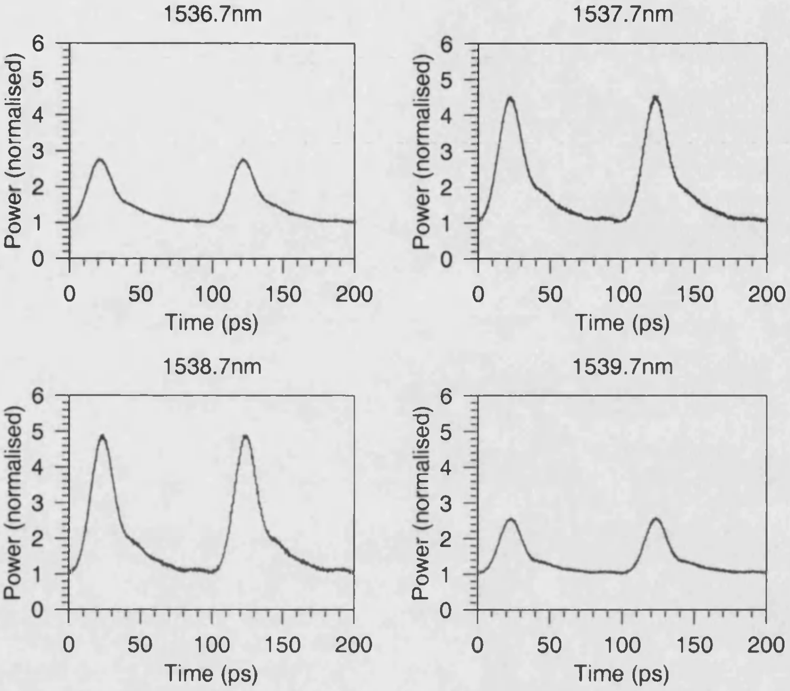

Figure 8.11: Output signals obtained following wavelength conversion of a 10 GHz pulse stream to different wavelengths. The plots are based on time averaged oscilloscope data.

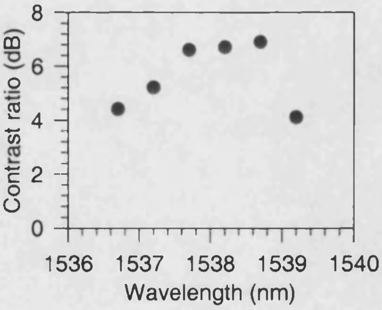

Figure 8.12: Wavelength conversion of 10 GHz pulse stream: dependence of output contrast ratio on output wavelength.

Optimum contrast ratios were observed when the output wavelength was 1538.7 nm. This is significantly longer than 1534 nm, which was determined to be the resonance wavelength of the AFP cavity in Section 8.3.3. Red-shifting of the resonance is attributable to local heating of the device due to the high incident optical power.

The tails evident on the output pulses in the results of Figure 8.11 are attributable to the defect level saturation phenomenon discussed in [1].

8.5 MR1419 device: wavelength conversion of 40 Gb/s pseudo-random bit stream

8.5.1 Experiment

Following the demonstration of wavelength conversion of a 10 GHz pulse stream described in the preceding section, wavelength conversion of a 40 Gb/s pseudo-random bit stream (PRBS) using the same device was investigated. The configuration used is shown Figure 8.13. It incorporated variable attenuators to allow control of the PRBS and CW powers incident on the device. Measurements were made with PRBS wavelengths of 1545 nm and 1550 nm; no significant dependence of the wavelength converted signal on the input wavelength was observed.

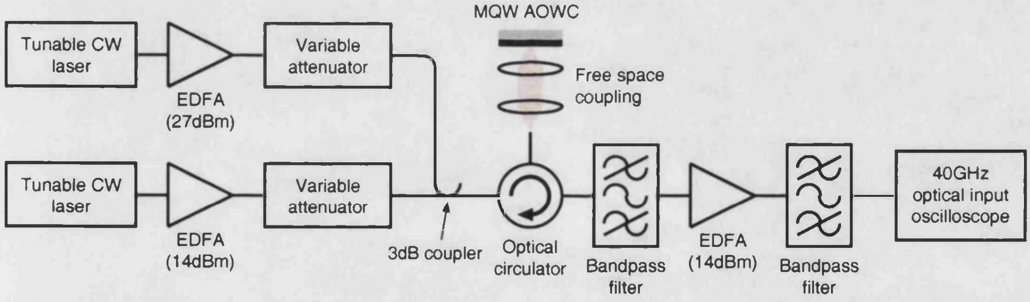

Figure 8.13: Wavelength conversion of 40 Gb/s PRBS: experimental configuration.

Practical investigation showed that it was necessary to set the attenuation of the CW signal to 0 dB to maximise the output signal, and hence minimise the output noise. Under this condition the CW power incident on the device was 4.5 dBm. Measurements were made with the CW input tuned to wavelengths between 1535.5 nm and 1539.5 nm. It was found that, for each wavelength, the power of the PRBS signal incident could be adjusted to a different value to optimise the output contrast ratio.

8.5.2 Results

The dependence of the optimum power of the PRBS signal incident on the device on the output wavelength is shown in Figure 8.14. It is consistent with red-shifting of the cavity resonance due to heating of the device. Optimum PRBS powers were used in the following measurements.

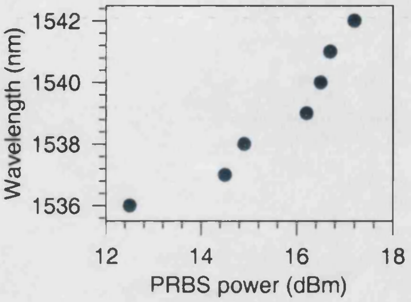

Figure 8.14: Wavelength conversion of 10 Gb/s PRBS: dependence of the AFP resonance wavelength on the average power of the incident PRBS signal.

Examples of the output signal, as observed on the sampling oscilloscope, are shown in Figure 8.15. Amplified spontaneous emission (ASE) noise from the EDFA used to amplify the wavelength converted signal made a significant contribution to the output signal degradation which is manifested as closure of the eye diagram.

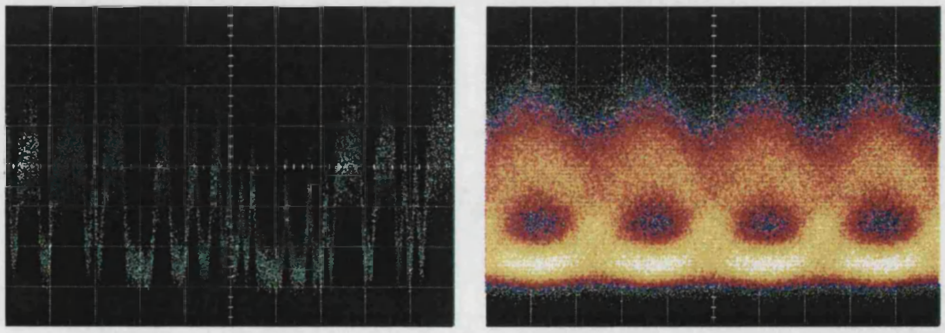

Timebase: 250 ps/div

Timebase: 10 ps/div

Figure 8.15: Wavelength conversion of 10 Gb/s PRBS: output pattern and eye diagram observed on the oscilloscope with input and output wavelengths of 1541 nm and 1545 nm.

To allow analysis of causes of eye closure other than ASE noise oscilloscope data was recorded with 256 times averaging. Data at an output wavelength of 1541 nm is shown in Figure 8.16. Two forms of signal degradation are visible. Firstly, there is an offset from the zero level, indicating limited output signal contrast. Secondly, patterning is evident: there is a systematic increase of pulse amplitude within groups of adjacent pulses.

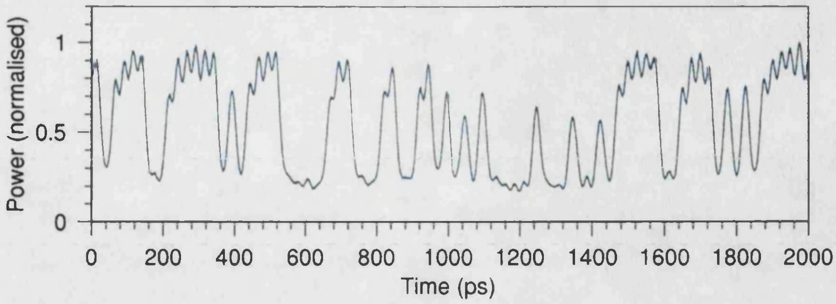

Figure 8.16: Wavelength conversion of 40 Gb/s PRBS: time averaged output signal observed at an output wavelength of 1541 nm.

The signal degradations discussed above are more clearly visible if the time averaged data is wrapped around to form eye diagrams. Eye diagrams for each output wavelength at which measurements were made are shown in Figure 8.17. As the output wavelength increases the contrast ratio improves, but there is more eye closure due to pulse patterning.

Contrast ratios were calculated from the time average data by calculating the mean levels of the ones and zeros at the centre of the eye diagrams of Figure 8.17. These are plotted as a function of wavelength in Figure 8.18.

8.5.3 Discussion

The noise levels on the wavelength converted output signals were high enough that there was no possibility of measuring output bit error rates low enough for systems applications. Output noise is not, however, a fundamental limitation. Given that the saturated output power of the EDFA is 14 dBm, and the output in the experimental of Figure 8.13 is 0 dBm, the EDFA is clearly unsaturated. This situation will result in high levels of ASE noise.

Similarly to the pulse tails in the 10 GHz measurements of Section 8.4, output signal patterning can be attributed to defect level saturation. It is clear from the eye diagrams of Figure 8.17 that patterning becomes stronger at longer wavelengths. Since the power of the PRBS signal was increased at longer wavelengths there is thus a correlation between the average power incident on the device and the degree of patterning. This is consistent with the patterning being due to some average power effect.

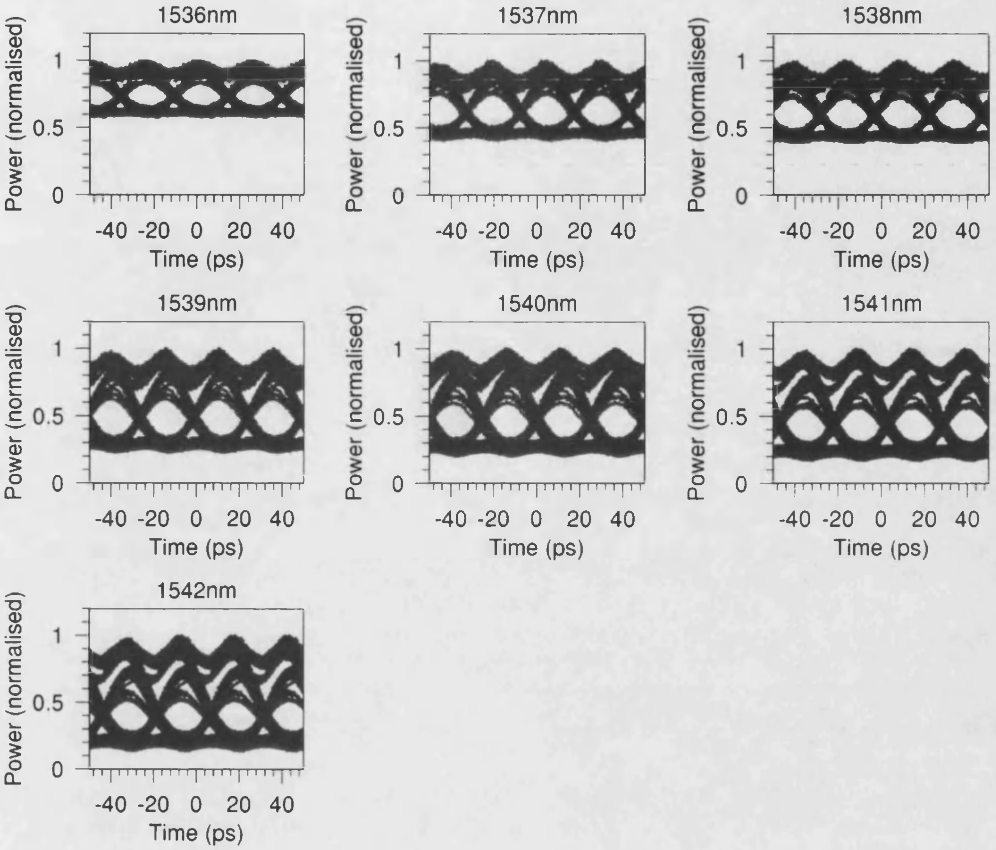

Figure 8.17: Wavelength conversion of 40 Gb/s PRBS: eye diagrams produced from time averaged output signals observed at different output wavelengths.

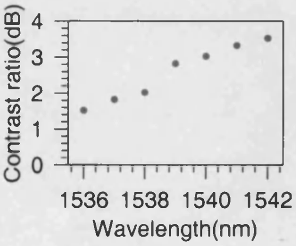

Figure 8.18: Wavelength conversion of 40 Gb/s PRBS: dependence of output signal contrast ratio on output wavelength.

Chapter summary

It has been shown that ion implantation can be used to reduce the recovery times in InGaAsP MQW structures to picosecond values. This technique was used to realise fast, high contrast, switching in an AFP cavity device suitable for applications in ultra-fast communications. Characterisation experiments showed that the contrast ratio obtained was critically dependent on the wavelength of the switched signal, the expected behaviour for a device employing a high-finesse cavity. The experiments showed the behaviour of the devices to be polarisation independent. This is a desirable quality in systems applications.

Wavelength conversion of a 10 GHz pulse stream, and of a 40 Gb/s PRBS were demonstrated. In the 40 Gb/s PRBS case the quality of the output signal was limited by ASE noise from the unsaturated EDFAs used to boost the wavelength converted signal prior to detection, and by patterning of the output signal. The patterning was attributed to saturation of defect levels within the implanted MQW structure. Whilst it should be possible to avoid such saturation in devices implanted with ion species heavier the nitrogen, the facilities required to perform such implantations were not available.

A maximum contrast ratio of 3.5 dB was calculated for the output signal in the 40 Gb/s experiment. The 10 dB contrast ratios required for wavelength conversion in systems applications could be achieved by further optimisation of the AFP cavity, such that it came closer to the impedance matching condition described in Section 3.7.

References

[1] J. Mangeney, H. Choumane, G. Patriarche, G. Leroux, G. Aubin, J. Harmand, J. Oudar, and H. Bernas, "Comparison of light- and heavy-ion-irradiated quantum-wells for use as ultrafast saturable absorbers," *Applied Physics Letters*, vol. 79, pp. 2722–2724, October 2001.

Chapter 9

Conclusions

This thesis has described an investigation of devices exploiting optical non-linearities in multiple quantum well (MQW) structures. The investigation was motivated by the possibility of using such devices as saturable absorbers (SAs) for soliton control, or as all-optical wavelength converters (AOWCs), in ultra-fast fibre optic transmission systems. This final chapter summarises the work done and discusses the suitability of the various devices investigated for systems applications.

The results of modelling of systems employing SA soliton control and AOWCs are summarised in Section 9.1. Investigations of field screening in reverse biased p-i-n devices, of switching using non-linear polarisation rotation (NPR), and of fast excitonic absorption bleaching (EAB) in ion-implanted MQW devices are discussed in Section 9.2.

In Section 9.3 the modelling and experimental results are used as the basis of a discussion of the suitability of the various devices studied for soliton control applications. Section 9.4 presents a similar discussion for wavelength conversion applications. It is evident from these discussions that improvements of device performance are desirable. Means of achieving these improvements are discussed in Section 9.5.

Section 9.6 compares the work done to the objectives laid out in Section 1.5. The most significant achievements are highlighted in Section 9.7.

Finally, suitable directions for continuation of the work are suggested in Section 9.8.

9.1 Soliton transmission system modelling

Modelling of periodically amplified 40 Gb/s average solitons transmission systems using multiple quantum well (MQW) devices as saturable absorbers (SAs) for soliton control, and as all-optical wavelength converters (AOWCs), has been described in Sections 2.6 and 2.7 respectively. The modelled systems employed dispersion shifted fibre (DSF). No further dispersion management (DM) techniques were used.

Soliton control was shown to be most effective when the MQW SA used had a recovery time of ≈ 5 ps, and the transmission change excited by the signal incident on the device was ≈ 2dB. The modelling showed performance enhancements to be possible with MQW excess losses as high as 15 dB. A reduction of overall system performance when using high contrast MQW SAs was predicted. This was suggested to be a consequence of the pulse narrowing which occurs as the signal passes through successive MQW SAs.

The AOWC modelling showed that a signal in a soliton system could be successfully transmitted for distances up 1000 km following wavelength conversion. The error free transmission distance increased as the transmission change excited by the input signal increased. Distance was less critically dependent on the MQW recovery time, suggesting that transmission was limited primarily by the finite contrast ratio of the wavelength converted signal, rather than by the pulse broadening which occurred during wavelength conversion. Successful transmission of the wavelength converted pulses required device transmission changes ≥ 10 dB and recovery times ≤ 10 ps.

9.2 Investigations of multiple quantum well optical non-linearities

9.2.1 Field screening devices

Results of investigations of field screening in reflective p-i-n MQW devices have been presented in Chapter 6. The devices were fabricated from MOVPE-grown wafers, which incorporated both MQW and distributed Bragg reflector (DBR) structures, using standard photolithographic techniques. Fast optical non-linearities were observed when high reverse bias voltages were applied to the devices such that their behaviour was dominated by field screening effects. The investigations concentrated on this regime.

The field screening optical non-linearities were characterised by relatively slow rise times, values ≈ 6 ps were observed. A fastest recovery time of 39 ps was observed in a device in which the front surface was anti-reflection coated (Section 6.2.4), such that an asymmetric Fabry-Perot (AFP) cavity was not formed. The associated reflectivity change magnitude was 6.1 %. High contrast ratios should be attainable in a suitably designed AFP cavity device employing a similar

MQW region.

The recovery time of the field screening non-linearity was found to be strongly dependent on the energy of the exciting pulse. This is consistent with the modelling of Section 3.4 which suggests that when strong field screening occurs following excitation by a high energy pulse free carrier drift velocities in the intrinsic region decrease and lifetimes of carriers in the wells of the MQW region increase. Both these effects will slow down the operation of a field screening based device. It was also shown that strong field screening can result in a transient restoration of exciton absorption bleaching (EAB) at wavelengths around the unbiased exciton resonance.

9.2.2 Non-linear polarisation rotation

Investigations of switching based on non-linear polarisation rotation (NPR) are described in Chapter 7. A number of different MQW structures were studied; NPR switching was only observed in a single structure. The switching recovery time was 8.8 ps.

The NPR rotation angle was calculated to be less than 1 °, compared to values of 45 ° achieved by other researchers. The only substantial difference between the experiments was the use of 2 ps pulses in the experiments described in this thesis; experiments achieving larger rotation angles have used sub-picosecond pulses. The low rotational angle was thus attributed to the pulse length used. The polarisation of the switched continuous wave (CW) signal was highly critical; a small drift in its state of polarisation was significant in comparison to the NPR rotation angle.

The NPR switching configuration is complicated by the requirement to launch two signals with different states of polarisation onto the device. This means that the signals must follow different free space paths, and be aligned such that they are coincident on the device.

9.2.3 Excitonic absorption bleaching in ion-implanted devices

Investigations of devices which were ion-implanted to achieve picosecond EAB recovery times are presented in Chapter 8. The devices studied utilised Q1.1/Q1.6 InGaAsP MQWs, and were implanted with 4 MeV nitrogen ions.

Initially, simple transmission devices were implanted, to allow study of the effects on the MQW in isolation from effects on the DBR. A recovery time less than 2.6 ps was observed in a device implanted with 10^{11} ions/cm^2. Measurements of devices implanted with doses between 9.8×10^9 ions/cm^2 and 9.8×10^{12} ions/cm^2 did not show the expected systematic dependence of recovery time on ion dose. This unexpected behaviour was attributable to problems with the implantation equipment.

High-contrast devices incorporating a DBR to form an AFP cavity were then implanted. A systematic reduction of recovery time was observed as the ion dose was increased. Implantation with 10^{12} ions/cm^2 led to a device with a recovery time of 5.8 ps and a contrast ratio, determined using pulse saturation measurements, of 9 dB. The measured high contrast demonstrated that the implantation process had not caused significant damage to the DBR beneath the MQW region.

It was found that variation of the states of polarisation of the pump and probe signals incident on the device in pump-probe recovery measurements did not lead to any variation in the observed optical non-linearities. In particular, there was no difference between the results of measurements in which the pump and probe and signal had the same, and the opposite, states of circular polarisation. Such measurements have been used by other researchers to observe spin-selective excitation of photocarriers, a possible source of polarisation dependence in devices relying on EAB (Section 3.5.1).

The device described above was used to demonstrate low repetition rate wavelength conversion of a stream of 2 ps pulses from a fibre mode-locked laser (MLL). The output contrast ratio was strongly dependent on the output wavelength, the behaviour expected from AFP cavity based devices. 10 GHz and 40 Gb/s wavelength conversion experiments.

The same device was then used to demonstrate wavelength conversion of an unmodulated 10 GHz pulse stream, and of a 40 Gb/s pseudo-random bit stream (PRBS). A 6.9 dB contrast ratio was observed in the 10 GHz experiment. The output pulses were characterised by tails of approximately 50 ps duration. High levels of noise were present on the output signal in the 40 Gb/s experiment, a consequence of the use of a non-saturated erbium doped fibre amplifier (EDFA). The output was also degraded by patterning which, together with the 50 ps tails in the 10 GHz experiment, was attributed to saturation of the defect levels created by ion implantation of the MQW. Output signal contrast ratios up to 3.6 dB were observed.

A red-shifting of the AFP cavity resonance was observed in both the 10 GHz and 40 Gb/s measurements. This was attributed to thermal effects resulting from local heating of the device.

9.3 Soliton control applications

The requirements for optimum soliton control derived from the systems modelling work of Section 2.6, 5 ps recovery time and 2 dB contrast ratio, are compared to the measured parameters of field screening-based p-i-n devices in Section 9.3.1, and to those of ion implanted devices in Section 9.3.2. There is no discussion of NPR which, being a switching mechanism, is not suitable for soliton control. Whilst the discussion is focused on soliton control, it is applicable to the more general problem of regeneration in non-linear supported transmission systems.

The possibility of using the devices in 10 Gb/s systems is also discussed.

9.3.1 Field screening devices

The fastest recovery time of 39 ps observed in the investigation of field screening based devices is not sufficiently fast for 40 Gb/s soliton control applications. If it is assumed that 40 Gb/s modelling results can be scaled to apply to slower systems, 39 ps recovery should be fast enough for 5 Gb/s applications.

The transient reflectivity change in devices with the experimentally observed rise times, ≈ 6 ps, will lag the reflectivity changes excited by the relatively short signal pulses in soliton, or other return-to-zero (RZ), systems operating at 10 Gb/s or higher speeds. The pulses will not, therefore, experience the desired preferential transmission.

The possibility of modifying the device geometry to achieve fast performance is discussed in Section 9.5.1.

The behaviour of field screening devices following pulse excitation has been shown to be qualitatively dependent on the operating wavelength. Specifically, transient restoration of the EAB can occur at wavelengths close to the exciton resonance. It is reasonable to assume that the AFP cavity resonance shifts observed in ion implanted devices on which high power optical signals were incident will also occur in field screening devices. The interplay between these behaviours complicates the design of field screening devices. The design problem is compounded by the dependence of recovery time on exciting pulse energy which characterises such devices.

9.3.2 Excitonic absorption bleaching in ion-implanted devices

Ion-implanted devices exploiting EAB do not suffer from slow rise times since photocarriers excited by the signal pulses make an immediate contribution to the absorption change in the MQW region. They also have the advantage that the recovery time is independent of the exciting pulse energy. The devices investigated have been shown to be polarisation independent.

Experiments have shown that 5.8 ps recovery, sufficiently fast for 40 Gb/s soliton control, can be achieved in conjunction with 9 dB contrast in an AFP cavity device. The device design could be modified to achieve reduced contrast ratios by reducing the thickness of the MQW region. This would increase the effective reflectivity of the rear mirror in the AFP cavity, such that destructive interference within the cavity in the intervals between signal pulses was less optimal. As the contrast ratio is reduced the wavelength range of the device will be increased.

The red-shifting of the cavity resonance, which occurs due to thermal effects when the high average optical powers required to excite significant non-linearities are incident on the device, will complicate device deployment. The effect would be less significant in low contrast devices designed for soliton control, due to their increased wavelength range.

The patterning observed in the wavelength conversion experiments of Section 8.5 is potentially a serious problem in soliton control applications since it will lead to variations in the peak power and energy of the pulses leaving the device. Strategies to overcome this patterning are discussed in Section 9.5.2.

9.4 All optical wavelength converter applications

The contrast ratio requirements for AOWC devices are more demanding than for those for soliton control applications. From the modelling of Section 2.7 contrast ratios of at least 10 dB are required. The recovery time requirement is less stringent with values of 10 ps or less being needed.

The rise time will also be less critical. A constant non-instantaneous rise time will simply result in the wavelength converted output pulses lagging the input pulses. Variations of the rise time will, however, jitter the output pulses.

As in the preceding discussion concerning soliton control, 40 Gb/s and 10 Gb/s applications are considered.

9.4.1 Field screening devices

The fastest recovery time observed for field screening devices, 39 ps, is clearly not fast enough for 40 Gb/s AOWC applications. Assuming that the 40 Gb/s modelling results can be scaled, the devices should be fast enough for 10 Gb/s operation. As discussed above, the finite rise time which characterises the field screening mechanism should simply delay the output pulses. The high contrast ratios required for wavelength conversion could be achieved in AFP cavity devices.

The complex behaviour of field screening devices, discussed in Section 9.3.1, are equally undesirable in wavelength conversion applications.

Modifications to the device geometry which will result in reduced recovery time are discussed Section 9.5.1.

9.4.2 Non-linear polarisation rotation

The requirement for sub-picosecond control input signal pulses means that NPR switching is not a suitable mechanism for wavelength conversion. The generation of sub-picosecond pulses, and their propagation in standard fibre, is not practical in transmission applications.

The dependence of NPR on the input signal polarisation would also pose a serious limitation in transmission applications where the state of polarisation of the propagating signal is not well known. The relative complexity of the free space part of the switching arrangement is undesirable for systems applications.

NPR switching at high repetition rates would require the use of a technique such as ion implantation to reduce the overall free carrier lifetime in the MQW structure used, an issue not addressed in the experimental investigations of Chapter 7.

9.4.3 Excitonic absorption bleaching in ion-implanted devices

An AFP cavity device implanted with 10^{12} ions/cm^2 was shown to have 9 dB contrast ratio and 5.8 ps recovery time. From the system modelling, these parameters are suitable for 40 Gb/s wavelength conversion applications.

Two limitations were revealed when the device was used to perform a demonstration of wavelength conversion at 40 Gb/s:

- The contrast ratio was limited due to practical restrictions on the power to which the input signal could be amplified before it was coupled on to the device.
- The high average power incident on the device resulted in saturation of the defect levels introduced by the ion implantation process. This led to patterning of the wavelength converted output signal.

The wavelength of the AFP resonance, corresponding to the optimum output wavelength in AOWC applications, was observed to shift to longer wavelengths when increasing optical powers were incident on the device. This behaviour, attributable to localised heating of the device, should be considered in the design of future devices.

Strategies to modify the device design to overcome the contrast ratio and patterning limitations are discussed in Section 9.5.2.

9.5 Modifications to improve device performance

This section discusses ways in which the p-i-n and ion implanted devices used to investigate field screening and fast EAB respectively can be modified to make them more suitable for the systems applications of interest in this thesis. Devices using NPR switching are not considered.

9.5.1 Field screening devices

Experimental investigations have suggested that modifications of the normal incidence p-i-n structure used to exploit the field screening non-linearity are required to produce devices fast enough for the applications of interest in this thesis.

Computer modelling has been used to investigate the behaviour of field screening in p-i-n devices in Section 3.4. The modelling results suggest that recovery would be faster in devices in which the width of the intrinsic region was reduced, or in which the width of the top p-region was increased.

A reduction of the intrinsic width implies a reduction of the MQW region width, and hence reduced transmission changes in the MQW region. The problem of dopant diffusion discussed in Section 5.3.3 will become more pronounced in devices with narrower intrinsic regions.

Increasing the width of the p-region would increase the diffusion coefficient and, as shown by the modelling, result in significantly faster recovery from field screening. This is, however, achieved at the expense of reduced electric field change in the intrinsic region which will reduce the magnitude of the resulting reflectivity change.

An alternative approach would be to use field screening in waveguide devices. A device can be designed to have a short intrinsic region for fast dynamics and a long waveguide to maximise contrast. Other researchers have shown waveguide field screening devices to be suitable for 10 Gb/s applications [1]. Unlike the normal incidence p-i-n devices investigated in this thesis such waveguide devices will not necessarily be polarisation independent

9.5.2 Excitonic absorption bleaching in ion-implanted devices

Whilst low repetition rate pump-probe experiments have shown that picosecond recovery times can be achieved in MQW AFP devices implanted with nitrogen ions, 40 Gb/s wavelength conversion measurements revealed significant patterning of the output signal.

This patterning, which was attributed to saturation of the defect levels in the MQW region due to the high average power incident on the device, must be avoided to achieve error-free wavelength conversion. Patterning is equally undesirable in soliton control applications.

An obvious strategy to reduce patterning is implantation with a heavier ion species [2]. This was not possible at the facility available for the work described in this thesis, as discussed in Section 5.4. It is possible that use of a heavier species, and the higher implantation energies which would be required to ensure that the ions were deposited below the MQW region, would result in damage to the DBR which is beneath the MQW region in the MQW AFP device structure.

The contrast ratios observed in the 40 Gb/s wavelength conversion experiment were substantially smaller that the 10 dB which the modelling of Section 2.7 suggested to be the requirement for wavelength conversion. Contrast ratio can be enhanced by adjustment of the of the AFP cavity parameters, such that the devices are closer to the impedance matching condition. Achieving impedance matching is complicated by the red-shifting of the AFP cavity resonance observed when the high input signal power required for wavelength conversion are incident on the device. To design optimal devices this effect must be quantified and considered.

Other work now in progress at UCL is investigating the behaviour of devices which were heated to ≈ 200 °C during the implantation process. The devices studied in this thesis were implanted at room temperature. High temperature implantation was shown to result in larger absorption changes in MQW structures implanted with high doses of nitrogen ions, whilst still achieving picosecond lifetimes [3]. It might thus be a useful approach to achieve high contrast devices. The impact of high temperature implantation on defect level saturation, and hence patterning effects, has not yet been assessed.

It is also possible that improved contrast ratios could be obtained in devices in which materials systems other than Q1.1/Q1.6 InGaAsP were used to grow the MQW region. This could allow larger MQW conduction and valence band offsets, leading to stronger confinement of carrier in the wells comprising the MQW, and hence stronger excitonic effects. Use of a different material system might also be expected to change the nature of the damage resulting from ion implantation.

9.6 Objectives realised

A number of objectives for this work were stated in Section 1.5. These are discussed below:

- A computer program to simulate signal propagation in transmission systems has been written and used to carry out investigations of soliton control and wavelength conversion. This work is described in Chapter 2.

- Theoretical descriptions of the various non-linear mechanisms investigated have been presented in Chapter 3. A simple computer program modelling carrier dynamics in MQW p-i-n devices was written to allow exploration of the consequences of varying the geometry of such devices.

- Experimental systems for the investigation of optically non-linear devices were designed and set up. These are described in Chapter 4. Characterisation of ultra-fast devices required a source of picosecond pulses. A fibre MLL, described in Appendix E was constructed to meet this requirement.

- Field screening optical non-linearities in p-i-n devices have been characterised. A fastest non-linear recovery time of 39 ps was observed. Limitations to the speed of the optical non-linearity in the devices were investigated, and means of overcoming them discussed.

- The possibility of NPR switching in a number of MQW structures has been investigated. NPR switching was successfully demonstrated in one of these structures. It was suggested that, due to its sensitivity to input signal polarisation and pulse length, NPR switching is not a suitable mechanism for applications of interest.
- The influence of ion implantation on EAB recovery was investigated. It was shown that picosecond lifetimes can be achieved in conjunction with high contrast in AFP devices.

Significant results from the investigations of ion-implanted devices are summarised in the following section.

9.7 Key results

Experimental investigations showed that the performance required for 10 Gb/s and 40 Gb/s applications could be most readily achieved in devices using fast EAB in ion-implanted MQW structures. Work was thus focused on these devices, resulting in the achievements summarised below:

- The first study of ion-implantation in InGaAsP MQWs has been described.
- It was shown that AFP devices incorporating DBRs could be ion-implanted without causing significant DBR damage.
- A high-contrast, fast recovery device was realised and used to demonstrate wavelength conversion at 10 Gb/s and 40 Gb/s. Results are summarised in Table 9.1.

Recovery time	5.8 ps
Contrast ratio measured with 2 ps pulses	9 dB
Wavelength conversion of 10 GHz clock	6.9 dB output contrast ratio
Wavelength conversion of 40 Gb/s PRBS	3.6 dB output contrast ratio

Table 9.1: Key ion-implanted MQW SA results

The MQW SA device design has significant practical advantages compared to those used by other researchers:

- Post-growth implantation was used to achieve fast recovery. MQW structures could therefore be grown using standard MOVPE, avoiding the need to use a specialised low-temperature molecular beam epitaxy (MBE) process with limited reproducibility.[4].

- Since the ion-implantation process used did not cause significant damage to the DBR the fabrication process was simple compared to that employed by other researchers who have had to rely on post-implantation etching to remove highly damaged regions of the substrate [5].

9.8 Further work

Of the devices investigated, those exploiting EAB in ion implanted MQW structures have been shown to be most suitable for systems applications. Future work would therefore most usefully be directed towards improvements of these devices. Several important areas for investigation have been identified:

- Implantation of devices with ion species other than nitrogen.
- Investigation of devices incorporating MQW structures in material systems other than InGaAsP.
- Detailed characterisation of the shift of the cavity resonance due to thermal effects which is observed when high optical powers are incident on the device.
- Further optimisation of the device cavity to allow improved impedance matching, and hence increased contrast ratios. This should consider the thermal behaviour discussed above.
- Investigation of the chirp introduced by the devices, in both soliton control and wavelength conversion configurations.

Further high repetition rate experiments with current and future devices are important, to allow realistic evaluation of contrast ratio and patterning performance.

It is probable that faster field screening devices could be most successfully realised by using a waveguide geometry. This would require the design of a suitable device, and fabrication process. Investigation of the requirement for short input pulses in NPR switching would be of interest, since no explanation can be found in the literature. Such work would not, however, be directly related the objectives of this thesis.

Chapter summary

This chapter has brought together the modelling and experimental work presented in this thesis, and used them as the basis of an analysis of the suitability of the various devices investigates for soliton control and wavelength conversion applications in ultra-fast transmission systems.

The most important results, concerning an ion-implanted AFP cavity device with a recovery time of 5.8 ps and a contrast ratio of 9 dB, which was used to demonstrated wavelength conversion of a 10 GHz optical clock, and of a 40 Gb/s PRBS, have been highlighted.

Further developments of the device design, which will be required to realise devices suitable for deployment as soliton control or wavelength conversion components in real-world transmission systems, have been discussed.

References

[1] P. Cho, D. Mahgerefteh, and J. Coldhar, "All-optical 2R regeneration and wavelength conversion at 20 Gb/s using an electroabsorption modulator," *IEEE Photonics Technology Letters*, vol. 11, pp. 1662–1664, December 1999.

[2] J. Mangeney, H. Choumane, G. Patriarche, G. Leroux, G. Aubin, J. Harmand, J. Oudar, and H. Bernas, "Comparison of light- and heavy-ion-irradiated quantum-wells for use as ultrafast saturable absorbers," *Applied Physics Letters*, vol. 79, pp. 2722–2724, October 2001.

[3] M. Pantouvaki, R. Gwilliam, E. Burr, A. Krysa, R. J.S., and A. Seeds, "Ultrafast recovery times and increased absorption nonlinearity in InGaAsP MQW saturable absorbers implanted at 200 C," in *IPRM 2003*, (Santa Barbara, U.S.A.).

[4] H. Loka and P. Smith, "Ultrafast all-optical switching in an asymmetric Fabry-Perot device using low-temperature-grown GaAs," *IEEE Photonics Technology Letters*, vol. 10, pp. 1733–1735, December 1998.

[5] O. Leclerc, P. Brindel, S. Barré, G. Aubin, J. Mangeney, H. Choumane, and J. Oudar, "20 Gbit/s polarization-insensitive quantum well saturable absorber for 1.5 μm long-haul transmission," in *ECOC 2000*, (Munich, Germany).

Appendix A

Rate equation description of excitonic absorption bleaching

This appendix describes the rate equations used to describe multiple quantum well saturable absorbers in the systems modelling of Chapter 2.

A.1 Introduction

Haus and Silberberg have described a pair of rate equations which can be used to model excitonic absorption saturation in multiple quantum well (MQW) devices [1]. Whilst, in deriving these rate equations, the two dimensional populations of excitons and free carriers in the quantum wells (QWs) comprising the MQW, and the free carrier and exciton screening areas are considered, normalised variables are introduced such that they can be written in terms of saturation intensity, I_s. I_s is defined to be the intensity of continuous wave (CW) illumination required to reduce the absorption of the MQW, α, by a factor of two.

A.2 Derivation of the rate equations

The two dimensional populations of excitons and free carriers confined in each QW are represented by the area densities N_{ex} and N_{fc}. The absorption coefficient of the MQW, α, is assumed to have a linear dependence on N_{ex} and N_{fc},

$$\alpha \approx \alpha_0 (1 - A_{ex} N_{ex} - A_{fc} N_{fc}) \tag{A.1}$$

where α_0 is small signal value of α. A_{ex} and A_{fc} can be interpreted as the screening areas of the free carriers and excitons. From experimental measurements [2],

$$A_{ex} \approx 4A_{fc}. \tag{A.2}$$

It is convenient to make the normalisations

$$\begin{aligned} n_{ex} &= A_{ex}N_{ex} \\ &\approx 4A_{fc}N_{ex} \end{aligned} \tag{A.3}$$

and

$$n_{fc} = A_{fc}N_{fc}. \tag{A.4}$$

The absorption is totally screened, that is $\alpha = 0$, when

$$n_{ex} + n_{fc} = A_{ex}N_{ex} + A_{fc}N_{fc} = 1. \tag{A.5}$$

The intensity of illumination, I, is equal to I_s when

$$n_{ex} + n_{fc} = A_{ex}N_{ex} + A_{fc}N_{fc} = 1/2. \tag{A.6}$$

In reality, the approximation of Equation A.1 is only expected to be accurate for relatively low area densities of free carriers and excitons.

Assuming that n_{ex} and n_{fc} decay exponentially with the time constants τ_{ex} and τ_{fc}, they can be described by the rate equations

$$\frac{dn_{ex}}{dt} = \frac{2\bar{\alpha}}{\tau_{fc}}\frac{I}{I_s} - \frac{n_{ex}}{\tau_{ex}} \tag{A.7}$$

and

$$\frac{dn_{fc}}{dt} = \frac{1}{2}\frac{n_{ex}}{\tau_{ex}} - \frac{n_{fc}}{\tau_{fc}}, \tag{A.8}$$

where $\bar{\alpha}$ = normalised absorption coefficient. The normalisation of $\bar{\alpha}$ is such that $\bar{\alpha} = \alpha/\alpha_0$.

The factor of a half in the growth term of Equation A.8 appears because every exciton decays to two free carriers, and the screening area of the free carriers is a quarter of that of the excitons (from the approximation of Equation A.2.)

The ratio between I and the consequent rate of increase of n_{ex} expressed by the growth term of Equation A.7 is such that, assuming $n_{ex} \ll n_{fc}$, the condition of Equation A.6 is satisfied when $I = I_s$. This can be confirmed by solving Equations A.7 and A.8 for the CW case with $I = I_s$.

The assumption that $n_{ex} \ll n_{fc}$ can be justified for MQWs with exciton and free carrier lifetimes such that $\tau_{ex} \ll \tau fc$ by considering the CW solution of Equation A.8,

$$n_{ex} = \frac{2\tau_{ex}}{\tau_{fc}} n_{fc}. \tag{A.9}$$

A.3 Transmission of the multiple quantum well layer

Ignoring non-saturable losses, and assuming a uniform absorption profile, the transmission of an MQW layer of thickness d will be

$$T = \exp(-\alpha_0 \bar{\alpha} d). \tag{A.10}$$

Unsaturable losses can be considered by introducing T_s, the fully saturated transmission of the MQW,

$$T = T_s \exp(-\alpha_0 \bar{\alpha} d). \tag{A.11}$$

A.4 Use of contrast ratio in the rate equations

Rather than using the thickness and small signal absorption of the MQW, it is convenient to refer to its contrast ratio,

$$R = \exp(\alpha_0 d). \tag{A.12}$$

This is the ratio between T_s and the small signal, unsaturated, transmission. From Equation A.11,

$$\begin{aligned} T &= T_s \exp(\alpha_0 d)^{-\bar{\alpha}} \\ &= T_s R^{-\bar{\alpha}}. \end{aligned} \tag{A.13}$$

A.5 Use of power and saturation power

For practical work it is convenient to assume the area of the optical spot on the MQW to be constant and work in terms of saturation power, P_s, and power incident on the device, P. Equation A.7 is then written

$$\frac{dn_{ex}}{dt} = \frac{2\bar{\alpha}}{\tau_{fc}} \frac{P}{P_s} - \frac{n_{ex}}{\tau_{ex}}. \tag{A.14}$$

A.6 Simplification to consider a single population

If the MQW is excited by a pulse which is long compared to the 300 fs exciton lifetime, as is the case with the picosecond pulses employed in transmission systems, the rate equation model can be simplified to assume that free carriers are directly excited by absorbed photons. The free carrier population then directly reduces the probability of free carrier excitation. Ignoring the excitons,

$$\alpha = \alpha_0 (1 - A_{fc} N_{fc}) \tag{A.15}$$

and

$$\bar{\alpha} = 1 - n_{fc}. \tag{A.16}$$

The evolution of n_{fc} is simply

$$\frac{dn_{fc}}{dt} = \frac{\bar{\alpha}P}{P_s\tau_{fc}} - \frac{n_{fc}}{\tau_{fc}}. \tag{A.17}$$

and the transmission is of the MQW layer is

$$\begin{aligned} T &= T_s R^{-\bar{\alpha}} \\ &= T_s R^{n-1}. \end{aligned} \tag{A.18}$$

The validity of this simplification is confirmed by Figure A.1, which shows the modelled absorption change in an MQW with $P_s = 100\,\text{mW}$, $\tau_{ex} = 300\,\text{fs}$ and $\tau_{fc} = 100\,\text{ps}$. Results are shown for 200 fs, 1 ps and 5 ps full width half maximum (FWHM), 5 pJ sech^2 pulses. In the case of the 5 ps result there is negligible difference between results obtained considering (Equations A.8 and A.14) and ignoring (Equation A.17) the exciton population. As the pulse length decreases the error due to ignoring the excitons increases.

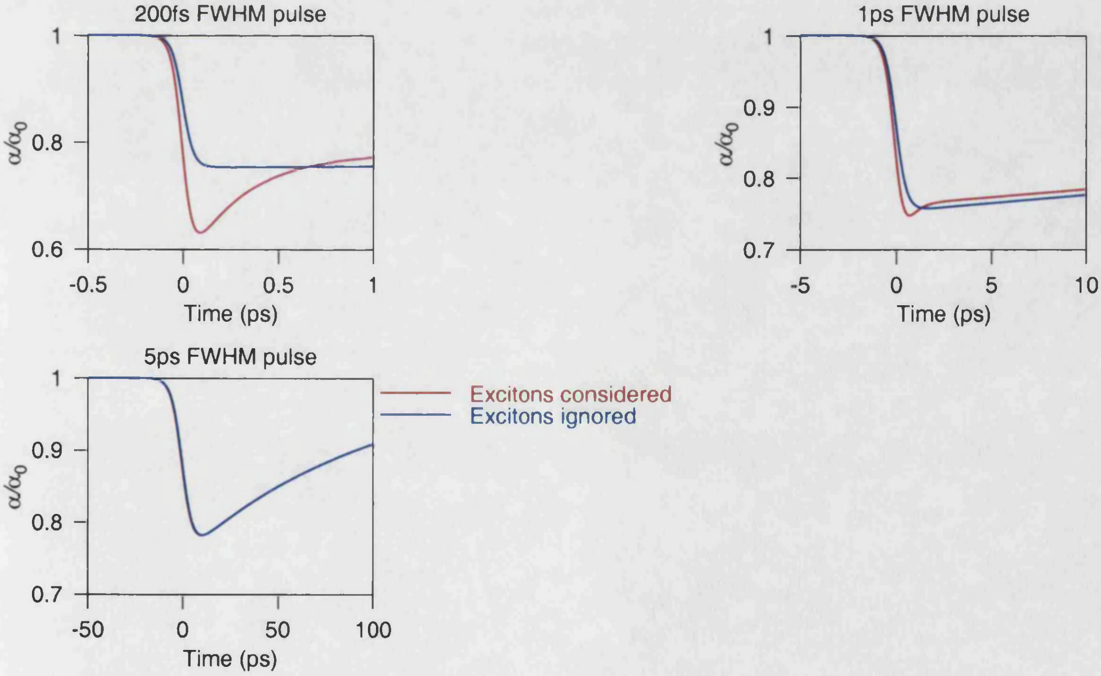

Figure A.1: Absorption change of an MQW in response to pulses of different lengths modelled with and without consideration of the exciton population. The two lines in the 5 ps plot are coincident.

A.7 Reduction of carrier lifetime

If the carrier lifetime in the MQW is reduced, through some mechanism such as ion implantation (Section 3.6) then, provided that the free carrier and exciton screening areas remain unchanged, the product $P_s\tau_{fc}$ can be expected to remain constant. A simple argument can be used to demonstrate this. The growth term in Equation A.18, $(1-n)P/P_s\tau_{fc}$ must remain constant as the value of τ_{fc} decreases, since the absorption process is independent of the recovery process.

Since $P_s\tau_{fc}$ is expected to remain constant as the carrier lifetime is reduced, it is convenient to use this, rather than P_s, to describe a given MQW saturable absorber (SA). $P_s\tau_{fc}$ can be given a physical meaning. It is the energy of an infinitely short pulse which will cause the free carrier population to increase from 0 to 1, and is thus referred to as the pulse saturation energy, E_s. When written in terms of E_s Equation A.17 becomes

$$\frac{dn}{dt}=\frac{(1-n)P}{E_s}-\frac{n}{\tau_{fc}}. \tag{A.19}$$

Use of E_s in the systems modelling allowed consistent comparisons of MQWs with different recovery times to be made.

A.8 Continuous wave solution

The CW solution of Equation A.19 can be found by putting $dn/dt=0$,

$$n=\frac{P/E_s}{1/\tau_{fc}+P/E_s}. \tag{A.20}$$

Since CW light is being considered is it more intuitive to state this in terms of P_s rather than E_s, and hence eliminate τ_{fc},

$$n=\frac{P/P_s}{1+P/P_s}. \tag{A.21}$$

Substituting this into Equation A.18, the CW transmission of the MQW will be

$$T=T_sR^{-1/(1+P/P_s)}. \tag{A.22}$$

References

[1] H. Haus and Y. Silberberg, "Theory of mode locking a laser diode with a multiple quantum well structure," *Journal of the Optical Society of America B*, vol. 2, pp. 1237–1243, July 1985.

[2] D. Chemla and D. Miller, "Room-temperature excitonic nonlinear-optical effects in semiconductor quantum-well structures," *Journal of the Optical Society of America B*, vol. 2, pp. 1155–1173, July 1985.

Appendix B

Results of transmission system modelling

This appendix presents plots of Q factor versus distance showing the results of the modelling of transmission systems using saturable absorbers for soliton control, and for all-optical wavelength conversion, which was described in Sections 2.6 and 2.7.

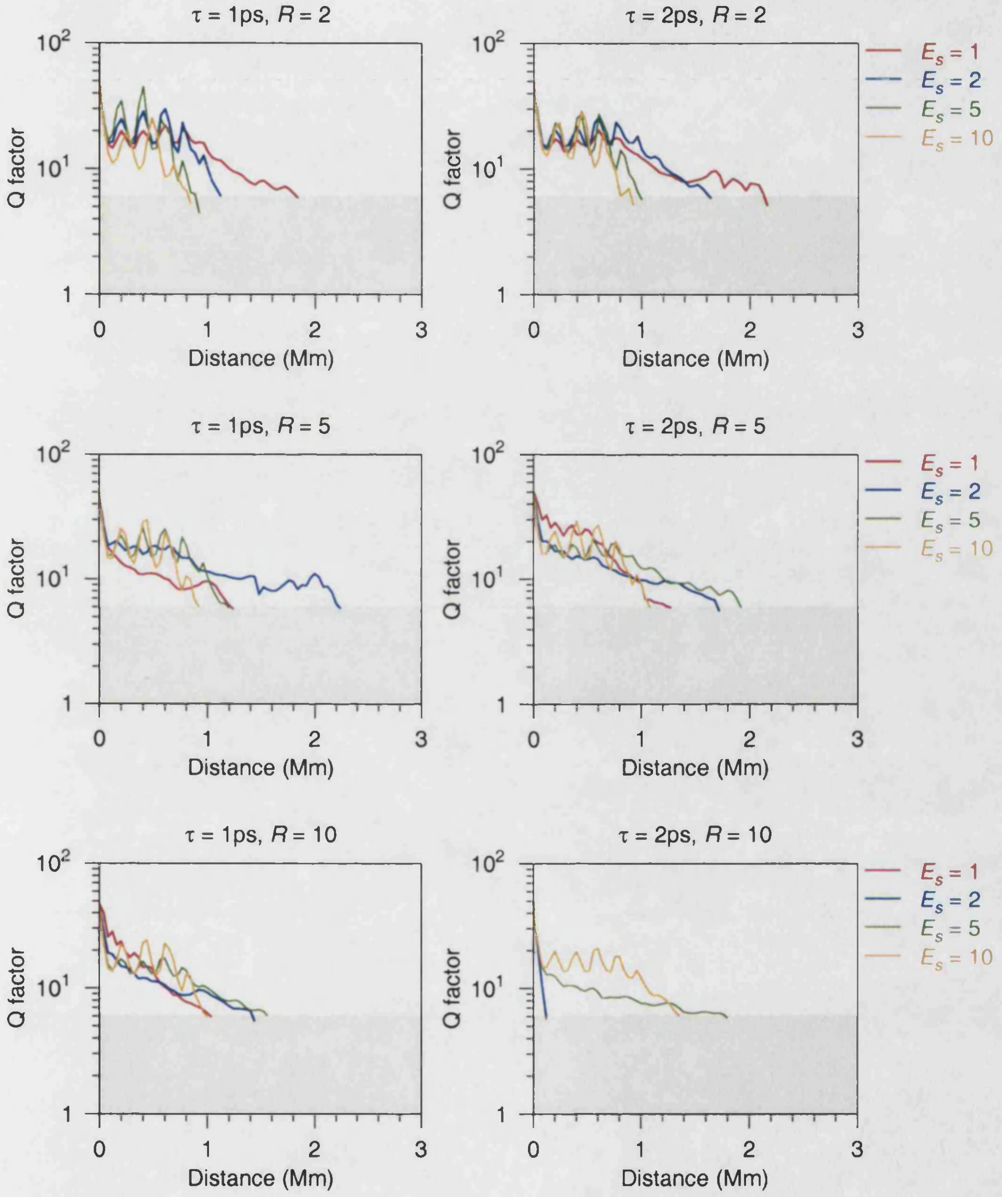

Figure B.1: Q factor versus distance plots for systems using 0.6 nm guiding filters and SAs with 10 dB excess loss and recovery times of 1 ps and 2 ps for soliton control.

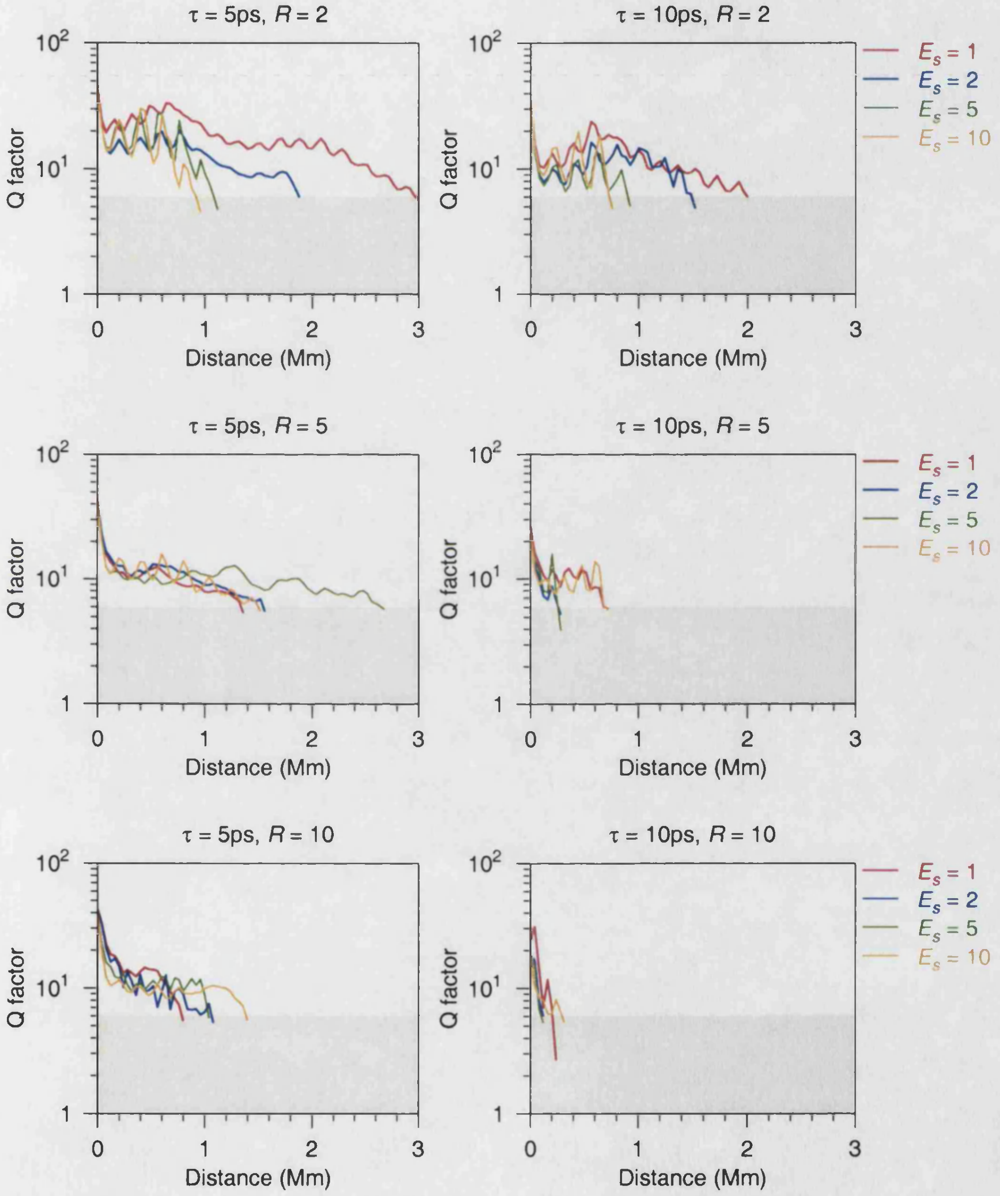

Figure B.2: Q factor versus distance plots for systems using 0.6 nm guiding filters and SAs with 10 dB excess loss and recovery times of 5 ps and 10 ps for soliton control.

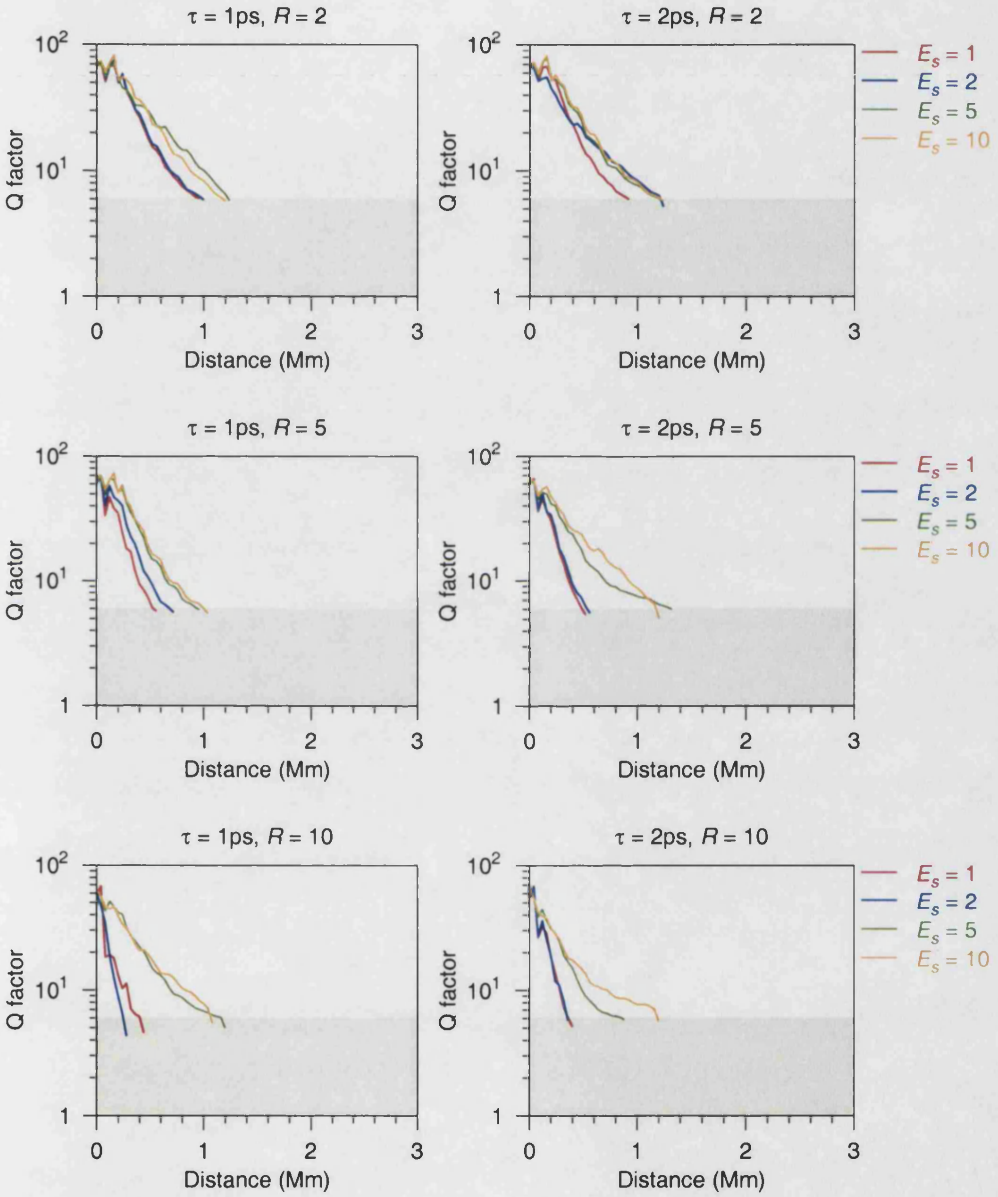

Figure B.3: Q factor versus distance plots for systems using 1.0nm guiding filters and SAs with 10dB excess loss and recovery times of 1 ps and 2 ps for soliton control.

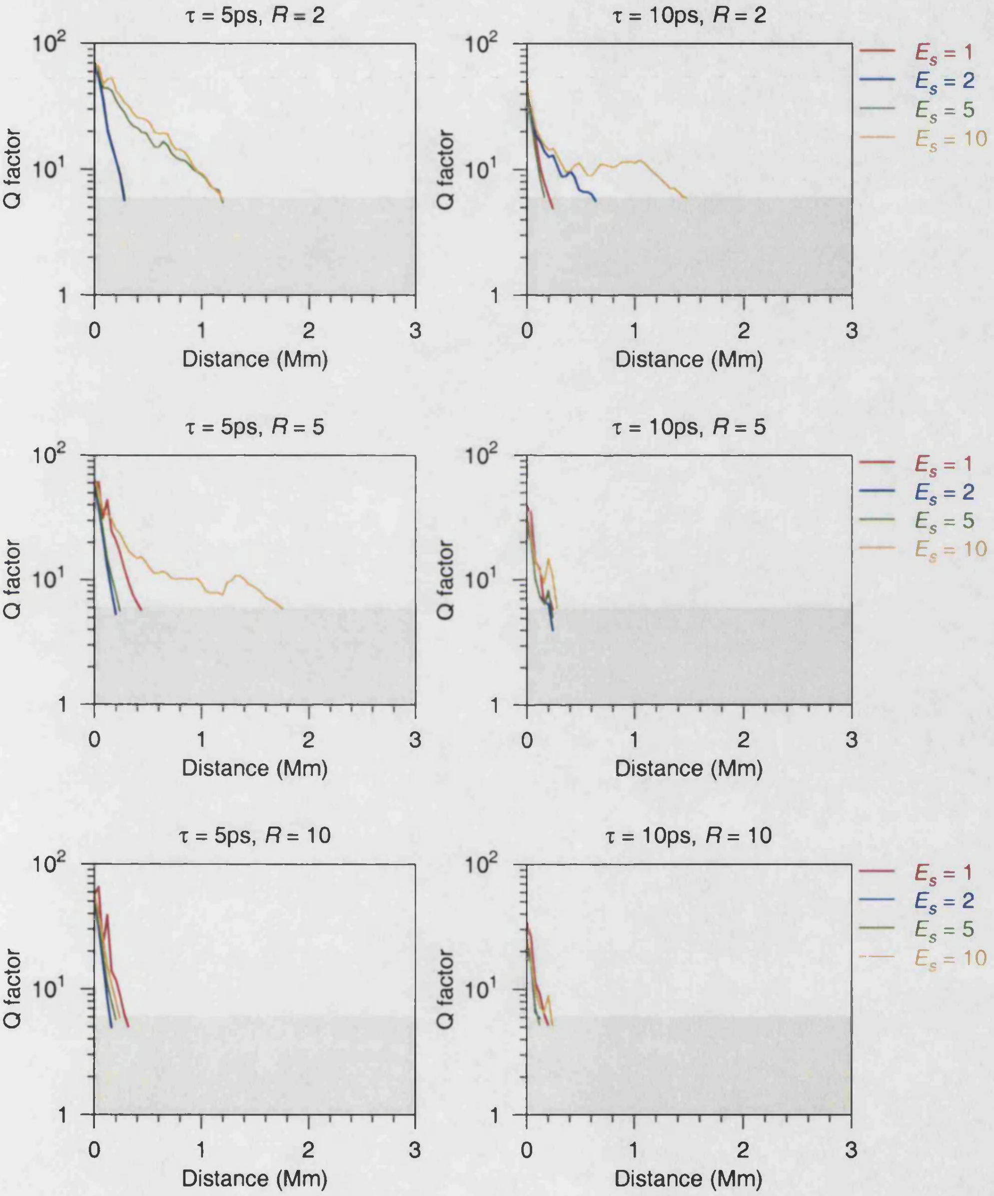

Figure B.4: Q factor versus distance plots for systems using 1.0 nm guiding filters and SAs with 10 dB excess loss and recovery times of 5 ps and 10 ps for soliton control.

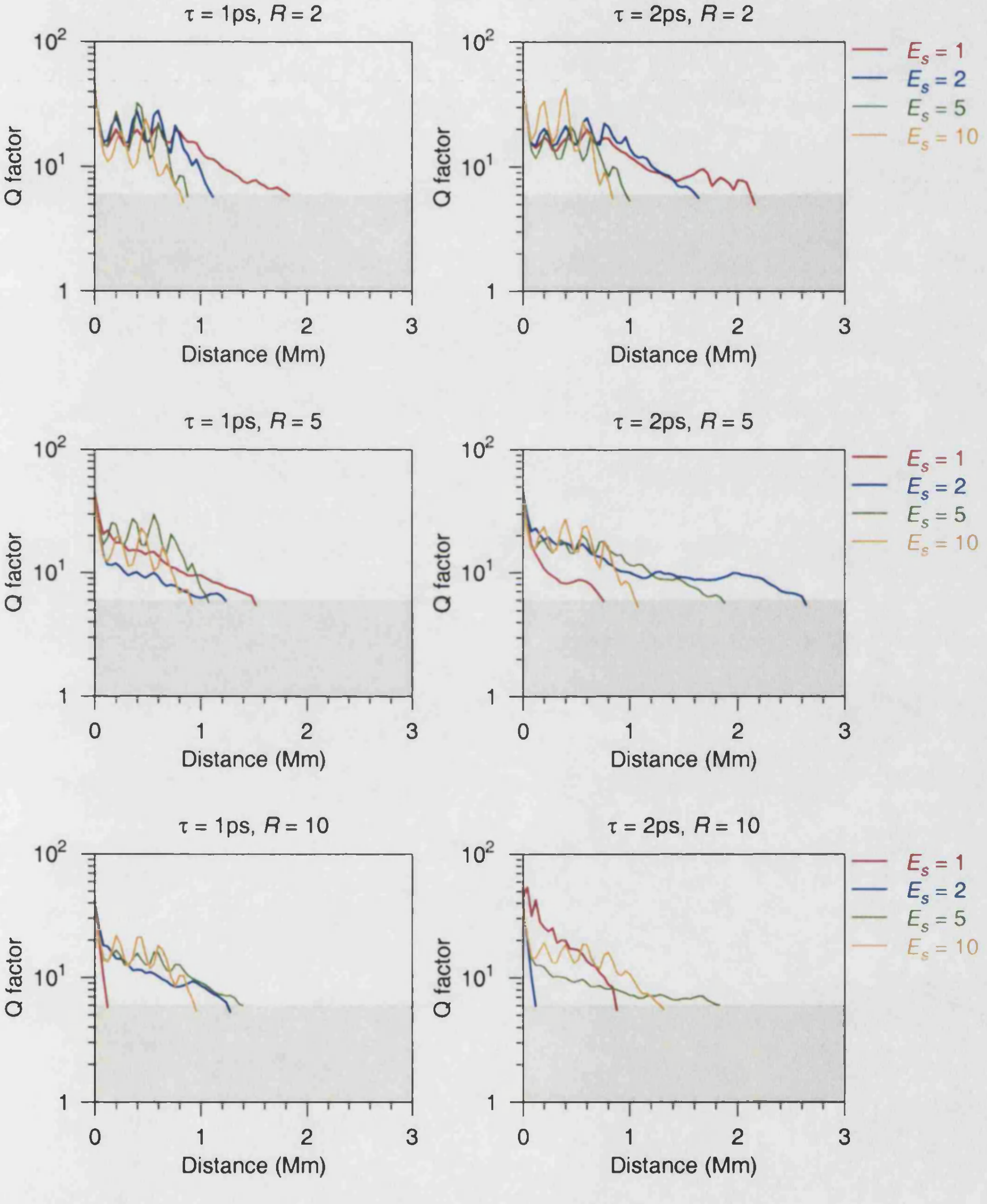

Figure B.5: Q factor versus distance plots for systems using 0.6 nm guiding filters and SAs with 16 dB excess loss for soliton control and recovery times of 1 ps and 2 ps.

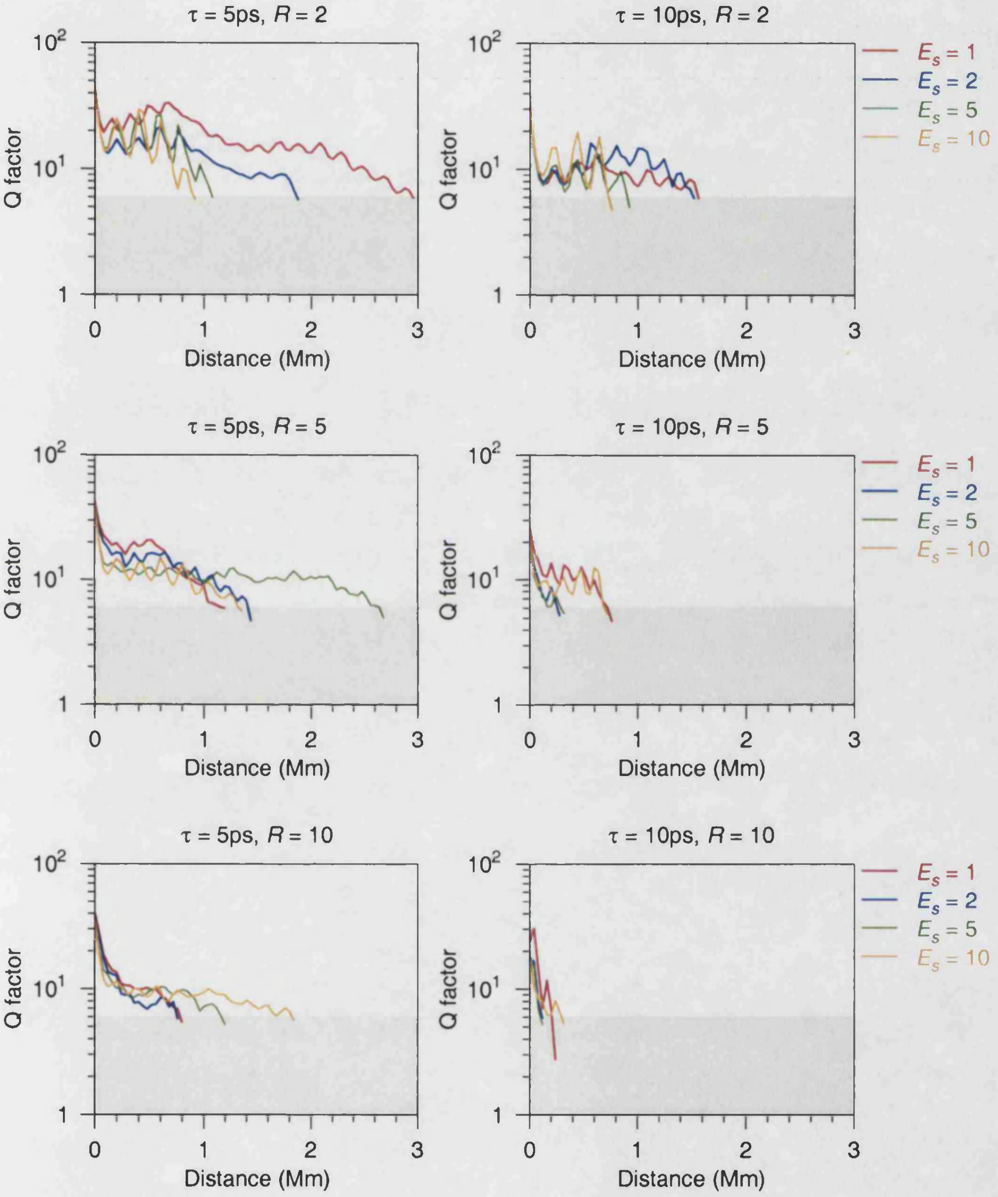

Figure B.6: Q factor versus distance plots for systems using 0.6 nm guiding filters and SAs with 16 dB excess loss and recovery times of 5 ps and 10 ps for soliton control.

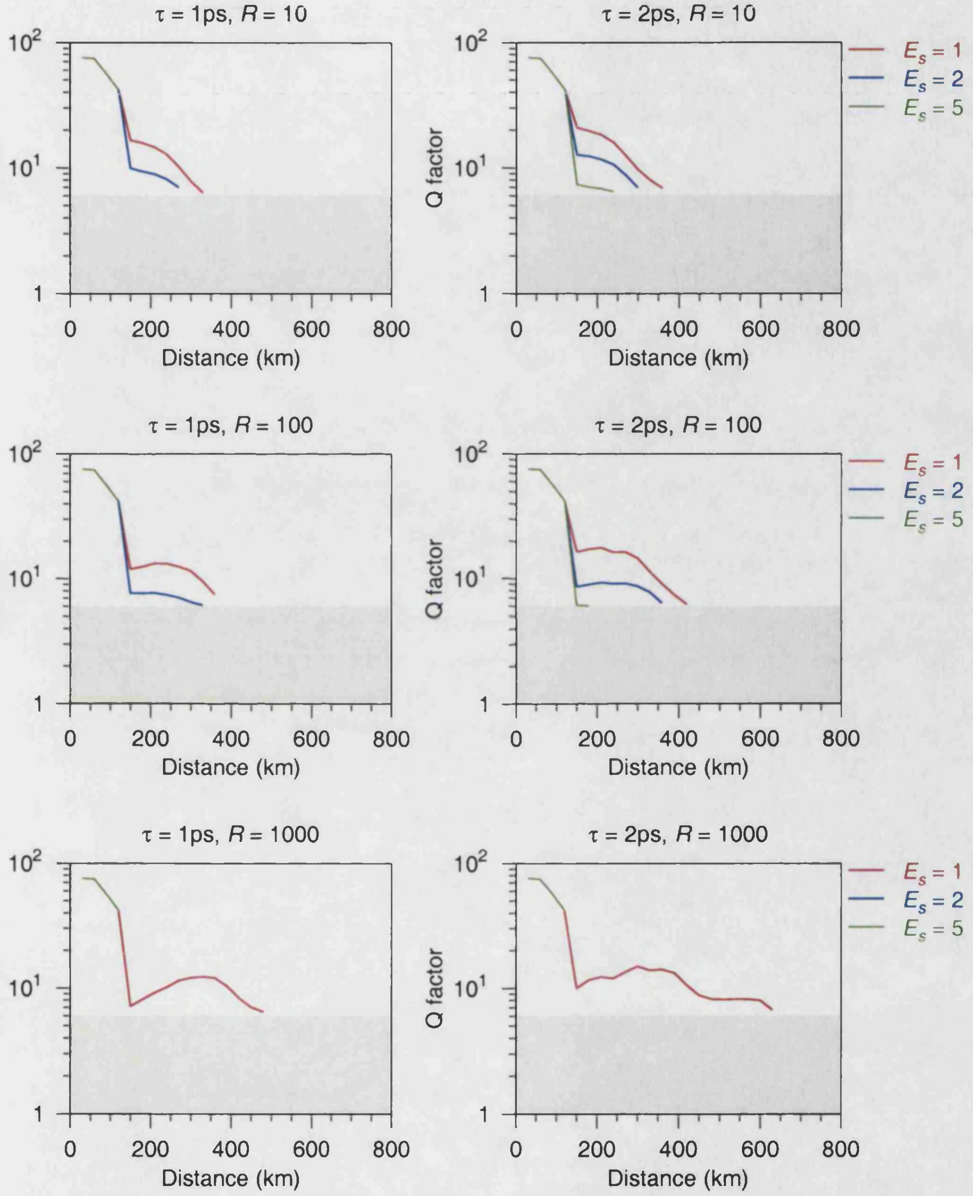

Figure B.7: Q factor versus distance plots for systems using SAs with recovery times of 1 ps and 2 ps for all-optical wavelength conversion.

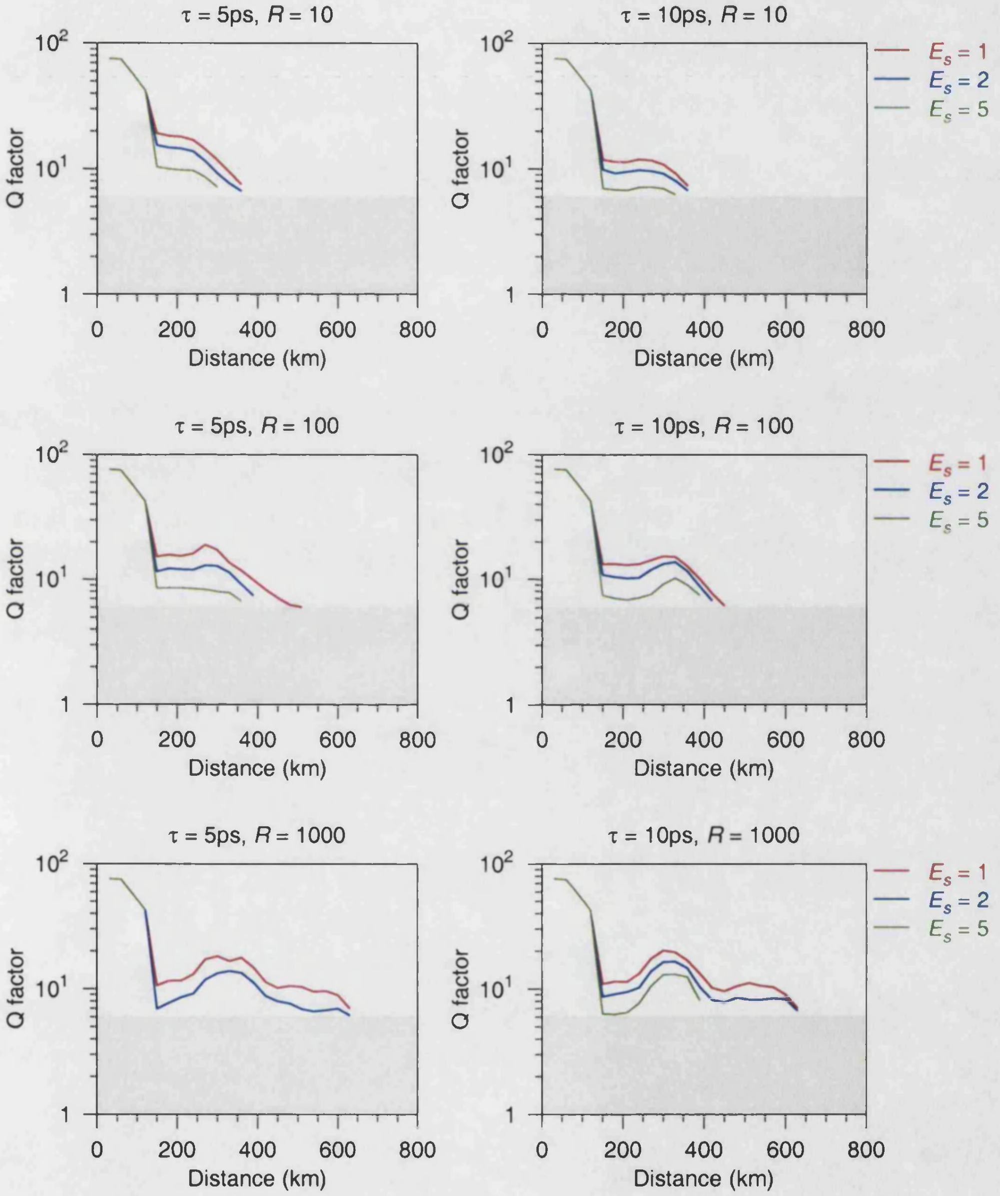

Figure B.8: Q factor versus distance plots for systems using SAs with recovery times of 5 ps and 10 ps for all-optical wavelength conversion.

Appendix C

Field screening device model

This appendix describes the computer model of field screening in p-i-n multiple quantum well (MQW) asymmetric Fabry-Perot (AFP) devices which was used to obtain the results of Section 3.4. The model allowed investigation of the following factors which influence the magnitude and timescale of the electric field change, and hence also of the MQW region absorption and device reflectivity changes, observed following absorption of picosecond optical pulses:

- The pulse energy.
- The pulse length.
- Diffusion coefficient for potential diffusion, which is determined by the p-region doping concentration and thickness.
- MQW region length.

The model does not attempt to accurately describe device behaviour in the regime in which the field in the intrinsic region of the p-i-n device approaches zero following absorption of a high energy optical pulse. Device behaviour in this regime is complicated by the increasing escape times for carriers generated in the wells, and the reduction of the carrier drift velocities. The model can, however, indicate the excitation energies which will lead to this regime.

C.1 Overview of the model

The model uses a cylindrical polar geometry. Circular symmetry of the p-i-n device is assumed, as illustrated in Figure C.1. Illumination is assumed to be by a uniform, circular optical spot, of radius r_0, incident at the centre of the optical window, which has the radius r_1. An optical cavity is formed between the air-semiconductor interface at the optical window, and a rear mirror, which is assumed to be 100% reflective. The model considers optical absorption and carrier transport in the intrinsic region, and movement of depletion charge due to the diffusive conduction process.

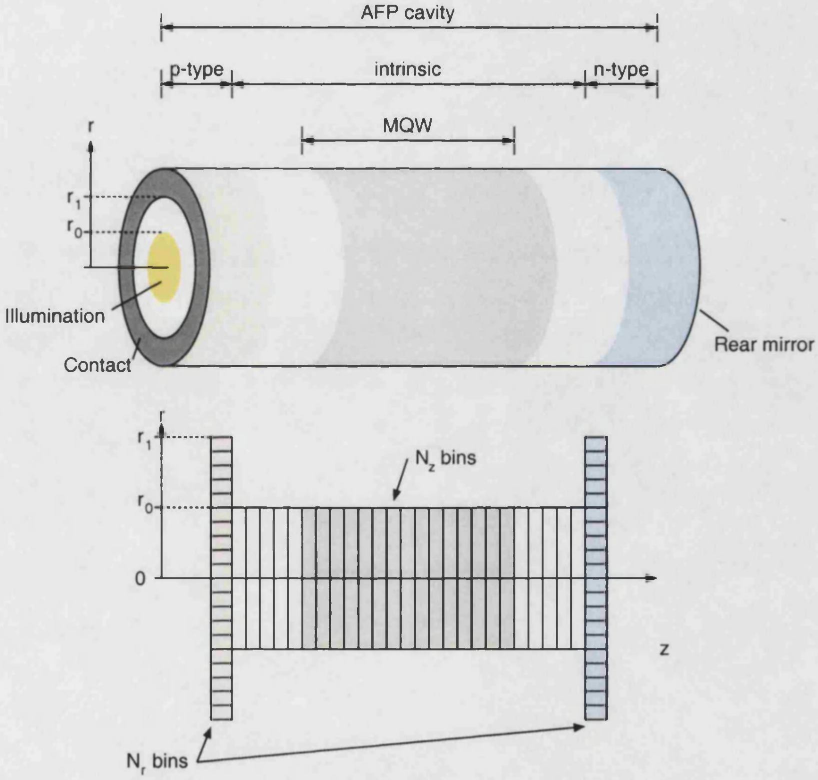

Figure C.1: Cylindrical geometry used for modelling. The n-type substrate and metal contact at the rear of the device are not shown.

It is assumed that, under the high reverse bias conditions which are of interest for fast field screening operation, carrier movement within the intrinsic region will be dominated by drift. Carrier diffusion in the intrinsic region is thus ignored. Only drift parallel to the direction of the applied field is considered. This simplification, which ignores drift along the potential gradients perpendicular to the z axis, is that used by Williams et. al. [1] for modelling of p-i-n photodetectors subject to intense illumination. Since carrier transport only occurs parallel to the z-axis, photocarrier populations and space charge within the intrinsic region can be considered within

N_z thin circular bins of radius r_0. Two-dimensional charge density due to depletion at the p-region/intrinsic region n-region/intrinsic region interfaces is considered in N_r ring shaped bins. The n_{th} bin extends from $r = n\Delta r$ to $r = (n+1)\Delta r$. The depletion charge changes as photocarriers drift out of the intrinsic region, and as carriers in the doped regions move to establish a uniform potential distribution across the area of the device through the diffusive conduction process.

C.2 Modelled quantities

To model photon absorption and hole and electron drift a number of variables are considered within N_z bins of length Δz along the z axis which determined these at intervals of Δt. These variables are, in the j_{th} bin during the i_{th} time interval,

- Optical power due to the standing wave in the cavity formed between the optical window and the rear mirror ($P_{s_{i,j}}$).
- Number of electrons ($N_{e_{i,j}}$).
- Number of electrons ($N_{e_{i,j}}$).
- Three dimensional charge density ($\rho_{i,j}$).
- Electric field ($\mathscr{E}_{i,j}$).

Charge density is considered within N_r ring shaped bins with radial extent Δ_r. The variables used, in the k_{th} bin during the i_{th} time interval, are

- Two dimensional density of depletion charge at the intrinsic region/p-region interface ($\rho_{p_{i,k}}$).
- Two dimensional density of depletion charge at the intrinsic region/n-region interface ($\rho_{n_{i,k}}$).
- Potential different across the intrinsic region ($V_{i,k}$).

C.3 Modelled processes

C.3.1 Absorption

The increase to the electron population due to optical absorption in can be expressed

$$N_{e_{i+1,j}} = N_{e_{i,j}} + \alpha\Delta L \frac{\Delta t P_{s_{i,j}}}{hf} \tag{C.1}$$

Similarly, for holes,

$$N_{h_{i+1,j}} = N_{h_{i,j}} + \alpha\Delta L \frac{\Delta t P_{s_{i,j}}}{hf} \tag{C.2}$$

C.3.2 Calculation of the electric field distribution

The electric field distribution in the illuminated region of the device is determined by summing the charge density. In the discrete notation of Section C.2

$$\mathscr{E}_{i,j} = \frac{1}{\varepsilon_r \varepsilon_0}\left(-\rho_{n_{i,0}} + \frac{1}{A}\sum_{j'=N_z-1}^{j'=j} e(N_{h_{i,j'}} - N_{e_{i,j'}})\right) \tag{C.3}$$

where ε_r = relative permittivity and ε_0 = permittivity of free space. The depletion charge density, and hence the depletion potential, is assumed to be constant throughout the illuminated part of the device.

C.3.3 Drift

$N_{e_{i,j}}$ and $N_{h_{i,j}}$ also change as electrons and holes drift along the z-axis. The electron and hole velocities, v_e and v_h are taken to be 10^7cm/s and 8^6cm/s respectively (see Section 3.7.3 for explanation) in large fields ($\mathscr{E} > 10^5$ kV/m). For smaller fields linear relationships between $\mathscr{E}$ and v_e and v_h are assumed, such that the carrier velocities are zero when $\mathscr{E} = 0$. This simplification of the relationship between field and drift velocity is not intended to be accurate, but to stabilise the model under heavy field screening conditions.

Electron drift is expressed as

$$N_{e_{i+1,j}} = \begin{cases} N_{e_{i,j}} - v_e \frac{\Delta t}{\Delta z} N_{e_{i,j}} & \text{for } i = 0 \\ N_{e_{i,j}} - v_e \frac{\Delta t}{\Delta z} N_{e_{i,j}} + v_e \frac{\Delta t}{\Delta z} N_{e_{i,j-1}}, & \text{for } i > 0 \end{cases} \tag{C.4}$$

and hole drift as

$$N_{h_{i+1,j}} = \begin{cases} N_{h_{i,j}} - v_h \frac{\Delta t}{\Delta z} N_{h_{i,j}} + v_h \frac{\Delta t}{\Delta z} N_{h_{i,j+1}} & \text{for } i < N_z \\ N_{h_{i,j}} - v_h \frac{\Delta t}{\Delta z} N_{h_{i,j}}. & \text{for } i = N_z \end{cases} \tag{C.5}$$

C.3.4 Diffusive conduction

To model diffusive conduction the potential across the device is first calculated. In the illuminated region,

$$V_{i,k} = \rho_{n_{0,k}} L \sum_{i'=N_z-1}^{i'=i} \mathscr{E}_{i,j} dz \tag{C.6}$$

and, in the non-illuminated region,

$$V_{i,k} = \rho_{n_{i,k}} L. \tag{C.7}$$

Diffusive conduction is considered by solving equation 3.4. In the representation used for the model

$$V_{i+1,k} = \begin{cases} V_{i,k} + \dfrac{1}{D}\dfrac{2V_{i,j} - 2V_{i,j+1}}{\Delta z^2} & \text{for } i = 0 \\ V_{i,k} + \dfrac{1}{D}\dfrac{2V_{i,j} - V_{i,j-1} - V_{i,j+1}}{\Delta z^2} & \text{for } 0 < i < N_r \end{cases} \tag{C.8}$$

where the diffusion coefficient, D, is defined in Section 3.3.1. $V_{N_{r,j}}$ is fixed at the reverse bias potential, V_R.

The rate of change of $V_{i,k}$ from Equation C.8 is used to determine rates of change for $\rho_{p_{i,0}}$ and $\rho_{n_{i,0}}$.

C.4 Iterative procedure

The model uses an iterative procedure, with the following steps being performed in each iteration:

- Model the effects of photon absorption using Equations C.1 and C.2.
- Calculate the electric field distribution using Equation C.3.
- Model the effects of carrier drift using Equations C.5 and C.5.
- Model the effects of potential diffusion using Equation C.8.

References

[1] K. Williams and R. Esman, "Design considerations for high-current photodetectors," *Journal of Lightwave Technology*, vol. 17, pp. 1443–1454, August 1999.

Appendix D

Detailed results of field screening device modelling

This appendix contains plots showing the evolution of the electric field distribution in the field screening device modelling described in Section 3.4.

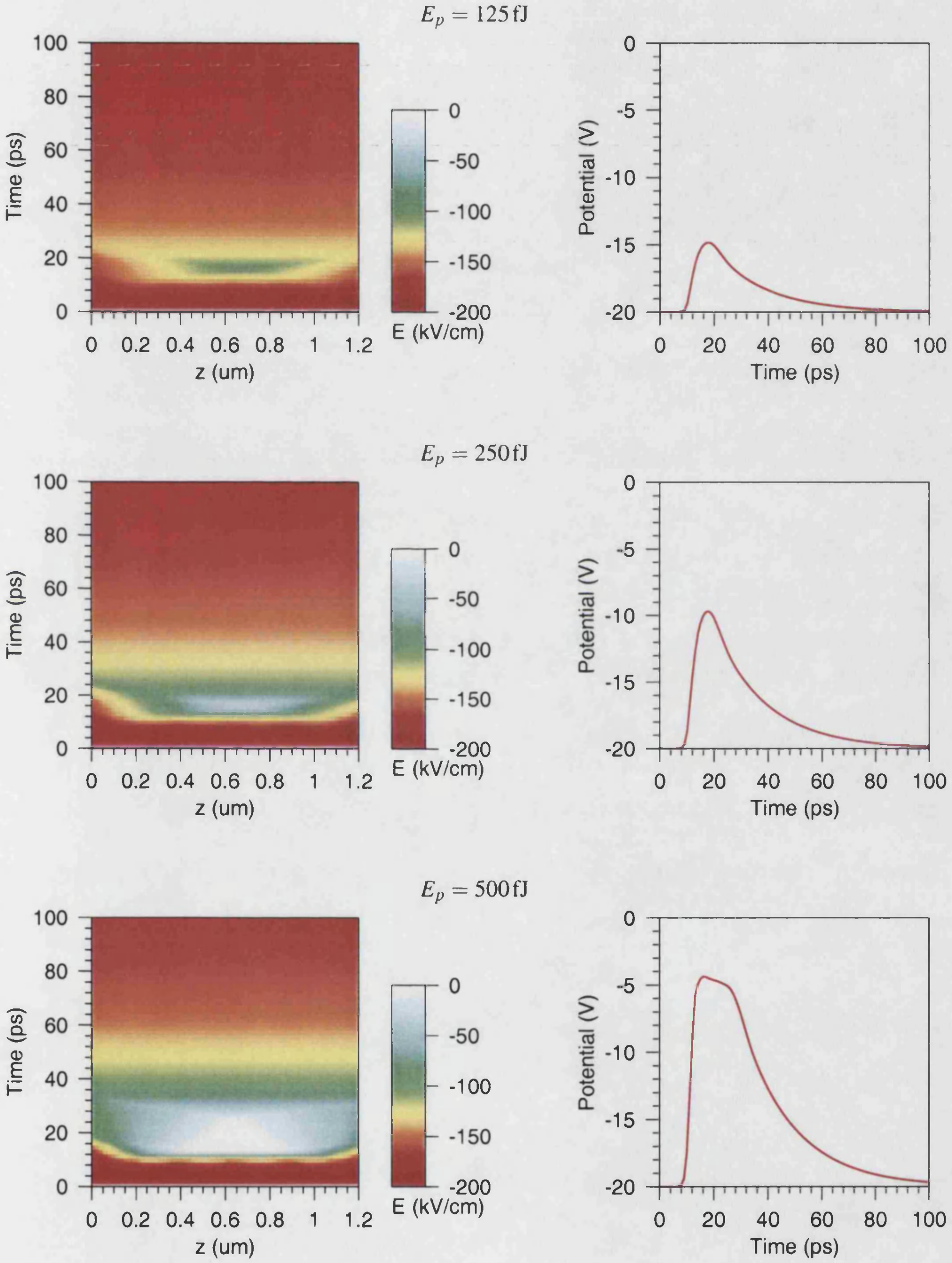

Figure D.1: Results showing the consequences of varying the energy of the exciting pulse, E_p, between 125 fJ and 500 fJ.

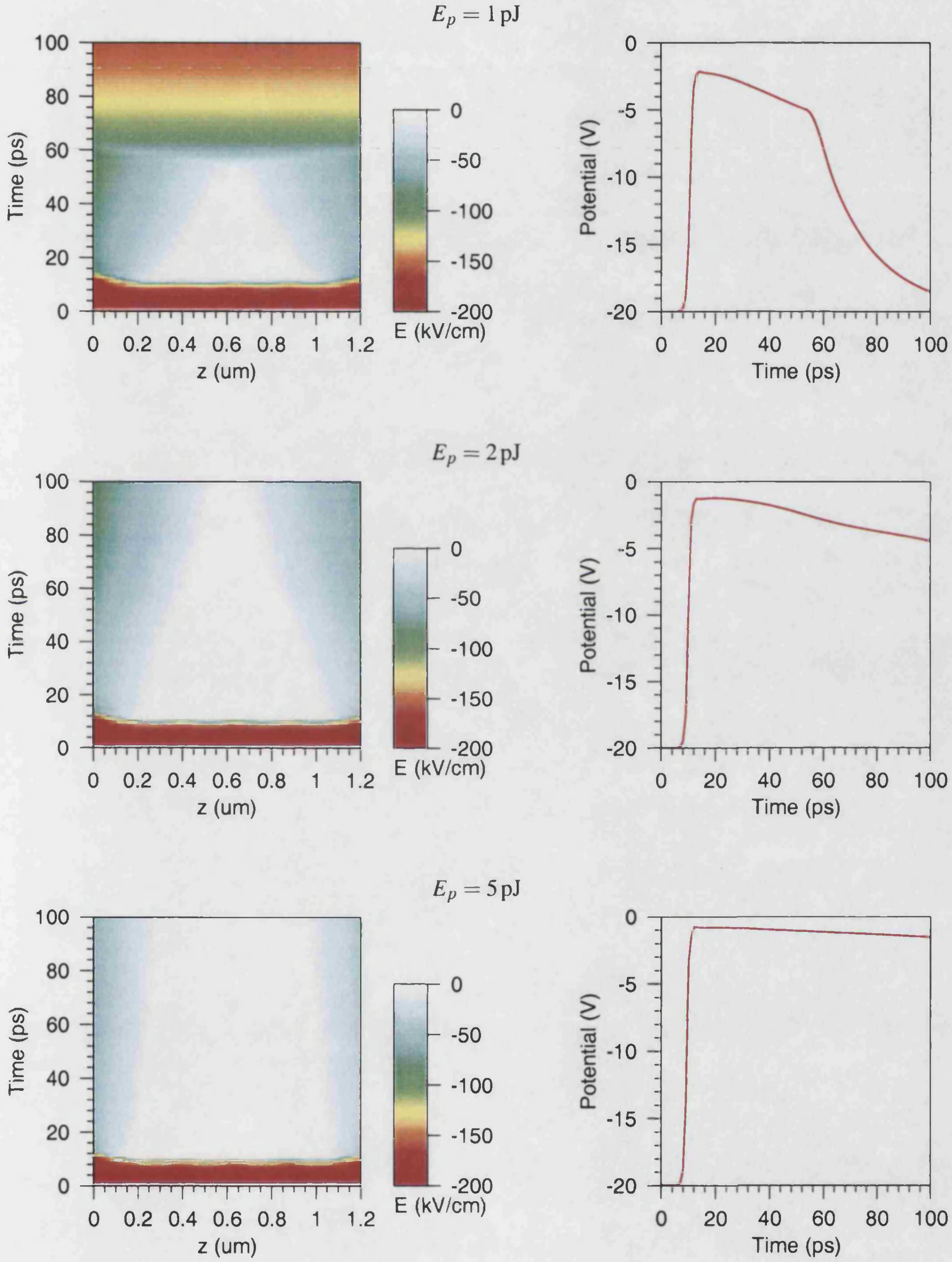

Figure D.2: Results showing the consequences of varying the energy of the exciting pulse, E_p, between 1 pJ and 5 pJ.

$\tau_{FWHM} = 2\,\mathrm{ps}$

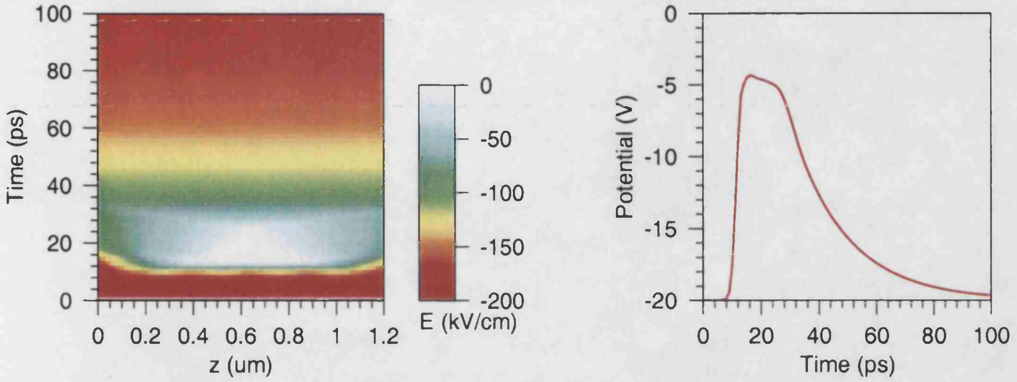

$\tau_{FWHM} = 5\,\mathrm{ps}$

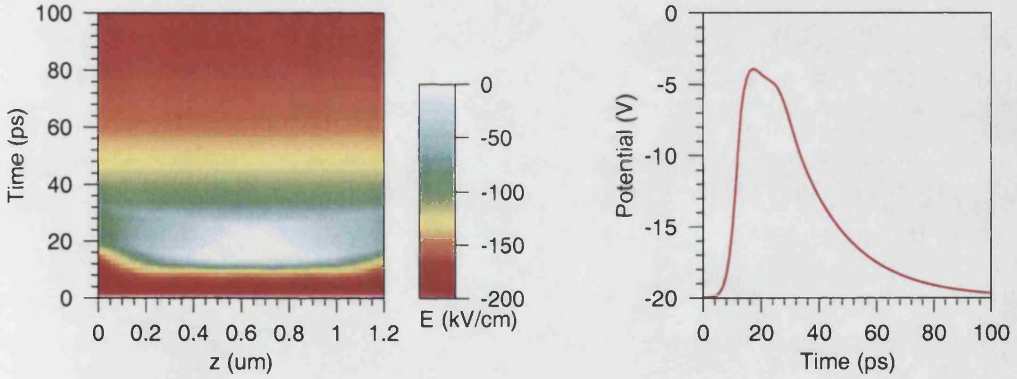

$\tau_{FWHM} = 10\,\mathrm{ps}$

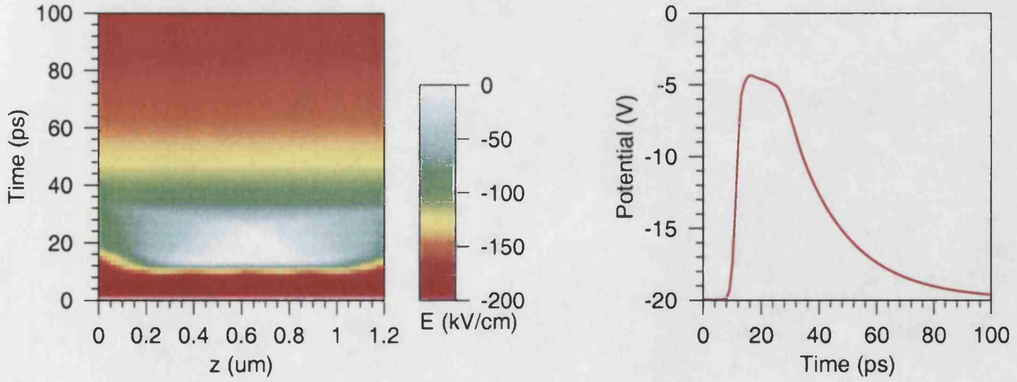

Figure D.3: Results showing the consequences of varying the FWHM width of the exciting pulse, τ_{FWHM}.

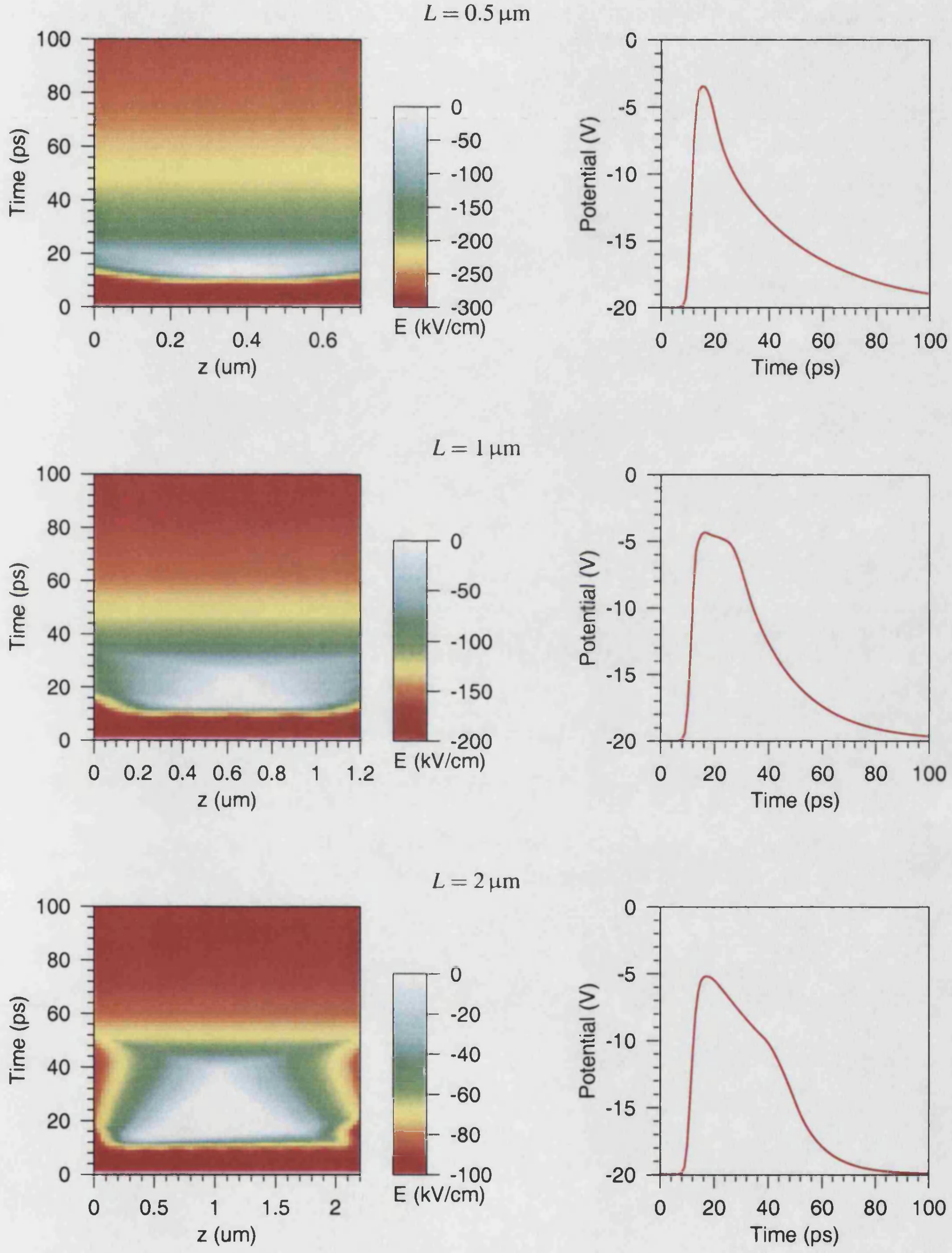

$L = 0.5\,\mu\mathrm{m}$

$L = 1\,\mu\mathrm{m}$

$L = 2\,\mu\mathrm{m}$

Figure D.4: Results showing the consequences of varying the MQW region length, *L*.

$L_p = 0.15\,\mu\text{m}$

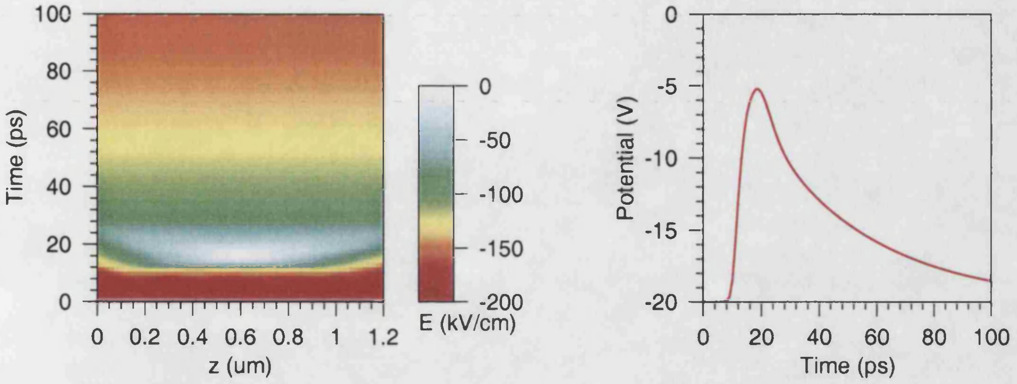

$L_p = 0.30\,\mu\text{m}$

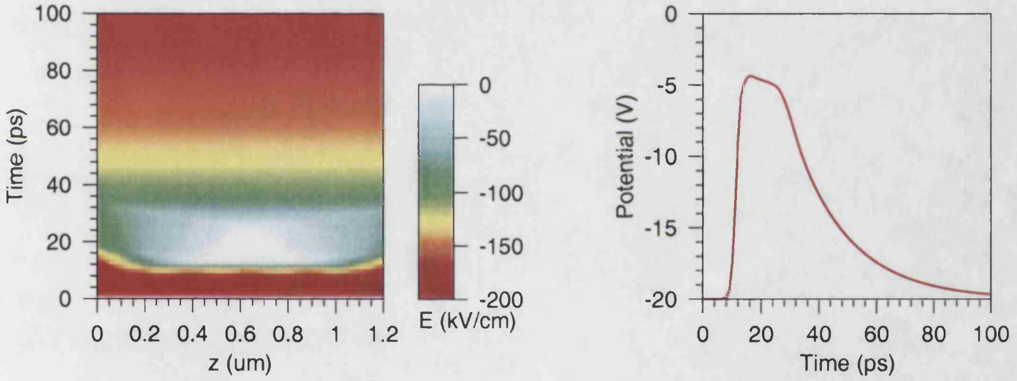

$L_p = 0.60\,\mu\text{m}$

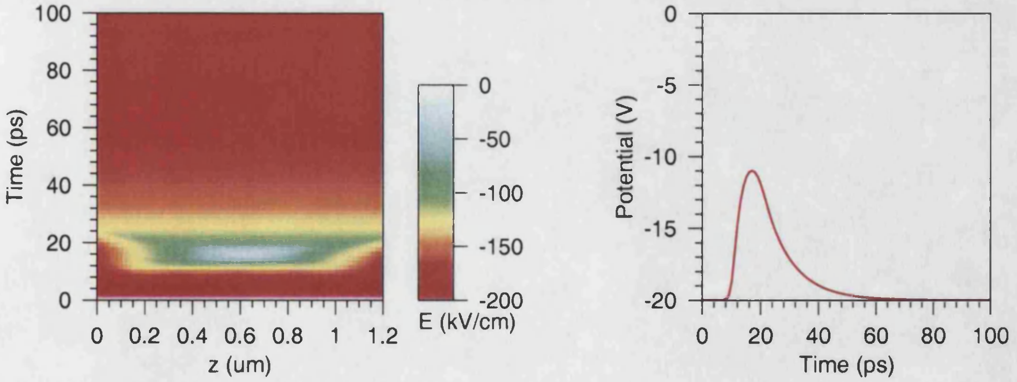

Figure D.5: Results showing the consequences of varying the p-region length, L_p.

Appendix E

Figure-of-eight mode-locked laser

A figure-of-eight mode-locked laser (MLL) was used as a source of short pulses in the experimental systems of Chapter 4. Section E.1 is a theoretical description of the operation of such lasers. The design of the laser which was constructed for use in the experiments is described in Section E.2.

E.1 Operation

The cavity of a fibre laser can support many closely spaced modes. If the laser operates in multiple modes with mutual phase coherence, and there is a suitable phase relationship between adjacent modes, the modes will interfere to produce a periodic signal in the time domain. This is known as mode-locking. Locking of many modes will result in the laser producing short pulses at the fundamental frequency of the cavity, which is the reciprocal of its round trip time (RTT).

The cavity of a passively mode-locked laser (MLL) incorporates a saturable absorber such that its loss is lower during mode-locked operation than during continuous wave (CW) operation. Harmonic MLL operation, in which pulses are produced at a multiple of the fundamental frequency, and the production of random pulse groups which are repeated at the fundamental frequency, are also possible.

An MLL may also be realised by incorporating a modulator in the cavity of a fibre laser. The modulator must be driven at the fundamental frequency of the cavity, or at a multiple for harmonic operation. Such MLL are said to be actively mode-locked.

The figure-of-eight MLL uses a non-linear amplifying loop mirror (NALM) as a saturable absorber. Since the NALM switches solitons [1], solitonic pulses are produced. A generic figure-of-eight MLL is illustrated in Figure E.1. This consists of two loops, referred to as the passive loop and the NALM loop, which are connected by a 3 dB fibre coupler to form a laser cavity. The gain of the NALM is set by the lasing condition. It must exactly compensate for the loss in the passive loop.

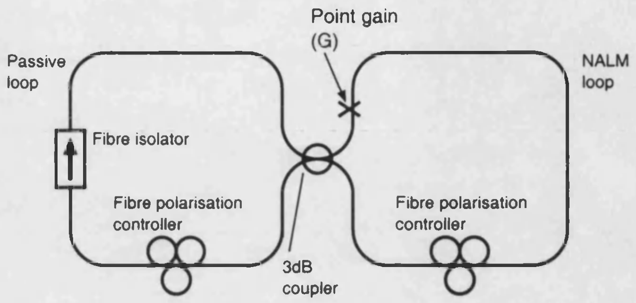

Figure E.1: Generic figure-of-eight MLL.

The polarisation controller in the NALM loop must be set such that the two counter-propagating signals in the NALM loop have the same polarisation when they return to the fibre coupler and can hence interfere. Additionally the non-reciprocal phase changes experienced by the signals in this polarisation controller must be such that the NALM is biased to preferentially transmit solitons. The polarisation controller in the passive loop must be set such that the polarisation of the signal is maintained over one round trip time.

E.2 Practical tunable laser

The figure-of-eight MLL used in the experiments described in this thesis, which was based on a design by Margulis et. al. [2], is shown in Figure E.2. Gain is provided by a 3 m length of erbium doped fibre (EDF) pumped at 980 nm through a wavelength division multiplexing fused biconical taper (FBT) coupler. The output is taken from the NALM loop immediately after the EDF for maximum pulse energy. The laser is tunable within the gain region of the EDF by means of a 3 nm bandwidth rotatable interference filter in the passive loop. In the absence of this filter the wavelength of operation would be determined by a combination of the EDF gain spectrum and the polarisation controller settings.

When the polarisation controllers are correctly set mode-locking is initiated by disturbing the cavity of the laser whilst it is pumped with approximately 200 mW. It initially produces random groups of first and higher order solitons, which are repeated at the cavity fundamental frequency. The pump power can be gradually reduced until the cavity contains a single first order soliton. Under this condition 2 ps full width half maximum (FWHM) pulses with an average power of 30 μW at a repetition rate of 4 MHz are produced.

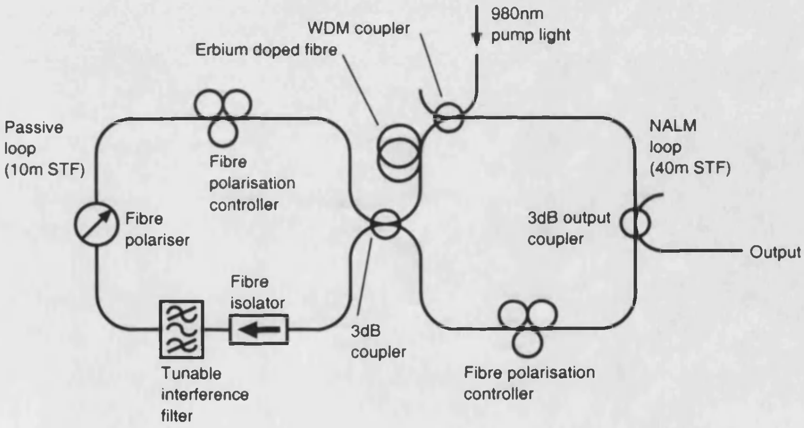

Figure E.2: Practical tunable figure-of-eight MLL.

References

[1] M. Fermann, F. Haberl, M. Hofer, and H. Hochreiter, "Nonlinear amplifying loop mirror," *Optics Letters*, vol. 15, pp. 752–754, July 1990.

[2] W. Margulis, K. Rottwitt, and J. Taylor, "High-power figure-of-eight laser for soliton transmission experiments," *Electronics Letters*, vol. 31, pp. 645–647, April 1995.

Appendix F

Alignment procedures for the experimental systems

This appendix describes alignment procedures for the experimental systems of Chapter 4.

F.1 Basic techniques

F.1.1 Mounting and positioning of optical fibres and objectives

Light was coupled into and out of fibre using the configuration of Figure F.1. The fibre is mounted on the moving platform of a Melles-Griot MicroBlock stage, allowing it to be translated along the x, y and z-axes. A 12 mm focal length laser diode objective, from Melles-Griot or Newport, is mounted on a fixed world platform attached to the MicroBlock stage.

The fibre is fitted with an FC/PC or FC/APC connector, which can be screwed to a standard bracket. This arrangement was found to offer better mechanical stability than the use of a bare fibre in a V-groove. The use of FC/APC (angled facet) connectors allows the reflection at the air-silica interface to be minimised. The same benefit could be achieved using angle cleaved or angle polished fibres.

F.1.2 Collimation of light launched from fibre

Many of the experiments required the arrangement of Figure F.1 to be used to collimate the light launched from the fibre. Movement along of the fibre along the z-axis controls the divergence or convergence of the beam, and hence allows collimation to be achieved. The collimated beam can be steered by moving the fibre along the x and y-axes.

When aligning for collimation light is launched from the fibre, and observed some metres

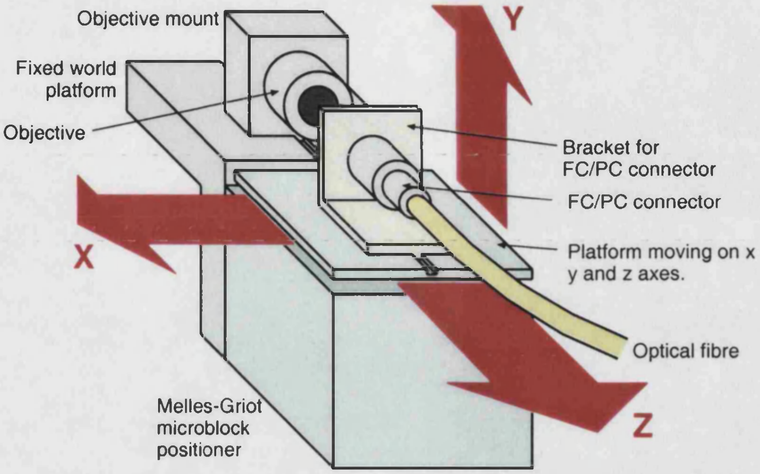

Figure F.1: Optical fibre and objective mounted on Melles-Griot MicroBlock and attached fixed world platform. The controls used to position the platform are omitted.

away using a fluorescent spot card. This technique has the disadvantage that components in the path of the free space beam must be removed whilst the alignment is made.

F.1.3 Coupling of light into fibre

When coupling light from free space into fibre using the arrangement of Figure F.1 movement along the x and y-axes is used to control the position, and movement along the z-axis the size, of the beam at the fibre facet. The beams is made coincident with the fibre core for optimal coupling efficiency. Coupling efficiencies of 60 % are possible.

F.2 Optical coupling for reflective devices

F.2.1 Configuration in which reflected light is coupled back into the input fibre

1. Objective 1 and the fibre are mounted using the arrangement of Figure F.1. The fibre is positioned such that the launched light is well collimated.

2. Objective 2 is mounted on a fixed platform attached to a second MicroBlock stage. The stage is positioned such that the axis of objective 2 is coincident with that of the beam.

3. The reflective non-linear device is mounted on the moving platform of the second MicroBlock stage, such that its pitch and yaw can be adjusted.

4. In the case of p-i-n devices, high power light is launched into the system and the device position on the x and y axes is adjusted to maximise the photocurrent.

5. An initial coarse alignment is carried out with high power light launched into the system. The pitch, yaw, and z-axis position of the device are adjusted for optimal coupling of the light back into the input fibre. The input fibre can also be translated along the x and y-axes to steer the beam.

6. The power of the launched light is then reduced sufficiently that it should not excite any optical non-linearity of the device and the device is re-positioned for optimal coupling. The symmetry of the system is such that, when it is aligned for optimal coupling in the absence of device non-linearity, the beam has the same geometry when it is incident on the device as when it is initially launched from fibre.

F.2.2 Configuration in which reflected light is coupled into an output fibre

1. Objective 1 and the fibre are mounted using the arrangement of Figure F.1. The fibre is positioned such that the launched light is well collimated.

2. Objective 2 is mounted on a fixed platform attached to a second MicroBlock stage. The stage is placed such that the axis of objective 2 is parallel with that of the beam, but displaced along the x-axis by approximately 1 mm.

3. The reflective non-linear device is mounted the moving platform of the second MicroBlock stage using a mount which allows its pitch and yaw, to be adjusted.

4. The device is positioned such that the reflected beam travelling between objective 2 and objective 1 is collimated, is parallel to the forward beam, and is horizontally displaced from the forward beam by approximately 2 mm. This alignment is made by observing the reflected beam using a fluorescent spot card.

5. The mirror is installed, such that its edge is almost blocking the beam travelling back from objective 2, and the beam reflected from it will be deflected through 90°.

6. Objective 3 and the output fibre are mounted on a MicroBlock stage. The position of the fibre is such that the launched light is well collimated.

7. With high power light launched into the input fibre, this stage is placed in the path of the light reflected from the mirror so that light is coupled into the output fibre.

8. The power launched into the input fibre is then reduced such that it is not sufficient to excite any device non-linearity. The x and y-axis positions of the output fibre, and the z-axis position of the device are adjusted to optimise coupling of light into the output fibre. The symmetry of the system is such that, when it is thus aligned for optimal coupling in the absence of device non-linearity, the beam has the same geometry when it is incident on the device as when it is initially launched from fibre.

F.3 Optical coupling for transmission devices

1. Objective 1 and the input fibre are mounted using the arrangement of Figure F.1. The fibre is positioned such that the launched light is well collimated.

2. Objective 2 is mounted on a fixed platform which is placed such that the axis of the objective is coincident with that of the beam. The geometry of the beam at the waist one focal length from the centre of objective two will be same as that of the beam initially launched from fibre.

3. Objective 3 is mounted on a MicroBlock stage and positioned such that its axis is coincident with that of the beam, and it re-collimates the beam.

4. Objective 4 and the output fibre are mounted using the arrangement of Figure F.1. The stage is placed such that the axis objective 4 is coincident with that of the beam.

5. The output fibre is positioned such that light is efficiently coupled into it.

6. The non-linear device is placed between objectives 3 and 4.

7. The beam waist is located by launching high energy pulses from the input fibre and monitoring the power coupled into the output fibre as the device sample is moved along the axis of the beam. The non-linearity results in a peak in the output power which is observed as the sample moves through the beam waist. This peak can be readily distinguished from fluctuations due to variations of the efficiency with which the beam is coupled into the output fibre.

8. The position of the output fibre is again adjusted to optimise coupling.

F.4 Variable delay

The alignment procedure for the variable delay of Figure 4.7 which was used in the pump-probe experiments is described below. The procedure aim to achieve coupling of reflected light back into the fibre which is efficient and, as far as possible, uniform when the mirror is moved along the length of the translation stage.

1. Objective 1 and the input fibre are mounted using the arrangement of Figure F.1. The fibre is positioned such that the launched light is well collimated.
2. The mirror is mounted on a stage which allows adjustment of its pitch and yaw. This stage is mounted on the translation stage which is moved to its central position.
3. The translation stage is moved to its central position and the pitch and yaw of the mirror are adjusted top couple reflected light back into the fibre.
4. The position of the fibre on the x and y-axes is adjusted to optimise coupling.

F.5 Coupling system for time resolved transmission and reflectivity measurements

1. Initially the lengths of the fibre components in the pump-probe interferometer are adjusted such that the pump and probe pulses are launched into free space at approximately the same time. Fibre can be spliced into, or removed from, the pump or probe paths as required.
2. The probe input fibre, and the associated objective, are mounted using the arrangement of Figure F.1. The fibre is positioned such that the launched light is well collimated.
3. The mirror is mounted on a stage allowing adjustment of its pitch and yaw and placed such that it almost blocks the probe beam, and is at an angle of 45° to the probe beam.
4. The probe input fibre, and the associated objective, are mounted using the arrangement of Figure F.1. The fibre is positioned such that the launched light is well collimated. The MicroBlock stage is placed so that the probe beam is launched at an angle of 90° to the pump beam, hits the mirror, and is deflected to be parallel with the probe beam. The distance between the two beams should be approximately 2 mm. The arrival time of the pump and probe pulses at the device should be identical when the variable delay is set to some value close to its minimum.

5. The remaining components in the probe path are mounted using the relevant procedure from Section F.2.
6. The block is placed such that the pump light reflected from, or transmitted by, the device is obstructed.
7. The variable delay is set such that the probe pulses arrive at the device under test later than the pump pulses, but with the delay between them not significantly greater than the device recovery time. This is most easily done if the non-linear device under test has a slow recovery time. Practically, the system is aligned using such a slow device, which can then be replaced with a faster device.
8. The pump beam is then steered to be coincident with the probe beam at the device. Steering is accomplished moving the pump fibre along the x and y-axes of the MicroBlock on which it is mounted, and by adjusting the pitch and yaw of the mirror. Coincidence is detected by monitoring the signals on the lock-in amplifier.

F.6 Coupling system low repetition rate wavelength conversion

The alignment procedure is identical to that for the coupling system for time resolved transmission and reflectivity measurements described in Section F.5, with the exceptions that the lengths of the pump and probe paths are non-critical and, at the final stage, the trace on the fast oscilloscope is monitored to detect modulation of the reflected continuous wave (CW) light.

F.7 Coupling system for time resolved polarisation rotation measurements

1. The system for time-resolved measurements of reflectivity is set up, as described in Section F.5. This procedure is carried out with the polarisation beam splitter (PBS) cube and the quarter wave plate in the free space pump path, and the PBS cube in the free space probe path, in place and the lock-in measuring the non-polarisation-rotated component of the reflected pump signal.
2. The variable delay is set such that the probe pulses arrive at the device under test later than the pump pulses, but with the delay between them not significantly greater than the spin relaxation time.

3. Objective 3 and the associated fibre are mounted using the arrangement of Figure F.1 and placed such that the polarisation-rotated component of the reflected probe light is coupled into the fibre.
4. The lock-in amplifier is reconnected, such that it is measuring the polarisation-rotated component of the reflected pump signal.
5. The fibre is positioned for optimal coupling of the polarisation-rotated component of the reflected probe light.

Appendix G

Publication list

S. Bennett, B. Cai, E. Burr, O. Gough, and A.J. Seeds, *1.8 THz bandwidth, zero-frequency error, tunable optical comb generator for DWDM applications*, OFC 1999.

S. Bennett, B. Cai, E. Burr, O. Gough, and A.J. Seeds, *1.8 THz bandwidth, zero-frequency error, tunable optical comb generator for DWDM applications*, IEEE Photonics Technology Letters , Vol. 11, pp. 551–553, May 1999.

E. P. Burr, J. Song, A. J. Seeds and C. C. Button, *60 ps recovery time in an InGaAsP quaternary multiple quantum well saturable absorber employing carrier sweep-Out*, CLEO Europe 2000.

E. P. Burr, J.B. Song, and A. J. Seeds, and C. C. Button, *28 ps recovery time in an InGaAsP/InGaAsP multiple-quantum-well saturable absorber employing carrier sweepout*, Journal of Applied Physics, Vol. 90, pp. 3566–3569, October 2001.

E.P. Burr, M. Pantouvaki, A.J. Seeds, C.C. Button, S.M. Pinches and R.M. Gwilliam, *Wavelength conversion of 1.53 micron picosecond pulses in an ion-implanted multiple quantum well all-optical switch*, CLEO 2002.

M. Pantouvaki, E. Burr, R. Feced, M. Fice, R. Gwilliam, J.S. Roberts and A.J. Seeds, *40 Gb/s Optical Noise Suppression and Wavelength Conversion by MQW Saturable Absorber integrated in a Fabry-Perot cavity*, ECOC 2002.

E. P. Burr, M. Pantouvaki, A. J. Seeds, R. M. Gwilliam, S. M. Pinches and C. C. Button, *Wavelength conversion of 1.53-mm-wavelength picosecond pulses in an ion-implanted multiple-quantum-well all-optical switch*, Optics Letters, Vol. 28, pp. 483-485, March 2003.

M. Pantouvaki, R. Gwilliam, E. P. Burr, A. B. Krysa, J. S. Roberts and A. J. Seeds, *Ultrafast Recovery Times And Increased Absorption Nonlinearity In InGaAsP MQW Saturable Absorbers Implanted At* 200 °C, IPRM 2003.

M. Pantouvaki, E. P. Burr, A. J. Seeds, R. Gwilliam and A. B. Krysa, *Enhanced 10 Gb/s error-free transmission distance using all-optical 2R regeneration with ion-implanted MQW saturable absorber and non-linear fibre*, CLEO 2003.